System Identification and State Reconstruction for Autonomous Navigation of an Underwater Vehicle in an Acoustic Net

by

Archie Todd Morrison III
B. A., Engineering and Applied Science, Harvard University (1981)

Submitted in partial fulfillment of the
requirements for the dual degrees of
OCEAN ENGINEER
at the
MASSACHUSETTS INSTITUTE OF TECHNOLOGY
and the
WOODS HOLE OCEANOGRAPHIC INSTITUTION
and
MASTER OF SCIENCE IN OCEAN ENGINEERING
at the
MASSACHUSETTS INSTITUTE OF TECHNOLOGY
January 1994

Signature of Author _____

Department of Ocean Engineering, MIT and the
MIT-WHOI Joint Program in Oceanographic Engineering

Certified by _____

Dr. Dana R. Yoerger
Woods Hole Oceanographic Institution
Thesis Supervisor

Accepted by _____

Professor Arthur B. Baggeroer, Chairperson
Joint Committee for Oceanographic Engineering
Massachusetts Institute of Technology and the
Woods Hole Oceanographic Institution

System Identification and State Reconstruction for Autonomous Navigation of an Underwater Vehicle in an Acoustic Net

by

Archie Todd Morrison III

Submitted to the Massachusetts Institute of Technology/
Woods Hole Oceanographic Institution
Joint Program in Oceanographic Engineering
on January 14, 1994 in partial fulfillment of the
requirements for the dual degrees of

OCEAN ENGINEER

and

MASTER OF SCIENCE IN OCEAN ENGINEERING

Abstract

Closed loop control of an underwater vehicle in an acoustic position net requires an accurate hydrodynamic model of the vehicle. The model is essential to the control algorithm design process. Further, it is an integral part of the observer used to generate complete state estimates from the position measurements. An experimental apparatus and numerical analysis technique for vehicle system identification during the thruster induced hover limit cycle are described. Detailed comparisons to other techniques are made and extension of the technique to four degrees of freedom with coupling is discussed. A model of the Remotely Operated Vehicle Hylas is determined.

The model determined by the system identification procedure is then used in the designs of a state estimator and controller for trajectory following by the vehicle. The algorithms are initially evaluated in a numerical simulation. Tests are made for stability, trajectory following performance, and accuracy of the state estimator under varying system and environmental conditions.

Finally, the results of vehicle trials are presented. System stability and accurate trajectory following under the control of the algorithms are demonstrated using ROV Hylas. The high accuracy level of the simulation is also demonstrated by the trials and directions for continued research are discussed.

Thesis Supervisor: Dr. Dana R. Yoerger

Associate Scientist
Woods Hole Oceanographic Institution

Acknowledgements

First, I would like to thank my adviser, Dana Yoerger, for his support and advice while this research was conducted and documented.

I would also like to extend my thanks to those at Woods Hole, MIT, and other locales who have willingly offered their time and knowledge through discussion, instruction, and advice. Jake Peirson, John Farrington, Stella Callagee, Abbie Jackson, and Ronnie Schwartz have always been there with the answers when I had questions. Jim Lynch has provided valuable advice as well as appropriate prodding towards the completion of this thesis. I consider myself fortunate to have been taught by Sue Cloutier, Rod Spurr, Gordon Ivanosky, Ed Yarosh, Ed Herlin, Al Palumbo, Al Pandiscio, Mike Triantafyllou, Paul Sclavounos, James Williams, Tomasz Wierzbicki, Clay Thompson, Jae Lim, Jim Kirtley, and Jim Irish. They all stand out in my mind as teachers of note. Their instruction has made significant contributions to the sum of my knowledge and they have left lasting impressions on the way I approach problems. Turgut Sarpkaya has kindly contributed some of his data as well as his considerable knowledge of hydrodynamics to my endeavors here. Lastly, my thanks to Sandy Williams, another teacher of note, for his support and friendship.

Well designed software has been integral to this investigation so it seems appropriate to thank the The MathWorks, Inc., Leslie Lamport, Richard Stallman, and the Free Software Foundation, Inc.

The financial support of the National Science Foundation on Grant No. OCE-8820227 and the Office of Naval Research under Contract No. N00014-90-J-1912 is gratefully acknowledged.

These acknowledgements would be grievously incomplete without special mention of some people who have provided me with particularly valued support while this research was in progress. For knowledge shared, services rendered, and especially friendship I would like to thank Helen Huang, Hanumant Singh, Fred Thwaites, Tom Woodford, and Mohamed Yahiaoui.

Finally, I would like to thank my parents, Archie and Beverly, for teaching me the things I really needed to know.

Author's Biographical Note

Archie Todd Morrison III graduated from Harvard University in 1981 with a Bachelor of Arts degree, *cum laude*, in Engineering and Applied Science / Electrical Engineering. While there he maintained a minor subject in Early and Oral Literatures. From 1981 until 1986 he was employed as a Senior Field Engineer by Raytheon servicing missile fire control radars operated by the United States and foreign navies.

During 1986 and 1987, the author returned to academia to study mathematics as a special student at Yale University. In 1987 he married Hilary Ann Gonzalez and moved to Atlanta so she could accept a postdoctoral fellowship at the Centers for Disease Control. He spent the two subsequent years operating a soup kitchen and maintaining a secure mailing address for thirty-five hundred homeless residents of that city.

In 1989 they returned to New England where Todd began graduate work in the Massachusetts Institute of Technology / Woods Hole Oceanographic Institution Joint Program in Oceanographic Engineering. Hilary and Todd have a daughter, Abigail Michelle, born in 1992. They currently live in West Falmouth, Massachusetts and commute to Woods Hole where Hilary works at the Marine Biological Laboratory and the Woods Hole Oceanographic Institution, and Todd continues his research in the Joint Program.

For

Hilary

and

Abigail

who make getting home

the best part of any day.

Contents

List of Figures

List of Tables

Chapter 1

Introduction

1.1 Background and Objectives

Unmanned, remotely operated underwater vehicles (ROVs) currently enjoy wide use in ocean research and industry. Position control and trajectory following tasks are generally accomplished by a human operator interacting with the vehicle through video cameras, joysticks, and other information links. Human control of motion in one angular and three translational degrees of freedom is difficult. The problem is exacerbated by frequently poor visibility, limited fields of view, and variable environmental forcing. Full state, closed loop control of an ROV permits the automation of such tasks as fixed point hover, heading or depth maintenance during operator guided horizontal motion, and fully automated trajectory following. Positioning accuracy is increased and the operator is free to concentrate on observations and data collection. An illustrative example is guidance of a manipulator arm during object recovery. Automated station holding by the vehicle fixes the position of the base of the arm and reduces the multiple degree of freedom task load by more than half.

Closed loop control will also be essential for the coming generation of autonomous underwater vehicles (AUVs) currently under development or in the early phases of testing. These vehicles will be used for automated mapping and survey work at remote sites. For example, the evolution of a hydrothermal vent field, its plumes, and the surrounding benthic ecosystem, on time scales ranging from hours to months,

can be recorded by an AUV designed to operate in the benthos. Data collection and return will require abilities such as following preplanned trajectories and tracing and recording thermal and chemical contours and gradients in the environment. Long term deployments will require periodic return to and precise mating with a locking cradle to extend battery life with a low power mode between surveys. Closed loop control is the indispensable foundation of these capabilities.

Closing the control loop requires information about the vehicle state and an accurate understanding of the vehicle hydrodynamic characteristics. Partial state information is available from a network of acoustic transponders. The full state can be determined by a state estimator given an accurate understanding of sensor quality, software architecture, actuator behavior and capabilities, and the vehicle hydrodynamic characteristics.

Several of these areas have been investigated by others. The range measurement variance of the SHARPS (Sonic High Accuracy Ranging and Positioning System) acoustic network used by the Deep Submergence Laboratory (DSL) of the Woods Hole Oceanographic Institution (WHOI) has been measured by Yoerger [32]. Properties of SHARPS and the software structure that affect the timing and flow of information in the underwater vehicle system are known. And the actuators[1] used by ROVs operated by DSL have been well characterized by Cooke, Yoerger, and Slotine [4, 5]. The remaining areas, hydrodynamic characterization and state reconstruction, are the subjects of this thesis.

The trajectory of an underwater vehicle typically involves a limited number of extended, steady translations linking longer periods of hovering and tight maneuvering during which applications are largely accomplished. Operational and experimental experience with Hylas and other ROVs at DSL has demonstrated that the hover and small motion regimes of motion are the the most difficult to control. This is caused primarily by the dynamic response of the thrusters [4, 5]. However, the dependence of hydrodynamic characteristics on vehicle state history during unsteady

[1]The actuators are ducted propellers driven by direct current brushless motors. The combination of duct, propeller, and motor is commonly referred to as a "thruster".

motions is a further complication [23]. During steady motions the hydrodynamic characteristics for bluff bodies converge to constant values [23] and the thrusters are well behaved [4, 5]. For these reasons the investigation will focus on station keeping and short translations. Additionally, the development is carried out for one translational degree of freedom.[2] It can be extended to four degrees of freedom with coupling in a straightforward manner.

A number of preliminary goals must be reached to implement effective full state, closed loop control of an ROV. Primary among these will be the determination of an accurate hydrodynamic model of the vehicle. Note, however, that the need for accuracy in the model must be tempered by the need for computational simplicity when using it. Because of the complex dependence of drag and added mass on vehicle geometry and state history [1, 6, 23, 24], the determination will be empirical; an experimental system identification procedure will be required. ROV Hylas, a test bed vehicle built and operated by DSL, will be used for this procedure.

Once a suitable model has been determined, a state estimator can be constructed. This observer[3] will combine models of the vehicle and thrusters with position measurements to estimate vehicle state. The observer will also include compensation for various nonlinearities that are excluded from the models. Because vehicle time is limited, a computer simulation of the complete system will be developed. The simulation will include a numerical model of the vehicle that is faithful to the results of the system identification procedure. It will also reproduce the thruster, SHARPS, and software structure behavior and include forms of environmental forcing. The simulation can then be used to test the state estimator. The simulation will also be used in the stability analysis of the system. Simple PD (Proportional-Derivative) or PID (Proportional-Integral-Derivative) controllers will be used to complete the control loop. When the simulation phase of the development is complete, the observer

[2]In particular, it is carried out for vertical translations and closed loop depth control.

[3]The term "observer" is used interchangeably with the terms "state estimator" or "estimator" in this thesis. They refer to an algorithm, generally implemented in software, that estimates vehicle state (position and velocity) from a combination of model and measurement based information sources. Observers will be described in Chapter 3.

and controller algorithms will be incorporated into the software system of ROV Hylas for evaluation.

1.2 Thesis Outline

1.2.1 Thesis Organization

Chapter 2 documents the determination of the hydrodynamic characteristics of ROV Hylas. The experiment and analysis are described in detail and the extension of the method to four degrees of freedom is discussed. A comparison of related results from other researchers is also included. A complete set of plots from the analysis is included in Appendix A.

Chapter 3 develops the underlying linear structure of the observation and control algorithms. Compensation for nonlinearities in the hydrodynamics, thrusters, and software architecture is then added to the estimator and controller. Stability concerns for the overall nonlinear system are addressed.

In Chapter 4 the system described in Chapters 2 and 3 is cast in a flexible numerical simulation for evaluation. The structure and capabilities of the simulation are described and the algorithms modelling the real system are discussed. Stability questions are addressed and results are presented. A final section addresses the issue of PID control. Observer augmentation and system observability are examined and the new algorithms are evaluated in simulation.

Chapter 5 presents the results of observer evaluation in the test tank with ROV Hylas. Trajectory plots under varying degrees of compensation are discussed and robustness of the algorithms to errors in modelling is demonstrated. The simulation is given matching inputs to check its accuracy in reproducing the behavior of the vehicle system.

The results of the research are summarized in Chapter 6 and directions for future investigation are suggested.

1.2.2 A Word Concerning Chronology

The outline above and the thesis that follows chart a smooth course through the objectives mapped out in the previous section. The progression is logical and one can only wish that reality had been so cooperative. Concurrent availability of ROV Hylas and the author was limited to a few time slots that precluded the accomplishment of the objectives in logical order. Notwithstanding scheduling difficulties, all objectives were met with the exception of some vehicle tests. In particular, the system identification procedure has been well developed and the simulation has been shown to be a reliable indicator of vehicle system behavior.

A limited simulation was initially written to explore the relative merits of the pole placement and Kalman methodologies of estimator construction.[4] It had one translational degree of freedom and used a PD controller with the observers generating estimates of position and velocity. This was superceded by a new simulation based on a significantly more capable and flexible architecture. The code for this simulation has continued to evolve. Like its predecessor the new simulation is also a one degree of freedom, two state (position and velocity) system.

In parallel with the simulation development, system identification data was collected and supplemental testing of the thrusters was performed during three windows of vehicle availability. Based on the initial analysis of these data sets, code for vehicle control was generated and successfully used to control ROV Hylas in depth. Gains for the PD controller were calculated from the hydrodynamic model as it then existed. The two state observer generated estimates based on that model with compensation for thruster nonlinearities and system structure.

A more rigorous analysis of the system identification data and a literature search followed. Several changes resulted which were incorporated into the vehicle and observer portions of the simulation. The controller compensation for the thrusters was also refined. These changes should improve vehicle responsiveness in the hover and tight maneuvering regimes of motion. Additionally, the simulation was upgraded with

[4]Both methods will be described in Chapter 3. They differ only in how observer gains are determined. The form of the observer equations produced is the same.

some asynchronous features of the multiprocessor vehicle system. The processors had been synchronized before observer trials with the vehicle, however it was desirable to investigate what effect the asynchronous structure might have had in the past.

Finally, the simulation was used to investigate algorithms for PID control. The observer was augmented to accomodate the new state variable, the integral of position. To maintain observability a "measurement" of the new state variable was obtained by numerical integration of the raw SHARPS position measurement. The addition of integral control eliminates position offsets caused by steady environmental forcing such as currents or non-neutral buoyancy.

Unfortunately, the thrusters and other components of ROV Hylas were then required as spares for ROV Jason, also of DSL, for several lengthy deployments. As a result, evaluation of the additional compensation and PID control could only be done in simulation.

Chapter 2

System Identification†

2.1 General Discussion

The forces exerted by a viscous fluid on a bluff body moving relative to the fluid depend in a complicated way on the history of the relative motion. In many simple cases, however, the forces are well described by Morison's Equation [15] (below) once the added mass and drag coefficients have been determined experimentally [23]. Morison, et al., described the hydrodynamic forces with an inertial term proportional to the dry mass and a drag term proportional to the square of the relative velocity. One form of the equation, appropriate for a submerged, neutrally buoyant body, is

$$F = (1 + C_M^*)m\dot{U} + \frac{1}{2}\rho A C_D^* U|U| \tag{2.1}$$

where m is the dry mass, U is the velocity of the body relative to the fluid, A is the projected area along the direction of motion, and ρ is the density of the fluid. C_M^* and C_D^* are the (dimensionless) coefficients of added mass and drag that are to be determined. Other forms, particularly of the drag, may be appropriate in some flow regimes.[1]

†This chapter appeared in abbreviated form in *Proceedings OCEANS '93* [16].

[1]The coefficient of added mass is customarily defined as $C_M^* = \frac{m_{added}}{\rho V}$ where m_{added} is the added mass, ρ is the fluid density, and V is the volume displaced by the body [25]. For a submerged, neutrally buoyant body, the dry mass, m, is necessarily equal to ρV, the mass of the displaced

It should be noted that Equation 2.1 is an approximation. It does not account for the state history of the flow in any direct way. For example, the effect on the dimensionless coefficients of a step change in the amplitude of steady oscillatory motion may still be apparent four to five cycles after the step. Further, the changes for an oppositely directed step are not reciprocal [27]. It remains empirically true, however, that the form of Equation 2.1 is usually quite accurate, and that the dimensionless coefficients can reasonably be described as constants once the larger transients of the relative flow have decayed.

As stated in Chapter 1, the trajectory of an ROV can reasonably be characterized as either uniform translation or hover.[2] During uniform translation $\dot{U} = 0$ and the forcing, F, is entirely balanced by the quadratic drag term in Equation 2.1. There is, in general, some dependence of the coefficient of quadradic drag on the Reynolds number, Re,[3] but a $0.2 - 0.5\ m/s$ translation speed for a vehicle with a $1 - 2\ m$ characteristic length in water yields a Reynolds number on the order of 10^6. This is beyond the drag crisis and in a region where C_D^* is largely independent of changes in the value of Re. This relationship is plotted in Figure 2.1 for rough cylinders. For Reynolds values in the region of interest, C_D^* is approximately 1. Operational experience with ROVs at DSL has shown that $C_D^* = 1$ is a reasonable value for accurate closed loop control of an ROV during translation [32]. In contrast, the hover regime has proven much more difficult to control. This is primarily due to the poor low speed dynamic response of the thrusters. When the vehicle is commanded to hover under closed loop control the thruster dynamics produce a limit cycle [4, 5]. The resulting periodic motion has a strong effect on the values of C_M^* and C_D^*.

When the hydrodynamic forces are modelled by Equation 2.1 during oscillatory motion, C_M^* and C_D^* have been shown to have a nonlinear dependence on the

water. Therefore the definition of C_M^* implied by the form of Equation 2.1 is equivalent to the customary definition.

[2]The portions of the trajectory linking periods of uniform translation or hover can be characterized as uniform accelerations. Modelling this regime will be addressed in Section 2.4.

[3]$Re = UD/\nu$ where U is the velocity, D is the characteristic length, and ν is the kinematic viscosity of the fluid.

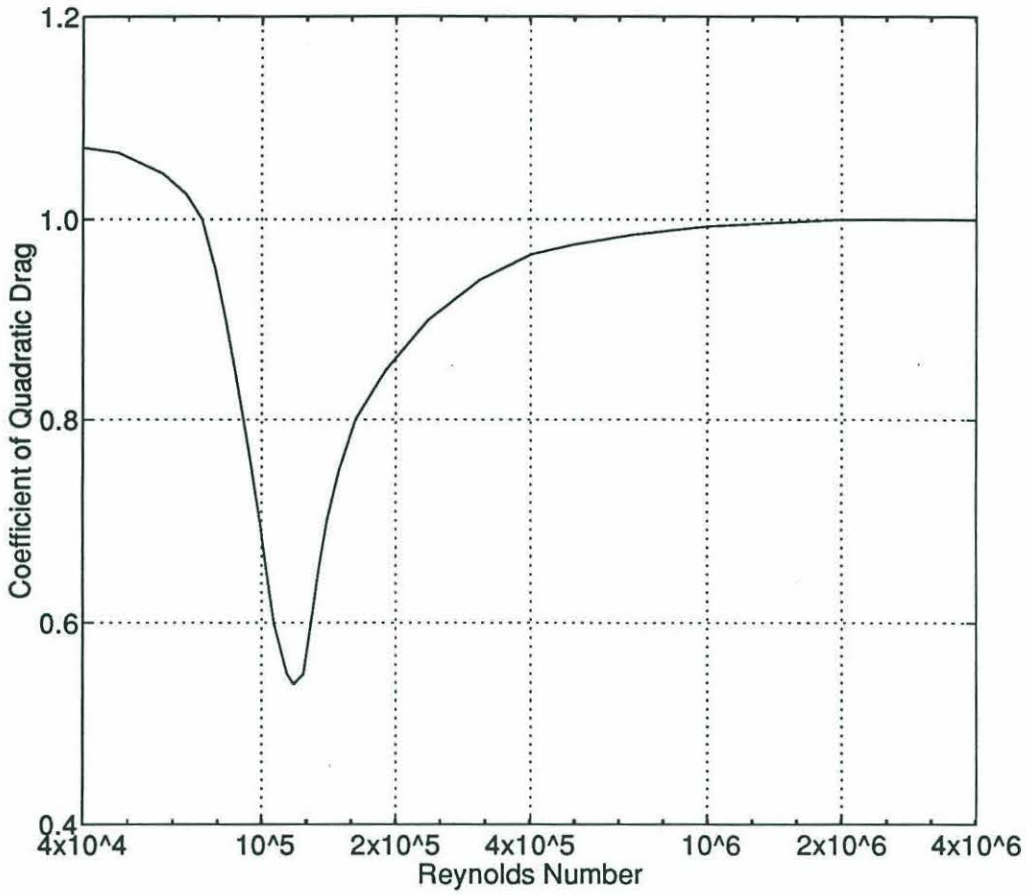

Figure 2.1: COEFFICIENT OF QUADRATIC DRAG FOR ROUGH CYLINDERS AS A FUNCTION OF REYNOLDS NUMBER - The sudden drop in C_D^* near $Re = 10^5$ is known as the "drag crisis". For an ROV it typically takes place at lower Re than that calculated from the characteristic length of the vehicle because of the multiscale geometry and sharp edges of the ROV. The curve summarizes the results of several studies and is redrawn from Sarpkaya and Isaacson [23], with the permission of the first author.

Keulegan-Carpenter number, KC.[4] The coefficients also depend on β, the frequency parameter,[5] and thus on the Reynolds number [1, 6, 19, 23, 24]. The Keulegan-Carpenter number may be thought of as proportional to the ratio of the amplitude of

[4] $KC = U_m T/D$ where U_m is the maximum velocity during the oscillation, T is the period of the oscillation and D is the characteristic length. The relationship was first described by Keulegan and Carpenter in several papers and reports published in the late 1950s. The research was supported by the National Bureau of Standards.

[5] $\beta = Re/KC = D^2/\nu T$. This ratio was first called the "frequency parameter" and its importance demonstrated by Sarpkaya: Sarpkaya, T., "Vortex Shedding and Resistance in Harmonic Flow About Smooth and Rough Circular Cylinders at High Reynolds Numbers", Report No. NPS-59SL76021, Naval Post Graduate School, Monterey, CA, 1976

the excursion to the characteristic length. This description becomes exact in the case of harmonic oscillations. The frequency parameter is convenient because it depends only on the frequency of oscillation for a given body, while the Reynolds number depends on both the frequency and the amplitude [1].

The Keulegan-Carpenter number for the limit cycle observed with ROVs Jason and Hylas is on the order of 10^{-1}.[6] This value is on or below the margins of the KC ranges investigated for cylinders by Bearman, et al. [1] and Sarpkaya [24]. Additionally, the frequency parameter for the limit cycle is in the range $10^4 < \beta < 10^5$ while Bearman and Sarpkaya worked with values between 10^2 and 10^4. Empirically derived formulas by Graham [11] and theoretical derivations by Wang [31] are comparable to the Bearman, et al. and Sarpkaya results for the lower values of β, but the agreement diverges systematically as β and roughness are increased.

The behavioral correspondence between a rough cylinder and an ROV of similar dimensions during uniform translation cannot be assumed to hold in the oscillatory regime. Further, the form of Equation 2.1 may not correctly describe the forces in that regime. For example, flow at extremely low KC values can be attached and laminar [24] giving the drag a linear component. Even if the form of Equation 2.1 is correct, the coefficients characterizing the vehicle could only be predicted by extrapolating outside the range of the published data and formulae for cylinders. Experimental determination of the hydrodynamic forces acting on ROV Hylas during closed loop hover is required.

During system identification the responses of the vehicle and a mathematical model to the same input forcing are compared. The coefficients of the model are adjusted to achieve the closest match. The form of the model may be modified if necessary and the comparison may be carried out by a variety of means. It is essential, however, that the input be known.[7] Cooke's analysis of the thrusters showed

[6] It is interesting to note that the Keulegan-Carpenter number is approximately 0.3 along both the longitudinal and the lateral axes when ROV Jason (length ≈ 2 m, width ≈ 1 m, mass ≈ 1200 kg) is under closed loop control. When the Research Vessel Knorr (length ≈ 75 m, beam ≈ 14 m, displacement ≈ 2300 *longtons* (2.3×10^6 kg)) is dynamically positioned under closed loop control the longitudinal and lateral Keulegan-Carpenter numbers are approximately 0.3 and 0.4.

[7] The forcing may not be used explicitly during system identification by some methods. However,

that output was a function of propeller angular velocity. That measurement cannot be easily or accurately made, particularly at slow speeds, in the oil filled (pressure compensated) motors used by DSL [4, 5]. Therefore, an oscillation in depth similar to the limit cycle must be generated by some other means.

A solution was suggested by the work of Sagatun and Fossen [19, 20]. During their own system identification procedure they performed a free decay test, with NEROV, the Norwegian Experimental Remotely Operated Vehicle. As with the previously cited work on cylinders, the KC of the limit cycle is on or below the margin of the reported range. For the test, the vehicle is suspended in water from a spring. An oscillation is started and recorded while it is allowed to decay. Although Sagatun and Fossen were not investigating limit cycle behavior, the method is ideal for this purpose. The spring provides a well defined input whose magnitude can be determined from the accurate position measurements possible with SHARPS. The spring constant and initial perturbation can be chosen to produce motion with an amplitude and period similar to the limit cycle. The vehicle hydrodynamics are then determined from the data record. The potential weakness of this approach is that the wake of the thrusters during operation will significantly distort the pattern of flow around the vehicle. However, the results presented in subsequent chapters indicate the alteration of the flow is insufficient to invalidate the model or cause large changes in its parameters.

The experiment and data collection with ROV Hylas are described in Section 2.2. The results are documented and analyzed in Section 2.3. For simplicity, attention is focused on the analysis of one of the nine tests. However, plots and tables describing the results and analysis of all runs are provided in Appendix A. Comparison is made to the analyses and results of Sagatun and Fossen [19, 20], Bearman, et al. [1], and Sarpkaya [24] in Section 2.3 as well. Section 2.4 argues for a description of the vehicle during periods of uniform acceleration based on the results of other researchers. Section 2.5 discusses the extension of the method to four degrees of freedom and Section 2.6 summarizes the conclusions of the analysis.

---

it is implicit in these methods that the forcing enters the equations in some well defined way that does not compromise the analysis. At a minimum the form of the input must be known.

2.2 Experimental Set Up and Procedure

ROV Hylas was designed and built to serve as a test tank and dockside vehicle for the evaluation of control algorithms. The overall dimensions are approximately $0.9\ m \times 0.9\ m \times 1.63\ m$ (Figure 2.2). The dry mass is $m = 500\ kg$ with some variation depending on the current instrument suite. Housings in a frame attached below the buoyancy material contain electronics, sensors, and a video camera. Space and an electronic interface are provided for additional packages. Six thrusters mounted on the vehicle allow maneuvering with four degrees of freedom. ROV Hylas is designed to have the same stiffness in pitch and roll as the somewhat larger Jason vehicle. The system is controlled by software running on three interconnected transputers located both on the surface and in the vehicle. The operator interface is provided by a '486 personal computer (PC) and a joystick. System parameters of interest can be logged with a time stamp and written to the hard disk of the PC for retrieval and analysis.

The usual operating environment of ROV Hylas is a cylindrical tank with a depth of 3.5 m and a diameter of 4.5 m (Figure 2.3). Three SHARPS transponders near the surface form the acoustic position net. Before testing, the depths of the net transponders and the speed of sound in the tank are passed by the operator to the net calibration software. The transponders then measure the range along each leg of the net. Transponder A is defined as the origin of a Cartesian coordinate system with the x-axis extending from there to transponder B. The xy-plane is defined to be parallel to the water surface. Fore and aft transponders on the vehicle are ranged by each net transponder on alternate cycles allowing the measurement of position and heading within the net coordinate system. In open water for distances up to 100 m the variance of the range measurement is $\approx 2\ cm^2$ [32]. Over the short ranges in the tank the variance is below 5 mm^2. The calculation of the "in tank" variance is given in Figure 2.6. These are extremely low noise levels for an acoustic range measurement.

Two common door springs were purchased at a local hardware store for the experiment. The force-displacement response of the springs was measured using a meter

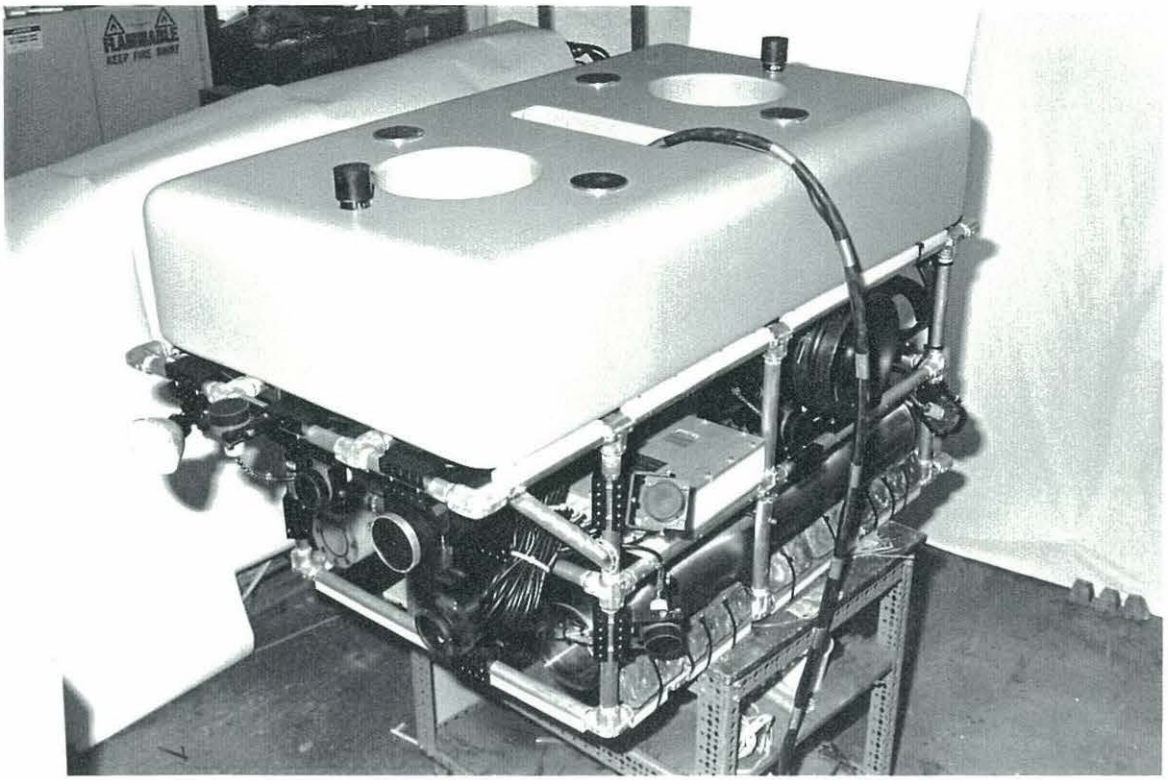

Figure 2.2: ROV HYLAS - The vehicle is shown in the high bay at DSL during preparation for initial tank trials. Tunnels for the vertical thrusters can be seen in the top surface. One of the lateral thrusters is visible on the port side aft. Cameras, lights, and a spot range sonar are mounted on the frame facing forward. The vehicle tether connects through the rectangular tunnel between the vertical thrusters. It contains conductors for DC and AC power, serial communications, a color video signal, and the fore and aft SHARPS transponders. The two small cylinders fore and aft of the vertical thrusters are acoustic dampers covering the transponders. Photo by Terri Corbett, WHOI.

stick and a load cell[8] for parallel, single, and series arrangements of the springs. The springs were found to be linear to the quantization limit of the load cell throughout the range of extension. The results of the spring calibration are shown in Figure 2.4.

ROV Hylas was then suspended in the tank from the overhead crane using each of the three spring configurations in turn. A threaded rod between the spring(s) and the crane placed the vehicle well below the surface. That position reduced surface wave formation that could affect the drag measurement. It also increased the depth

[8]The load cell calibration was checked with several known weights. The conversion coefficient was 0.38 *units/N*

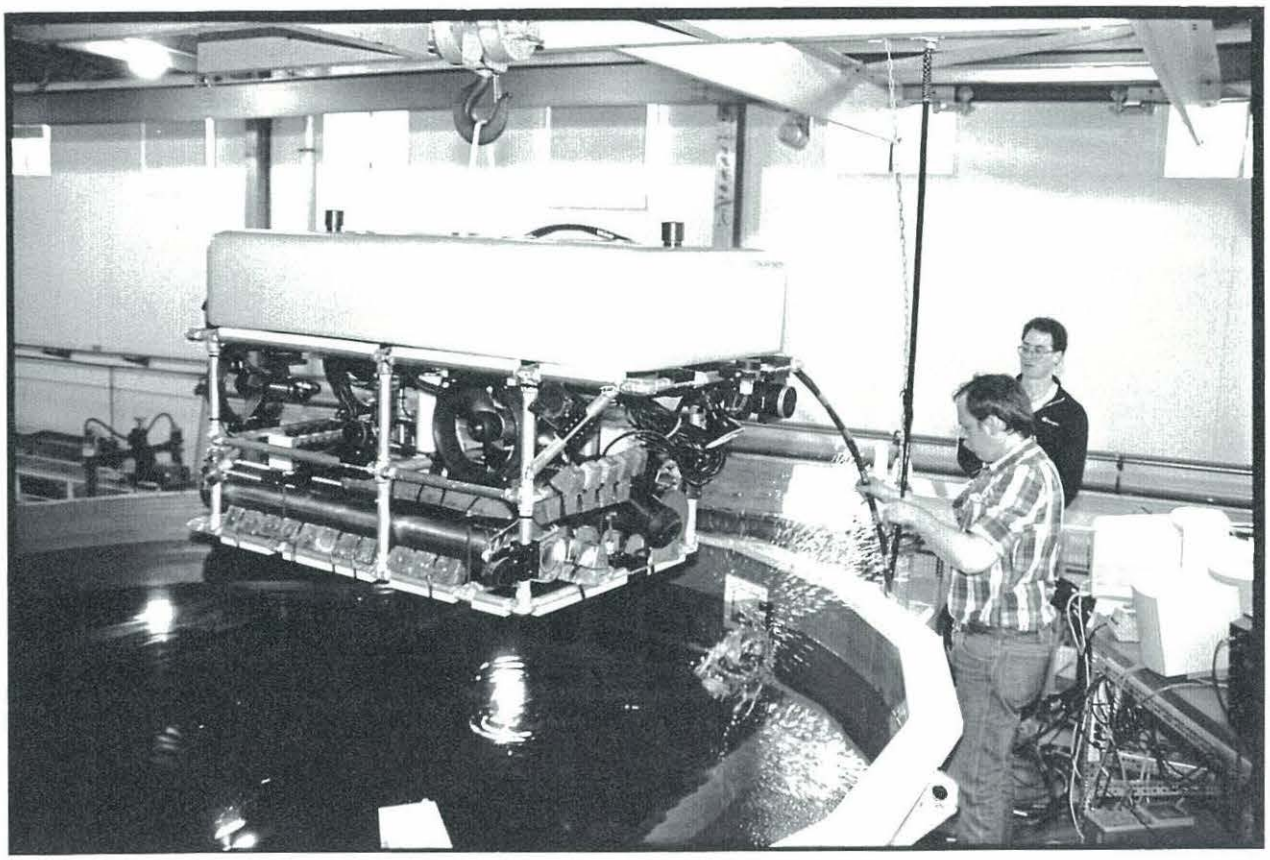

Figure 2.3: ROV HYLAS - The vehicle is shown suspended above the test tank immediately prior to christening. The tank is located in the Coastal Research Laboratory (CRL) of WHOI. Several monitors, part of the operating system, are visible on the bench at right. The three transponders forming the SHARPS net are normally suspended from wood frames clamped to the lip of the tank. One of these is visible in the foreground. The overhead crane is used to move the vehicle in and out of the water. Pictured are William Sellers (holding tether) and Nathan Ulrich, both of WHOI. Photo by Dave Gray, WHOI.

accuracy of the SHARPS measurement by increasing the angular separation from the plane of the net. For each configuration the vehicle was given sufficient negative buoyancy to bias the spring(s) into the middle of the measured force-displacement range. The arrangement is shown schematically in Figure 2.5.

Three runs were made with each of the spring configurations. The initial perturbation was generated by briefly firing the vertical thrusters. The decaying oscillations that resulted were recorded and logged by the system. Although the apparatus did not restrict horizontal or rotational motions, no horizontal translations or rotations

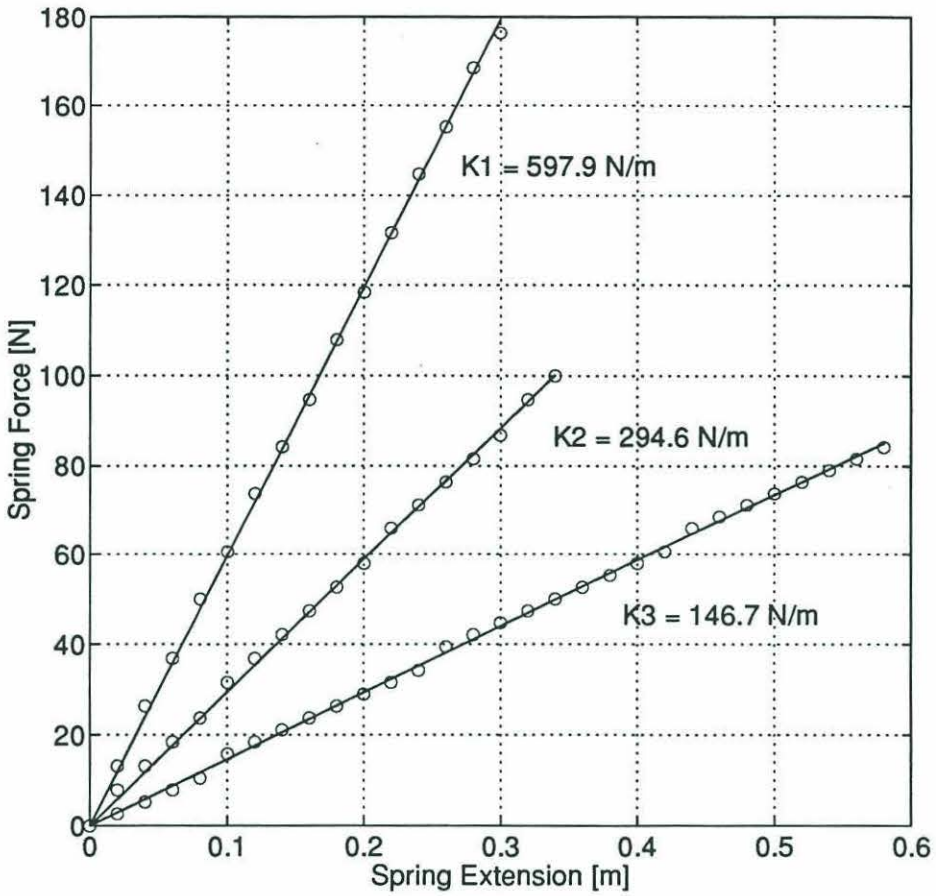

Figure 2.4: SPRING CALIBRATION FOR THE SYSTEM IDENTIFICATION - Data points for two springs in parallel, a single spring, and two springs in series are displayed as circles. The three lines are least squares fits to the data with the calculated spring constants shown on the plot. As expected, $K1 \approx 2 \times K2$ and $K2 \approx 2 \times K3$. Note the piecewise linearity of the data points, particularly visible in the series data. This is due to quantization of the load cell output.

about the vertical or horizontal axes were observed during the free decay. Some tension was maintained on the springs throughout each run and the springs were inspected and found free of overstretching at the conclusion of the experiment. The combination of varying initial conditions and three different spring constants yielded a range of Keulegan-Carpenter numbers that included the value calculated for the limit cycle.

Before the analysis of Section 2.3 was performed, the raw depth data was filtered to remove noise from two sources. The first source of noise was the variance in the SHARPS measurement. Noise was also generated by the asynchronous structure of

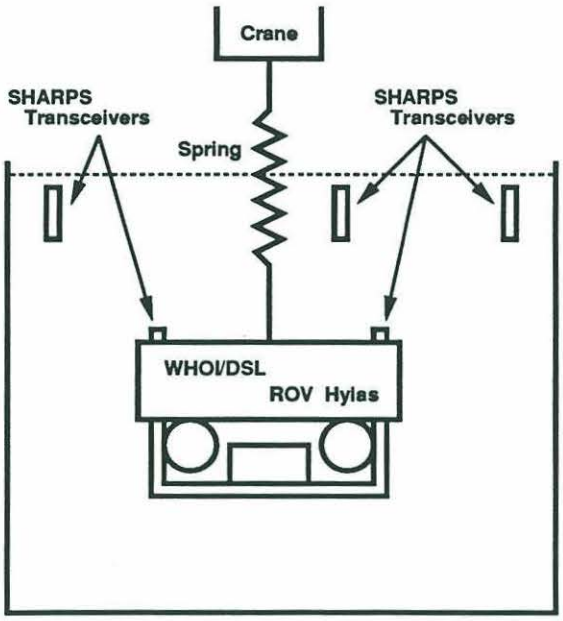

Figure 2.5: ROV Hylas System Identification Test Apparatus Schematic - The SHARPS net can be seen near the water surface. Range measurements from the three transponders in the net are made to each of the onboard transponders on alternate cycles. The Cartesian coordinates of the onboard transducers in the frame of the net are calculated and logged by the software.

the three transputer system. Logging operations took place 2 to 4 times during each SHARPS cycle causing position measurements to be repeated in the record.[9] Raw depth data for the fore and aft transponders was averaged and then bidirectionally passed through a 5^{th} order Butterworth lowpass filter. The second pass with the data set reversed eliminates phase distortion and makes the filter effectively 10^{th} order. Points at the start and termination of the data set are pared off to remove edge effects due to the finite length of the filter and data set. The smoothed data has high accuracy, low noise, and is suitable for the central difference approximations to the velocity that are used in the following analysis. The position and velocity curves from a typical run are shown in Figure 2.6.

[9]This problem was later removed by synchronizing all three transputers to the SHARPS period. In particular, the system was synchronized for the vehicle testing discussed in Chapter 5

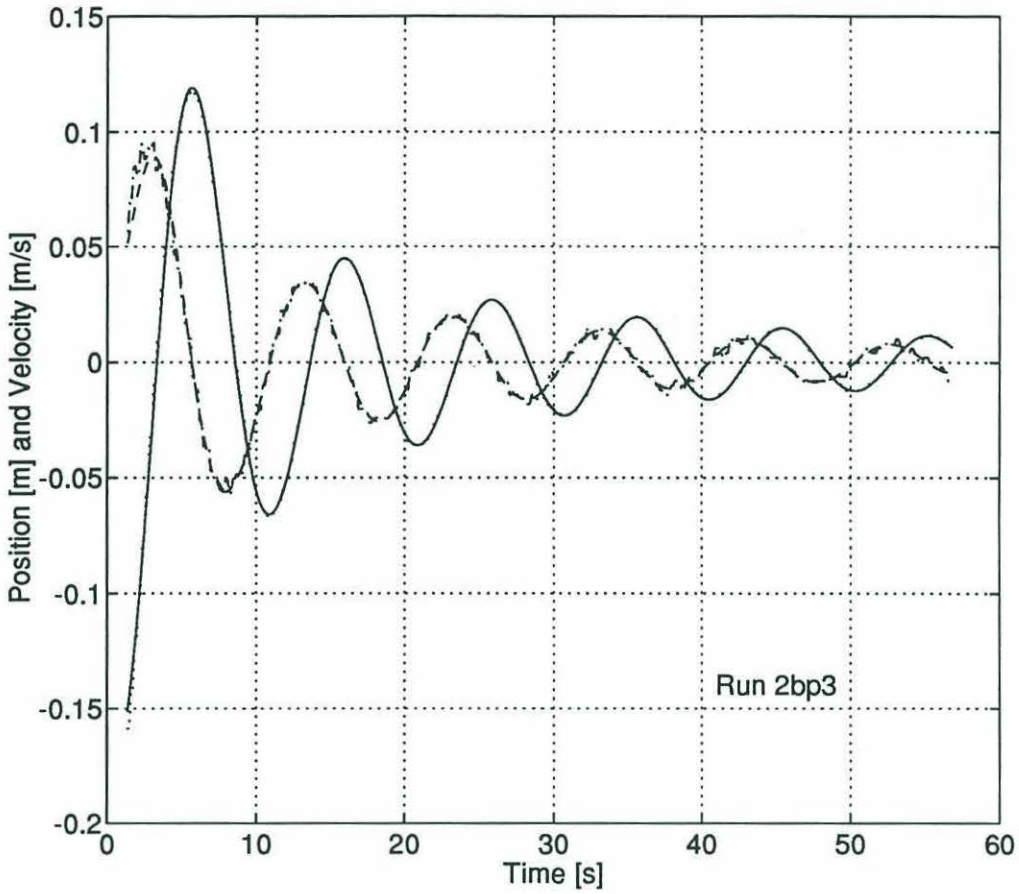

Figure 2.6: POSITION AND VELOCITY CURVES FROM THE SYSTEM IDENTIFICATION TEST - The average of the fore and aft transponder depths is shown as a dotted line. The filtered position is the solid line lying on top of the average. The filtering has a very small effect on the position. Velocity is calculated as a first order central difference approximation to the derivative of position. Higher order difference formulas did not change the result and were not used. The dash-dot line shows velocity derived from the averaged but unfiltered position. The dashed line shows velocity derived from the filtered position. The smoothing of velocity that results from filtering position can be clearly seen. The zero of position corresponds to a static depth for the top surface of ROV Hylas 1.35 m below the xy-plane of the net. An estimate of the SHARPS measurement variance in the tank can be made from the variance of the difference between the filtered and unfiltered position curves. That value is approximately 4×10^{-2} cm^2. Assuming a Gaussian distribution, the error in a SHARPS measurement in the test tank will be less than 4 mm 95 % of the time.

2.3 Analysis and Results

2.3.1 Existing Methods of Analysis

Two methods, Fourier averaging and the method of least squares, are commonly applied to determine the added mass and drag of a body in a harmonically oscillating flow.[10] Both assume forcing of the form given by Morison, et al. in Equation 2.1. The method of Fourier averaging expresses the hydrodynamic forces as a sum of odd harmonics.

$$\begin{aligned}\frac{F}{\frac{1}{2}\rho A U_m^2} &= 2\left[A_1 \sin\omega t + A_3 \sin 3\omega t + A_5 \sin 5\omega t + \cdots\right] \\ &\quad + 2\left[B_1 \cos\omega t + B_3 \cos 3\omega t + B_5 \sin 5\omega t + \cdots\right]. \end{aligned} \tag{2.2}$$

If the flow velocity is given by $U = -U_m \cos\omega t$ the sum can be recast in the form of Equation 2.1 as follows:

$$\begin{aligned}\frac{F}{\frac{1}{2}\rho A U_m^2} &= \frac{\pi^2}{KC} C_M^* \sin\omega t + 2\left[A_3 \sin 3\omega t + A_5 \sin 5\omega t + \cdots\right] \\ &\quad - C_D^* |\cos\omega t| \cos\omega t + 2\left[B_3 \cos 3\omega t + B_5 \sin 5\omega t + \cdots\right]. \end{aligned} \tag{2.3}$$

If it is further assumed that A_i and B_i are negligibly small for $i \geq 3$ and that C_M^* and C_D^* are constant functions of Re and KC, independent of ωt, the desired form is reached. The orthogonality properties of the sin and cos functions yield expressions for the coefficients.

$$C_M^* = \frac{2U_m T}{\pi^3 A} \int_0^{2\pi} \frac{F \sin\omega t}{\rho A U_m^2} d(\omega t) \tag{2.4}$$

$$C_D^* = -\frac{3}{4} \int_0^{2\pi} \frac{F \sin\omega t}{\rho A U_m^2} d(\omega t) \tag{2.5}$$

[10] Descriptions of these methods can be found in a variety of texts and papers. The source for this discussion is Sarpkaya and Isaacson [23]. The first systematic use of Fourier averaging was made by Keulegan and Carpenter in the late 1950s while studying the forces on submerged cylinders and plates at the node of a standing wave.

The method of least squares chooses coefficient values that minimize the error between the measured forces and those calculated from the reduced form of Equation 2.3.

$$\frac{F}{\frac{1}{2}\rho A U_m^2} = \frac{\pi^2}{KC} C_M^* \sin\omega t - C_D^* |\cos\omega t| \cos\omega t \tag{2.6}$$

The error is defined by the equation

$$E^2 = (F_{measured} - F_{calculated})^2, \tag{2.7}$$

and is minimized when $\frac{dE^2}{dC_M^*} = 0$ and $\frac{dE^2}{dC_D^*} = 0$. Thus the expression for C_M^* is the same as that obtained by Fourier averaging and the expression for C_D^* is only slightly modified.

$$C_D^* = -\frac{8}{3\pi} \int_0^{2\pi} \frac{F_{measured} |\cos\omega t| \cos\omega t}{\rho A U_m^2} d(\omega t) \tag{2.8}$$

Fourier averaging and the method of least squares were used by Sarpkaya [24] and Bearman, et al. [1], to determine the added mass and drag coefficients on cylinders in oscillatory flow at low KC values (Section 2.1). Although comparison will be made to those results, there are several objections to the use of these methods here. The experimental set up described in Section 2.2 does produce an accurate $F_{measured}$ from the filtered position data. However, the motion is not harmonic in character and both of these methods depend on that assumption. While it could be argued that the limit cycle itself is close enough to the harmonic form for these methods to be applied, there is no well known $F_{measured}$ when the thrusters provide the forcing.

More seriously, these methods can only be applied to a single, uncoupled, degree of freedom. While the vehicle is a strongly diagonal system, there is significant coupling between lateral translation and heading as well as weaker coupling between other degrees of freedom. Finally, Fourier averaging and the method of least squares are based on forcing in the form of Equation 2.1. Experience indicates that this is a reasonable approach. However, the system identification procedure that will be

described in Section 2.3.2, in addition to being extendable to fully coupled systems with multiple degrees of freedom, places no restraint on the hydrodynamic model of the vehicle.

The analysis of freely decaying motions is a traditional approach in naval architecture and its utility is not limited to oscillatory motion. One method of analysis for freely decaying oscillations was described and used by Sagatun and Fossen in the research that suggested this approach for ROV Hylas [19, 20]. The method is also described by Faltinsen [6]. The necessary equations are derived in the following manner. A governing equation of the form

$$\ddot{x} + a_1\dot{x} + a_2\dot{x}|\dot{x}| + a_3x = 0, \tag{2.9}$$

which involves both linear and quadratic drag, is assumed. A sinusoidal describing function can linearize $\dot{x}|\dot{x}|$ as $(8/3\pi)\dot{x}_{max}$ [10]. Assuming a sinusoidal form with period T, $\dot{x}_{max} = (2\pi/T)x_{max}$. Equation 2.9 can then be written in linearized form as

$$\ddot{x} + \left(a_1 + \frac{16}{3}\frac{x_{max}}{T}a_2\right)\dot{x} + a_3x = 0. \tag{2.10}$$

When the damping is sufficiently small for the poles to be complex, the solution of this linear equation is a sinusoid decaying inside an exponential envelope.

$$e^{\frac{t}{2}\left[-\left(a_1+\frac{16}{3}\frac{x_{max}}{T}a_2\right)+i\sqrt{4a_3-\left(a_1+\frac{16}{3}\frac{x_{max}}{T}a_2\right)^2}\right]} \tag{2.11}$$

The envelope defined by the real part of the poles requires that the magnitudes of the extrema, x_i, should approximately satisfy the equation

$$\frac{2}{T_n}\ln\left(\frac{x_{n-1}}{x_{n+1}}\right) = a_1 + \frac{16}{3}\frac{x_n}{T_n}a_2. \tag{2.12}$$

It is then a simple matter to pick off the peak values from the data and plot the left-hand side of Equation 2.12 against $\frac{16}{3}\frac{x_n}{T_n}$. The intercept and slope of the linear least squares line through the resulting plot determine a_1 and a_2. An example using

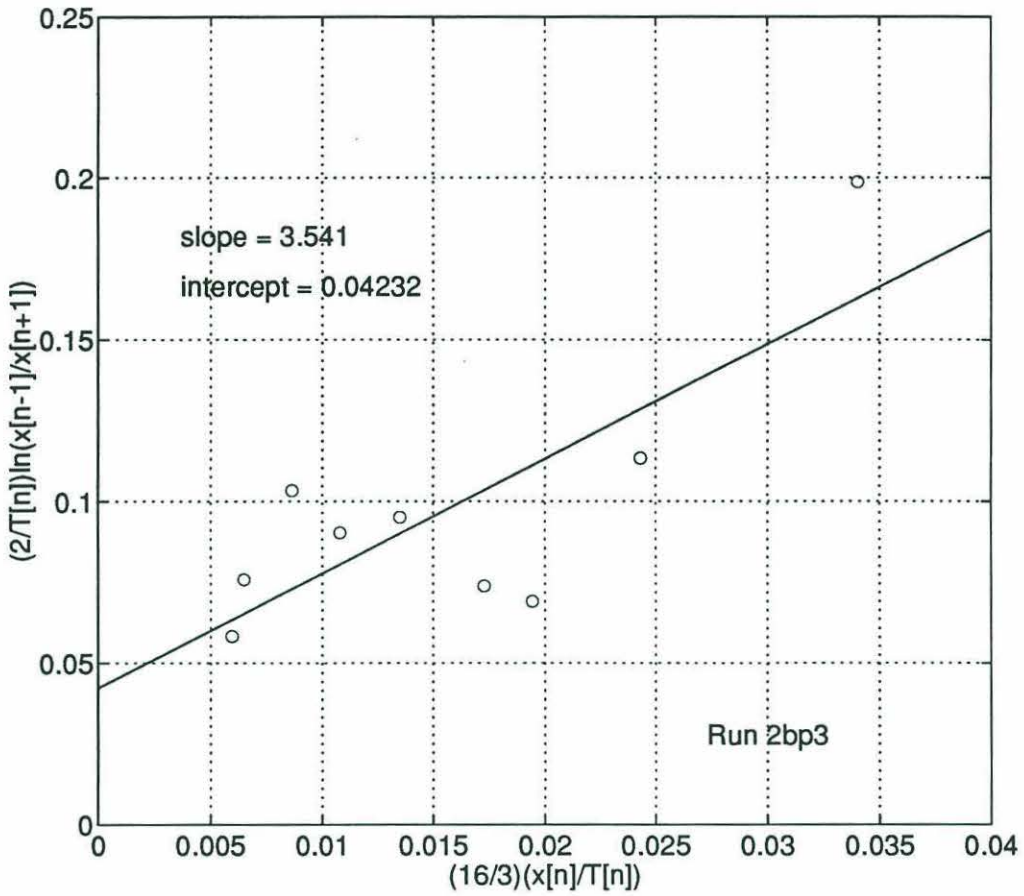

Figure 2.7: DETERMINATION OF DRAG COEFFICIENTS FROM A FREE DECAY TEST - Data points determined from the extrema and period of the position curve shown in Figure 2.6 are plotted as circles. The solid line is the linear least squares fit to the data. The slope and intercept of the line are shown on the plot.

the position data from Figure 2.6 is shown in Figure 2.7.

The value of a_3 is determined by recognizing that the imaginary portion of the poles is the frequency of oscillation. This yields the relation

$$a_3 = \frac{\omega_o^2}{1 - \frac{a^2}{4\omega_o^2 + a^2}} \tag{2.13}$$

where ω_o is the observed radian frequency and $a = a_1 + \frac{16}{3}\frac{x_{typ}}{T}a_2$. x_{typ} is a "typical" value from the set of position extrema magnitudes. The effective mass is then $m_{eff} = \frac{k_{spring}}{a_3}$ and the (dimensional) linear and quadratic drag coefficients, c_{ld} and

c_{qd}, are the products of a_1 and a_2 with m_{eff}.[11]

There are several objections to this approach as well. Many periods of oscillation are required to define a reliable least squares line through the data.[12] If the system is not lightly damped the magnitude of oscillation will change significantly over the period of decay. Large changes in the Keulegan-Carpenter and Reynolds numbers, on which the coefficients depend, will occur. As a result, it may be difficult or impossible to calculate a single pair of drag coefficients that are valid for the entire duration of the decay. Application of this method to the data in Figure 2.6 yields the dimensional quantities

$$\begin{aligned} m_{eff} &= 1460\ kg \\ c_{qd} &= 5170\ kg/m \\ c_{ld} &= 62\ kg/s. \end{aligned} \tag{2.14}$$

The dimensionless quantities are calculated from

$$\begin{aligned} m_{eff} &= (1 + C_M^*)m \\ c_{qd} &= \frac{1}{2}\rho A C_D^* \\ c_{ld} &= \frac{2\rho A D}{3\pi^2}\left(\frac{2g}{D}\right)^{\frac{1}{2}} C_{LD}^* \end{aligned} \tag{2.15}$$

where D is the characteristic length along the direction of motion and g is the acceleration due to gravity. The density is taken to be $\rho = 1000\ kg \cdot m^{-3}$ as the test tank

[11]The result given by Sagatun and Fossen in [19, 20] for the dimensionless coefficient of added mass contains an error. They equate the observed frequency of oscillation with the undamped natural frequency of oscillation. The ratio of these quantities is $\sqrt{1-\zeta^2}$ where ζ is the dimensionless damping coefficient. The ratio is close to 1 for light damping (small ζ). As will be explained, this method is only valid in the presence of light damping, so the error is unlikely to reveal itself in the results. For ROV Hylas the error is approximately 2 %.

[12]Perhaps 3 to 4 times as many oscillations as were used in the example above. The scatter of data points about the least squares line in Figure 2.7 reduces confidence in the significance of the result, yet it is difficult to say when the degree of scatter is sufficiently large to reject the result.

contains fresh water.[13] The normalization produces the dimensionless quantities

$$\begin{aligned} C_M^* &= 1.92 \\ C_D^* &= 7.05 \\ C_{LD}^* &= 0.15. \end{aligned} \tag{2.16}$$

All three coefficients, particularly C_D^*, are somewhat larger than those found for the NEROV vehicle by Sagatun and Fossen [19, 20]. However, the layouts of the vehicles are quite different. In particular, the more open design of NEROV lacks the large block of flotation material that forces vertical flow around ROV Hylas. More importantly, the NEROV results are for a Keulegan-Carpenter value near one. It will be shown below that quadratic drag decreases sharply with increasing KC in this range. The results for the two vehicles are not inconsistent.

For these values the damping coefficient is $\zeta = 0.1$ which does meet the requirement of light damping. Additionally, these values show reasonable agreement with the results to be presented in Section 2.3.2. It remains true, however, that this approach is not robust to heavier damping. And, as with the two harmonic methods, it cannot be extended to coupled systems. Nor can it flexibly treat or easily discriminate between alternative hydrodynamic models. Taylor or describing function approximations are required for nonlinearities and that further restricts the range of applicability. The method described in Section 2.3.2 addresses these issues.

Finally, none of the methods reviewed in this section provide direct indications to the researcher of the accuracy of the model. That information is inherent in the approach described below. The importance of feedback should not be underestimated at any stage in the development of a control system.

[13]The normalization for linear drag is from Sagatun and Fossen [19, 20]. Linear drag is not widely used in modelling the forces on bluff bodies and there is no commonly accepted formula for the normalization as there is with quadratic drag and added mass. An alternative choice is $c_{ld} = \mu D C_{LD}^*$. The dimensions are correct and the dependence is clear. However, it produces dimensionless values on the order of 10^4 which may be considered undesirable.

2.3.2 System Identification by Numerical Minimization

System identification by numerical minimization is conceptually straightforward. In principle it is similar to the method of least squares, although the procedure is entirely different. A model of the vehicle is given initial conditions matching a data set. The model is then numerically integrated and the scalar error norm between the vehicle and model trajectories is calculated. The model coefficients are then iteratively modified to minimize that error.[14]

Four models of the vehicle are considered. The first describes the vehicle as a simple mass. A good match with a decaying oscillation is not expected, but the known result for such a model provides a check on the stability of the integration and also a measure of the relative magnitude of the terms in each model. The other models are inertia with linear drag, inertia with quadratic drag, and inertia with both quadratic and linear drag. Other models are certainly possible, however, the literature indicates that a good match can be achieved with this selection. For simplicity, the models are written here with dimensional coefficients.

$$\begin{aligned} m_{eff}\dot{w} &= F \\ m_{eff}\dot{w} + c_{ld}w &= F \\ m_{eff}\dot{w} + c_{qd}w|w| &= F \\ m_{eff}\dot{w} + c_{qd}w|w| + c_{ld}w &= F \end{aligned} \tag{2.17}$$

w is the vertical velocity of the vehicle. In later equations z will denote vertical vehicle position. m_{eff}, c_{qd}, and c_{qd} are the model parameters to be determined by the numerical minimization.

For each of the nine data runs, each model was given initial conditions matching those of the run and numerically integrated using a combination of Runge-Kutta and Adams-Bashforth-Moulton techniques. The time interval between data points averages 0.125 s. The integration of the model between each pair of points steps through

[14]The basis of this technique has been referred to in the literature as a "learning model" or a "model reference". A discussion and additional bibliographic references can be found in Sage and Melsa [21].

10 subintervals. The duration of each subinterval is $\frac{1}{10}$ of the measured duration of the interval. The integration of each full interval of the model is initiated with three 4^{th} order Runge-Kutta steps and completed with 4^{th} order Adams-Bashforth-Moulton steps. The process yields position and velocity curves for the model. The Runge-Kutta and Adams-Bashforth-Moulton techniques are described by Beyer [2] and by Press, et al. [18] and have excellent stability and accuracy characteristics.

The model equations are expanded and restated to reflect the known nature of the forcing during the free decay test.

$$\begin{aligned} m_{eff}\ddot{z} + kz - b &= 0 \\ m_{eff}\ddot{z} + c_{ld}\dot{z} + kz - b &= 0 \\ m_{eff}\ddot{z} + c_{qd}\dot{z}|\dot{z}| + kz - b &= 0 \\ m_{eff}\ddot{z} + c_{qd}\dot{z}|\dot{z}| + c_{ld}\dot{z} + kz - b &= 0 \end{aligned} \tag{2.18}$$

k is the known spring constant. b is a bias term intended to eliminate position drift during the integration resulting from small errors in the values of the initial and rest positions of the vehicle.[15] m_{eff}, c_{qd}, and c_{ld} are parameters to be determined by the minimization. Because its value cannot be known in advance, b is also one of the parameters for the minimization. The value of k is included in the model, though any arbitrary value, e.g., 1, could be used. The coefficients could then be determined after minimization as the product of the final minimization parameters and the true value of k. It should be pointed out that k cannot be used as a parameter of minimization. The minimization process establishes vehicle behavior. This is equivalent to saying the process determines the poles of the transfer function, and the poles constrain only m of the $m+1$ coefficients of the m^{th} order characteristic polynomial. One coefficient necessarily remains arbitrary. Without prior knowledge of one of the coefficients, the process could only determine their ratios. It is the known value of k that makes calculation of m_{eff}, c_{qd}, and c_{ld} possible.

[15]The initial and rest positions of the vehicle are measured to millimeter precision by the SHARPS net. However, an error of 1 mm with a spring constant of 300 N/m results in a constant force of 0.3 N. Over the course of a 1 minute decay with a 1500 kg vehicle, the drift is more than 35 cm. The bias term absorbs the measurement errors and eliminates the drift during the integration.

The scalar error norm is the square root of the sum of the squared errors at each point of the run.

$$E_N = \left[\sum_j (data_j - model_j)^2\right]^{\frac{1}{2}} \tag{2.19}$$

If this calculation is based solely on the velocity curves, the minimization tends to produce a model position curve with a constant offset from the vehicle position curve. This offset should not be confused with the constant position drift absorbed by the bias term in the equations. One is a rate of divergence while the other is a constant difference. If, however, the error is determined from the position curves or from the combined position and velocity curves, the position offset is zero. Additionally, the coefficients determined by minimization of velocity error differ from those determined by position or position-velocity minimization by up to 6 %.[16] The results of minimization of position or position-velocity error are essentially identical. For these reasons the error is calculated as

$$E_N = \left[\sum_j \left(z_{veh_j} - z_{model_j}\right)^2\right]^{\frac{1}{2}}. \tag{2.20}$$

The error norm minimization process is controlled using the Nelder-Meade simplex algorithm described by Press, et al. [18]. A simplex is an irregular n-dimensional hyperprism with $n+1$ vertices. In two dimensions a simplex is a triangle; in three dimensions it is a tetrahedron. The n parameters of the model define an n-dimensional vector space. For each point in the vector space there exists an error norm that can be used in defining an undulating hypersurface whose global minimum, if it exists, is the solution of the problem. The coordinates of that point are the coefficients most closely describing the vehicle under the constraints imposed by the form of the model. The algorithm constructs a simplex from an initial guess of the coefficients and n additional vertices determined by vector sums of the initial guess with a basis

[16] For the run shown in Figure 2.6 the variation is 2.2 % for m_{eff} and 6.1 % for c_{qd} assuming the inertia and quadratic drag model.

set of vectors for the space. Each iteration of the algorithm then moves the vertex associated with the highest error according to a set of simple rules that reduce the error and avoid degeneracy. The resulting motion of the simplex through the vector space has given rise to the descriptive term "ameoba". A sequence of these steps will always converge to a minimum of the error hypersurface.

The number of iterations required for convergence increases with n. Several hundred iterations were commonly required for each model-run combination during the investigation. More efficient minimization algorithms do exist, but they are generally more complicated to implement. In the words of Press, et al. [18], "...the downhill simplex method may frequently be the *best* method to use if the figure of merit is 'get something working quickly' ...[it] has a geometrical naturalness about it which makes it delightful to describe or work through." The convergence can be observed graphically by plotting the vehicle trajectory with the model trace at intermediate stages of the process. This can provide a comfortable visual feedback about the accuracy of the model. The error at each iteration can also be stored and plotted against the count when the process is complete. This provides a simple graphical check that a steady minimum value was achieved by the algorithm. The issue of global versus local minima will be addressed below.

Application of this technique to the data set of Figure 2.6 is shown for the four models in Figures 2.8–2.11. Each figure contains separate position and velocity plots. The solid curves mark the vehicle trajectory. The model path with minimum error is shown by the dashed trace. Textual entries on the plots show the values of the minimizing model parameters, m_{eff}, c_{qd}, and c_{ld}, in appropriate SI units. Also included is the position measurement offset error which is calculated from the minimizing bias parameter for the model: offset $= b/k$. An offset significantly larger than a millimeter for a model including drag would be indicative of an input error or a numerical breakdown in the calculation. The offset for the inertia model is a function of the initial conditions and the first extrema. It can easily exceed several centimeters and should not cause concern as long as the oscillation is steady. The scalar error norms for both the position and velocity are shown with the scalar norm of the

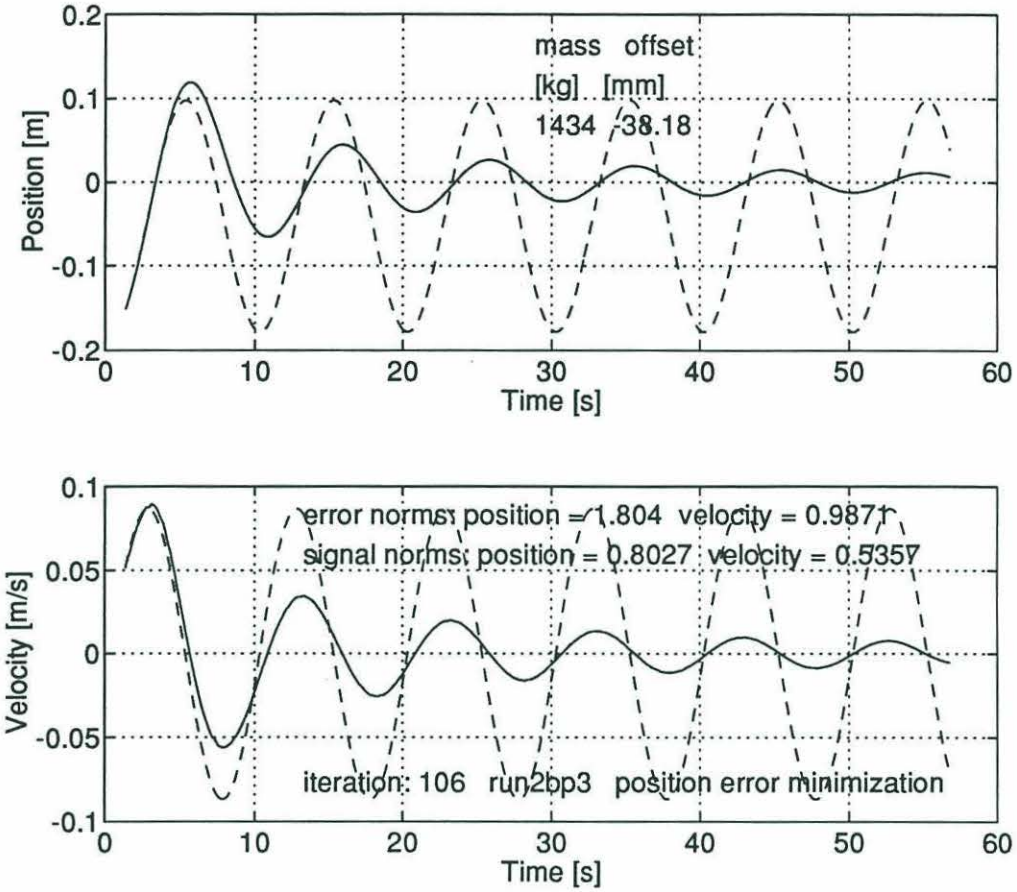

Figure 2.8: NUMERICAL MINIMIZATION EMPLOYING THE INERTIA MODEL - The vehicle trajectory is marked by the solid line. The dashed trace is the path followed by the model. Model and minimization parameters for the process are shown on the plots.

vehicle position and velocity about zero for comparison. The iteration count for the minimization process can be seen to increase with the number of parameters in the model. As stated above, minimization was based on position error. The run number is 2bp3 as in the previous examples. That designation indicates that this was the third of three runs with two springs arranged in parallel. Most of this information is collected in Table 2.1. Corresponding plots and tables for the other runs can be found in Appendix A.

Choosing the most accurate model requires consideration of several factors. It would be incorrect to base the judgment on a comparison of the minimized error norms. While the error norm is a good measure of accuracy within one model, its

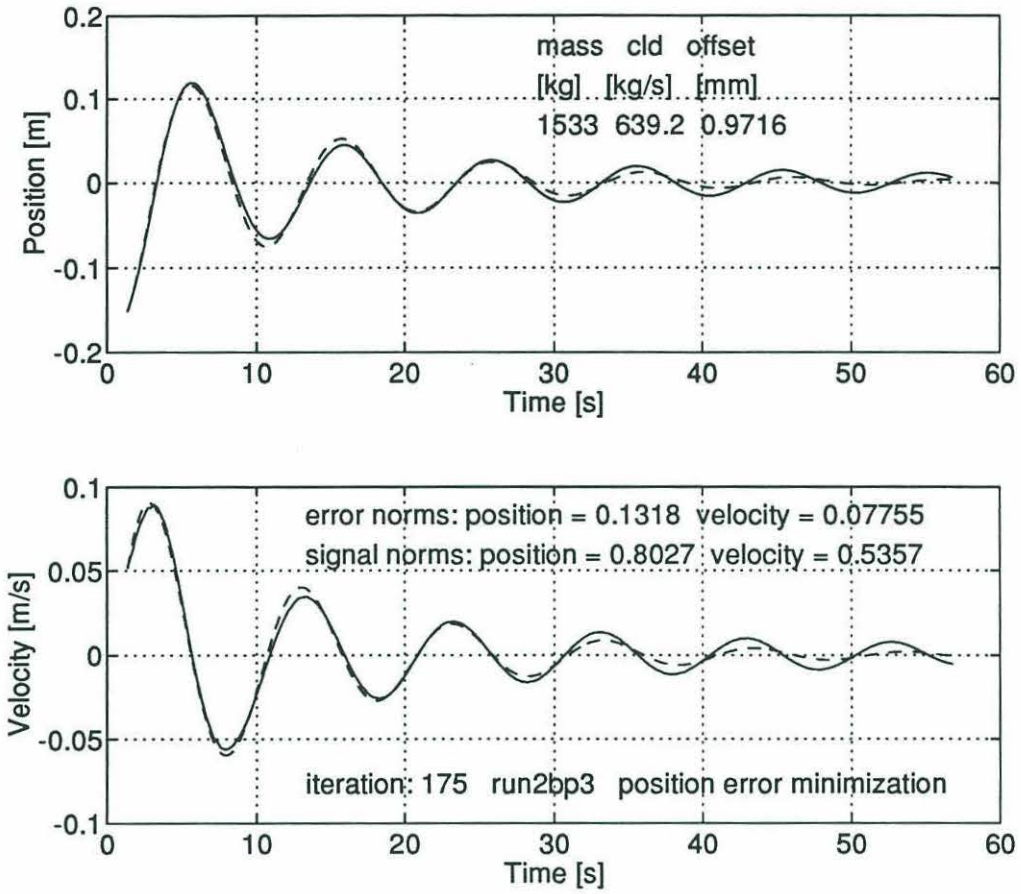

Figure 2.9: NUMERICAL MINIMIZATION EMPLOYING THE INERTIA WITH LINEAR DRAG MODEL - The vehicle trajectory is marked by the solid line. The dashed trace is the path followed by the model. Model and minimization parameters for the process are shown on the plots.

ability to discriminate between models is sharply limited by their structural differences. Instead, judgment is based on a visual comparison of the amplitude and frequency of each model with the vehicle trajectory and on a consideration of the relative strength of each term in the model force balances. These comparisons are made between models and between the models and the vehicle. Of the three, amplitude considerations are the most important. The frequency and force balance comparisons fill a corroborative role in the argument.

The strength of each term in the force balances is a function of either position, velocity, or acceleration. Since all of these quantities vary over the run, their standard deviations are used as representative characteristic values on which to base the calcu-

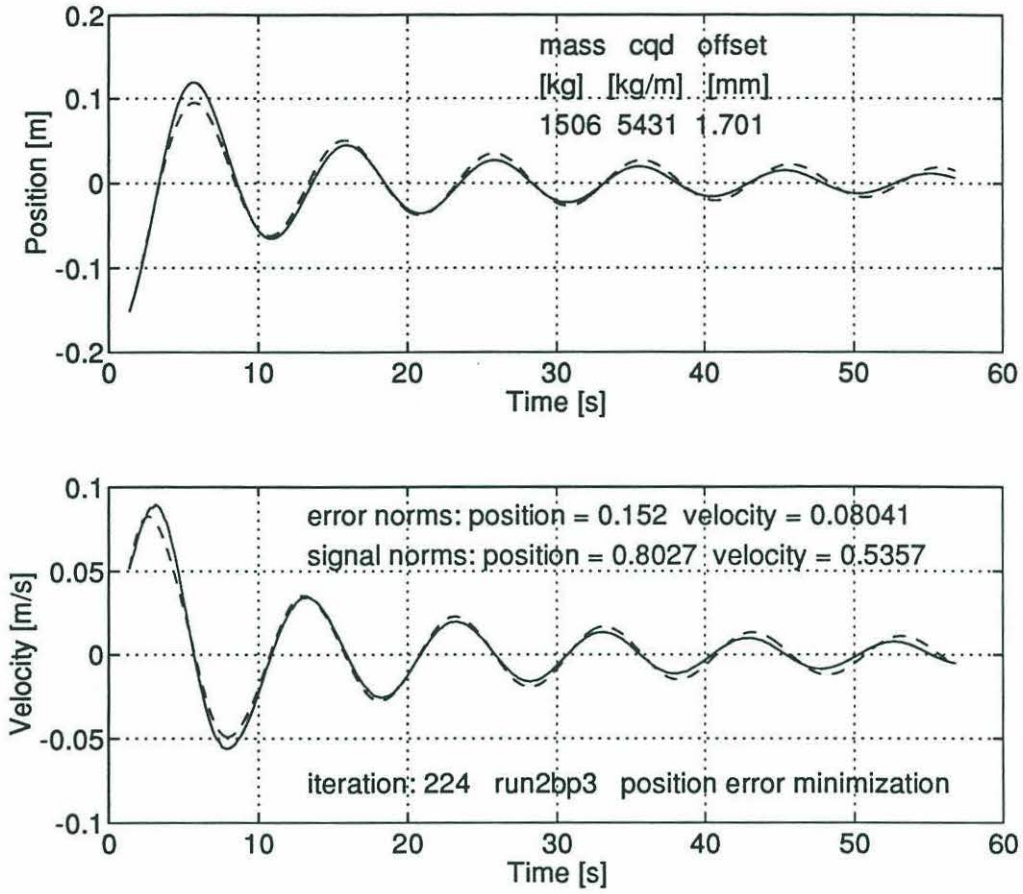

Figure 2.10: NUMERICAL MINIMIZATION EMPLOYING THE INERTIA WITH QUADRATIC DRAG MODEL - The vehicle trajectory is marked by the solid line. The dashed trace is the path followed by the model. Model and minimization parameters for the process are shown on the plots.

lations. If the standard deviation of x is denoted by σ_x, then the forces are calculated from the formulas:

$$\begin{aligned} F_{spring} &= k\sigma_{z_{veh}} \\ F_{inertia} &= m_{eff}\sigma_{\ddot{z}_{veh}} \\ F_{q-drag} &= c_{qd}\sigma_{\dot{z}^2_{veh}} \\ F_{l-drag} &= c_{ld}\sigma_{\dot{z}_{veh}}. \end{aligned} \tag{2.21}$$

The results can be found in Table 2.1. The trajectory of the vehicle rather than the model is used as a way of normalizing the comparison. With the exception of the inertia model, which is not under serious consideration, the difference between model and vehicle standard deviation is generally less than 5 %.

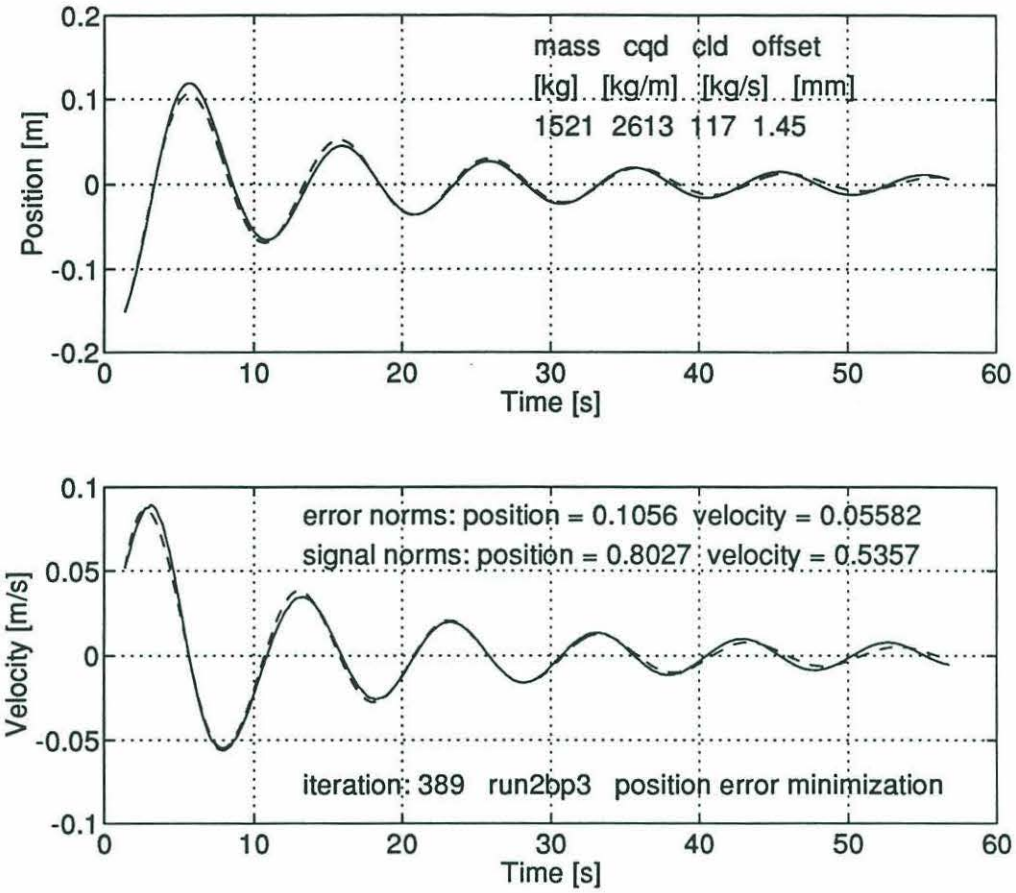

Figure 2.11: NUMERICAL MINIMIZATION EMPLOYING THE INERTIA WITH QUADRATIC AND LINEAR DRAG MODEL - The vehicle trajectory is marked by the solid line. The dashed trace is the path followed by the model. Model and minimization parameters for the process are shown on the plots.

The force balance for each model is summarized in the the last four columns of Table 2.1. Obviously the dominant forcing is provided by the mass and spring, neither of which is being considered for exclusion from the models. Focusing on the drag coefficients, observe that while both coefficients are reduced in the quadratic and linear drag model compared to their values in the quadratic drag and the linear drag models, the reduction of c_{ld} is much larger. The factor is 5.5 compared to 2.1 for c_{qd}. The point to be made here is that, when both types of drag are used to account for the decay, quadratic drag retains more of its solo influence than does linear drag. In the quadratic and linear drag model, the decay is largely explained by quadratic drag, with linear drag providing only a correction.

Model	m_{eff} $[kg]$	c_{qd} $[kg/m]$	c_{ld} $[kg/s]$	F_{spring}	$F_{inertia}$	F_{q-drag}	F_{l-drag}
				$[N]$			
inertia	1434			22.66	20.08		
inertia with linear drag	1533		639	22.66	21.46		16.11
inertia with quadratic drag	1506	5431		22.66	21.08	3.45	
inertia with quadratic and linear drag	1521	2613	117	22.66	21.29	1.66	2.95

Table 2.1: SUMMARY OF MINIMIZATION COEFFICIENTS FOR RUN 2BP3 - Two springs in parallel, effective spring constant: 597.9 N/m.

Consider now the amplitude of oscillation. Predictably, the simple inertia model (Figure 2.8) is a poor match to the vehicle behavior. However, it does indicate that the integration is stable. The addition of linear drag (Figure 2.9) is a significant improvement. Note, however, that linear drag damps out the motion too fast. After 45 to 50 seconds the model has essentially stopped while the vehicle continues to oscillate. The quadratic drag model (Figure 2.10) provides a much better match to the vehicle amplitude. While there is a small difference, it is constant and does not diverge over time. Based on consideration of the amplitude this model provides the best fit. That conclusion is further supported by the linear and quadratic drag model (Figure 2.11). The figure shows excessive damping similar to the linear drag model, though the damping is less severe. The explanation is fairly simple. Observe that as the amplitude of the velocity swings becomes smaller, linear drag must dominate quadratic drag. If a longer data record had been made of the oscillations, which were observed to continue after recording stopped, the value of c_{ld} would have to decrease so that the model would not stop prematurely. To maintain the match with the early portion of the record, c_{qd} would need to increase. As previously observed, both coefficients are smaller in the quadratic and linear drag model than in the quadratic

or linear drag models. Therefore, the trend of the quadratic and linear drag model as the duration of the decay lengthens is toward the simpler quadratic drag model.

Finally, consider the frequency of oscillation. The inertia model makes a better showing here and once again provides a validity check on the integration. The value of m_{eff} for the undamped system must be exceeded by the value of m_{eff} for a damped system with the same observed frequency of oscillation. The effective mass values of the drag models are consistent with this observation. Mass values increase monotonically with increasing model periods. Both models that include linear drag have periods of oscillation that are observably longer than the period of the vehicle. As with amplitude, the divergence is less pronounced for the quadratic and linear drag model. The explanation is the same and convergence to the inertia and quadratic drag model, which makes a good fit to the vehicle frequency, is once again indicated.

In summary, of the models tested, the inertia with quadratic drag model is observably the best fit to the vehicle trajectory. The plots show that the quality of the fit is quite high. A model with both linear and quadratic drag can match a finite data set with greater precision, but it will converge to a model with only quadratic drag as the number of oscillations is increased. While it could be argued that a model with fractional or higher order drag terms would provide a still better fit, there is no widespread support for this notion in the literature and the complexity of such a scheme would complicate the state estimation and control problem. Based on the observations the inertia with quadratic drag model is the correct choice to describe the vehicle hydrodynamics.

This finding is in agreement with the work of Morison, et al. [15], Keulegan and Carpenter, Sarpkaya and Isaacson [23], Bearman, et al. [1], and Sarpkaya [24]. The cited body of research covers both oscillatory and steady forcing of cylinders, plates, and other bluff bodies. The finding contradicts the conclusion of Sagatun and Fossen [19, 20] who used the other method of free decay analysis and worked with an underwater vehicle. They preferred a model including both quadratic and linear drag. However, the approach used here has a superior ability to discriminate between models. Analyzing trajectory plots has considerably more physical appeal than evaluating

the quality of the least squares line in Figure 2.7. Choosing between that line and one where a_1 was set to zero for the least squares calculation has no intuitive basis.[17] Numerical minimization is also more robust to heavy damping because of its ability to work with fewer oscillations now that the correct model has been identified. The runs driven by a single spring or two springs in series (Appendix A) bear out this last point.

Having chosen the model, it is important to verify that the simplex algorithm has located a global rather than a local minimum of the error norm hypersurface. This can be done graphically by choosing ranges of m_{eff} and c_{qd}, calculating the error norm at each grid point, and plotting the resulting surface in a 3 dimensional mesh plot. The result is shown in Figure 2.12. Similar plots for the other runs are included in Appendix A. Over a large range of m_{eff} and c_{qd} values the surface shows only the single, necessarily global, minimum. The two side views of the mesh plot in Figure 2.13 demonstrate this quite clearly. The most striking feature here is the steep gradient near the minimum along the effective mass axis compared to the much weaker gradient along the quadratic drag axis. In the vicinity of the minimum, a small change in mass alters the behavior much more than a small change in drag. This is not an effect of changing KC and β values; the model and error norm are ignorant of hydrodynamics. Rather, it reflects the relative magnitudes of the force balance values for this model (Table 2.1). The behavior of the model is largely determined by the combination of spring and mass. The contribution of the drag is relatively small, though obviously not without significance.

[17]Independent data to be presented in Section 2.3.3 will support the conclusion that there is no linear component to the drag.

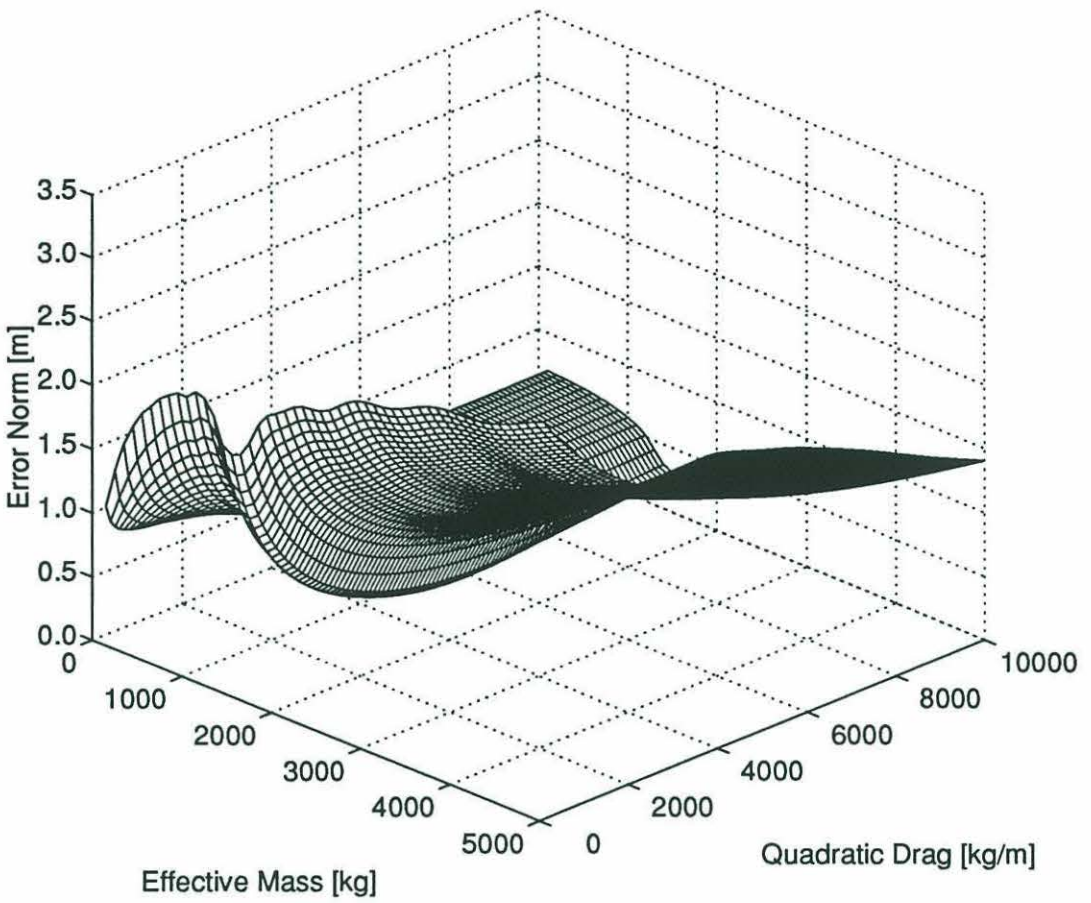

Figure 2.12: ERROR NORM SURFACE FOR THE INERTIA WITH QUADRATIC DRAG MODEL - The oblique view shows only the single, necessarily global, minima.

2.3.3 Comparison With Other Research

Sarpkaya [24][18] made measurements of the in-line forces on three smooth cylinders and one rough cylinder individually fixed in the harmonically oscillating flow of a U tube. The data cover a range of KC values for each of four βs. Sarpkaya determined

[18]Experimental and theoretical research into hydrodynamic forcing at small KC numbers has been performed by several investigators. The list includes but is not limited to Wang [31], Graham [11], Bearman, et al. [1], and Sarpkaya [24], all of whom are listed in the bibliography. In the interests of both clarity and brevity only the results of Sarpkaya are presented in this section. The exclusion is well justified as the original intent of Sarpkaya's research was verification of the formulas developed by Wang. He also discusses the paper by Bearman, et al. Bearman, et al. and Sarpkaya both measured forces on cylinders in oscillatory flow produced in a U tube. Their results show close agreement.

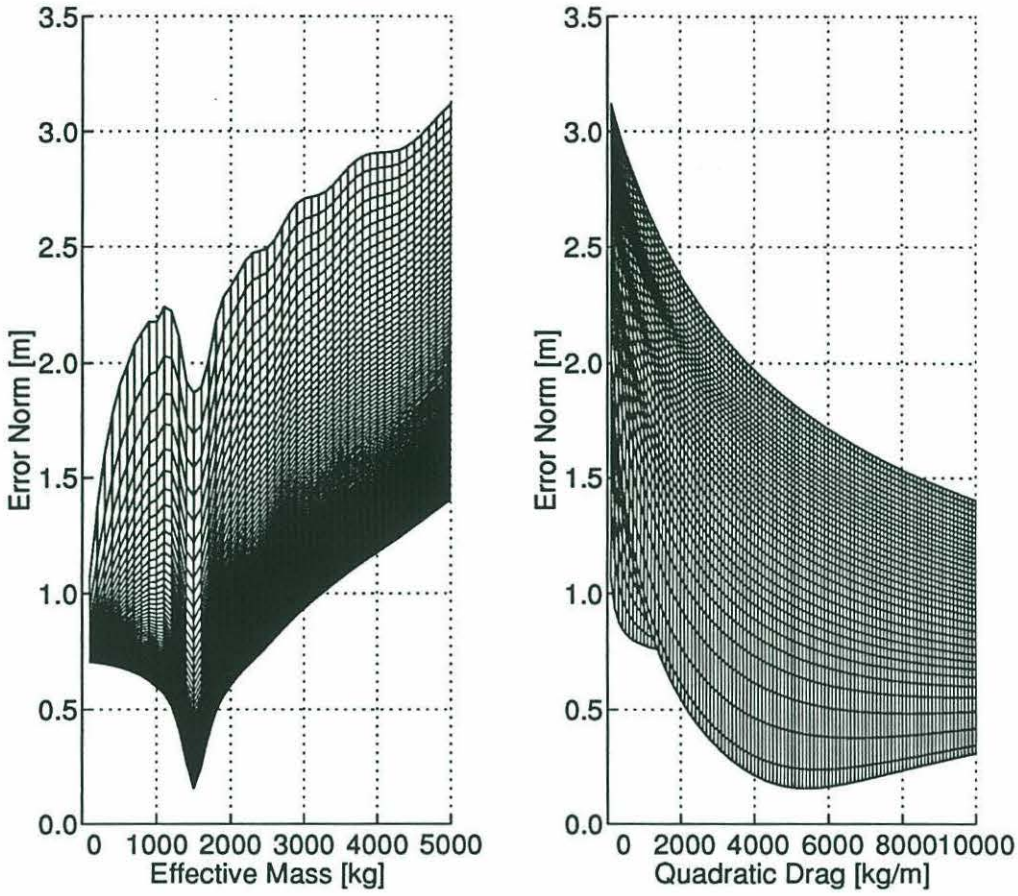

Figure 2.13: SIDE VIEWS OF THE ERROR NORM SURFACE - The global minimum identified by the simplex algorithm, $m_{eff} = 1506\ kg$ and $c_{qd} = 5431\ kg/m$, is clearly visible.

the dimensionless coefficients of added mass and quadratic drag from

$$C_M^* = \frac{m_{added}}{\rho V} \tag{2.22}$$

$$C_D^* = \frac{c_{qd}}{\frac{1}{2}\rho A}. \tag{2.23}$$

As noted when Equation 2.1 was introduced in Section 2.1, the normalization for C_M^* is equivalent to that used in Equations 2.15 for a submerged, neutrally buoyant body. On that basis the dimensionless coefficients for the cylinder and vehicle may be directly compared. His results are summarized in Figures 2.14–2.17.

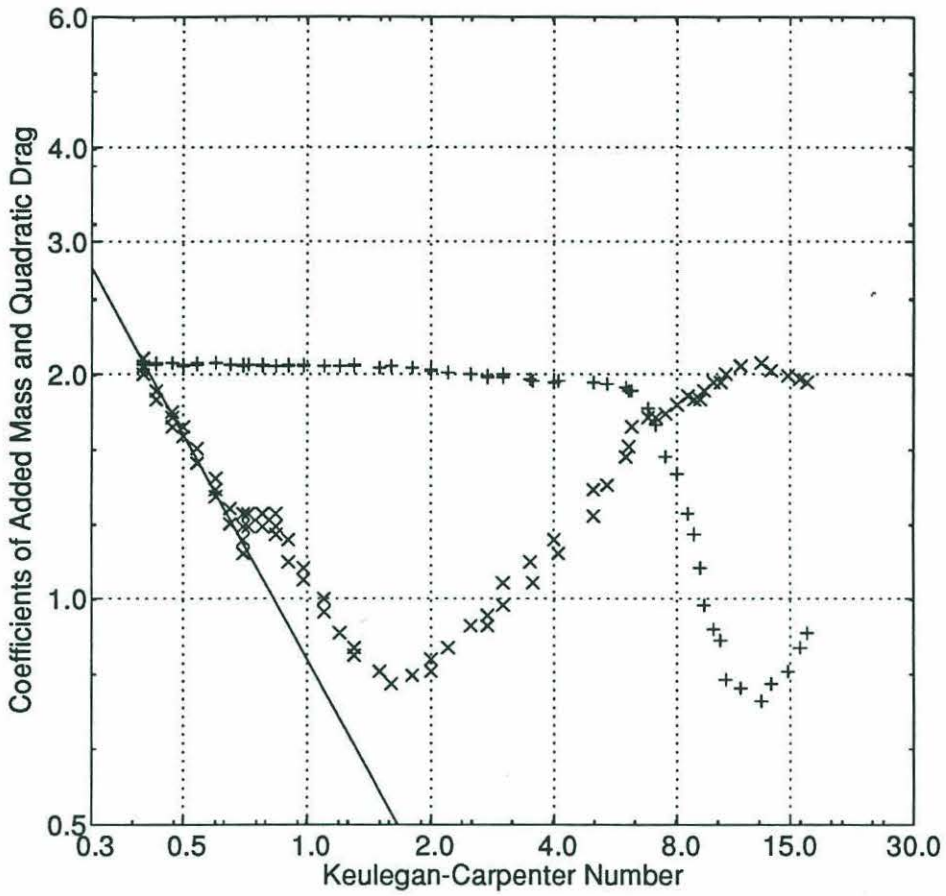

Figure 2.14: DIMENSIONLESS COEFFICIENTS OF ADDED MASS AND QUADRATIC DRAG, SMOOTH CYLINDER, $\beta = 1035$ - C_M^* is denoted by $+$. C_D^* is denoted by $\times$. The solid line is Wang's β dependent formula for C_D^*. Replotted from Sarpkaya [24] with the permission of the author.

The formulas derived by Wang [31] were written in the following form by Sarpkaya [24].

$$C_M^* = 2 + 4(\pi\beta)^{-\frac{1}{2}} + (\pi\beta)^{-\frac{3}{2}} \tag{2.24}$$

$$C_D^* = \frac{3\pi^3}{2KC}\left[(\pi\beta)^{-\frac{1}{2}} + (\pi\beta)^{-1} - \frac{1}{4}(\pi\beta)^{-\frac{3}{2}}\right] \tag{2.25}$$

The solid line in the figures from Sarpkaya was calculated from the formula for C_D^*. The formula for C_M^* is nearly constant with a value of 2 for the β range presented here. The four figures are drawn on identical scales to facilitate comparison.

As described by Sarpkaya, there are a number of interesting features to the flow at

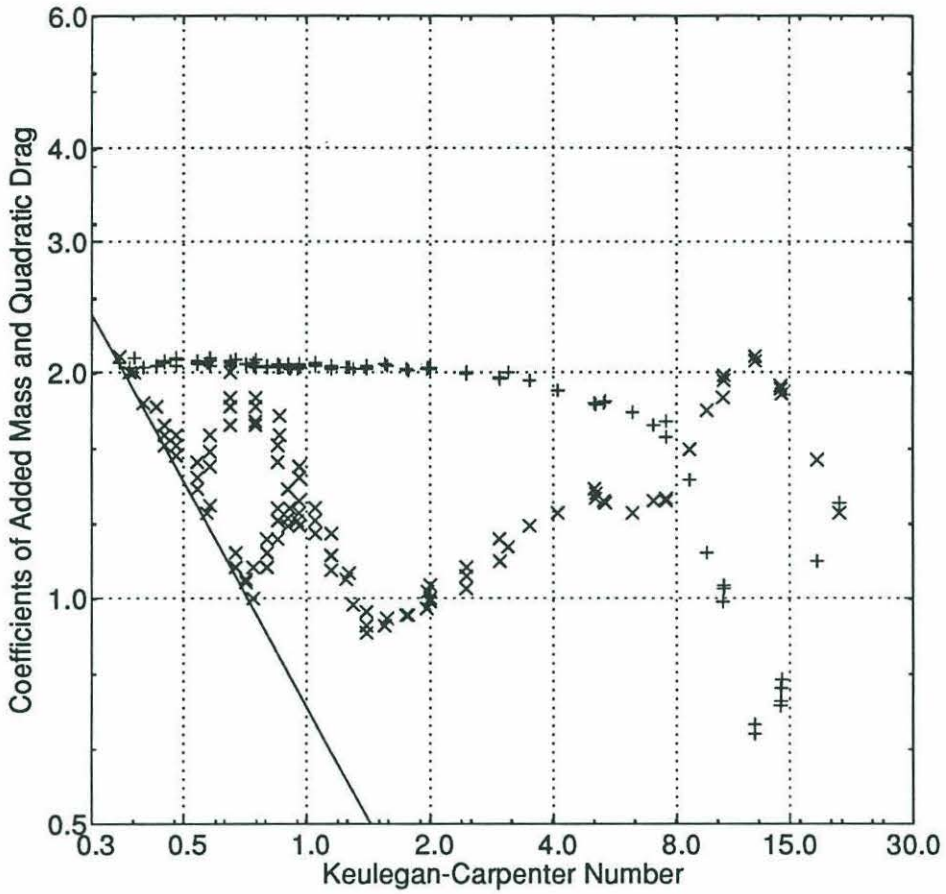

Figure 2.15: DIMENSIONLESS COEFFICIENTS OF ADDED MASS AND QUADRATIC DRAG, SMOOTH CYLINDER, β = 1380 - C_M^* is denoted by +. C_D^* is denoted by $\times$. The solid line is Wang's β dependent formula for C_D^*. Replotted from Sarpkaya [24] with the permission of the author.

low KC numbers. The main points can be summarized with reference to Figure 2.14. For $0 < KC < KC_{cr} \approx 0.75$[19] and $\beta = 1035$ the flow around the cylinder is laminar, attached, and stable. Wang's formula is quite accurate in this region. Just above KC_{cr} the laminar flow becomes unstable. As KC continues to increase the flow separates forming vortices. Approaching $KC \approx 1.6$, the flow becomes turbulent and C_D^*

[19] KC_{cr} is determined from a formula developed by Hall, P., "On the Stability of Unsteady Boundary Layer On a Cylinder Oscillating Transversely In a Viscous Fluid", *Journal of Fluid Mechanics* (1984), Vol. 146, pp. 347-367, and employed by Sarpkaya. The formula is

$$KC_{cr} = \frac{Re_{cr}}{\beta} = 5.778\beta^{-\frac{1}{4}}(1 + 0.205\beta^{-\frac{1}{4}} + \ldots).$$

Hall's stability analysis is valid only in the limit as $\beta \to \infty$ and $KC \to 0$. It is used here with some empirical justification. Details can be found in Sarpkaya [24].

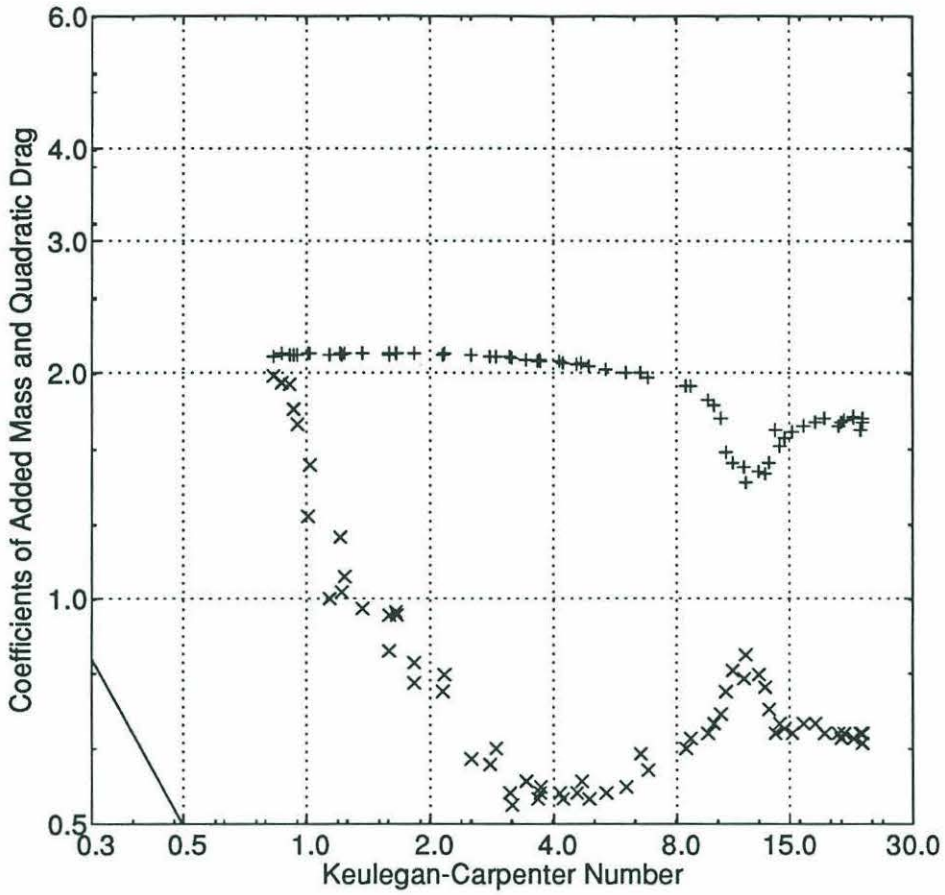

Figure 2.16: DIMENSIONLESS COEFFICIENTS OF ADDED MASS AND QUADRATIC DRAG, SMOOTH CYLINDER, $\beta = 11240$ - C_M^* is denoted by $+$. C_D^* is denoted by $\times$. The solid line is Wang's β dependent formula for C_D^*. Replotted from Sarpkaya [24] with the permission of the author.

reaches a minimum. Wang's formula is increasingly inaccurate in this range. Above $KC \approx 1.6$, C_D^* increases. Flow separation and vortex shedding become important and a half von Kármán vortex street forms in the transverse direction. These last effects are well outside the KC range of interest, however. Figure 2.15 shows the same features but also includes a region of hysteresis. However, the first transition, from stable to unstable flow at KC_{cr}, is not visible at the higher β of Figure 2.16. The boundary layer is already unstable at the lowest KC number achieved. The same is true of the rough cylinder in Figure 2.17 even though the value of β has been reduced. In summary, for extremely low values of the Keulegan-Carpenter, number flow remains attached and stable unless the frequency parameter is large or the bluff

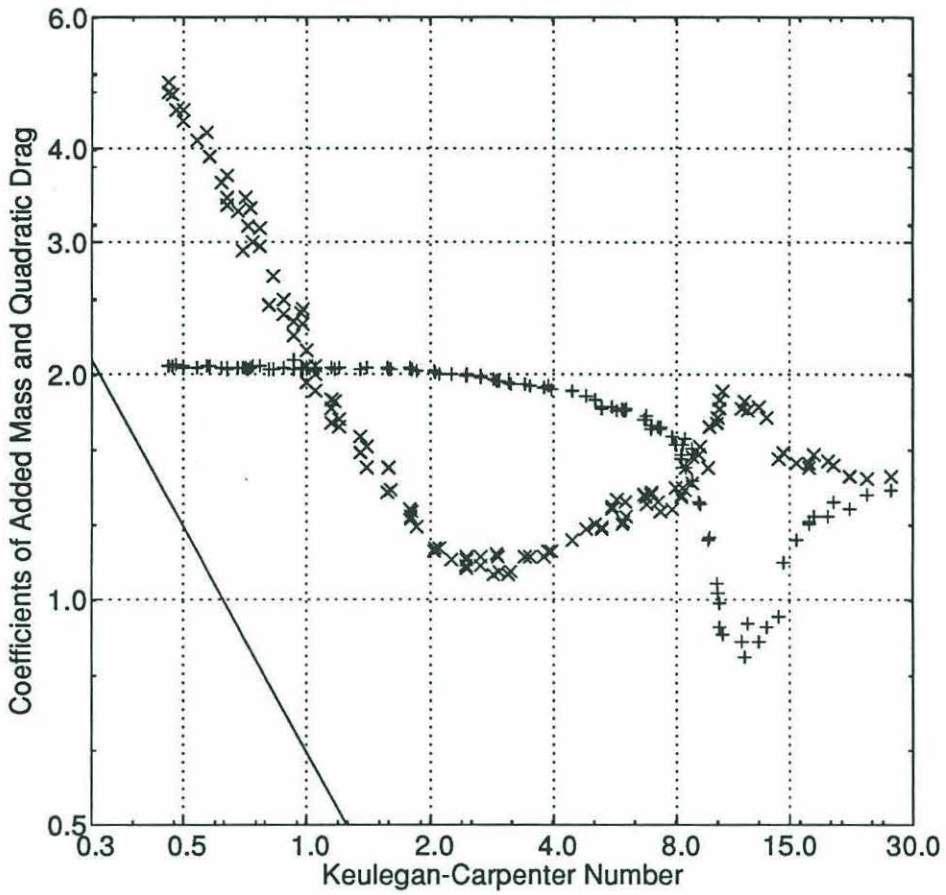

Figure 2.17: DIMENSIONLESS COEFFICIENTS OF ADDED MASS AND QUADRATIC DRAG, ROUGH CYLINDER, $\beta = 1800$, $k/D = 1/100$ - C_M^* is denoted by $+$. C_D^* is denoted by $\times$. The solid line is Wang's β dependent formula for C_D^*. Replotted from Sarpkaya [24] with the permission of the author.

body is rough or both. In the latter cases the flow has separated and may be turbulent. C_D^* will be well above the theoretical prediction of Wang. C_M^* will remain largely independent of both KC and β, however.

To make a comparison with the results of Sarpkaya, the dimensionless coefficients Re, KC, β, C_M^*, and C_D^* must be determined for each of the nine runs. The results of those calculations are summarized in Table 2.2. As before, the standard deviation of the vehicle velocity was used as the characteristic value for the calculations. The Keulegan-Carpenter numbers for the vehicle are below the boundary of the investigation of Sarpkaya. Additionally, the frequency parameter is significantly larger. Using Hall's formula, the three values of β yield $KC_{cr} = 0.35,\ 0.39,\ 0.41$, which are

Run	Re $[10^4]$	KC $[10^{-1}]$	β $[10^4]$	C_M^* $[kg]$	C_D^* $[kg/m]$
2bp1	1.5	1.8	8.1	1.95	8.57
2bp2	1.5	1.9	8.1	2.01	8.31
2bp3	2.3	2.8	8.1	2.01	7.40
1b1	1.2	2.2	5.4	2.00	9.13
1b2	0.8	1.4	5.4	1.93	10.80
1b3	1.4	2.6	5.4	2.00	8.52
2bs1	1.6	4.0	4.1	2.11	7.64
2bs2	1.0	2.4	4.1	1.90	7.54
2bs3	1.2	3.0	4.1	2.03	8.10

Table 2.2: COEFFICIENT SUMMARY OF ALL RUNS FOR THE INERTIA AND QUADRATIC DRAG MODEL - Normalization was performed using the standard deviation of the vehicle velocity.

marginally above the limit cycle KC of 0.2 to 0.3; however, the vehicle is irregular and the frequency parameter is quite large, so the formula is not expected to predict the onset of instability in the flow. Instead, the flow is expected to be unstable and separated. It may also be turbulent. The nonlaminar flow regime supports the contention of the numerical minimization procedure that the drag on the vehicle during limit cycle oscillation does not have a linear component. If the cylinder is a reasonable indicator of the hydrodynamics, as it is for steady translation, C_M^* will be very close to 2 and C_D^* will be more than a factor of 4 above the prediction of Wang.

Figure 2.18 is a plot of the vehicle data from Table 2.2. Clearly the data are a strong qualitative match to the expectations stated above. C_M^* is almost exactly 2 throughout the range and C_D^* is a factor of 10 or more above the prediction of Wang. A more careful inspection shows that the agreement is excellent on a quantitative basis as well. Figure 2.19 shows the Hylas data with Sarpkaya's data for the rough cylinder (Figure 2.17). The strength of the agreement is clear from inspection of the graph.

This completes the essential portions of the system identification procedure. The consistency with the work of other researchers using different methods of analysis is a strong validation of the technique. While some remarks remain to be made, the results of the analysis can be simply stated here. The hydrodynamics of ROV Hylas

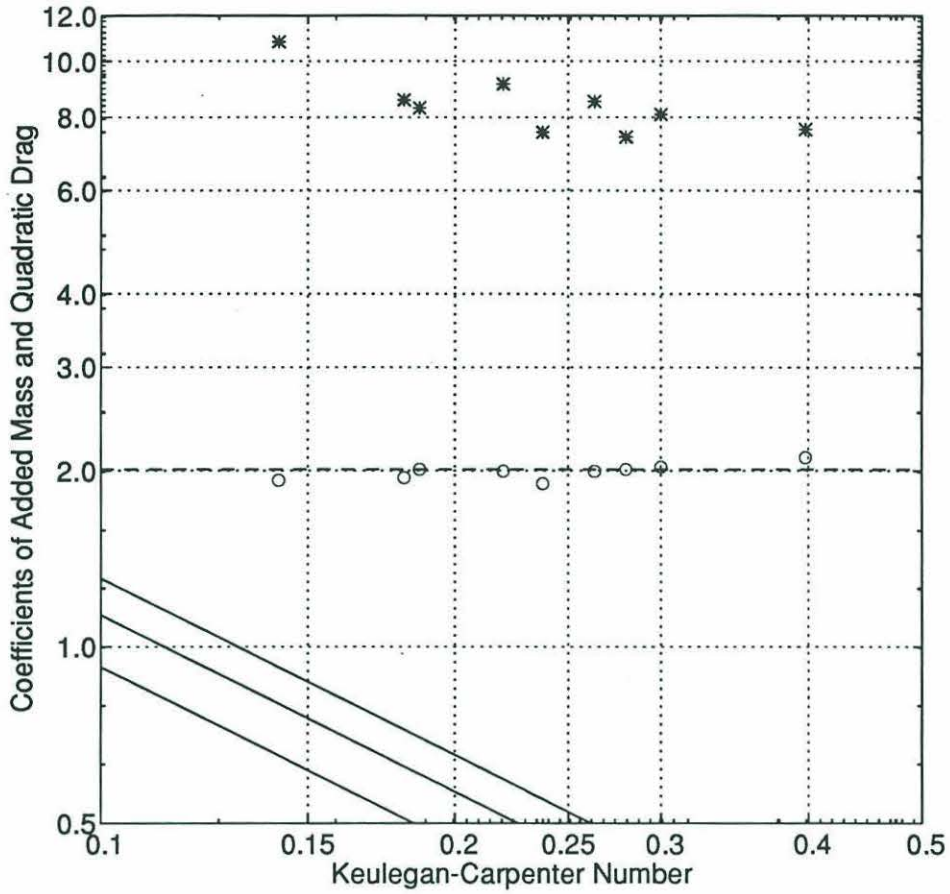

Figure 2.18: DIMENSIONLESS COEFFICIENTS OF ADDED MASS AND QUADRATIC DRAG FOR ROV HYLAS - C_M^* is denoted by $\circ$. $C_D^*$is denoted by $*$. The dashed line is Wang's value for C_M^* at all three values of the frequency parameter. The three solid lines are Wang's values for C_D^* at the three values of the frequency parameter.

are well modelled by Equation 2.1.

$$F = (1 + C_M^*)m\dot{U} + \frac{1}{2}\rho A C_D^* U|U| \tag{2.1}$$

Suitable values for the dimensionless coefficients are

$$\begin{aligned} C_M^* &= 2 \\ C_D^* &= 8. \end{aligned} \tag{2.26}$$

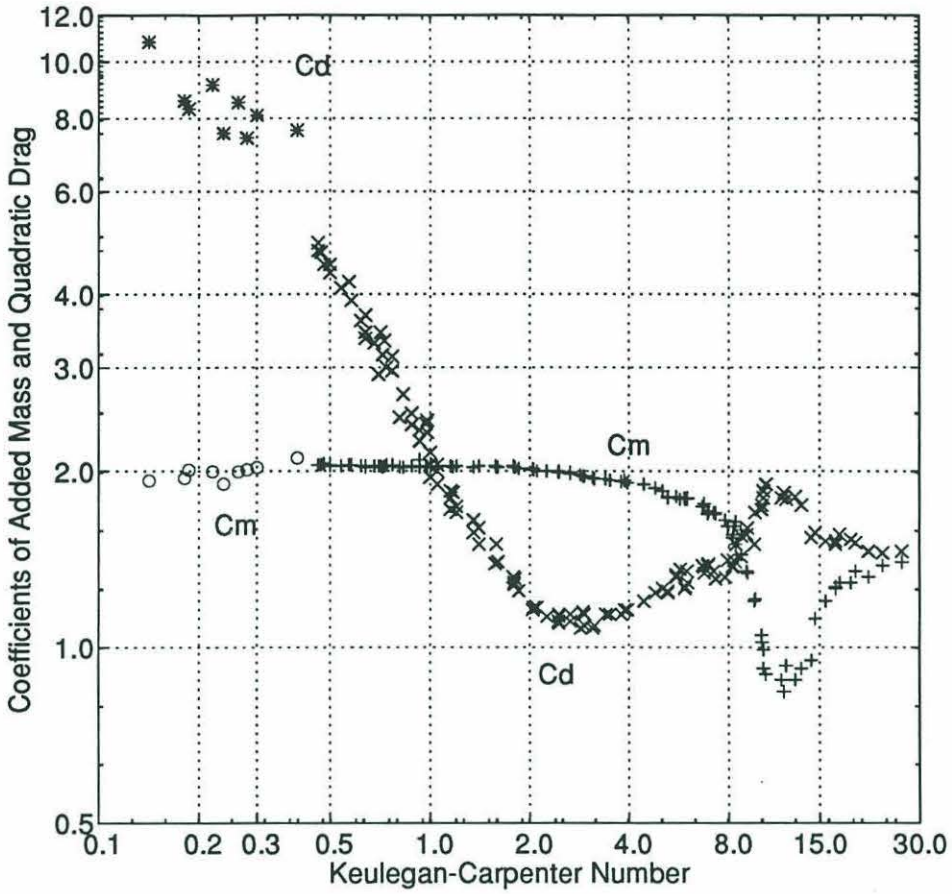

Figure 2.19: DIMENSIONLESS COEFFICIENTS OF ADDED MASS AND QUADRATIC DRAG FOR ROV HYLAS AND A ROUGH CYLINDER - C_M^* is denoted by $\circ$ for the vehicle and by $+$ for the cylinder. C_D^* is denoted by $*$ for the vehicle and by $\times$ for the cylinder. Values for the frequency parameter of the vehicle were in the range $4.0 \times 10^4 < \beta_{Hylas} < 8.1 \times 10^4$. For the cylinder the frequency parameter was $\beta_{cylinder} = 1800$ and the roughness was $(k/D)_{cylinder} = 1/100$. The data from Sarpkaya [24] is replotted with the permission of the author.

Alternatively, the vehicle can be modelled in dimensional terms as

$$F = m_{eff}\ddot{z} + c_{qd}\dot{z}|\dot{z}|. \tag{2.27}$$

Suitable values for the dimensional coefficients for the vertical direction in fresh water are then

$$\begin{aligned} m_{eff} &= 1500\ kg \\ c_{qd} &= 5870\ kg/m. \end{aligned} \tag{2.28}$$

Finally, it is apparent that, in the absence of empirical measurements, the appro-

priately scaled hydrodynamic characterization of a rough cylinder, which can be found in the literature, is a reasonable first approximation to the hydrodynamic behavior of an ROV with structural similarity to ROV Hylas.

2.4 Uniform Acceleration

It has been stated that the trajectory of an ROV can be characterized by periods of hover joined by periods of uniform translation. Both of these regimes can now be modelled accurately. At the beginning of this chapter the idea that intervals of uniform acceleration provided the link between the two regimes was proposed. Combining this approximation with the final remark of the previous section, a model for the vehicle during acceleration from hover to steady translation can be advanced.

The behavior of the dimensionless coefficients of added mass and drag for cylinders during periods of uniform acceleration from rest has been studied by Sarpkaya and Garrison [22] and by Sarpkaya [26]. Important parameters include the relative travel distance and the first and higher order derivatives of the acceleration. The latter have a particularly strong effect during the transition to uniform velocity. The magnitude of the acceleration also affects the result. With the caveat that this is a simplification of a more complicated process, the variation of the dimensionless coefficients of added mass and drag with relative displacement is shown in Figure 2.20. The oscillations of the values decrease with increasing relative displacement and converge to values somewhat greater than one. While the details of the mechanism are not clear, the variations can be associated with flow separation and wake generation, the onset of wake asymmetry, and von Kármán vortex shedding as the relative displacement increases [22, 26].

Conducting these experiments successfully is difficult, even with simple cylinders. Determination of the coefficients from the force measurements requires special techniques such as discrete vortex analysis or inviscid free streamline theory [23]. With no experimental measurements available for a vehicle in this regime it is reasonable to propose that the dynamic changes of Figure 2.20 describe the vehicle when under-

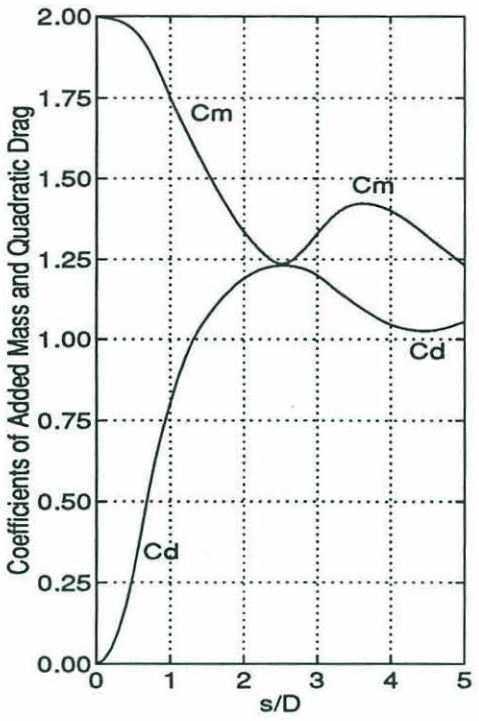

Figure 2.20: VARIATION WITH RELATIVE DISPLACEMENT OF THE DIMENSIONLESS COEFFICIENTS OF ADDED MASS AND QUADRATIC DRAG FOR A UNIFORMLY ACCELERATING CYLINDER - s/D is the ratio of distance traveled to characteristic length. The curves are redrawn from Sarpkaya [22] with the permission of the author.

going uniform acceleration. Certainly this should be verified, but it does provide a framework for the experiments.

Assuming the model is correct, the coefficients defining behavior can be approximated during operation by determining which of four motion regimes the vehicle inhabits. It is appreciated that the dynamic behavior of the vehicle is more complicated than this simplification, but, for the purpose of closed loop control, this level of accuracy may be sufficient. Cases such as deceleration or a transition to uniform translation from uniform acceleration before s/D exceeds 2.5 have not been addressed, but, if similarity with the cylinder remains valid, these regimes can also be approximated with data that already exist in the literature. The possibility of adding a few cases to Table 2.3 and obtaining a hydrodynamic description of an ROV that is sufficiently complete and accurate for both numerical simulation of the vehicle system and closed loop control during all phases of an operation is very attractive. The work done here shows that this may be achievable.

Regime	C_M^*	C_D^*
Hover	2	8
Uniform Acceleration $s/D < 2.5$	$2 - 0.4s/D$	$0.4s/D$
Uniform Acceleration $s/D > 2.5$	1	1
Uniform Translation	1	1

Table 2.3: DIMENSIONLESS COEFFICIENTS OF ADDED MASS AND QUADRATIC DRAG DURING OPERATION OF ROV HYLAS - Known or projected values of the dimensionless coefficients during various regimes of motion.

2.5 Extension to Four Degrees of Freedom

The experimental set up described in Section 2.2 and the analysis of Section 2.3 can be extended to four degrees of freedom with coupling. Springs connecting the bow and stern or the port and starboard sides of the vehicle to the walls of the tank will allow damped oscillations in the remaining translational degrees of freedom. A torsional spring from which the vehicle is suspended provides forcing for the rotational degree of freedom. This could also be accomplished with the four horizontal springs if care is taken with the geometry. In all of these cases the vehicle should be ballasted for neutral buoyancy and placed well below the surface. The initial perturbation would be provided by the thrusters. The vertical degree of freedom could be done in a similar manner with springs connecting the top and bottom of the vehicle to an overhead support and to the bottom of the tank. Ballasting for negative buoyancy would no longer be necessary.

The diagonal terms would be determined exactly as described in previous sections of this chapter. A single degree of freedom would be excited with the thrusters, the position trajectory would be recorded, and numerical minimization would determine

the coefficients of added mass and quadratic drag. Experimentally this would be most easily accomplished if only the springs associated with that degree of freedom were installed. Incidental excitation of the other degrees of freedom could be inhibited if necessary. The other translational degrees of freedom will probably be best described by Equation 2.1. Modelling rotation may require some experimentation with careful comparison of the model and vehicle trajectories.

Many of the possible coupling terms for a vehicle similar to ROV Hylas can be set to zero by symmetry arguments. Others will be eliminated from consideration by activating a single degree of freedom with the thrusters and observing the resulting motion. In the case of ROV Hylas, asymmetry between the fore and aft ends of the vehicle causes readily observable coupling between heading and lateral translation. With appropriate springs in place these two degrees of freedom would be excited with the thrusters and the resulting trajectory recorded by the SHARPS network. Different models of the coupling could then be tried with numerical minimization until a good fit was achieved. Established values for the diagonal elements could be used to reduce the number of parameters during minimization. This would reduce the number of iterations required by the Nelder-Meade simplex algorithm.

Assuming, for the purpose of illustration, that Equation 2.1 describes the rotational degree of freedom, one potential model of the coupling is the simple linear connection shown in Equations 2.29. Observation of ROV Hylas shows that the magnitude of the coupling is not large. A lateral translation at $0.2\ m/s$ induces a heading rate of less than $2°/s$ ($< .035\ rad/s$). The linear approximation of the interaction may well be adequate.

$$\begin{aligned} m_{eff_y}\dot{v} + c_{qd_y}v|v| + c_{vr_y}r &= F_y \\ I_{eff_\psi}\dot{r} + c_{qd_\psi}r|r| + c_{vr_\psi}v &= \tau_\psi \end{aligned} \tag{2.29}$$

v denotes lateral velocity, r is heading rate, and ψ is heading. m_{eff_y}, I_{eff_ψ}, c_{qd_y}, and c_{qd_ψ} are known from the single degree of freedom tests. c_{vr_y} and c_{vr_ψ} are to be determined.

Integrating coupled second order equations can be tedious in practice, but is not, in principle, more difficult than integrating a second order, single degree of freedom equation. Code complexity is only slightly greater. The major concern is processing time as the number of parameters increases. The analyses described in this chapter were implemented using MATLAB© numerical and graphics software.[20] The most complex models run during this investigation had four parameters and were integrated over approximately ten thousand time step subintervals for each iteration. For the four parameter model, three to four hundred iterations were typically required for convergence to the minimum error. The number of parameters multiplied by one hundred is often a good estimate of the number of iterations required by the simplex algorithm to satisfy intrinsic minimization checks. More efficient algorithms exist but their implementation is often more complicated. The actual integration at each iteration was carried out by compiled C code dynamically linked to the MATLAB© kernal by the MEXfile utility.[21] The balance of the code was written in the interpreted MATLAB© language. Hardware platforms included Sun-4© and Sun-SPARC© work stations.[22] Run times under these conditions varied from one to three minutes depending on the platform used.

Considerably more complicated models could therefore be used without processing time becoming an impediment to development. More complexity may not be desirable, however. One of the attractions of this approach is the ease with which it can be implemented. The experimental set up is simple and contains no critical tolerances beyond accurate position information from the existing network. The model that evolves from the process only needs enough precision to satisfy a control system that has considerable natural robustness. Adding orders of complexity to the model to achieve increasingly small corrections to the output will eventually make it impossible to run the model in real time. It could not be used as part of a control loop. Additionally, increasing the complexity of the model will also require tighten-

[20]MATLAB© is a registered tradmark of The MathWorks, Inc.

[21]MEXfiles are dynamically linked subroutines providing an external interface to the MATLAB kernal. They are one of the utilities included in the MATLAB package.

[22]Sun-4© and Sun-SPARC© are registered trademarks of Sun Microsystems, Inc.

ing the tolerances on the experiment. Growing practical difficulties in performing the measurements will result. In principle, numerical minimization could be extended to very complicated models, but a diagonal model with a few instances of mild coupling is almost certainly sufficient for closed loop control of an underwater vehicle. The method is well equipped for that goal.

2.6 Conclusions

System identification by numerical minimization has several features and capabilities to recommend it for the study of underwater vehicles. It is easily implemented experimentally. Code generation is a larger undertaking. The underlying architecture is, however, readily understandable and the necessary capabilities can be built on that in a natural sequence. The method is robust to fairly heavy damping because it can reliably calculate model coefficients from a limited number of oscillations during the decay. The approach is flexible in terms of the models it can evaluate and extension to multiple degree of freedom systems with coupling is straightforward. The graphic output permits good discrimination between alternate models and provides an intuitive level of feedback about the accuracy of any particular model. The agreement of the results with the work of other investigators is a strong validation of the technique.

One important outcome of this research is the possibility that, for accurate numerical simulation and closed loop control, a very limited number of regimes adequately describe the hydrodynamics of a vehicle. The use of this idea in the designs of the system simulation and of the vehicle observers and controllers will be addressed in the following chapters.

In conclusion, the system identification procedure performed with ROV Hylas has produced an accurate description of the hydrodynamics of the vehicle during the limit cycle that occurs when hovering under closed loop control. Under those conditions and others, the vehicle behaves as an inertia with a drag term that is quadratic in

velocity. The form of the model is given by

$$F = (1 + C_M^*)m\dot{U} + \frac{1}{2}\rho A C_D^* U|U| \tag{2.1}$$

where m is the dry mass of the vehicle and A is the projected area along the direction of motion. U is the relative velocity between fluid and vehicle and ρ is fluid density. Forcing is denoted by F. Values for the dimensionless coefficients of added mass and quadratic drag during hover, as determined by numerical minimization, are

$$\begin{aligned} C_M^* &= 2 \\ C_D^* &= 8. \end{aligned} \tag{2.26}$$

Chapter 3

State Estimation and Control

3.1 Introduction

State estimation and control are the subjects of numerous papers and text books. A selection of these can be found in the biliography [3, 7, 8, 9, 10, 14, 17, 28]. It is not the intent of this chapter to review or otherwise summarize this body of information. Working familiarity with control theory on the part of the reader is assumed. Section 3.2 presents the notation convention used while outlining the underlying linear approach to state estimation followed in this investigation. Underwater vehicle systems possess intrinsic nonlinearities, however, and estimators and controllers must take these into account. Section 3.3 describes the major nonlinearities associated with ROV Hylas. It also details the compensation for the nonlinearities that is built into the observer and controller structure.

Because the observer and controller are implemented in software on a digital computer, the state space equations describing them here are discrete. However, much of the language of control has evolved from the continuous time approach and the Laplace transform domain. When the terminology of the complex s-plane is employed here, a mapping to the complex z-plane in the actual implementation should

be understood. The mapping is described by

$$z = e^{sT} \tag{3.1}$$

where T is the discrete time interval. The behavior of this mapping is well known and will not be elaborated here.

3.2 Linear State Estimation and Control

Control algorithms depend upon both an accurate model of the system to be controlled and full knowledge of the state of the system. In the case of an underwater vehicle the state vector consists of position and velocity. For this development, the vehicle is modelled as a simple mass. The quadratic drag term and the thruster nonlinearities will be addressed in Section 3.3. That linear model of the vehicle is contained in the discrete time equation

$$\mathbf{x}_{k+1} = \mathbf{A}\mathbf{x}_k + \mathbf{B}\mathbf{u}_k \tag{3.2}$$

where $\mathbf{x}_k$ is the state vector at time step k, $\mathbf{A}$ is the system matrix describing the unforced dynamics, and $\mathbf{B}$ is the input matrix acting on the input $\mathbf{u}_k$. The state vector is defined by

$$\mathbf{x}_k = \begin{bmatrix} z_k \\ \dot{z}_k \end{bmatrix} = \begin{bmatrix} z_k \\ w_k \end{bmatrix} \tag{3.3}$$

where z_k and $\dot{z}_k$ are the vehicle position and velocity as defined in Chapter 2. The system and input matrices have the forms

$$\mathbf{A} = \begin{bmatrix} 1 & T \\ 0 & 1 \end{bmatrix}, \quad \mathbf{B} = \begin{bmatrix} T^2/2m_{eff} \\ T/m_{eff} \end{bmatrix} \tag{3.4}$$

where m_{eff} is the effective mass described in Chapter 2 and T is the discrete time interval.

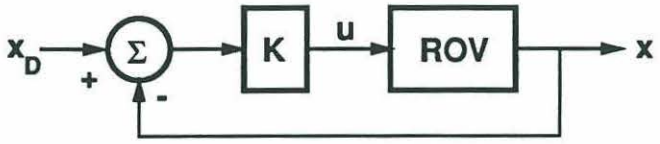

Figure 3.1: Closed Loop Trajectory Following with Full State Feedback and PD Control

A PD control law for trajectory following can be defined by

$$\mathbf{u_k} = \mathbf{K^T}(\mathbf{x_{Dk}} - \mathbf{x_k}) \tag{3.5}$$

where $\mathbf{K}$ is the control matrix and $\mathbf{x_{Dk}}$ is the desired trajectory through state space.

The closed loop system described by these equations is shown in block diagram form in Figure 3.1. Nonlinear control laws may be of advantage for the thruster-ROV combination. However, observer rather than controller development is the focus of this research. The underlying structure here is linear, and the chosen control law can be shown to be optimal under these conditions in the sense that it minimizes a quadratic performance index specified by the designer [29]. It will be shown in Chapters 4 and 5 that selected nonlinear modifications to the PD control law are sufficient for closed loop control of ROV Hylas.

The gains of the control matrix can be determined by any of several methods. In the absence of other considerations, a Butterworth configuration of the poles is often suitable [8]. For the two pole system represented by the vehicle (two states, vertical position and vertical velocity) the poles will be located on the "45° lines" in the left half plane with damping coefficient $\zeta = \sqrt{2}/2$. Operational experience with ROV Jason shows that a natural frequency of $\omega_{n_{cl}} = 0.7\ s^{-1}$ then gives acceptable closed loop performance. Alternatively, minimizing a quadratic performance index that strongly emphasizes position tracking over actuator use will yield the same poles. The poles are the eigenvalues of $\mathbf{A} - \mathbf{BK^T}$, and numerous standard techniques exist

to determine $\mathbf{K}$ from that relationship.[1]

Implicit in this structure is the assumption that the full state of the vehicle is available for feedback. This assumption is known to be incorrect; only the vehicle position is available from the SHARPS network. Thus the need for state reconstruction with an estimator. The sensor information is carried in the output equation of the system.

$$\mathbf{y_k} = \mathbf{C}\mathbf{x_k} = z_k \tag{3.6}$$

where $\mathbf{y}$ is the output vector of the system and $\mathbf{C}$ is the output matrix, $\mathbf{C} = [\ 1 \quad 0\ ]$. A stochastic noise process is also associated with the SHARPS measurement and the output equation is more correctly given by

$$\mathbf{y_k} = \mathbf{C}\mathbf{x_k} + \mathbf{v_k} \tag{3.7}$$

where $\mathbf{v_k}$ is an additive noise process with known statistical attributes. Similarly, an additive noise process can be associated with the vehicle equation to model its imperfections. This process, $\mathbf{w_k}$, is assumed to be uncorrelated with $\mathbf{v_k}$. Values for its statistical attributes are considerably more difficult to determine.

The classical approach to state reconstruction was developed in the late 1950s and early 1960s. The approach minimizes, in the least squares sense, the error between the true and estimated states based on the system model and knowledge of the two stochastic processes [30]. The name most commonly associated with this development is R. E. Kalman, although many others took part both before and after his contributions were made. A well written exposition on the mathematics can be found in Sorenson [29]. Other approaches have been developed since that time with varying degrees of intuitive appeal. The observer structure produces a state estimate based on a weighted combination of model based and measurement based

[1]This statement is also true in the continuous domain when $\mathbf{A}$, $\mathbf{B}$, and $\mathbf{K}$ are replaced by their continuous equivalents. An algorithm described in Kautsky, J., Nichols N. K., "Robust Eigenstructure Assignment in State Feedback Control", Numerical Analysis Report NA/2/83, School of Mathematical Sciences, Flinders University, Bedford Park, SA, 5042, Australia, and used in the MATLAB© function *place.m* was used here because of its reliability and robustness.

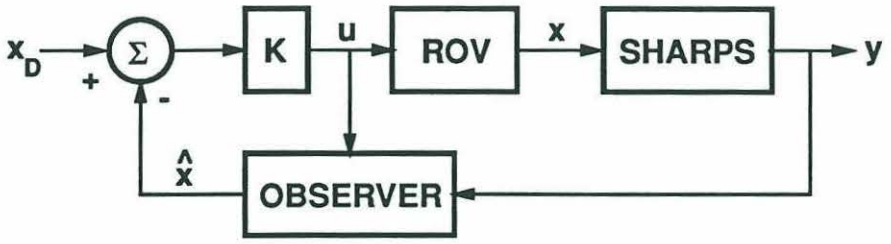

Figure 3.2: Closing the Control Loop with a State Estimator

information. That balance is set by the observer gains and their selection, rather than structural changes to the observer, is commonly the focus of the different approaches to state reconstruction. A current rather than a predictive estimator was used in this investigation. The equation describing it is

$$\hat{\mathbf{x}}_{k+1} = \mathbf{A}\hat{\mathbf{x}}_k + \mathbf{B}\mathbf{u}_k + \mathbf{M}[\mathbf{y}_{k+1} - \mathbf{C}(\mathbf{A}\hat{\mathbf{x}}_k + \mathbf{B}\mathbf{u}_k)] \tag{3.8}$$

where $\mathbf{M}$ is the observer gain matrix. $\hat{\mathbf{x}}_k$ is the estimated state vector that now takes the place of the actual, but unknown, state vector, $\mathbf{x}_k$, in the control law.

$$\mathbf{u}_k = \mathbf{K}^T(\mathbf{x}_{Dk} - \hat{\mathbf{x}}_k) \tag{3.9}$$

Note that there are two inputs to the observer. The measurement from the SHARPS array is compared to the model estimate of position. The second input is the the control law output or force command that drives both the vehicle and the model.

As written, Equation 3.8 shows the model-measurement balance governed by the gain matrix. Alternatively, the measurement input can be viewed as a check on an imperfect model that corrects drift in what is essentially a numerical integration. This interpretation may be clearer from the block diagram of Figure 3.2.

The gain matrix, $\mathbf{M}$, can be determined by the iterative algorithm developed by Kalman [3, 12, 13]. However, this requires estimates of the variance of the two stochastic processes, $\mathbf{w}_k$ and $\mathbf{v}_k$. This is easily determined in the case of the SHARPS

noise from empirical measurements. System noise associated with the model can generally be estimated only from experience, a physical intuition that is difficult to develop. Alternatively, the gains can be set by pole placement. A Butterworth arrangement or a repetition of the closed loop pole pattern is often sufficient with the caveat that the estimator poles be somewhat faster than the closed loop poles. A reasonable range is three to five times faster. Slower poles respond less quickly than the actual system and can cause instability. Faster poles create noisy state estimates that can overstress the actuators or excite undesirable high frequency behaviors. Both methods were evaluated early in the course of this investigation. Pole placement, with its greater intuitive appeal, was selected.

The poles of the observer are the eigenvalues of $\mathbf{A} - \mathbf{MCA}$.[2] The observer gains, $\mathbf{M}$, can be calculated by the same techniques used to determine the controller gains, $\mathbf{K}$, from the placement of the closed loop poles. The Separation Principle [7, 8, 14] insures that the two gain selection procedures may proceed independently. The controller gains have no effect on the observer poles and the observer gains have no effect on the closed loop poles. Stability of the overall linear system requires only that the observer and controller poles be placed in the left half of the complex plane. Unmodelled and nonlinear characteristics of the actual vehicle system can shift the poles and cause poor or unstable behavior, however. Contending with that tendency will be discussed in the following sections.

In summary, the linear structure on which the observer and controller for ROV Hylas are based treats the vehicle as a simple mass equal to the effective mass determined during the system identification procedure of Chapter 2. Observer and controller gains will be calculated from pole placement techniques using the linear model. In general, the pole positions are specified in terms of the damping coefficient, ζ, and the natural frequency, ω_n, of the equivalent continuous time, second order system.

[2]This expression must be modified for the continuous domain. If $\mathbf{A}$, $\mathbf{M}$, and $\mathbf{C}$ are the continuous equivalents of the discrete matrices, then the poles of the continuous observer are the eigenvalues of $\mathbf{A} - \mathbf{MC}$.

3.3 Nonlinearities and Compensation

3.3.1 Thruster Dynamics

The dominant nonlinearity of the vehicle system is the thruster characteristic described by Cooke, Yoerger, and Slotine [4, 5]. The thruster dynamics are directly responsible for the limit cycle observed during hover under closed loop control. The behavior is well described both statically and dynamically by the equations

$$\begin{aligned} \dot{\Omega} &= \frac{\alpha}{C_t}\mathbf{u} - \alpha\Omega|\Omega| \\ F_{thrust} &= C_t\Omega|\Omega| \end{aligned} \tag{3.10}$$

where Ω, the state of the thruster, is the angular velocity of the propeller, $\mathbf{u}$ is the commanded force from the controller defined in Section 3.2, and F_{thrust} is the force generated by the thruster. C_t and α are parameters of the model. The response time to meet a step change in commanded thrust is an inverse function of the size of the step as shown in Figure 3.3. The response is exacerbated by distributing the load to two thrusters, a common arrangement for ROVs.

Changing the dynamic response requires a measurement of the thruster state that can be used in a local feedback loop around the thruster. Algorithms to accomplish this were developed by Cooke assuming the availability of thruster state information. The DC brushless motors used by DSL are intended for work at ocean depths as great as 6000 m. To achieve that operational depth the housing is oil filled and hydraulically connected to an exposed bladder for pressure compensation. Measurement of the propeller angular velocity, particularly at slow speeds where the response is poorest, requires a high resolution resolver capable of working in translucent oil at high pressures ($9,000$ psi). This is a nontrivial engineering problem and not an object of this research. Without significant hardware changes, the thruster dynamics described by Cooke cannot be compensated for by the observer or controller software.

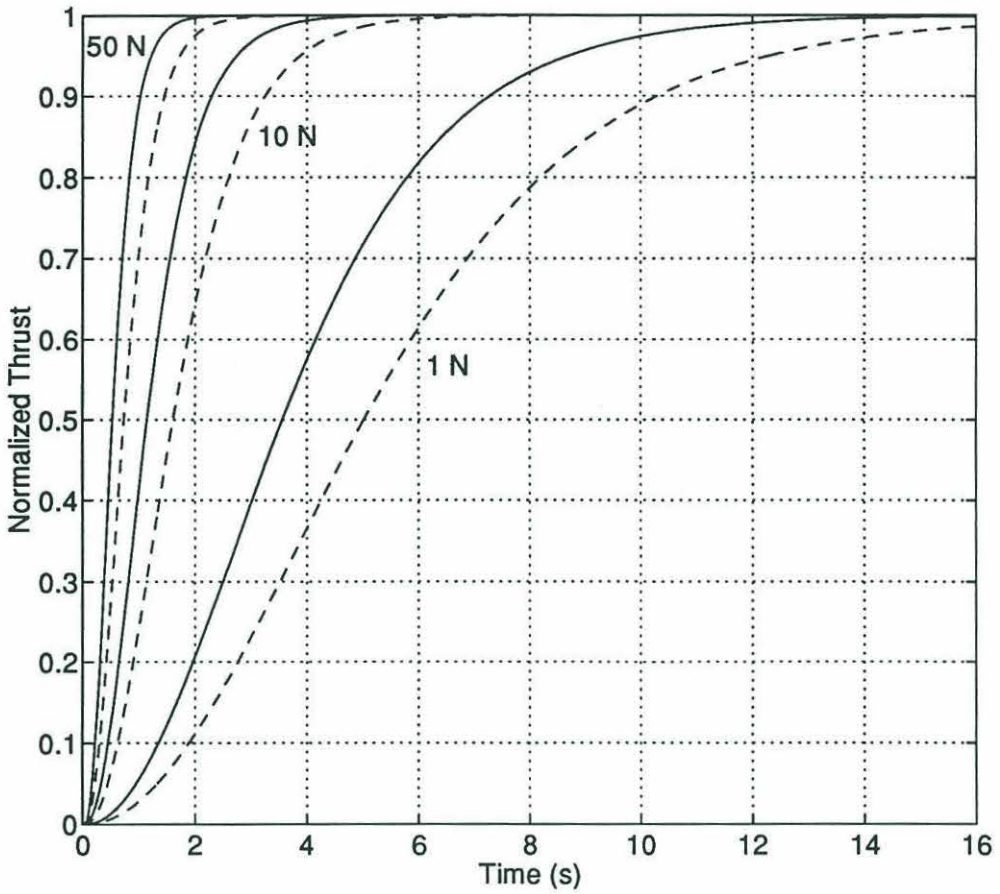

Figure 3.3: NORMALIZED THRUSTER RESPONSE TO A STEP INPUT - The magnitude of the step command is shown beside each response pair. All responses have been normalized to 1. The solid lines show the response of a single thruster, the dashed lines show the dual thruster response typical for ROV Hylas.

3.3.2 Thruster Deadband and Saturation

The thrusters also possess a steady state deadband and saturation characteristic. The data from two tests are shown in Figures 3.4 and 3.5. In the first test, a single thruster was mounted in the test tank to thrust horizontally at the end of the lower leg of a seesaw test rig. Thrust was measured by a load cell connected to the end of the upper leg. A basketball was moored on the surface to prevent the whirlpool that formed at high angular velocity from channeling air to the propeller blades. The control voltage was increased in increments from 0 to +10 V and then decreased by the same increments back to zero to check for hysteresis. The same procedure was

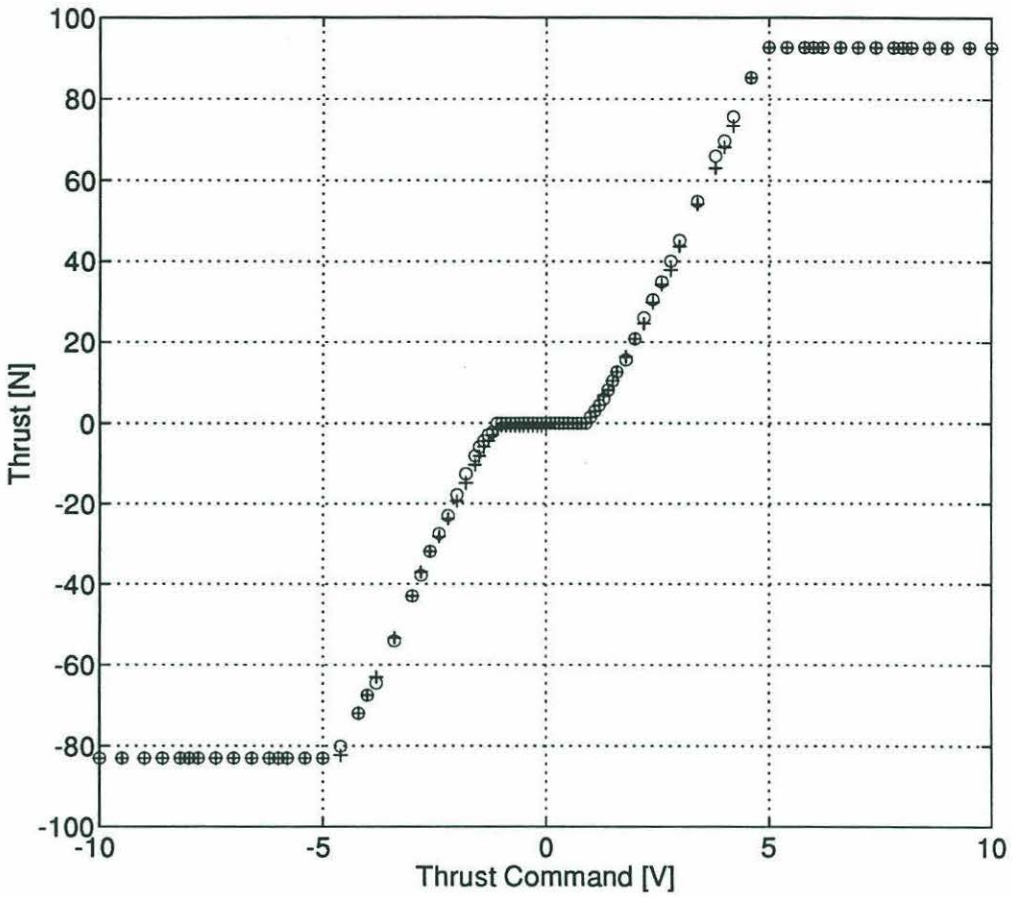

Figure 3.4: SINGLE THRUSTER STEADY STATE INPUT-OUTPUT RELATION - The response shown here is for a single thruster mounted in a test rig. o symbols mark the response as the input magnitude was increased away from zero. + symbols mark the response as the input magnitude was decreased towards zero.

followed with negative voltages for reverse thrust. The second test was performed in the test tank using ROV Hylas. The vehicle was suspended from a load cell and the two vertical thrusters were commanded in increments from zero to the maximum downward thrust.

The results of both tests show a classic deadband and saturation response. There is no hysteresis and the curve is essentially piecewise linear. The deadband is caused by shaft friction in the motor. Saturation occurs when the maximum angular velocity of the shaft is reached. The $5 - 10$ % difference in magnitude between the forward and reverse saturation levels in Figure 3.4 is due to the asymmetry of the blades about a radial line drawn from the hub of the propeller. The ragged appearance of

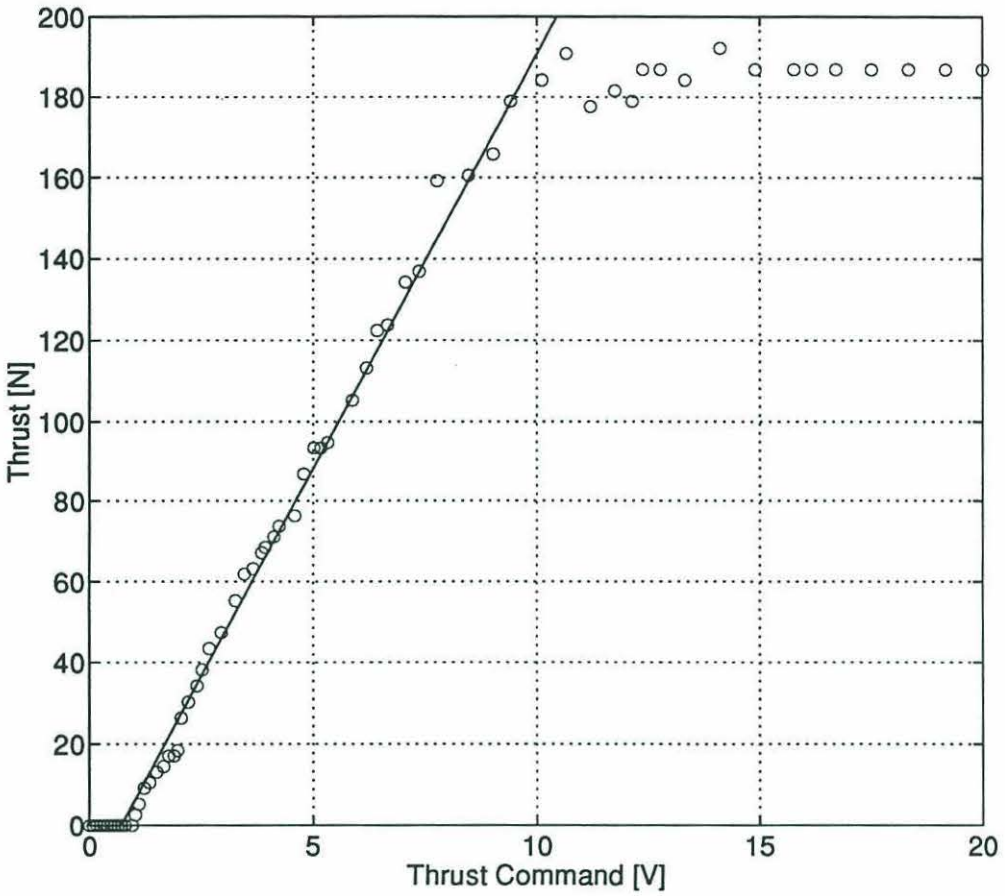

Figure 3.5: DUAL THRUSTER STEADY STATE INPUT-OUTPUT RELATION - The response shown here is for two thrusters mounted on ROV Hylas. ∘ symbols mark the response as the downward thrust was increased. The deadband for the aft thruster extended to 0.5 V (1 V thrust command). The deadband for the forward thruster extended to 0.8 V (1.6 V thrust command). The solid curve is a straight line fit to the portion of the data between deadband and saturation. The slope is 20.5 N/V and the crossing of the Thrust Command axis occurs at 0.7 V = 14.4 N. Saturation occurs at 9.7 V = 185 N.

the saturation in Figure 3.5 may be caused by surface effects. The downward thrust caused upwelling above the thruster channels. At high thrust the upwelling reached heights several centimeters above the undisturbed surface and fluctuated irregularly.

Variations in deadband and saturation characteristics, both between thrusters and for a single thruster over time, exist, but appear to be small. The slope of the curve between deadband and saturation is approximately 20.5 N/V. The deadband ends at 15 N and the saturation begins at 185 N (92 N for a single thruster). A line drawn to those specifications is a good fit to that part of the curve as seen in Figure 3.5.

This suggests two methods of compensation that can be added to the observer or the controller or both.

In the observer, software can mimic the deadband and saturation response of the thrusters. Applying that algorithm to the incoming force command will mean the model is driven by the same steady state forcing seen by the vehicle. This will improve the state estimates. Alternatively, in the controller, separate force commands for the vehicle and observer can be generated. Those going to the vehicle will simply be increased by 15 N (or decreased by that amount in the case of reverse thrust). A saturation characteristic must still be applied in one of the software modules to the observer command. This approach has the advantage of improving vehicle performance by compensating for the deadband. The accuracy of the estimates is the same for either method. Errors are primarily due to deviation of the actual thruster characteristic from the model and parameters used.

3.3.3 Hydrodynamic Nonlinearities

The system identification procedure of Chapter 2 established that the vehicle is subject to quadratic drag and that the dimensionless coefficient of the drag varies in magnitude with the regime of motion. Nonlinear drag cannot be directly incorporated into the basic linear structure of the observer and controller. However, it can be compensated for by adding a feed forward term to the vehicle force command. The additive term is calculated from the state estimate as

$$F_{added} = c_{qd}\dot{\hat{z}}|\dot{\hat{z}}| \tag{3.11}$$

where c_{qd} is the dimensional coefficient of quadratic drag defined in Chapter 2 and $\dot{\hat{z}}$ is the estimated velocity. This works well with the dual controller structure suggested in Section 3.3.2. The vehicle and observer controllers each receive the full state estimate of the observer. Based on that input each generates a force command from the PD control law determined for the linear model (Equation 3.9). Then the vehicle controller determines the appropriate sign for the deadband compensation and

calculates the feed forward quadratic drag term from Equation 3.11. Both terms are added to the vehicle control signal. The observer controller, or the observer, simply applies a saturation characteristic to the observer force input. The model continues to treat the vehicle as a pure inertia.

The compensation for the quadratic drag is imperfect in the sense that model and vehicle are not as well matched as the system identification procedure allows them to be. However, a fully nonlinear observer entails considerably more computational complexity than is needed here. An extended Kalman filter used in this situation would require accurate numerical integration of no less than six variables at each time step [9]. Extension to four degrees of freedom raises that value to 72 variables which might preclude operation in real time. The advantage of the linear approach is computational simplicity combined with reasonable accuracy. The balanced structure of the observer allows this. By design it is robust to errors in both measurement and modelling.

The remaining hydrodynamic problem is determination of m_{eff} and c_{qd} during active operation. The effective mass and quadratic drag change continuously with the history of the vehicle motion. However, it was shown in Chapter 2 that a nearly complete description of the vehicle requires only a single model form and a finite set of hydrodynamic parameter pairs. The set can reasonably be restricted to the hover and uniform translation regimes. Those two motions describe most of the trajectory of an underwater vehicle and they apparently bracket the range of parameter values. The selection algorithm only needs to make a binary choice which can be based on the desired velocity, an unambiguously known quantity. If $\dot{z}_{\mathrm{D_k}} = 0$ is true, then $C_M^* = 2$ and $C_D^* = 8$. If the statement is false, then $C_M^* = 1$ and $C_D^* = 1$. The largest variability is seen in C_D^*. However, the magnitude of the drag force is only large at relatively high velocities where the uniform translation model is accurate. At low speeds and during tight manuvering, when the motion regime is most ambiguous, the drag force is very small and the vehicle is dominated by the less variable inertia (and the thruster dynamics). A more complicated structure that more fully describes the vehicle is possible, but the correction of small, generally transient, errors may

not warrant the additional complexity. The compensation suggested here is probably sufficient.

3.3.4 Measurement Errors and Delays

The initially asynchronous structure of the transputer network prevented timely reporting of position measurements. Two to four observer cycles commonly occured using the same measurement while waiting for an update. The result was a degradation of the state estimates. Partial compensation was possible within the observer by adjusting the balance away from the measurement and towards the model. This was tantamount to ignoring what should have been the most accurate part of the observer. The eventual compensation was both simpler and more satisfying. The processor network has been synchronized to the SHARPS network.

Because of the Gaussian nature of the noise process associated with the SHARPS measurement and the possibility of ambiguous multipath signals in some environments, the position measurement is occasionally wildly inaccurate. The resulting spike in the state estimate is generally eliminated within one to three observer cycles. The spike in the control law necessarily has the same transience and cannot cause large changes in the vehicle trajectory. However, even small changes are undesirable and the voltage spike may affect the thrusters adversely.[3] The problem can be easily compensated for in software. The maximum acceleration of ROV Hylas is less than $0.2\ m/s^2$.[4] If the distance between the last position estimate and the current position measurement cannot be explained by a forward Euler approximation based on the last velocity estimate, the time interval, and an acceleration of $\pm 0.4\ m/s^2$, a bad measurement can be declared. The current measurement is discarded and replaced by a forward Euler approximation.

Finally, there is a delay of one half SHARPS period inherent in the network timing.

[3]When the control law includes a term proportional to the integral of position (PID control will be discussed in Section 4.4), the position spike can have a lasting rather than a transient effect. The spike must be eliminated to avoid possibly large deviations from the desired trajectory.

[4]The maximum thrust is less than 200 N. The minimum mass is 1000 kg during steady translation. At very slow velocities the drag force is negligible and Newton's second law determines the maximum acceleration. The maximum deceleration must be less than twice that figure.

Two transponders are mounted on ROV Hylas to provide the heading information necessary to determine the location of the center of mass or any other portion of the vehicle. The stiffness in pitch and roll is assumed to keep the vehicle level. The position of each transponder within the net is determined on alternate SHARPS cycles. If the vehicle is motionless, the vector average of the two positions is the true current location of the point on the vehicle midway between the transponders. The vector difference is the true current heading. However, if the vehicle is moving, the vector average of the two positions is the location of the midpoint one half period earlier (assuming steady motion over the period). Similarly the heading is outdated by one half period. Compensation is once again simple. The current measurement, which is the vector average of the two transponder positions (or the vector difference in the case of heading) is extrapolated over one half period with a forward Euler approximation based on the previous velocity estimate.

This completes the discussion of the major nonlinearities in the vehicle system. Compensation that does not compromise the simplicity of the linear observer and controller structures is possible in most cases. However, stability of the system is no longer guaranteed by the pole locations of the linear model. The final section of this chapter discusses the effect of the uncompensated nonlinearities on the overall stability of the system.

3.4 Stability of the Nonlinear System

Stability is a primary concern in the design of control systems. For linear systems stability is assured by placing the system poles in the left half of the complex plane. There are no corresponding criteria nor straightforward analytic approaches to the determination of stability in nonlinear systems. The two methods of Lyapunov are often employed, but there is no guarantee of success and numerical or empirical methods are often required.

Several portions of the vehicle system, particularly the nonlinearities described in Section 3.3, should be considered for their impact on system stability in the absence

of compensation. The thruster dynamics have been shown to cause a stable limit cycle under closed loop control [5] so it can be assumed that they are not directly or solely responsible for system instability. Drag is stabilizing by its nature, quadratic drag even more so than linear drag, and the magnitude of the hydrodynamic parameters is now well known. The effects of bad measurements are transient and easily removed. Measurement delay and the deadband and saturation characteristic of the thrusters remain of concern. Additionally, operational experience with ROV Jason indicated that the presence of the controller force input to the observer could cause instability [32].

The first method of Lyapunov,[5] which examines local stability in the vicinity of an equilibrium point, can be applied to this investigation in the following manner. The vehicle system can be approximately described by six equations modelling the vehicle, the thrusters, the observer, and the delayed measurement.

$$\begin{aligned}
\dot{z} &= w \\
\dot{w} &= \tfrac{C_t}{m_{veh}}\Omega|\Omega| - \tfrac{c_{qd_{veh}}}{m_{veh}} w|w| \\
\dot{\Omega} &= \tfrac{\alpha}{C_t} u_{veh} - \alpha\Omega|\Omega| \\
\dot{\hat{z}} &= \hat{w} + M_1 y - M_1 \hat{z} \\
\dot{\hat{w}} &= \tfrac{u_{obs}}{m_{obs}} + M_2 y - M_2 \hat{z} \\
\dot{y} &= \tfrac{1}{\tau}(z - y)
\end{aligned} \tag{3.12}$$

where

$$\begin{aligned}
u_{veh} &= -K_1\hat{z} - K_2\hat{w} + c_{qd_{obs}}\hat{w}|\hat{w}| \\
u_{obs} &= -K_1\hat{z} - K_2\hat{w}
\end{aligned} \tag{3.13}$$

By modifying the equation for u_{veh} appropriately the three portions of the deadband and saturation curve can be investigated as separate cases. Similarly, u_{obs} can be removed or included to investigate the effect of the observer force input. This creates a total of six cases with the delay, τ, used as a parameter in each of them.

Equilibrium points are identified for each case by setting the time derivatives equal

[5]The first method of Lyapunov is also referred to as the indirect method of Lyapunov and Lyapunov's linearization method.

to zero and solving the resulting equations. The system will be locally stable if the eigenvalues of the Jacobian matrix evaluated at the equilibrium points are all in the left half of the complex plane. Conversely, if the eigenvalues are unstable, the system is locally unstable. Finally, if one or more of the eigenvalues falls on the imaginary axis, the first method of Lyapunov fails and no conclusions about stability may be drawn [28].

Several physically meaningful equilibrium points exist for the system of equations above. However, in each instance, the Jacobian matrix has multiplicities of eigenvalue zero. No conclusions about stability can be drawn using this method.

The second method of Lyapunov[6] can be used to prove global stability for a nonlinear system. The method is based on a theorem originally proved by Lyapunov. If a scalar function of the system state, the six variables of Equations 3.12, can be shown to be positive definite while its time derivative is negative definite, and if the function becomes infinite as the magnitude of the state becomes infinite, then there is an equilibrium point at the origin that is globally asymtotically stable.[7] This is essentially an energy argument. The function defines a state space energy surface that is minimum at the origin and over time all trajectories are shown to approach the minimum.

Under the second method of Lyapunov, global stability of the system is shown by identifying a scalar function that satisfies the conditions of the theorem. Such a function is referred to as a Lyapunov function and in mechanical systems some combination of the kinetic and potential energy is often a good candidate. There is no procedure that will reliably generate a suitable function for an arbitrary system, however. A variety of functions have been tried in this case without success. The thruster dynamics are particularly troublesome in this respect. Failure to identify a Lyapunov function does not imply that one or more with different root structures do not exist. However, it does mean that no conclusions about stability can be drawn from the second method.

[6]The second method of Lyapunov is also referred to as the direct method of Lyapunov.
[7]The theorem and its proof can be found in most text books on control theory.

The failure of the primary analytic techniques for the study of stability in nonlinear systems suggests the use of numerical or empirical methods. Chapters 4 and 5 will address stability with a full simulation of the vehicle system and experiments with ROV Hylas. One additional numerical approach will be described here.

Using the bilinear transform, the Laplace transforms of the continuous vehicle and thruster models can be mapped to their z-transform analogs. The continuous measurement delay can be modelled on the z-plane using a technique described by Franklin, Powell, and Workman [7]. The model allows the delay duration to be slewed in arbitrarily small increments through any required number of discrete system time steps. These approximations can be combined with the z-transforms of the observer and controller to provide a discrete time description of the vehicle system. The poles of the system are easily determined from the resulting transfer function. Stability requires that they fall inside the unit circle.

The use of the observer force input in the presence of delay can be investigated here through suitable alterations to the system transfer function while the delay is increased from zero until one or more of the poles move outside the unit circle. An example is shown in Figure 3.6.

Maintaining the observer force input over a range of observer and controller gains invariably improved the margin of stability in the presence of delay. This is not an unexpected result. While a large enough delay will produce instability in either case, a large enough delay will produce instability in any closed loop system. The magnitude of the delay required to cause instability in this system, even in the weak case of the disabled observer model, is far larger than the identifiable delays found in the system. Loop delays are less than one SHARPS period and a delay of three to six periods is required to push the poles outside the unit circle.

This particular numerical analysis is built on several approximations and does not explicitly include the deadband and saturation characteristic. It cannot be regarded as conclusive proof of system stability. However, it strongly implies that the system, as designed and without compensation, is stable. The margin of stability can be expected to improve when the compensation strategies described in Section 3.3

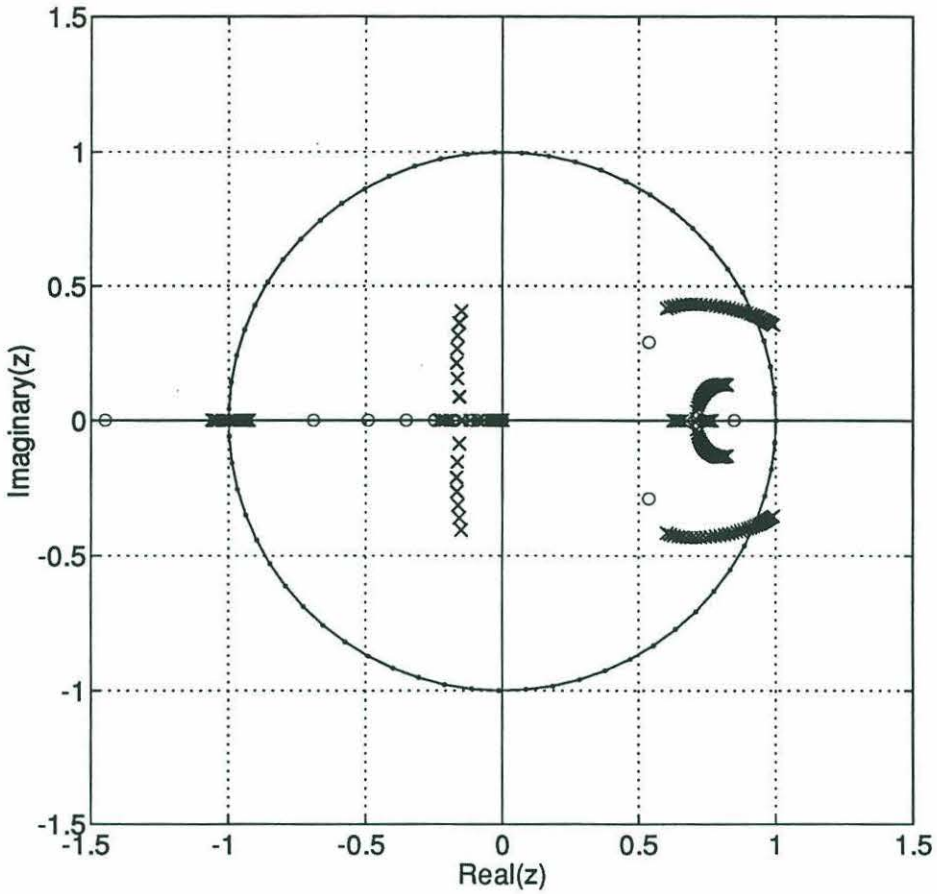

Figure 3.6: ROOT LOCUS STABILITY ANALYSIS - System poles are denoted by $\times$, system zeros are denoted by $\circ$. As the time delay is increased, the sytem poles migrate across the z-plane and eventually cross the unit circle, signalling the onset of instability. In the case shown the observer force input has been disconnected. Instability occured when the delay reached approximately three full SHARPS periods. When the observer force input is used the delay reaches six or more full SHARPS periods before the onset of instability. The pole near -1 may be ignored.

are implemented. Stability and vehicle behavior under these circumstances will be explored more fully using a numerical simulation in the following chapter. Stability and performance of the system, with the observer, controller, and compensations described here, will be demonstrated empirically in Chapter 5.

Chapter 4

Simulation

4.1 Development Background

The simulation was originally intended to serve as a development tool in the design of a state estimator that could be used to close the control loop without causing instability. New questions about the behavior of the system and experience with the vehicle during system identification and vehicle system trials have driven the evolution to greater capability, accuracy, and speed. The simulation can now be used to investigate the stability and behavioral effects of system parameters and nonlinearities, observer and controller software architectures, nonlinear compensation techniques, and environmental forcing. Limited vehicle availability has made the existence of an inexpensive and flexible test platform particularly important.

The code is a combination of the interpreted MATLAB© language and C code that is dynamically linked to the MATLAB© kernal by the MEXfile utility. The structure is philosophically similar to the system identification software in combining speed of execution with a flexible operator interface and graphic output. The simulation architecture and its capabilities are described in Section 4.2 and a sampling of the results is presented in Section 4.3. Section 4.4 briefly discusses the augmentation of the observer and controller for PID control. Section 4.5 presents the conclusions drawn from the simulation.

4.2 Simulation Architecture and Capabilities

A block diagram of the vehicle simulation is shown in Figure 4.1. The Initialization, Executive, and Plotting blocks are interpreted MATLAB© code while the Desired Trajectory and Simulation Loop blocks are compiled C MEXfiles. The flows of information and control are jointly indicated by the arrows. The Simulation Loop is composed of functional blocks that reflect the structure of the vehicle system. In the descriptions that follow the term "vehicle" refers to the simulated vehicle, which is based on the system identification of Chapter 2. The term "model" refers to quantities on which the construction of the observer and controllers are based. The term "observer controller" refers to the controller that generates the observer force input. "Vehicle controller" should be similarly interpreted.[1]

The two inputs to the vehicle block are the force command from the vehicle controller and environmental forcing. The form and magnitude of the environmental forcing can be configured to simulate the action of waves, currents, tether loads, and non-neutral ballasting with combinations of random, steady, and periodic inputs. The force command drives the thruster equations (Equations 3.10) developed by Cooke [4] in combination with the deadband and saturation characteristic described in Section 3.3.2. The output of the thruster dynamics is added to the environmental forcing to drive the inertia and quadratic drag model of the vehicle identified in Chapter 2. The equations describing the vehicle and thruster dynamics are integrated over 10 subintervals for each SHARPS time step. The process is initiated with three 4^{th} order Runge-Kutta steps and completed using a 4^{th} order Adams-Bashforth-Moulton algorithm.

The core structure of the vehicle block can be altered in several ways. The coefficients of the vehicle and thruster equations are adjustable and alternative hydrodynamic models can be selected for testing purposes. A four regime hydrodynamic model of the vehicle, as described in Section 2.4, can be enabled or disabled. The

[1] "Observer controller", a noun modified by an adjective, should not be confused with "observer-controller", an unmodified noun occasionally used in the literature to refer to the combination of observer and controller modules.

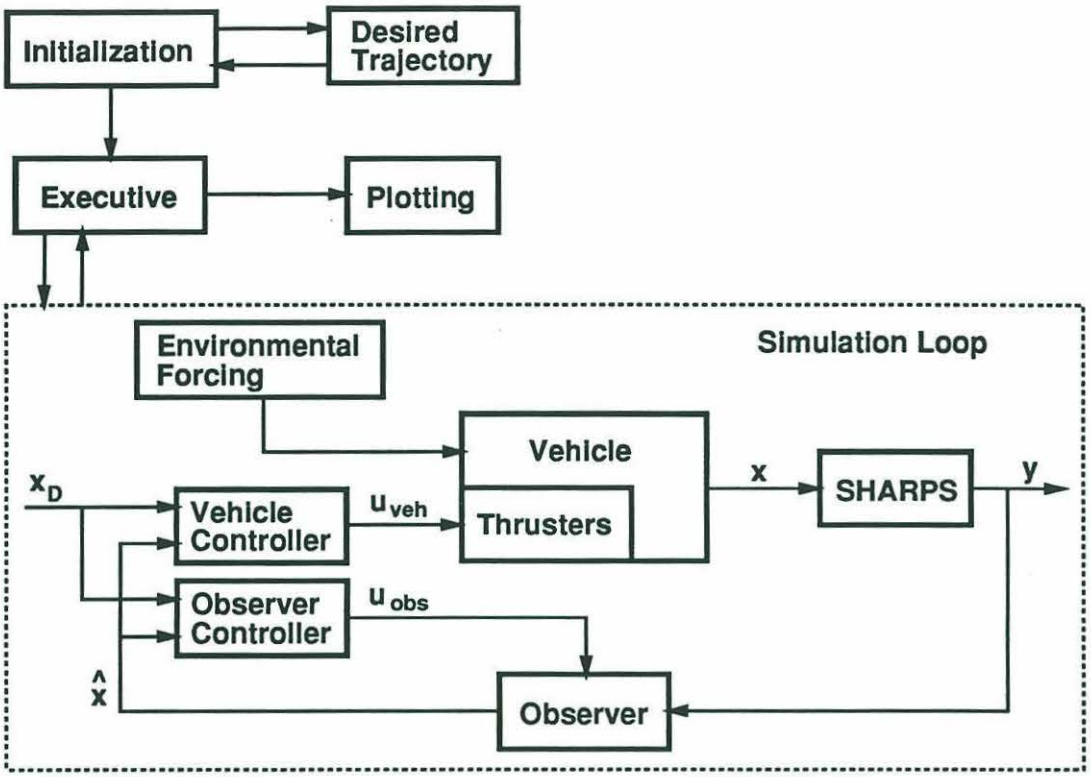

Figure 4.1: Vehicle Simulation Block Diagram

appropriate regime is determined from the known shape of the desired trajectory. The thruster dynamics and the environmental forcing can be enabled or disabled independently. The deadband and saturation can be enabled or disabled independently and with arbitrary strengths. The number of thrusters for distribution of the force command is selectable.

The SHARPS block adds Gaussian noise with an adjustable variance to the position output of the vehicle block. The measurement can be delayed up to 11 SHARPS periods in increments of the integration subinterval with a series of software shift registers. The measurement drop out associated with processor asynchronicity (Section 3.3.4) is simulated by repeating a measurement for a number of SHARPS periods determined from a weighted random distribution. All three features can be enabled, disabled, or varied independently.

The observer and the controllers are described in Chapter 3. The core structure is linear with the gains determined by pole placement techniques. Compensation for nonlinearities can be enabled or disabled independently within each of the three blocks. The status of the nonlinearities in the vehicle does not affect their status in the observer or controllers. Compensation levels are set with similar independence.

The force command to the observer can be passed through deadband and saturation characteristics before it is applied to the model. The force input can be disabled to test the stability considerations reported in Section 3.4. The measurement input can be delay compensated using a forward Euler algorithm. The observer uses a two regime model of the vehicle (Section 2.4), selecting between hover and translation coefficients based on the current and previous values of the desired velocity.[2] For testing purposes the observer can include linear drag in the model.

Both controllers implement the control law given in Equation 3.9 using the desired and estimated states as inputs. A feed forward quadratic drag term can be added to the output of the vehicle controller and both controllers can compensate for the thruster deadband. The controllers use the same two regime model of the vehicle employed by the observer. They also can use a model with linear drag.

The structure of the simulation loop can be altered to pass complete and accurate state information directly to the vehicle controller, eliminating the SHARPS measurement, the observer, and the observer controller blocks. This configuration can be used to compare the performance of the observer to the full state feedback system it is designed to emulate. Compensations in the vehicle controller, if enabled, remain active during athe evaluation.

Coefficient values and the flags enabling or disabling features are set in the initialization block. This module also determines SHARPS noise, measurement delays and drop out, environmental forcing, initial conditions for vehicle, model, and desired trajectories, other parameters for desired trajectory determination, and the discrete time models of the vehicle for each motion regime. The desired trajectories sub-

[2]If both values are zero, hover is assumed and hover based coefficients and gains are used. Otherwise translation is set and translation based coefficients and gains are used. A more complicated algorithm may be used, but is not necessarily desirable as discussed in Section 3.3.3.

routine calculates four set position and velocity profile pairs based on the duration and magnitude characteristics set during initialization. The profiles are typical ROV trajectories with periods of hover, uniform velocity, and uniform acceleration. An unconstrained fifth profile can be set in the initialization block. Among other possibilities, the special profile can be used to determine the impulse and step responses of the system. Figure 4.2 shows the frequency response for the compensated and uncompensated closed loop systems. Each point was obtained by using the special profile to introduce a single frequency sinusoid as the desired trajectory.

The simulation can be restarted at the executive block without changing the parameters of the system set during initialization. Within the executive module the operator selects the observer and controller gains for the run by placing the observer and closed loop poles. The complex pole pairs are described by their natural frequency, ω_n, and their damping coefficient, ζ. Several sets of gains are calculated from the pole selection because of the two regime vehicle model used in the observer and controllers and the possible inclusion of linear drag. The desired trajectory is also operator selectable. After execution of the simulation loop the executive calls a plotting routine to display the results and returns control to the operator. A small suite of plotting routines is available to view different aspects of the system. Essentially all characteristics of vehicle operation, many of which are not available from the real vehicle system, are logged by the software for display.

4.3 Simulation Results

The key issues to be investigated with the simulation are stability and the effects of software architecture and compensation for the nonlinearities on system performance. To provide a baseline for the evaluation, Figures 4.3–4.6 show the response of the system to a specific desired trajectory. The vehicle is commanded from rest to a translation at uniform velocity covering approximately 35 m. The vehicle is then commanded to hover at that location. The transitions between rest and steady translation are driven by uniform accelerations. The vehicle is using the four regime

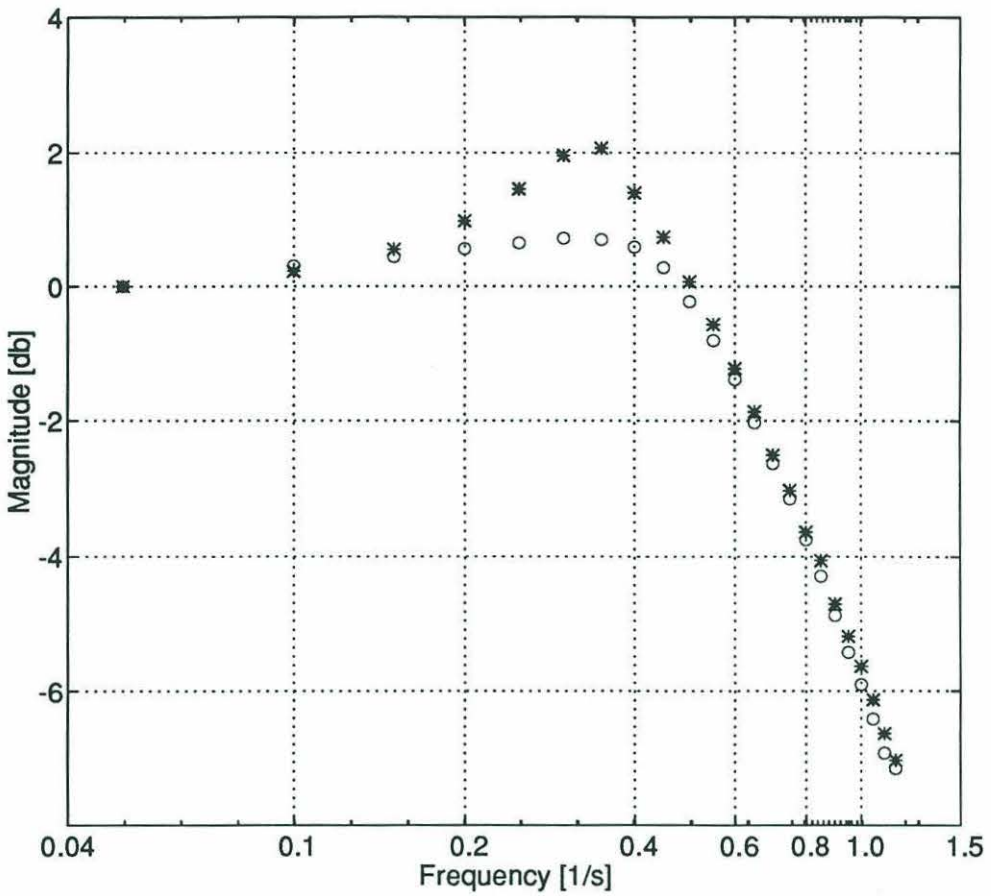

Figure 4.2: FREQUENCY RESPONSE OF THE CLOSED LOOP SYSTEM - The response of the system with no compensation is denoted by ∘. The response with all compensations enabled is denoted by ∗. The Keulegan-Carpenter number ranges from 56 down to 2.4 as the radian frequency ranges from 0.05 s^{-1} up to 1.15 s^{-1}. For this reason the values $C_M^* = 1$ and $C_D^* = 1$ were assumed. The closed loop poles, assuming a linear system, have a natural frequency of $\omega_{n_{cl}} = 0.7\ s^{-1}$ and a damping coefficient $\zeta = 0.707$. The magnitude is defined by $M_{db} = 20 \log_{10} \left(\frac{z_{max}}{z_{D_{max}}} \right)$ where z_{max} and $z_{D_{max}}$ are the extrema of the vehicle and desired positions during the oscillations. The shapes of the curves and the positions of the peaks suggest that nonlinearities in the system have lowered the effective damping coefficient to $\zeta_{eff} = 0.5$ without compensation and to $\zeta_{eff} = 0.55$ with compensation.

hydrodynamic model described in Section 2.4. The thruster dynamics, deadband, and saturation of the vehicle are enabled. The SHARPS measurement has a half period delay and includes an appropriate noise level. Both controllers are active and implementing only the PD control law (Equation 3.9). The thrust command to the vehicle is distributed to two thrusters. The model used by the observer and controllers is a simple mass and no compensation is employed. Closed loop poles were placed at

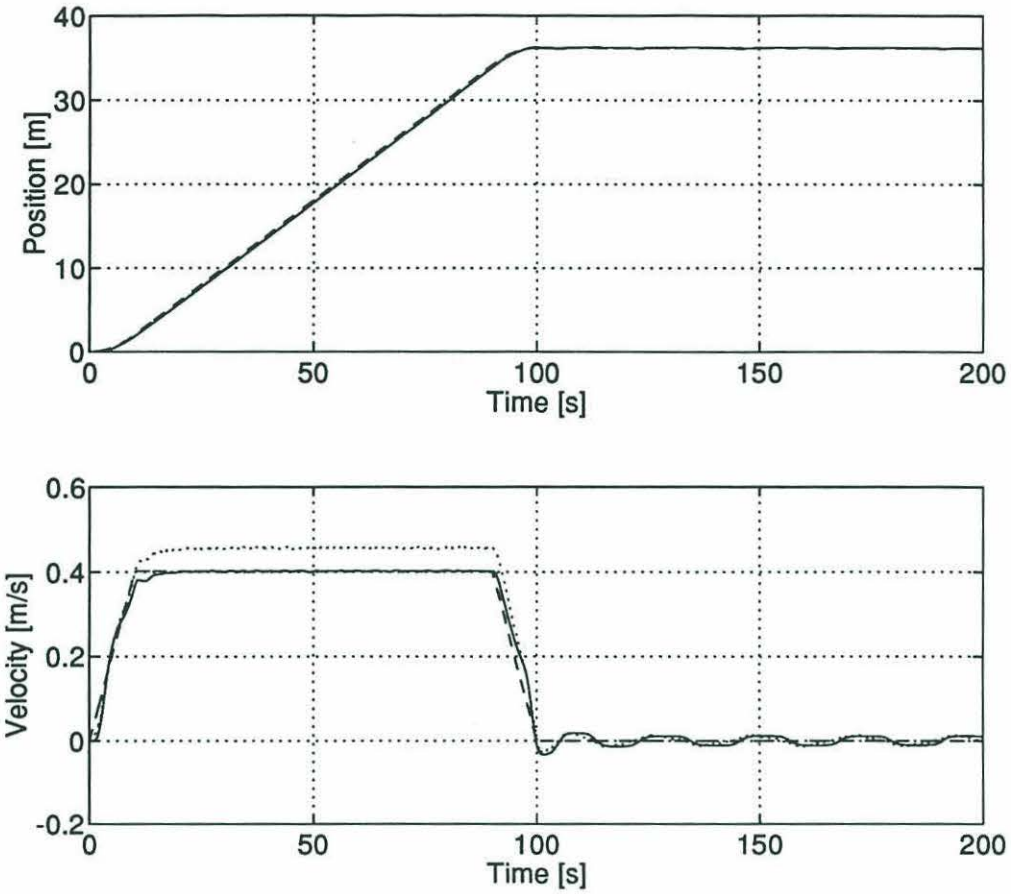

Figure 4.3: VEHICLE TRAJECTORY WITH COMPENSATION DISABLED AND THE OBSERVER FORCE INPUT ENABLED - The solid lines mark the position and velocity of the simulated vehicle over time in response to the desired trajectory shown by the dashed lines. The state estimates are shown by the dotted lines. Details of the position plot are obscured by the scale of the translation; small features can be seen more clearly in the trajectory error plot below (Figure 4.4). The limit cycle behavior caused by the thruster dynamics during hover is visible in the velocity plot.

$\omega_{n_{cl}} = 0.7\ s^{-1}$ and $\zeta = 0.707$. The observer poles have the same damping and are three times faster, $\omega_{n_{obs}} = 2.1\ s^{-1}$. Observer and controller gains were determined using only the hover values of the coefficients of added mass and drag, $C_M^* = 2$ and $C_D^* = 8$, rather than the steady translation values, $C_M^* = 1$ and $C_D^* = 1$. This raises the gains and reduces some of the trajectory following and state estimation errors. Forcing from the environment is set to zero.

The important initial observation is that the system is stable even without compensation. While the tracking performance and state estimates are weak, the vehicle

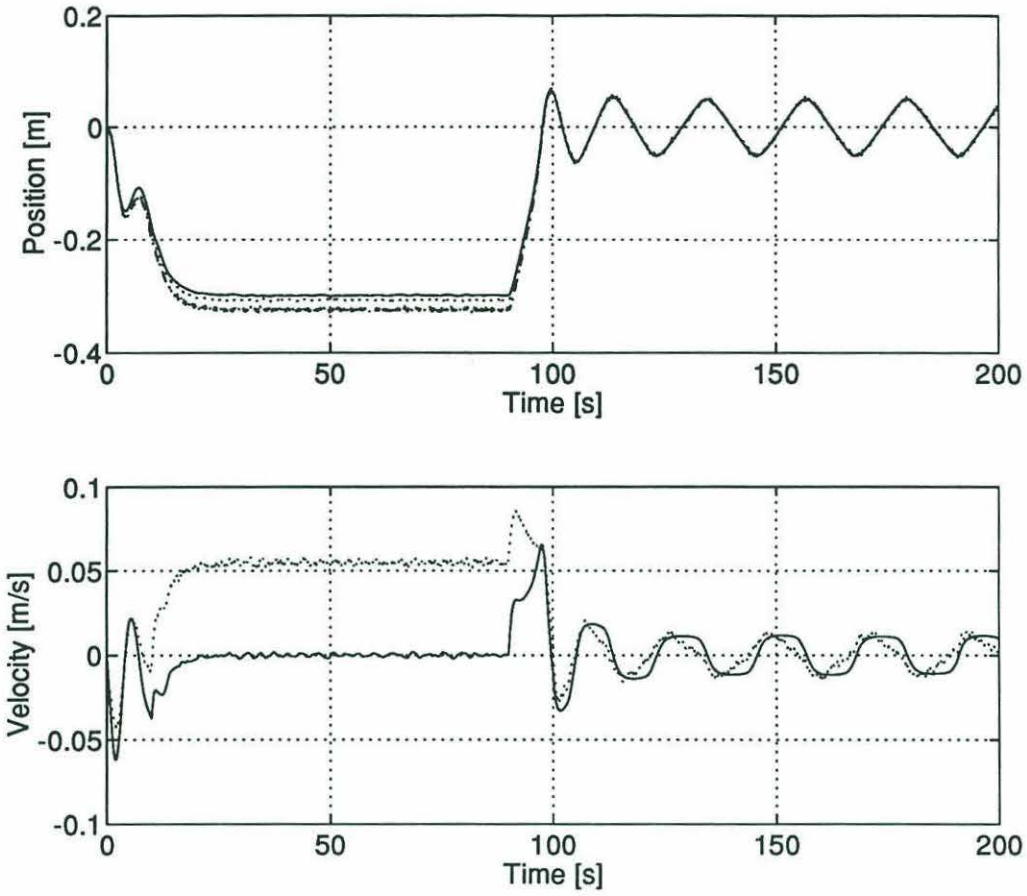

Figure 4.4: TRAJECTORY FOLLOWING ERROR WITH COMPENSATION DISABLED AND THE OBSERVER FORCE INPUT ENABLED - To make a closer examination of vehicle behavior, the desired trajectory has been subtracted from the actual (solid lines), estimated (dotted lines), and measured (dash-dot, position plot only) trajectories and plotted here against time. The limit cycle is clearly evident in both plots. The observer balance between model and measurement can be seen in the position plot during the translation when the effect of the measurement delay is most pronounced due to the relatively high speed. During hover, when velocities are low, the position estimates are more accurate. The velocity estimates suffer by comparison because of their greater dependence on an inaccurate model.

does not diverge from the desired trajectory without limit, nor does it exhibit extreme or growing oscillations. During the translation, position estimates show the observer balance between measurement and model based information. The 2.5 cm separation of the position and measurement is caused by the half period SHARPS delay. (The SHARPS period is 0.125 s and the steady speed is 40 cm/s.) The 30 cm tracking error is expected for a mass with drag plant driven by a PD controller when

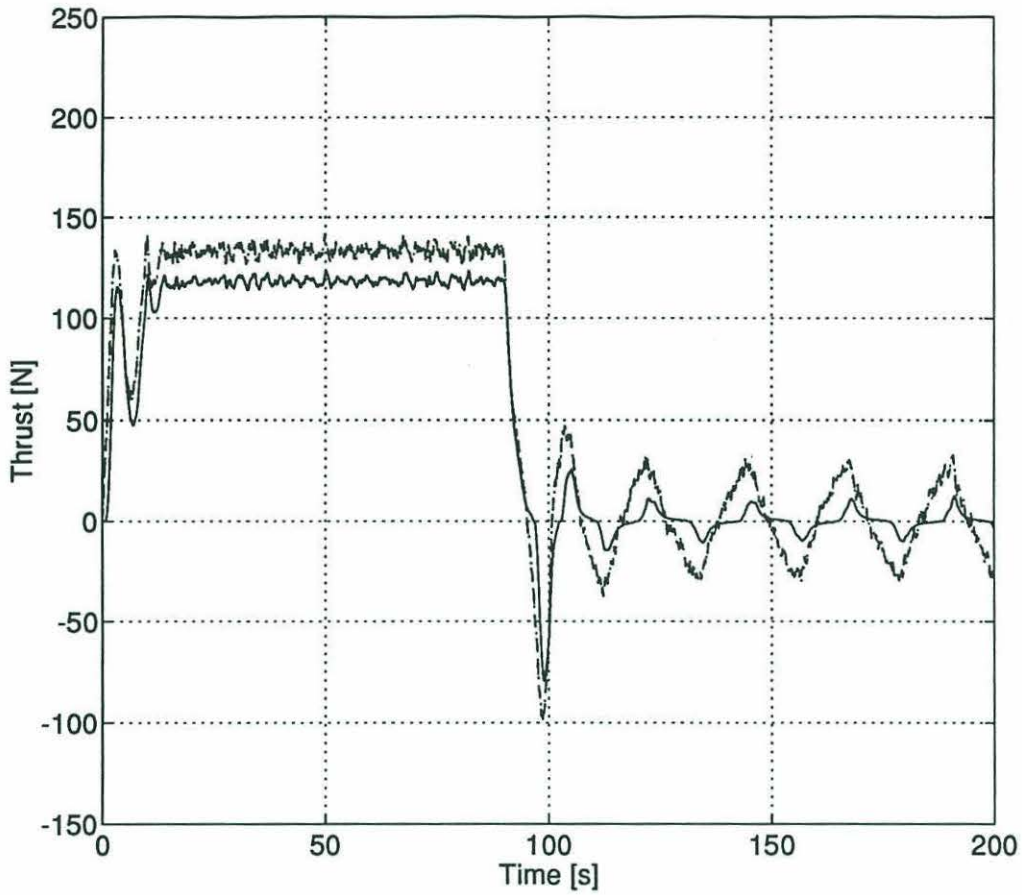

Figure 4.5: ACTUATOR COMMANDS AND RESPONSE WITH COMPENSATION DISABLED AND THE OBSERVER FORCE INPUT ENABLED - The dashed line marks the vehicle controller command and the dotted line marks the observer controller command. In this case the two are identical. The solid line is the output response of the simulated thrusters to the vehicle controller command due to the deadband, saturation, and dynamics of the thrusters. The reduction in static output above the deadband (Figures 3.4 and 3.5) is apparent during the period of translation. The combined effects of the deadband and the thruster dynamics are visible during hover. Output is reduced to near zero until deviation from the desired trajectory drives the thrust command above the deadband. The response is delayed and otherwise modified by the thruster dynamics (Figure 3.3 and Equations 3.10).

the input is a ramp. Appropriate compensation can drive this error to zero as will be seen below. Velocity tracking is fairly good during the translation. However, velocity estimates have a 5 cm/s error. The nonzero observer controller output maintained by the position error imposes a velocity on the model. Alternatively stated, the 5 cm/s error is simply the level necessary to balance the the PD control law (Equation 3.9) which is driven by the position error. A physical interpretation is not possible for

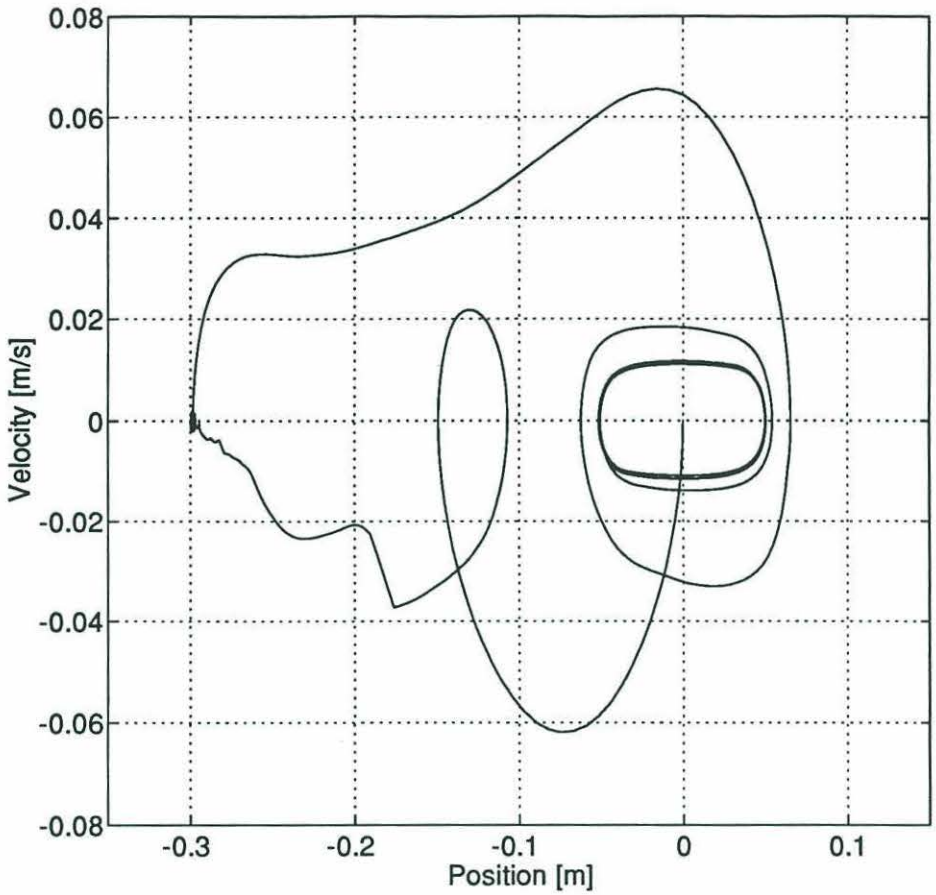

Figure 4.6: STATE SPACE TRAJECTORY WITH COMPENSATION DISABLED AND THE OBSERVER FORCE INPUT ENABLED - The solid line is the path of the trajectory following error through state space. Alternatively one can interpret the curve as the state space trajectory of the vehicle when the state space origin follows the desired trajectory. The track begins at the origin, diverges during the acceleration, and maintains a 30 cm position error with small velocity fluctuations during the steady translation. Another large swing occurs during the deceleration and the vehicle converges to the limit cycle during hover.

a situation where a constant velocity difference does not cause a growing position difference.

While hovering the position estimates improve due to the lower velocity. The measurement is still delayed, but at peak velocities of 1.25 cm/s the measurement error is less than 0.8 mm; the standard deviation of the SHARPS measurement in the test tank is 2 mm. Velocity estimates have improved, but now show a phase lag. Tracking errors are associated with the limit cycle which is driven by the thruster dynamics [4, 5]. The effects of the deadband and the thruster dynamics on actuator

output during hover can be seen in Figure 4.5. The period of the oscillations is 22 s with peaks of 5 cm and 1.25 cm/s. This period is longer than the limit cycle period observed during the operation of ROV Jason. However, Jason is a larger vehicle than ROV Hylas, which has been simulated here, and the Jason observations were of two degrees of freedom oscillations in the horizontal plane rather than single degree of freedom oscillations along the vertical axis. These differences change the dimensional constants of the hydrodynamic model and cause some alteration in the period. However, a larger portion of the difference is due to the ROV Jason observer structure which did not include a forcing input from the controller [32]. Disabling the observer force input in the simulation reduces the limit cycle period during hover to 9 s with peaks of 5 cm and 3 cm/s (Figures 4.7–4.9). Those values show good agreement with empirical data and are an indication of the accuracy of the simulation. Note that the Keulegan-Carpenter number matches the empirical value of $KC = 0.3$ in both cases.

Overall performance is degraded when the model is hobbled in this way, however. This is evident from the persistent oscillatory behavior in response to the translation command. As will be discussed in Chapter 5, the slowly suppressed oscillations are associated with the limit cycle of the thruster dynamics. They are not simply a very lightly damped second order step response. Observe, for example, that the supression envelope is linear rather than exponential. The higher frequency is related to the high level of mean thrust during the translation. Peak trajectory following errors during the ringing behavior are sufficient to saturate the thrusters.[3]

Thruster command levels during the limit cycle have doubled (Figure 4.8) compared to the previous system configuration (Figure 4.5). Position estimates now follow the delayed measurements. One positive byproduct of this configuration is

[3]The term "ringing" is used here with some reluctance. Typically, ringing refers to the exponentially damped oscillations of a lightly damped second order step response. The phenomenon here, as will be shown during the vehicle trials of Chapter 5, is a linearly suppressed excitation of the limit cycle. If this were an audio system, however, the phenomenon would sound like ringing. As no other convenient label exists, the terminology will be used here with the understanding that it refers exclusively to a linearly suppressed excitation of the limit cycle. Unmodified references to the limit cycle should still be understood to imply the sustained limit cycle behavior that takes place when the vehicle hovers.

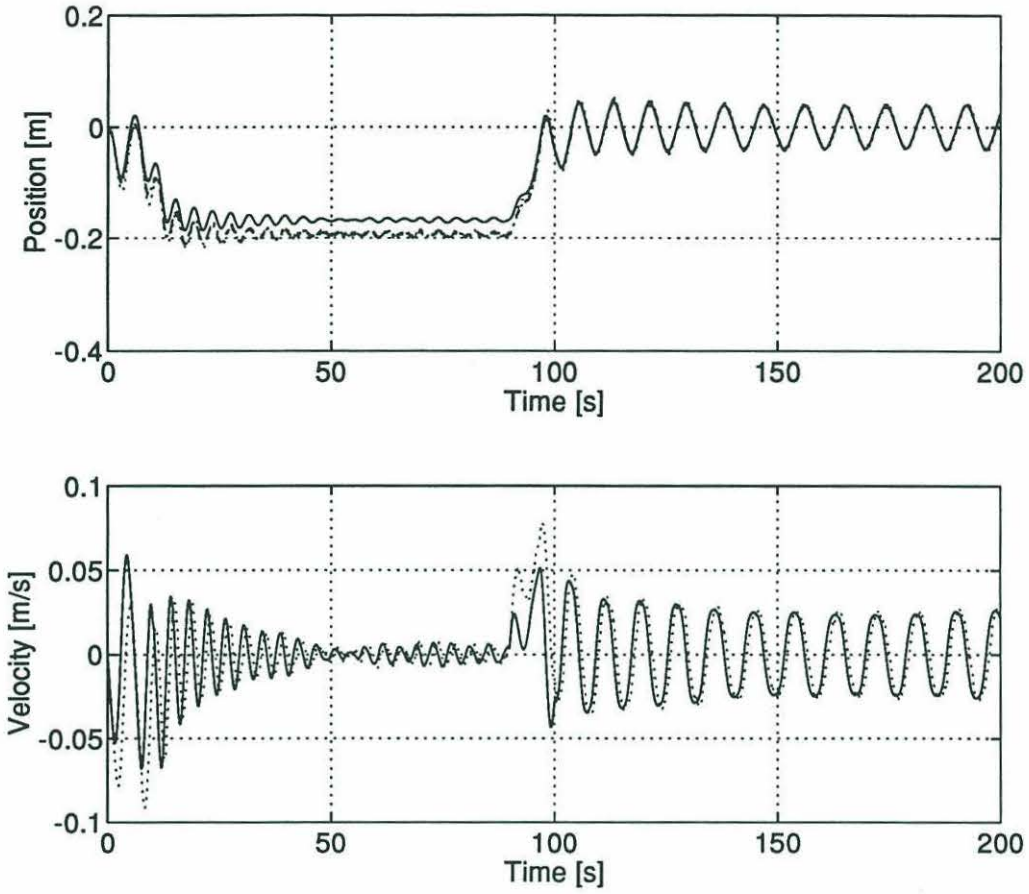

Figure 4.7: TRAJECTORY FOLLOWING ERROR WITH COMPENSATION AND THE OBSERVER FORCE INPUT DISABLED - As in Figure 4.4, the desired trajectory has been subtracted from the plotted quantities so that the apparent desired state is the zero vector. The solid lines are the vehicle trajectory, the dotted lines are the state estimates, and the dash-dot line is the position measurement. The limit cycle period has been reduced and position estimates now track the delayed measurements. A slowly suppressed excitation of the limit cycle occurs in response to the "step" in desired velocity.

an improvement in the velocity estimates during translation. With the model forcing disabled the observer is essentially a second order filter, calculating velocity estimates by taking the derivative of the position measurements. The velocity estimates exhibit a phase lag caused by the measurement delay and the observer during the oscillatory portions of the trajectory. Note that while the performance is unsatisfactory, the system is still stable.

Now consider the effects of added compensation. Beginning with the baseline system (Figures 4.3–4.6), feed forward quadratic drag and deadband compensations

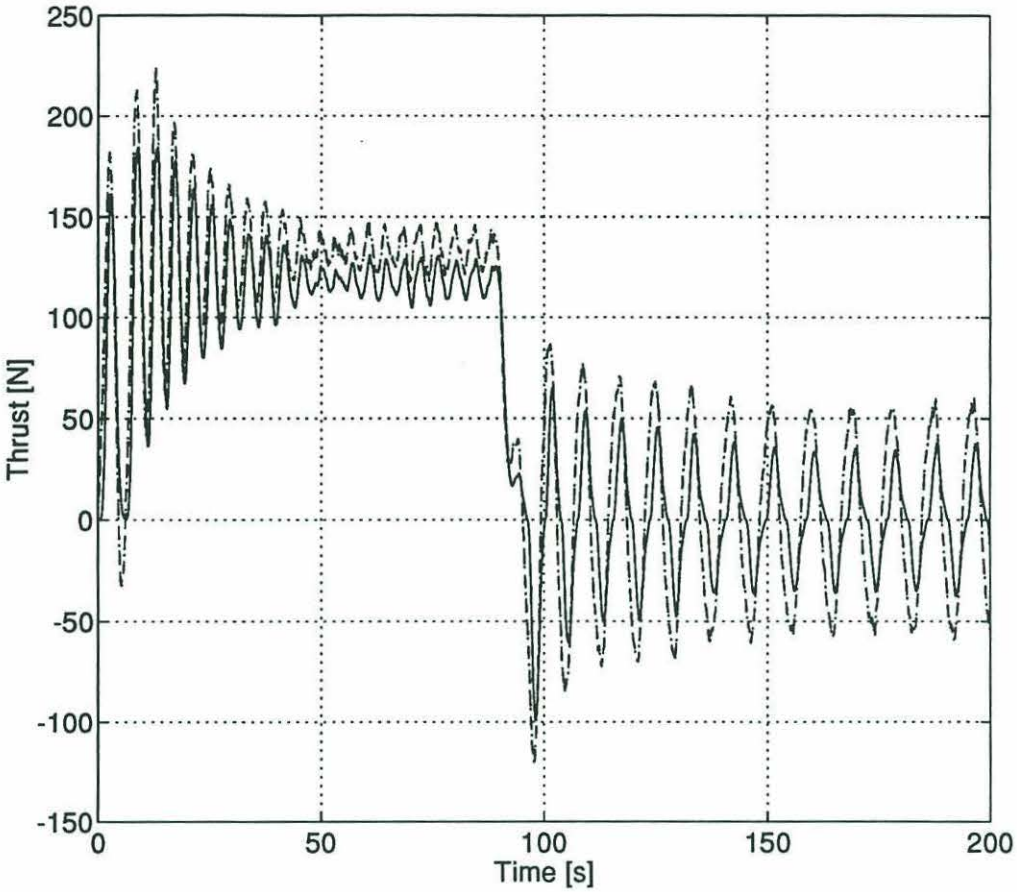

Figure 4.8: ACTUATOR COMMANDS AND RESPONSE WITH COMPENSATION AND THE OBSERVER FORCE INPUT DISABLED - The dashed line marks the vehicle controller command and the dotted line marks the observer controller command. As in Figure 4.5, the command levels are the same, however, the observer controller command is no longer sent to the observer. The solid line is the output response of the simulated thrusters. Saturation of the thrusters at 185 N is visible in the early ringing extrema. Peak thruster commands during the limit cycle are over 50 N compared with $25 - 30$ N when the force input to the observer is enabled.

are added to the vehicle controller and saturation compensation is included in the observer. Additionally, the two regime hydrodynamic model of the vehicle is incorporated into the observer and both controllers. Finally, the measurement delay is compensated with a forward Euler extrapolation.[4] The observer force input remains disabled. The result is shown in Figures 4.10–4.12.

As in the previous configurations, the system is stable. Compensation has signifi-

[4]This set of compensations will be referred to collectively as the "compensation suite" in the remainder of the chapter.

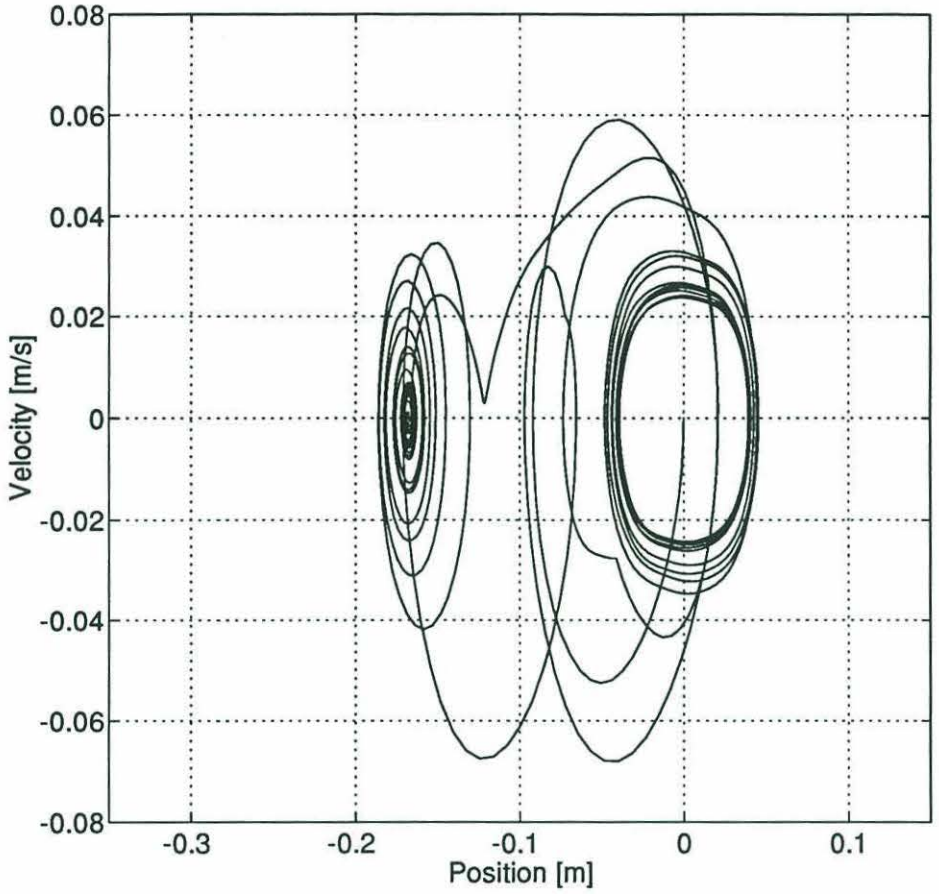

Figure 4.9: STATE SPACE TRAJECTORY WITH COMPENSATION AND THE OBSERVER FORCE INPUT DISABLED - The solid line is the path of the trajectory following error through state space. The ringing about a constant position error of 1.75 cm during translation and the limit cycle oscillations during hover are clearly visible.Note that the size of the limit cycle excursions, particularly in velocity, has increased compared to the uncompensated configuration with the observer force input enabled.

cantly improved both vehicle tracking and estimator performance during translation. The standard deviation of the position error about the desired position is 0.45 mm. The standard deviation of the position estimate about the vehicle position is 1 mm, half of the 2 mm standard deviation of the measurement error. Similarly, the velocity and velocity estimate errors have standard deviations of 0.47 mm/s and 1.4 mm/s. The small errors drive the observer controller output near zero as well. This is appropriate physically given that the observer model is a simple mass traveling at uniform velocity. There is no position error requiring a nonzero estimated velocity for balance

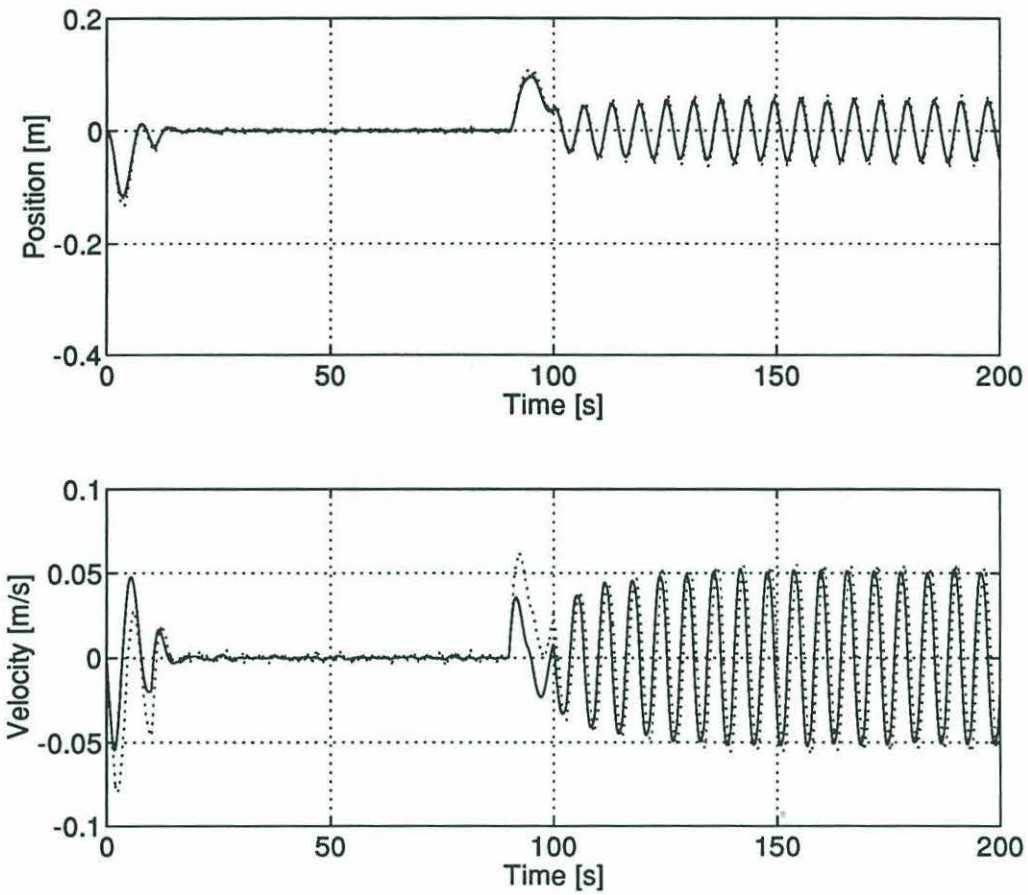

Figure 4.10: TRAJECTORY FOLLOWING ERROR WITH THE COMPENSATION SUITE ENABLED AND THE OBSERVER FORCE INPUT DISABLED - The desired trajectory has been subtracted from the actual (solid lines), estimated (dotted lines), and measured (dash-dot, position plot only) trajectories and plotted here against time. Vehicle tracking and estimator performance levels are high during translation. Limit cycle oscillations are exceptionally strong during hover, however.

as there was in the baseline case. Additionally, there is no evidence of limit cycle ringing during translation as there was in the uncompensated case with the observer force input disabled.

The magnitudes of the limit cycle extrema during hover have increased markedly in this configuration. The oscillation period is 6 s with peaks of 5.5 cm and 5 cm/s. This is the strongest sustained limit cycle behavior seen in any of the four system configurations presented here.[5] The Keulegan-Carpenter number is still $KC = 0.3$.

[5]The configurations are the four combinations possible given the enabled or disabled status of the compensation suite and the observer force input.

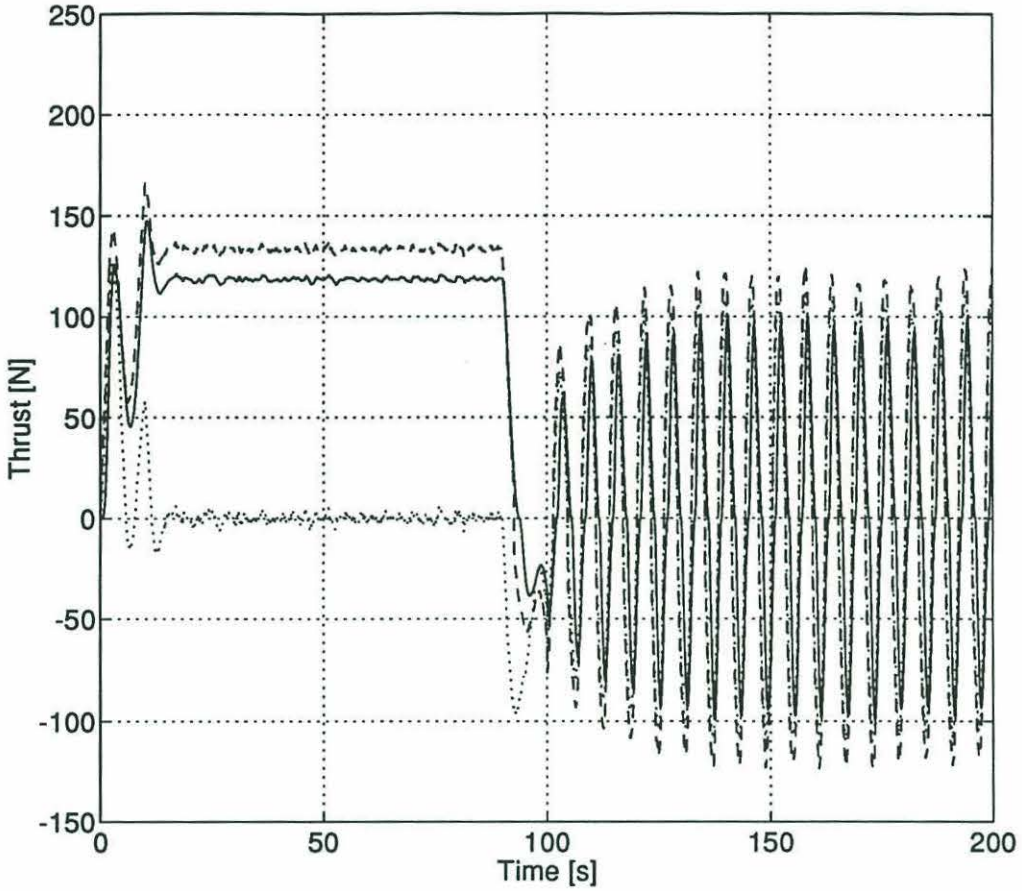

Figure 4.11: ACTUATOR COMMANDS AND RESPONSE WITH THE COMPENSATION SUITE ENABLED AND THE OBSERVER FORCE INPUT DISABLED - The dashed line marks the vehicle controller command (including the quadratic drag and deadband compensations) and the dotted line marks the observer controller command. The solid line is the output response of the thrusters. The observer controller output remains near zero during the steady translation because the model has no drag. No force is required to maintain a constant velocity. Unlike the baseline case, there are no large tracking or estimation errors to upset the balance. The effect of the uncompensated thruster dynamics is still visible during the limit cycle, however compensation for the deadband has improved thruster response. Recall when interpreting these traces that with the compensation suite enabled the observer controller output is simply the PD control law while the vehicle controller output contains the PD control law augmented by feed forward quadratic drag and deadband compensations.

The strength of the oscillations has again doubled commanded thrust (Figure 4.11) compared to the previous system configuration (Figure 4.8). Peak levels are now in excess of 100 N. Note that, while both controller outputs are based on the PD control law (Equation 3.9), the vehicle controller now augments that output with quadratic drag and deadband compensations. Velocity estimates exhibit a distinct phase lag

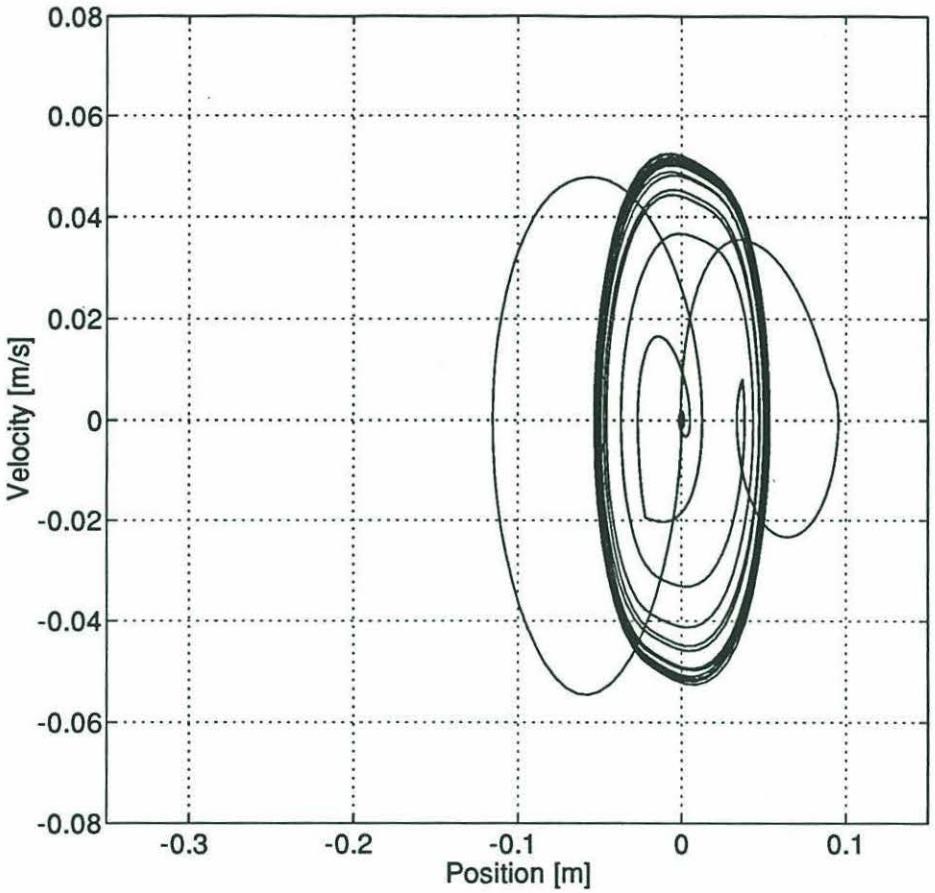

Figure 4.12: STATE SPACE TRAJECTORY WITH THE COMPENSATION SUITE ENABLED AND THE OBSERVER FORCE INPUT DISABLED - The solid line is the path of the trajectory following error through state space. The track begins at the origin, diverges during the acceleration and returns to the origin during the translation. Deceleration causes another divergence and the vehicle converges to the limit cycle during hover. Note the particularly large velocity extrema of the limit cycle. This is the strongest sustained limit cycle behavior seen in any of the system configurations presented here. Task performance during hover would be difficult or impossible given the range and speed of this motion.

during the oscillations, but position estimates follow the vehicle fairly closely.

In sum, the compensation suite has generated some improvement compared to the previous configuration. However, system performance, particularly with the observer force input disabled, remains less than satisfactory. The fourth system configuration is presented in Figures 4.13–4.16. The combination of enabled compensation suite and enabled observer force input preserves the small tracking and estimation errors during translation seen with the previous configuration and greatly reduces the extent

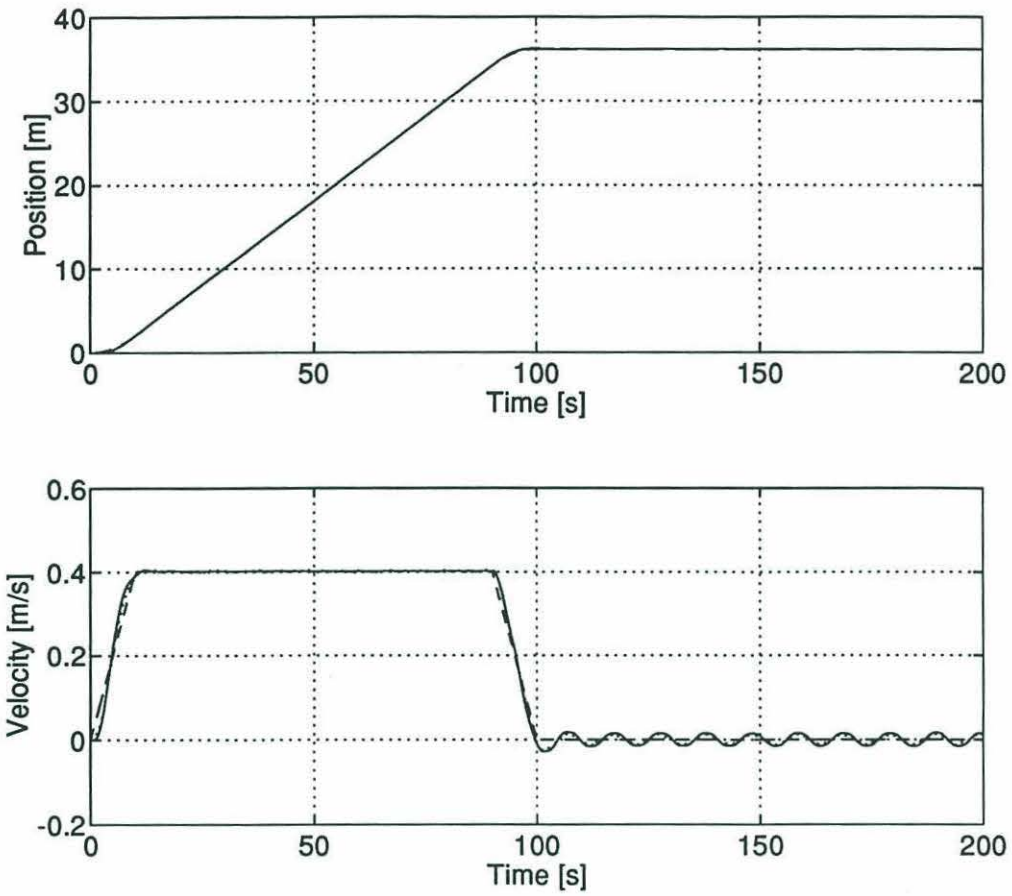

Figure 4.13: VEHICLE TRAJECTORY WITH THE COMPENSATION SUITE AND THE OBSERVER FORCE INPUT ENABLED - The solid lines mark the position and velocity of the simulated vehicle over time in response to the desired trajectory shown by the dashed lines. The state estimates are shown by the dotted lines. Even on this scale it is apparent that tracking errors have been reduced and state estimates have improved when compared to the previous configurations.

of the limit cycle in both position and velocity.

As in the previous configurations, the important initial observation is that the system is stable. Tracking performance and state estimates have improved measurably during all portions of the trajectory. As in the previous configuration, compensations for the quadratic drag and the measurement delay have driven the position and velocity errors of the vehicle and the estimates close to zero during the translation. The standard deviation of the position error about the desired position is now 0.4 mm. The standard deviation of the position estimate about the vehicle position is still 1 mm. Again, this is half of the 2 mm standard deviation of the measurement er-

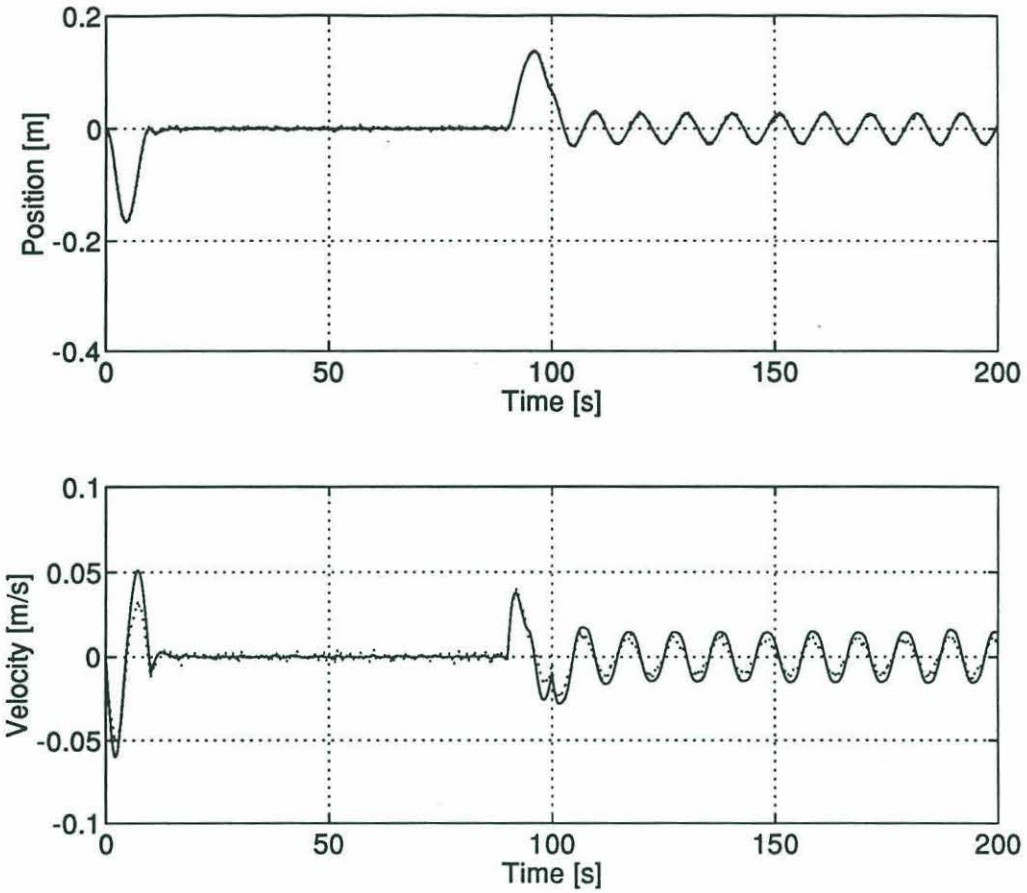

Figure 4.14: TRAJECTORY FOLLOWING ERROR WITH THE COMPENSATION SUITE AND THE OBSERVER FORCE INPUT ENABLED - The desired trajectory has been subtracted from the actual (solid lines), estimated (dotted lines), and measured (dash-dot, position plot only) trajectories and plotted here against time. Errors in tracking and state estimates have been reduced dramatically during both translation and hover.

ror. Similarly, the standard deviations of the velocity and velocity estimate errors have been reduced to 0.4 mm/s and 1.2 mm/s. As before, the small errors drive the observer controller output near zero, appropriate for a simple mass traveling at uniform velocity (the observer model). The absence of a position error also eliminates the nonzero estimator velocity seen in the baseline configuration. Finally, the high frequency variations in the state estimates have been reduced, smoothing the output of the thrusters.

During the limit cycle, the standard deviations of the of the state estimates about the vehicle state rise to 1.9 mm and 4.6 mm/s. These values should be compared

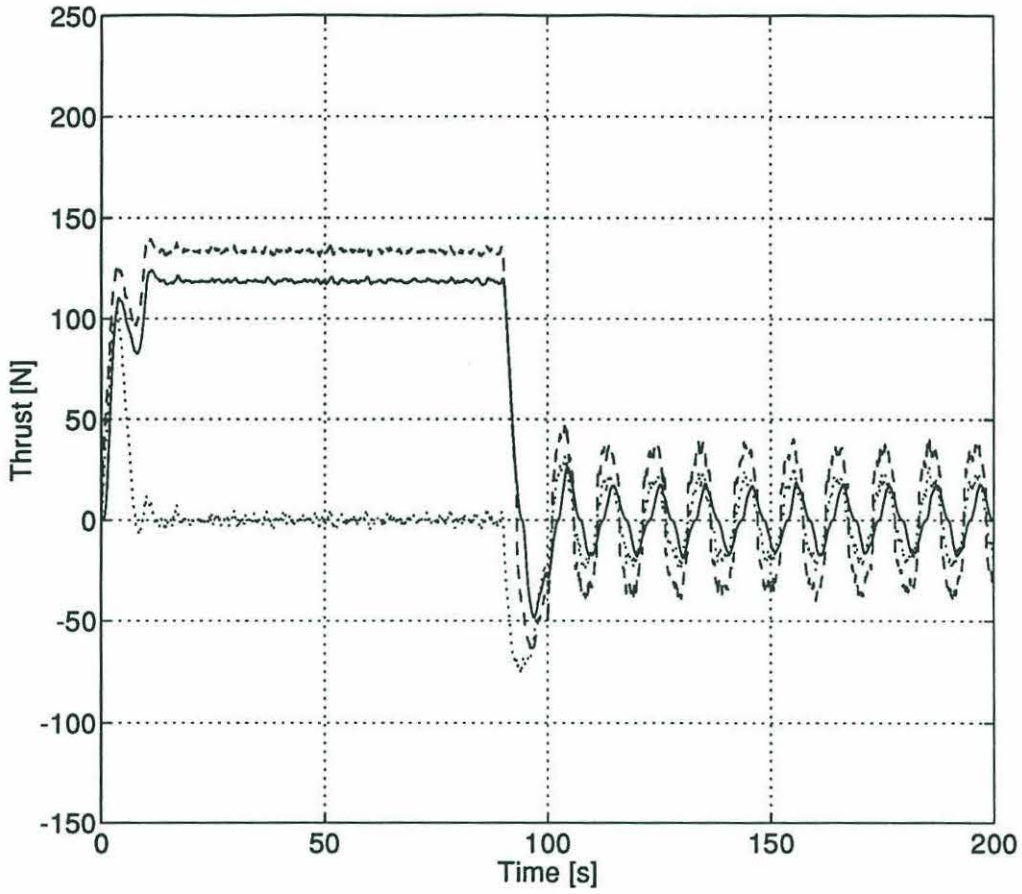

Figure 4.15: ACTUATOR COMMANDS AND RESPONSE WITH THE COMPENSATION SUITE AND THE OBSERVER FORCE INPUT ENABLED - The dashed line marks the vehicle controller command (including the quadratic drag and deadband compensations) and the dotted line marks the observer controller command. The solid line is the output response of the thrusters. The observer controller output remains near zero during the steady translation because the model has no drag. No force is required to maintain a constant velocity. Unlike the baseline case, there are no large tracking or estimation errors to upset the balance. The effect of the uncompensated thruster dynamics is still visible during the limit cycle, however, compensation for the deadband has greatly improved thruster response. Recall when interpreting these traces that with the compensation suite enabled the observer controller output is simply the PD control law while the vehicle controller output contains the PD control law augmented by feed forward quadratic drag and deadband compensations.

with 3.0 mm and 7.1 mm/s from the baseline case. The position excursion has been reduced by half with a small increase in peak velocity. The period of the oscillations is 10 s with peaks of 2.5 cm and 1.5 cm/s. This has reduced the Keulegan-Carpenter number to $KC = 0.17$. The improved response of the thrusters due to deadband compensation can be seen in Figure 4.15. The uncompensated dynamic effects are

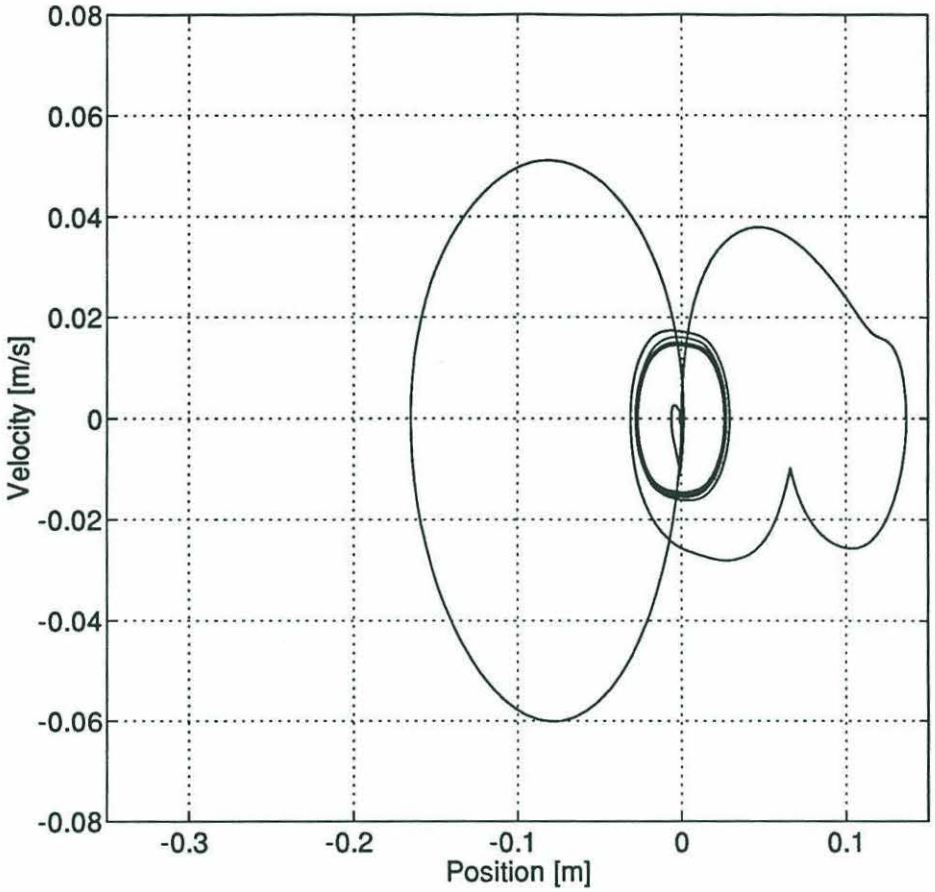

Figure 4.16: STATE SPACE TRAJECTORY WITH THE COMPENSATION SUITE AND THE OBSERVER FORCE INPUT ENABLED - The solid line is the path of the trajectory following error through state space. The track begins at the origin, diverges during the acceleration and returns cleanly to the origin during the translation. Deceleration causes another divergence and the vehicle converges to the limit cycle during hover. Compared to the baseline case (Figure 4.6) there is no constant error during translation and position extrema during the limit cycle have been reduced by half.

also visible. Peak thruster command levels are comparable to the baseline case, even with the shorter period. This is largely due to the improved response. Note that actuator command levels doubled when the observer force input was disabled to reduce the period and no deadband compensation was employed (Figure 4.8).

Thruster saturation compensation is only necessary when large trajectory following errors or a desired velocity greater than the maximum vehicle speed occur. Neither situation applies here. However, the compensation is effective in reducing estimation errors when called upon. The benefits of the two regime hydrodynamic model in-

cluded in the observer and controllers are not apparent in these plots. The quadratic drag compensation term in the vehicle controller can cause large, periodic deviations from the desired trajectory if the coefficient of quadratic drag used by the model is larger than the vehicle coefficient (Figure 4.17). For example, this would occur during translation if the model contained only the hover value of the quadratic drag coefficient. If the compensation coefficient is smaller than the vehicle coefficient or the compensation is disabled, constant errors in tracking and state estimation occur. The latter was seen with the baseline configuration. The two regime hydrodynamic model, with accurate coefficient values, prevents both types of errors. Note that the improvement in system performance results from the interaction of the two compensations. Without coefficient variability, quadratic drag compensation in the vehicle controller can actually degrade system performance.

The performance results for the four configurations clearly show that using the observer architecture of Figure 4.1 dramatically improves system behavior. Including the force input in the observer structure is the single most important action that can be taken to reduce the effects of the thruster limit cycle without redesigning the thrusters. The compensation suite also makes significant contributions to both tracking and estimator accuracy. The performance level of the compensated, full architecture system in fact compares favorably with a system that has complete state information available. The performance of this "perfect information" system is shown in Figures 4.18–4.20. For this simulation run the SHARPS measurement, the observer, and the observer controller have been removed from the loop and the complete vehicle state is passed directly to the vehicle controller. Within the vehicle controller the two state hydrodynamic model, quadratic drag, and deadband compensations are still active.

The simulation has so far indicated that the compensated, full architecture system is stable and well behaved in a quiescent environment. In the ocean, a vehicle may be subjected to wave action, currents, tether loads, and ballasting offsets. To simulate these effects a wave spectrum was created by passing random noise through a low pass filter. The spectral content is concentrated in a band between 0.03 Hz and 0.3 Hz.

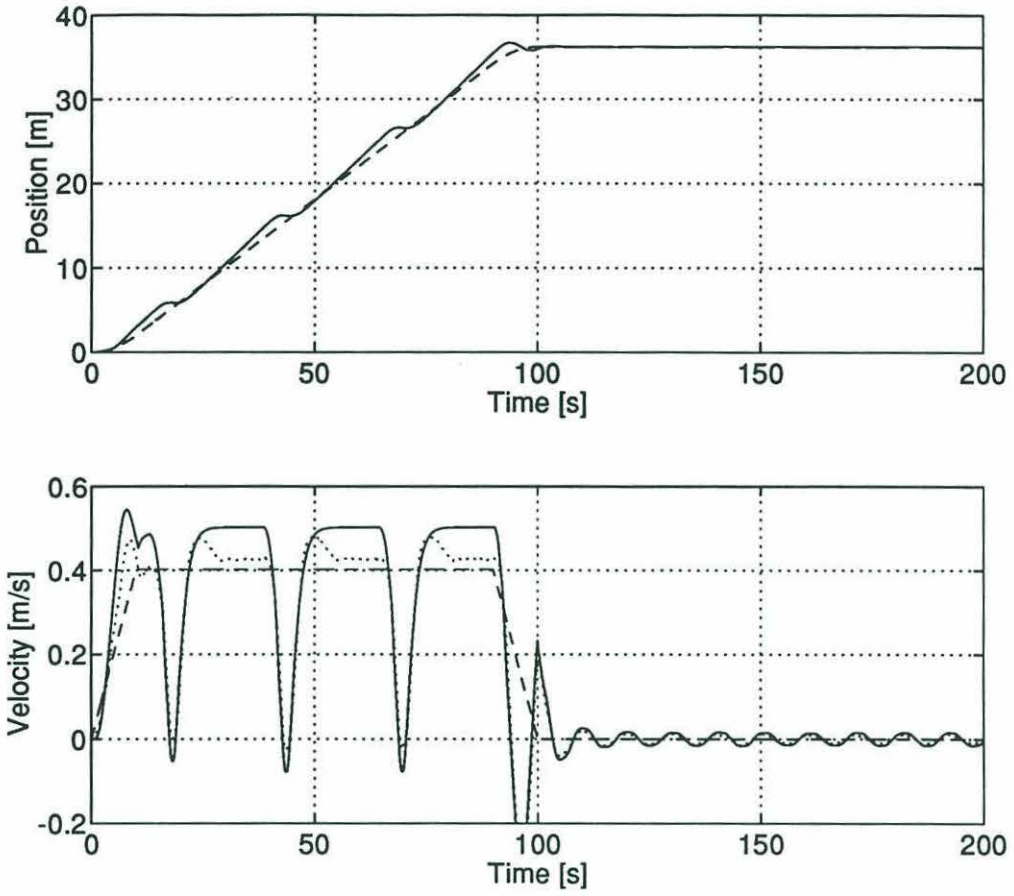

Figure 4.17: VEHICLE TRAJECTORY DUE TO AN INACCURATE HYDRODYNAMIC MODEL - The solid lines mark the position and velocity of the simulated vehicle over time in response to the desired trajectory shown by the dashed lines. The state estimates are shown by the dotted lines. The errors occur during translation when the drag coefficient of the vehicle is $C_D^* = 1$ while the vehicle controller quadratic drag compensation is calculated based on $C_D^* = 8$. Error extrema are smaller and more frequent as the controller coefficient is reduced.

The standard deviation of the forcing it provides is 4.3 N. Steady forcing was added to the wave forcing to simulate a current. The strength of the steady forcing is 30 N. This corresponds to a current of 20 cm/s if the uniform translation value of the drag coefficient is assumed. The steady component of the environmental forcing opposes the desired translation. The trajectory following error is shown in Figure 4.21. The compensation suite and the observer force input are both enabled. The latter will remain enabled for the balance of this chapter.

The constant position offset of approximately 5 cm is caused by the steady portion

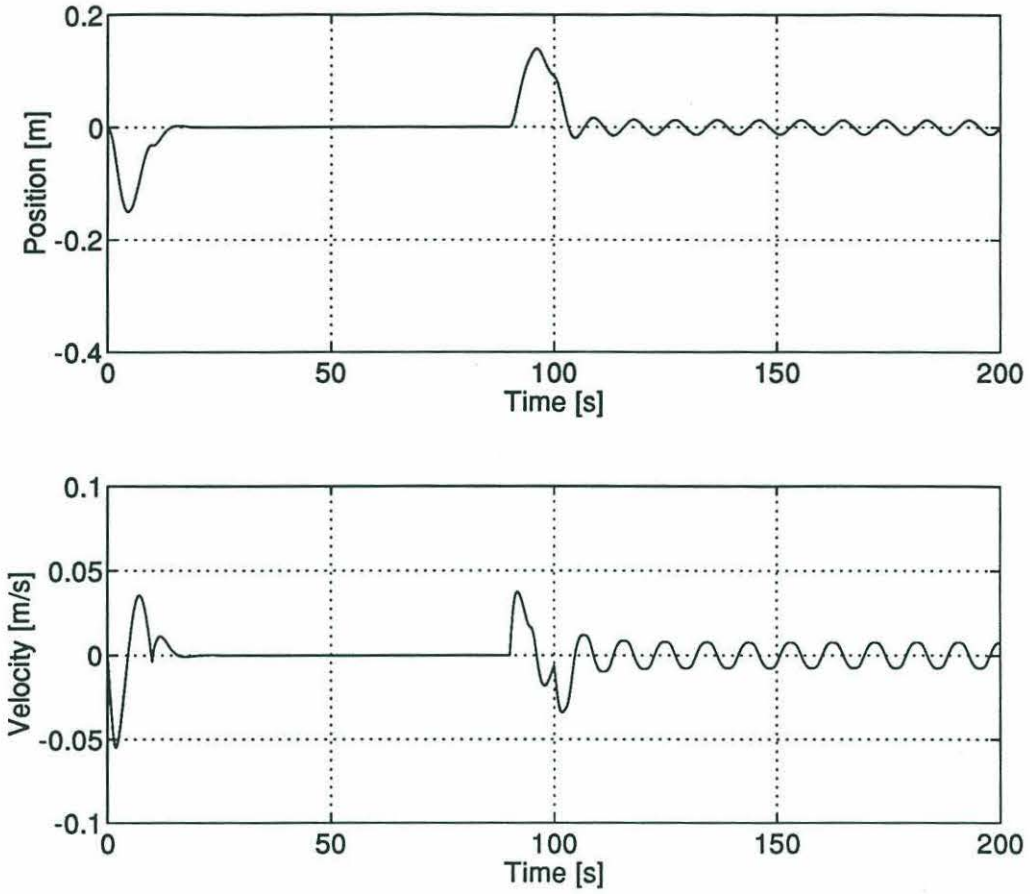

Figure 4.18: TRAJECTORY FOLLOWING ERROR WITH COMPENSATION ENABLED AND COMPLETE STATE INFORMATION - The solid lines show the trajectory of the vehicle after the desired trajectory has been subtracted away. Perfect state information is used in the feedback loop and compensations in the vehicle controller are still active. The result should be compared with Figure 4.14, the corresponding plot for the fully compensated system with complete observer architecture.

of the forcing and is normal for a PD control loop. The expected error is $4 - 6$ cm depending on which set of hydrodynamic coefficients are used for the calculation of controller gains. The error can be eliminated using PID control as discussed in Section 4.4. The offset causes a nonzero observer controller output which is responsible for the small error in estimated velocity. Estimated position errors remain small as in the quiescent case. The steady forcing also drives the thruster away from the deadband region during hover with the result that the limit cycle is suppressed. Movement about the mean offset is caused by the random component of the environmental forcing, not by the thruster dynamics. Suppression of the limit cycle will be seen

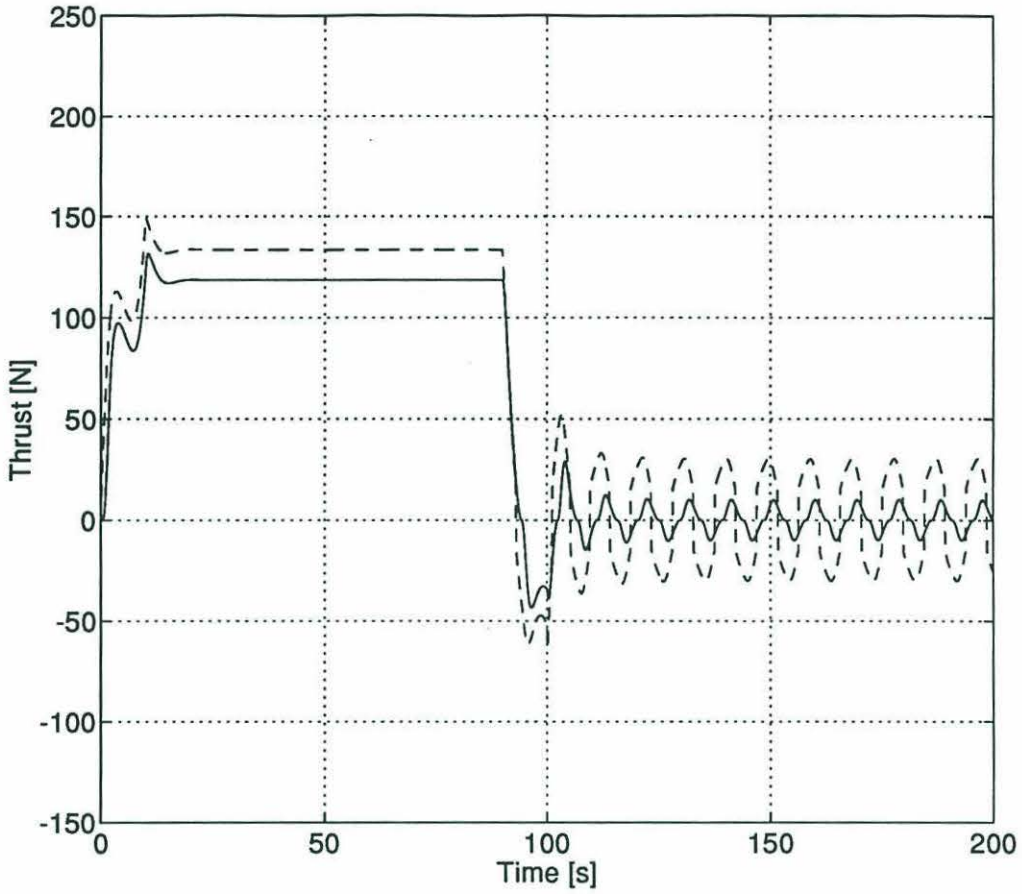

Figure 4.19: ACTUATOR COMMAND AND RESPONSE WITH COMPENSATION ENABLED AND COMPLETE STATE INFORMATION - The dashed line marks the vehicle controller command and the solid line is the output response of the thrusters. Perfect state information is used in the feedback loop and compensations in the vehicle controller are still active. The result should be compared with Figure 4.15, the corresponding plot for the fully compensated system with complete observer architecture.

with ROV Hylas in Chapter 5. The performance of the compensated system in the presence of forcing from the environment is seen to be quite good. For comparison, the response of the baseline system to the same environmental forcing is shown in Figure 4.22.

Two final concerns are measurement drop out and multiperiod control loop delays. Neither is a current concern because the newly synchronized architecture of the transputer network regulating ROV Hylas effectively eliminates both problems. It is sufficient to note that a weighted random distribution of measurement drop outs

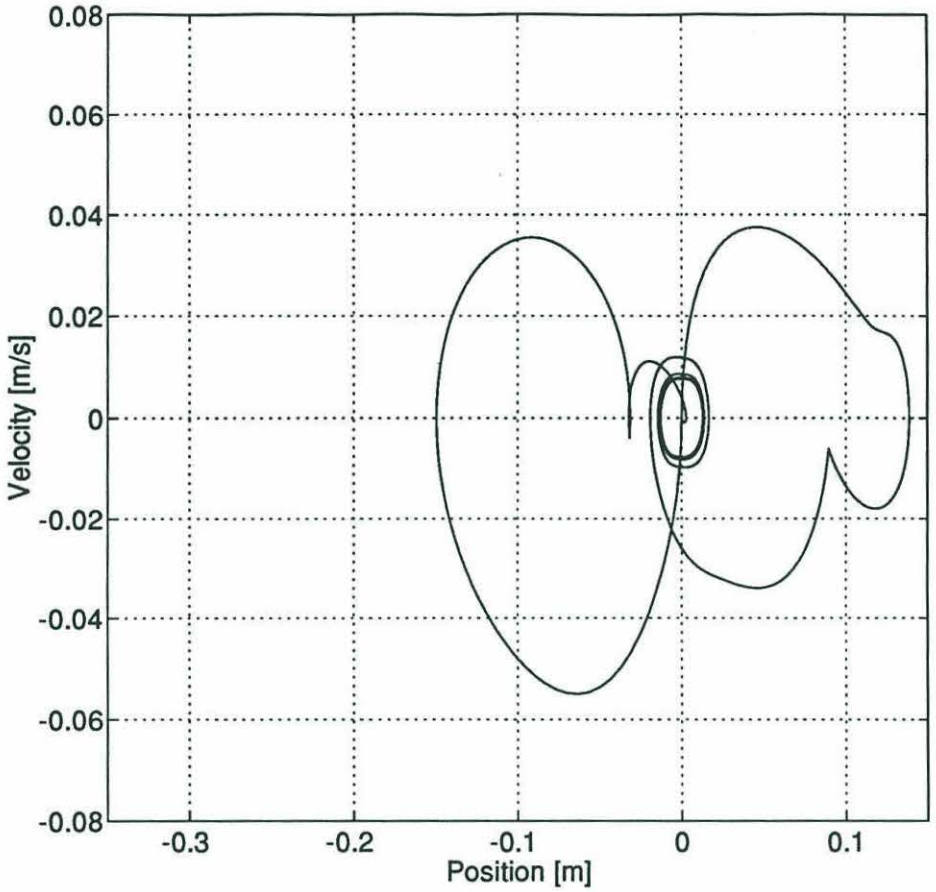

Figure 4.20: STATE SPACE TRAJECTORY WITH COMPENSATION ENABLED AND COMPLETE STATE INFORMATION - The solid line is the path of the trajectory following error through state space. Perfect state information is used in the feedback loop and compensations in the vehicle controller are still active. The result should be compared with Figure 4.16, the corresponding plot for the fully compensated system with complete observer architecture.

caused only a small degradation of system performance. Long delays are a greater problem, but do not necessarily lead to vehicle instability. Delays from 5 to 11 SHARPS periods provoke oscillations with peak values that increase with both the delay and the period. The vehicle does not diverge without limit from the desired trajectory, but the magnitude of the oscillations is too large to permit task performance. Compensation for the delay is limited to a few SHARPS periods. Beyond that limit the state estimates become unstable, diverging from the actual state without limit while the vehicle continues large oscillations about the desired trajectory. A higher order extrapolation than the forward Euler formula used here might permit

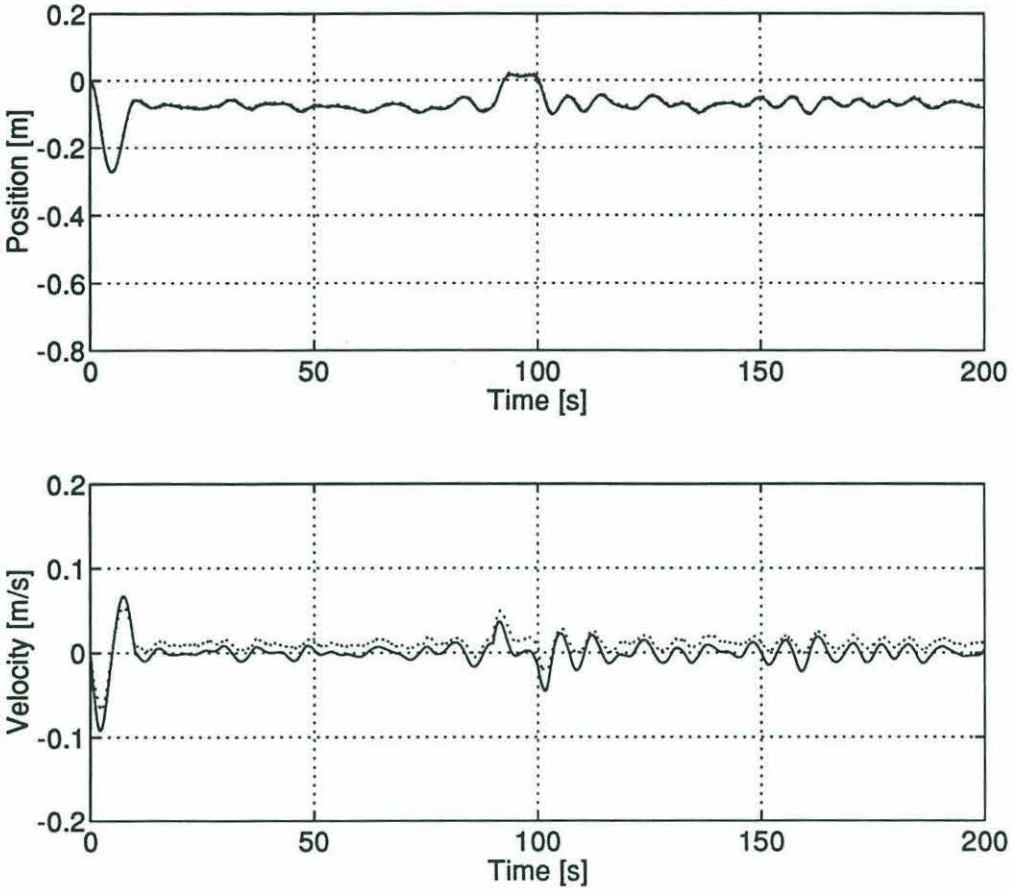

Figure 4.21: TRAJECTORY FOLLOWING ERROR IN THE PRESENCE OF ENVIRONMENTAL FORCING, COMPENSATION SUITE AND OBSERVER FORCE INPUT ENABLED - The desired trajectory has been subtracted from the actual (solid lines), estimated (dotted lines), and measured (dash-dot, position plot only) trajectories and plotted here against time. Note the change of scale on the vertical axes compared to the earlier trajectory following error plots. Note also the constant position offset and the suppression of the limit cycle. Movement about the mean offset is caused by the random component of the environmental forcing, not by the thruster dynamics.

compensation for slightly longer delays. However, drop out has been eliminated and measurement delays are restricted to a fraction of one period. Further investigation of these topics is not warranted.

The conclusions to be drawn from the simulation results presented in this section can be simply summarized. The proposed observer and controllers will produce a stable closed loop vehicle system. The complete observer architecture is fundamental to good system performance and effective reduction of detrimental limit cycle behaviors. Further, the suggested suite of compensations for system nonlinearities significantly

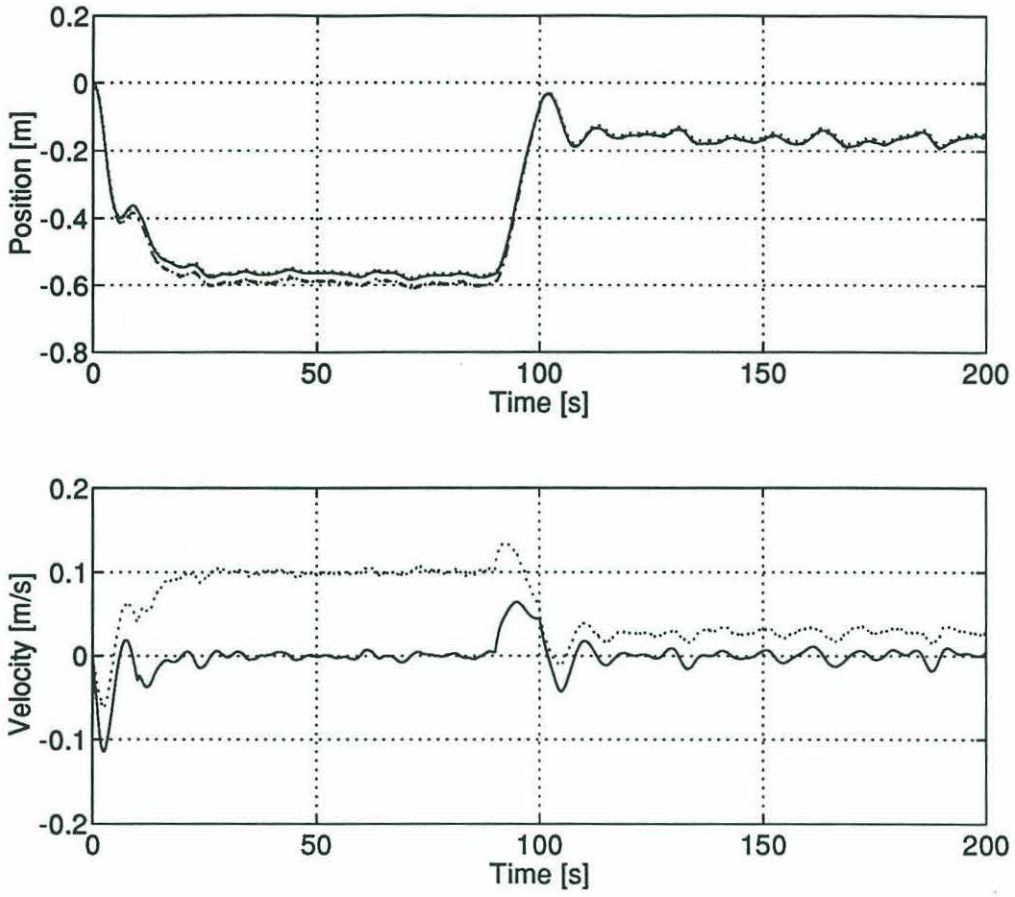

Figure 4.22: TRAJECTORY FOLLOWING ERROR IN THE PRESENCE OF ENVIRONMENTAL FORCING, COMPENSATION DISABLED AND OBSERVER FORCE INPUT ENABLED - The desired trajectory has been subtracted from the actual (solid lines), estimated (dotted lines), and measured (dash-dot, position plot only) trajectories and plotted here against time. Note the change of scale on the vertical axes compared to the earlier trajectory following error plots. Controller gains were calculated assuming steady translation values for the hydrodynamic coefficients, $C_M^* = 1$, $C_D^* = 1$. The position error is 55 *cm* during translation and 15 *cm* during hover. The position errors drop to 35 *cm* during translation and 10 *cm* during hover when the limit cycle values of the hydrodynamic coefficients ($C_M^* = 2$, $C_D^* = 8$) are used to compute the controller gains. Compare these values to the 5 *cm* offsets observed in the compensated case. The tracking errors can be reduced, but not eliminated, using PID control. Movement about the mean offset is caused by the random component of the environmental forcing, not by the thruster dynamics.

enhances the accuracy of both the system and the estimator. The performance level of the compensated system with complete observer architecture compares favorably with a system that has complete state information available to it. The only significant weakness exhibited in tracking is inherent in the PD control law and not attributable

to the observer structure or the compensation algorithms. This issue will be addressed in the following section.

4.4 PID Control

To implement PID control the state vector describing the vehicle must be augmented with the integral of position. It then takes the form

$$\mathbf{x} = \begin{bmatrix} z \\ \dot{z} \\ \tilde{z} \end{bmatrix} \tag{4.1}$$

where $\tilde{z}$ is the integral of the position, z. The system and input matrices are correspondingly enlarged. The resulting controllability matrix, $\mathcal{C} = [\mathbf{B}\vdots\mathbf{AB}\vdots\mathbf{A}^2\mathbf{B}]$, has rank three and the system is controllable. However, the system is not observable when only position is measured. Specifically, if the output matrix is $\mathbf{C} = [\ 1 \quad 0 \quad 0\ ]$, then the observability matrix, $\mathcal{O} = [\mathbf{C}^{\mathrm{T}}\vdots\mathbf{A}^{\mathrm{T}}\mathbf{C}^{\mathrm{T}}\vdots(\mathbf{A}^{\mathrm{T}})^2\mathbf{C}^{\mathrm{T}}]$, has rank two.

To make the system observable, either velocity or the integral of position must be provided as an input to the observer. This can be accomplished numerically by calculating the derivative or the integral of position from the SHARPS measurement at each iteration of the system. Integration is the better choice because the position measurement contains noise and integration is inherently a low pass operation. Differentiation would increase the noise content of the signal. The output matrix now has the form

$$\mathbf{C} = \begin{bmatrix} 1 & 0 & 0 \\ 0 & 0 & 1 \end{bmatrix} \tag{4.2}$$

and $\mathcal{O}$ has rank three. The system is observable.

A low order integration technique with a fast execution time is appropriate for the "measurement" of the integral of position. The observer is robust to input noise by design. The stability of the integration algorithm is not a concern because the measured value can be replaced by the output of the estimator at each iteration.

Filtering is not required for the same reason. Trapezoidal integration, with a local error of order T^3, is used in the simulation runs.

The performance of the system under PID control is sensitive to the placement of the real valued closed loop pole. The Butterworth configuration suggested by Friedland [8] will eliminate the tracking error caused by steady forcing from the environment. However, the system is subject to fairly severe, though well damped, excitations of the limit cycle as seen in Figure 4.23 and described in Section 4.3. The thrusters are completely saturated by the ringing that begins with the transition from deceleration to hover. Commanded thrust peaks at -2200 N followed by $+700$ N on the subsequent swing. Additionally, the limit cycle is no longer suppressed during hover by the environmental forcing.

It should be noted here that, for the simulation runs in this section, the desired trajectory of Section 4.3 is unchanged, the compensation suite and the observer force input are enabled, and the environmental forcing previously described is active. The control loop is now PID. Pole placement will be described in the Laplace domain. The complex conjugate closed loop poles are placed as before, with $\omega_{n_{cl}} = 0.7\ s^{-1}$ and $\zeta = \sqrt{2}/2$. The observer poles are placed in a Butterworth configuration with a magnitude of $2.1\ s^{-1}$. Only the position of the real valued closed loop pole will be changed in the discussion that follows. It has been placed at $-0.7\ s^{-1}$ for Figure 4.23 to fill out the Butterworth configuration. The span of the position and velocity axes has been enlarged compared to the trajectory following error plots of Section 4.3.

An alternative to the Butterworth approach is minimization of a quadratic performance index as in Section 3.2. A performance index that strongly emphasizes position tracking over actuator use, the criteria used in the PD case, will place the real valued closed loop pole very near the origin while leaving the complex conjugate pair relatively undisturbed. This configuration yields a near match in the step response of the linear analogs of the PD and PID systems. With the real valued closed loop pole placed at $-0.007\ s^{-1}$ and the system otherwise unchanged, limit cycle ringing is no longer excited by the step. However, the gains are now too weak to cancel the tracking error caused by the steady current. The error is 5 cm as previously seen

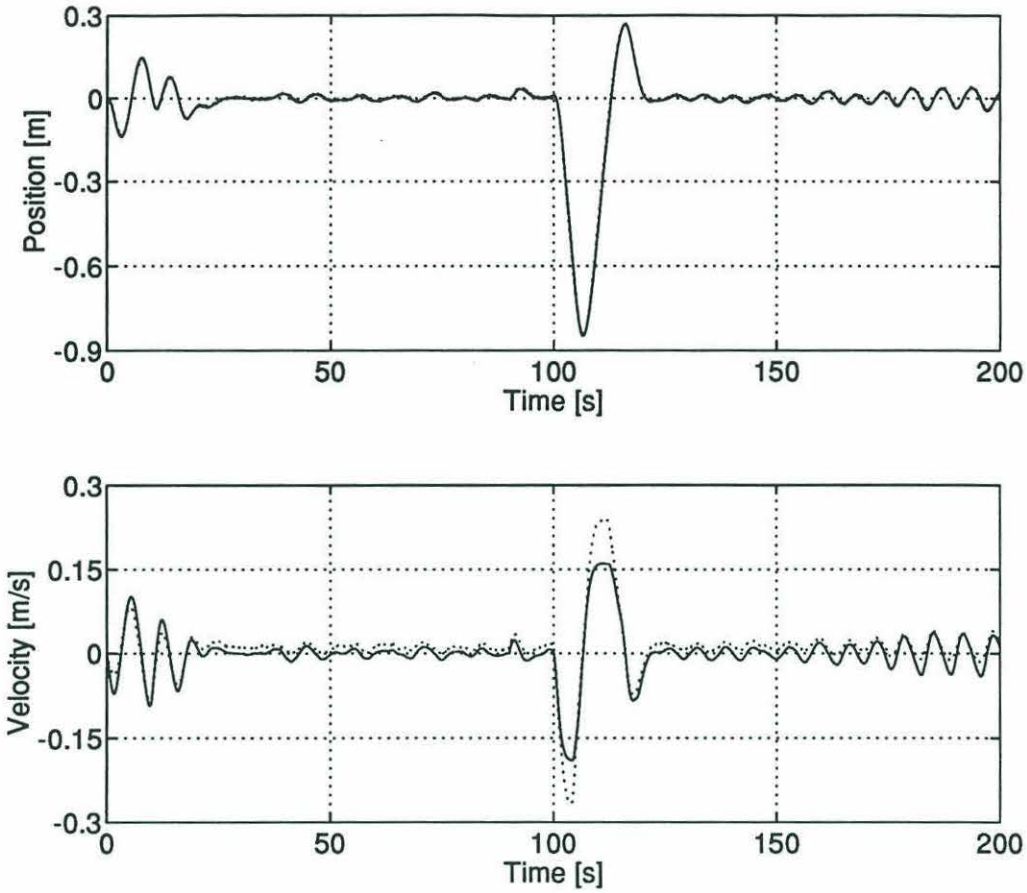

Figure 4.23: TRAJECTORY FOLLOWING ERROR IN THE PRESENCE OF ENVIRONMENTAL FORCING, COMPENSATED SYSTEM UNDER PID CONTROL, OBSERVER FORCE LOOP ENABLED, REAL CLOSED LOOP POLE AT $-0.7\ s^{-1}$ - The desired trajectory has been subtracted from the actual (solid lines), estimated (dotted lines), and measured (dash-dot, position plot only) trajectories and plotted here against time. The real valued closed loop pole has been placed at $-0.7\ s^{-1}$ to form a Butterworth configuration with the complex conjugate closed loop poles. The constant tracking error caused by steady environmental forcing under PD control has been eliminated but fairly severe ringing is now present.

under PD control (Figure 4.24). The hover limit cycle is now suppressed. Given the step response similarity, this is not an unexpected result.

These results suggest an intermediate pole position on the negative real axis to achieve a balance between elimination of the ringing and elimination of the tracking error. Figure 4.25 shows the result with the pole placed at $-0.07\ s^{-1}$. Limit cycle ringing is greatly reduced and the tracking error has been removed. However, the thrusters still saturate, though less severely, and there is now a long time constant

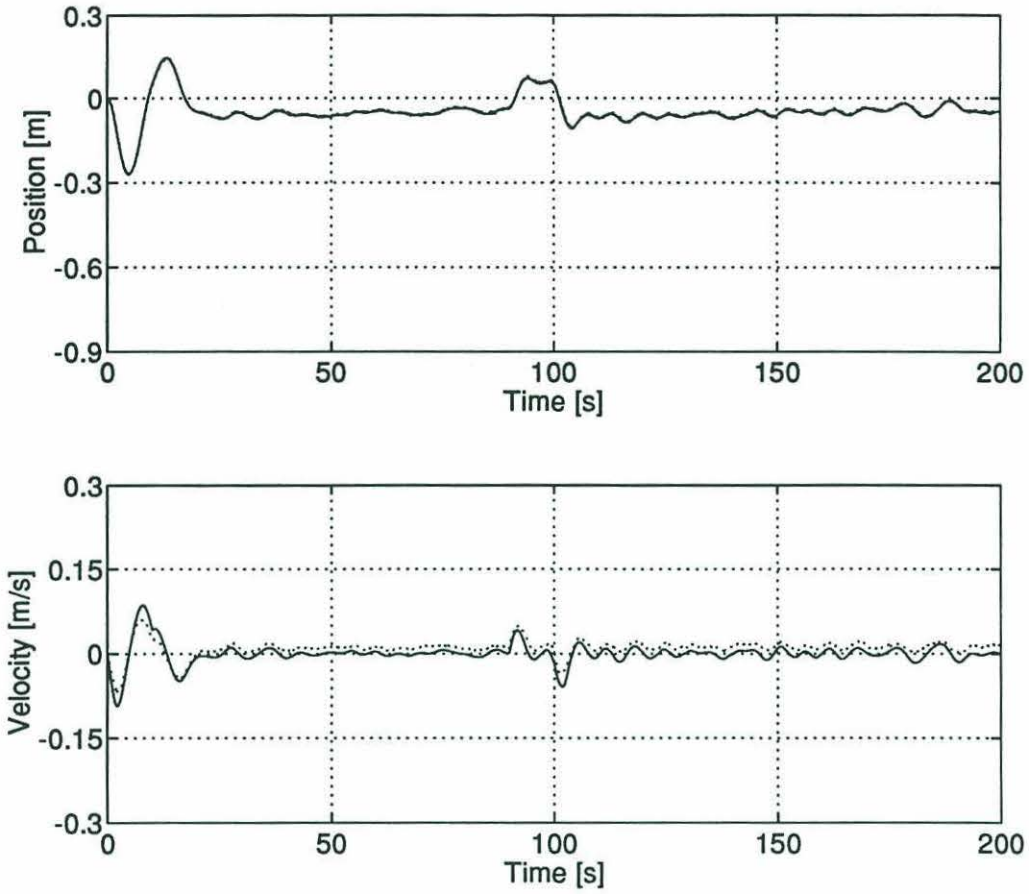

Figure 4.24: TRAJECTORY FOLLOWING ERROR IN THE PRESENCE OF ENVIRONMENTAL FORCING, COMPENSATED SYSTEM UNDER PID CONTROL, OBSERVER FORCE LOOP ENABLED, REAL CLOSED LOOP POLE AT $-0.007\ s^{-1}$ - The desired trajectory has been subtracted from the actual (solid lines), estimated (dotted lines), and measured (dash-dot, position plot only) trajectories and plotted here against time. The real valued closed loop pole has been placed at $-0.007\ s^{-1}$ to satisfy a quadratic performance index that emphasizes position tracking over actuator use. The ringing has been eliminated, but the steady tracking error has the same magnitude as the PD case.

associated with convergence to the desired trajectory. The hover limit cycle has remained suppressed.

The goal in using PID control is elimination of constant tracking errors caused by steady environmental forcing. The simulation runs presented here indicate that the error can be eliminated, but only if performance degradation in the form of limit cycle ringing or long time constants for tracking convergence are acceptable. The performance of the PD algorithm is generally superior which suggests two alternate means of defeating the offset. In a steady current that will not undergo changes

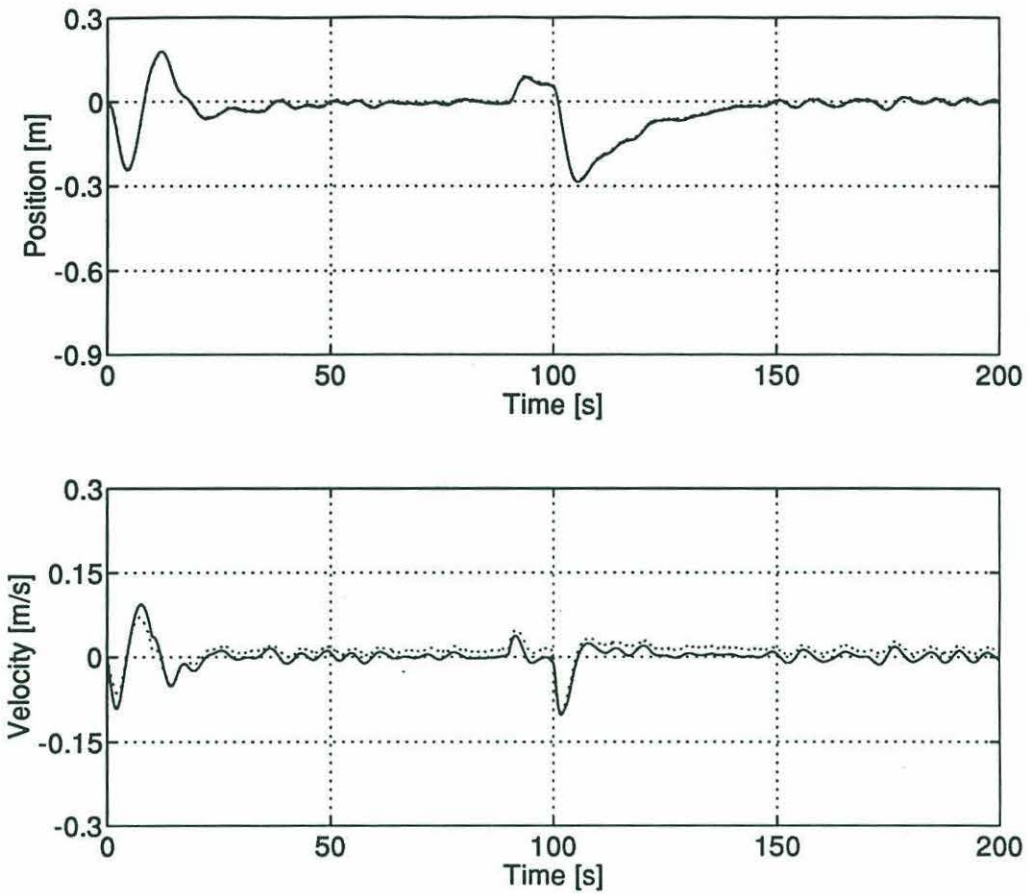

Figure 4.25: TRAJECTORY FOLLOWING ERROR IN THE PRESENCE OF ENVIRONMENTAL FORCING, COMPENSATED SYSTEM UNDER PID CONTROL, OBSERVER FORCE LOOP ENABLED, REAL CLOSED LOOP POLE AT $-0.07\ s^{-1}$ - The desired trajectory has been subtracted from the actual (solid lines), estimated (dotted lines), and measured (dash-dot, position plot only) trajectories and plotted here against time. The real valued closed loop pole has been placed at $-0.07\ s^{-1}$. Ringing has been reduced and the tracking error has been eliminated. A long time constant is now associated with convergence to the desired trajectory.

that are large compared to the mean, the desired position can simply be changed to offset the error. Flows of this nature occur in rivers, pipes, and many portions of the ocean. Alternatively, the system can toggle between PD and PID control depending on the changing situation and the operational requirements of the project. Other, nonlinear, control algorithms may be more successful, but these are outside the scope of this investigation. The simulation has shown that PID control is possible, but not necessarily desirable, within an acoustic position net.

4.5 Conclusions

It is important, when evaluating these results, to remember that this is only a simulation. Each part of the system has been modelled in software and, while some of the models are precise or nearly so, others are only a fair match to the actual system under some conditions. For example, the observer and controllers of the simulated and the actual systems are identical and the model of the SHARPS measurement is quite precise. The thruster model has performed well empirically, but small variations between thrusters and over time are known to exist. This may make compensation for the deadband in the actual system more difficult and certainly means the forcing applied to the vehicle model is imperfect. The weakest part of the simulation is the hydrodynamic characterization of the vehicle, particularly during the transitions between flow regimes.[6] The flow field around ROV Hylas and the resulting hydrodynamic forcing are considerably more complicated than the four regime model used here. However, the transitions are transient events. The most accurate portions of the hydrodynamic model are hover and steady translation, the regimes in which the vehicle accomplishes tasks. That accuracy has been empirically demonstrated by this investigation to be quite high. Therefore, simulation results may be taken to be qualitatively correct. During hover and steady translation the results are quantitatively accurate as well. This statement is supported by the results to be presented in Chapter 5.

The strong indication of the simulation is that the proposed observer and controller system is stable and well behaved. Dramatic improvements in system performance are realized when the observer force input is enabled. In particular, the effects of the thruster limit cycle are greatly reduced without redesign of the thrusters. System performance is also measurably improved by compensation for the nonlinearities. With the compensation suite enabled, estimation and tracking errors during translation are small. Tracking performance during hover is limited by the thruster limit cycle, but

[6] Operational experience with ROV Hylas suggests that the deviations from the desired trajectory during the transient periods of uniform acceleration are neither as large nor as abrupt as the simulation indicates. However, a controlled study has not been performed.

state estimates remain accurate. In the interest of brevity, the individual effects of all compensation permutations have not been presented here. Generally, each form of compensation improves performance individually. For example, one effect of the deadband compensation appears to be a reduction in the magnitude of the limit cycle excursions. However, some compensations work best in combinations. Consider that feed forward quadratic drag in the vehicle controller was shown to cause periodic tracking errors during translation if a static and inaccurate hydrodynamic model was used in the observer and controllers. The addition of a two or more regime model eliminates the errors and permits the performance improvements possible with the feed forward term. Although the four regime model is inadequate to fully describe the vehicle, a simple two regime model for the observer and controllers is sufficient to significantly improve system performance. The fully compensated system with complete observer architecture approaches the performance level of the equivalent system with perfect state information available for the feedback loop. When applied to ROV Hylas, the system can be expected to perform well.

The simulation was originally written to aid in the development and evaluation of state estimators. Having fulfilled that role, it currently exists as a resource for further investigation and testing of the vehicle system. In particular, it might now be used for preliminary evaluation and development of more complicated controller algorithms. Sliding mode control and other nonlinear techniques can be quite powerful, but implementation requires complete state information. That can now be provided by the estimator developed here. It will also be useful to extend the code to four degrees of freedom in conjunction with the expansion of the system identification procedure. Once accomplished, the expanded simulation can continue to serve as an inexpensive and flexible test platform. Ultimately, however, trials must still be performed with the vehicle system itself.

Chapter 5

Closed Loop Control of ROV Hylas

5.1 Background Discussion

The vehicle trials described in this chapter were conducted using the preliminary results of the system identification and simulation investigations.[1] The chronology is described in Section 1.2.2. ROV Hylas was successfully controlled in depth using earlier versions of the algorithms described in Chapters 3 and 4. No instabilities were observed for a range of conditions. Overall, the vehicle system performed well. However, these trials should in some sense be regarded as preliminary. The results raise questions that suggest changes to the existing procedure as well as several additional tests. Some of these ideas are discussed below.

Closed loop and observer poles for the underlying linear system were placed with natural frequencies of $\omega_{n_{cl}} = 0.7\ s^{-1}$ and $\omega_{n_{obs}} = 2.1\ s^{-1}$. The damping for both conjugate pairs was $\zeta = 0.707$. Because of the ongoing status of the system identification analysis, the effective mass during hover was high by 6.7 %. Similarly, the dimensional

[1]Specifically, the preliminary results were based on simplex minimization of the velocity error rather than the position error. This issue is discussed in Chapter 2. The simulated vehicle used immediately prior to vehicle trials was based on those results. Additionally, many of the more advanced features had not yet been added to the simulation and the numerical integration was of relatively low order.

coefficient of quadratic drag was low by 2.9 % during hover. Observer and controller gains were calculated using only the hover values because the variable hydrodynamic model had not yet been developed. One result is that the closed loop gains were high by 6.7 % during hover and by 60 % during translation. Additionally, the feed forward quadratic drag term in the vehicle controller output was low by 2.9 % during hover and high by a factor of 6.8 during translation. Because of the restricted maneuvering volume of the test tank (Section 2.2), most trajectories consisted of short steps in position followed by long hover periods. The combination of transient periods of translation and robust observer and controller designs was sufficient to prevent poor performance and instability.

Other compensation methods were modified because of the ongoing status of the simulation investigation. Although the feed forward quadratic drag term mentioned above was used, the output of the vehicle controller was not augmented with compensation for the deadband. Rather, deadband and saturation characteristics were both applied to the output of the observer controller. This should not affect the accuracy of the state estimates, but it does degrade tracking performance compared to accurate deadband compensation in the vehicle controller. Measurement delay compensation and removal of patently bad measurements were included. Closed loop control could be turned on and off by the operator during tests. The status of the deadband, saturation, and delay compensations and of the observer force input were also controlled by the operator. Closed loop vehicle performance was evaluated for different combinations of the four switchable conditions.

A brief description of the experimental set up and the procedures used for the vehicle trials is contained in Section 5.2. The results of the trials are presented and discussed in Section 5.3. The primary goal of the section is successful demonstration of the observer and controller algorithms developed in previous chapters. System stability, estimator performance, and simple trajectory following will be evaluated. A secondary goal of Section 5.3 is confirmation of the qualitative and quantitative capabilities of the the simulation. Section 5.4 summarizes the conclusions.

5.2 Experimental Set Up and Procedure

The vehicle trials were conducted in the test tank used for the system identification procedure and described in Section 2.2. The conditions and equipment configuration were essentially the same for both tests. The only significant software change was synchronization of the transputer network to the SHARPS period of 0.125 s. Additionally, ROV Hylas was no longer suspended from a spring, but was free to move within the tank. The ballasting in use at the time gave the vehicle a small negative buoyancy. The major effect of the constant downward forcing was suppression of the limit cycle.

Predetermined desired trajectories were not available at the time of testing. Instead, a desired depth was entered by the operator using the keyboard of the PC. This limited the test paths to series of positive and negative going steps with dynamic changes limited by typing speed. The desired velocity was set to zero when the vehicle was within 15 cm of the desired position. The 15 cm watch circle was intended to prevent limit cycle oscillations from forcing the desired velocity away from zero during hover. The effects of environmental forcing on the limit cycle had not been seen before and were not anticipated. Outside the watch circle, the desired velocity was calculated from the formula

$$\dot{z}_D = 0.166(z_D - z), \tag{5.1}$$

where z is vehicle position and z_D is the desired position. The constant was chosen so that a large position error would not require a desired velocity that exceeded the capability of the vehicle.[2] The intent is simply to provide for a nonzero desired velocity while the vehicle is moving to the desired position. This reduces the conflict inherent in a position step requiring a finite translation at zero velocity. The desired velocity determined from Equation 5.1 is not the derivative of the desired position.

[2]The depth of the tank is 3.5 m and the height of the vehicle is 0.9 m. Therefore the largest possible position error is 2.6 m. The maximum vertical velocity of ROV Hylas is in the range $0.45 - 0.50\ m/s$. $0.43\ m/s \div 2.6\ m = 0.166\ s^{-1}$.

The stability and trajectory following performance of the system were observed with varying combinations of the observer force input and the deadband, saturation, and delay compensations enabled. Observer deadband and saturation were set at 20 N and 185 N. The deadband setting is arguably somewhat high (Section 3.3.2 and Figure 3.5), but this was the most accurate value known at the time of the trials. The observer delay extrapolation was half of the SHARPS period. During each run the measured position, estimated state, and desired state were logged with a time stamp. The filtered numerical derivative of the measured position was also logged. The velocity signal is noisy, but roughly correct. In addition to the state quantities, each record included the vertical force command for the observer and the force and torque commands for the vehicle in all four degrees of freedom. The heading and horizontal translation commands were generated by the joystick as part of the perturbation testing described below. The vertical force commands were generated by the vehicle and observer controllers. Both used the PD control law (Equation 3.5) and the vehicle controller included the feed forward quadratic drag term. The final logged quantities were a logic bit indicating the status of the closed loop depth control system and a logic word indicating the status of each of the four test parameters.

The response of the vehicle to perturbations in the environment was also observed. Perturbations took two forms. Initially a pole, manipulated from the surface, was used to push the vehicle below the desired depth and then removed. The second form, which will be presented here, was produced by the horizontal thrusters. Thruster positions and orientations on ROV Hylas cause significant wake interaction when horizontal and vertical thrusters are on simultaneously. The interaction decreases the output thrust. As a result, the hovering, negatively buoyant vehicle will begin to sink when horizontal translation is commanded unless the depth control system corrects the position error with added vertical thrust. The speed and accuracy of depth correction are measures of system performance.

5.3 Vehicle Trials

5.3.1 Vehicle Step Response

The runs presented in this section show the response of the vehicle system to a positive step in the desired position followed by a period of hover. In each case the vehicle was manually positioned near $z = -1.4\ m$ (1.4 m below the plane of the SHARPS net). Depth control was then enabled with the desired position set to $-0.75\ m$. The initial points of the traces coincide with the first SHARPS period under closed loop control. The scales of corresponding plots are the same to facilitate visual comparison. Comparisons will be made to the simulation runs presented in Section 4.3, particularly Figures 4.4, 4.7, 4.8, 4.21 and 4.22.

The first run (Figures 5.1–5.3) was performed with delay and deadband compensations disabled, saturation compensation enabled, and the observer force input enabled. Position estimates follow the SHARPS measurement with a steady error of 0.5 cm during hover. The delayed measurements are accurate during hover because velocities are near zero. The error reflects an internal balance between the observer and controllers to produce sufficient thrust to hold position against the environmental forcing. The position error settles to approximately 7.5 cm and continues to vary slowly. A constant offset is characteristic of a PD control loop under these conditions.[3] The offset causes a nonzero observer controller output which is responsible for the 1.5 cm/s error in estimated velocity. Note that both errors are half of the corresponding offsets in Figure 4.22 where the mean of the constant forcing was 30 N. The buoyancy deficit of ROV Hylas can be calculated from the position error and the closed loop gains or from the output level of the vehicle controller with allowance made for the deadband of Figure 3.5. Both methods yield a value close to 15 N, indicating that the simulation is quantitatively accurate.

The oscillations in the trajectory record have some of the characteristics of a lightly damped, second order step response. However, the cumulative indication of

[3] A PID control loop had not been implemented at the time of vehicle trials.

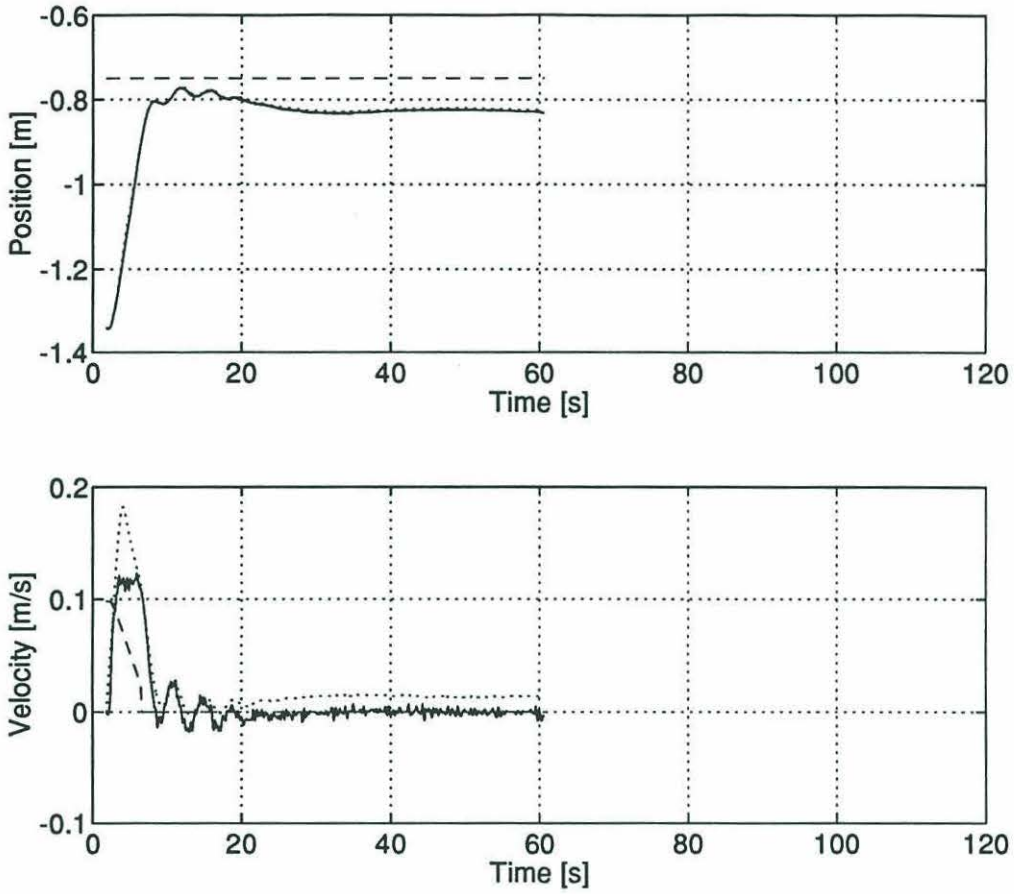

Figure 5.1: VEHICLE TRAJECTORY WITH DELAY AND DEADBAND COMPENSATIONS DISABLED AND SATURATION COMPENSATION AND THE OBSERVER FORCE INPUT ENABLED - The solid lines indicate the SHARPS position and its filtered derivative. The dashed lines mark the desired trajectory of the vehicle and the dotted curves are the state estimates. The constant position error and suppression of the limit cycle during hover are caused by the negative ballasting of the vehicle. The 5 cm/s error in the velocity estimate during the short translation matches the error recorded in the simulation (Figure 4.4).

the other trials and the simulation (below) is that the oscillations are a transient appearance of the limit cycle subsequently suppressed by the constant forcing of the environment. The magnitudes of the thruster deadband and the negative buoyancy are both approximately 15 N. This appears to place the system near a soft threshold for existence of the limit cycle. The step perturbation excites the limit cycle which then is suppressed by the environmental forcing or persists indefinitely depending on the structure of the observer. A sustained limit cycle is obtained when the observer force input is disabled and the observer delay compensation is enabled. The

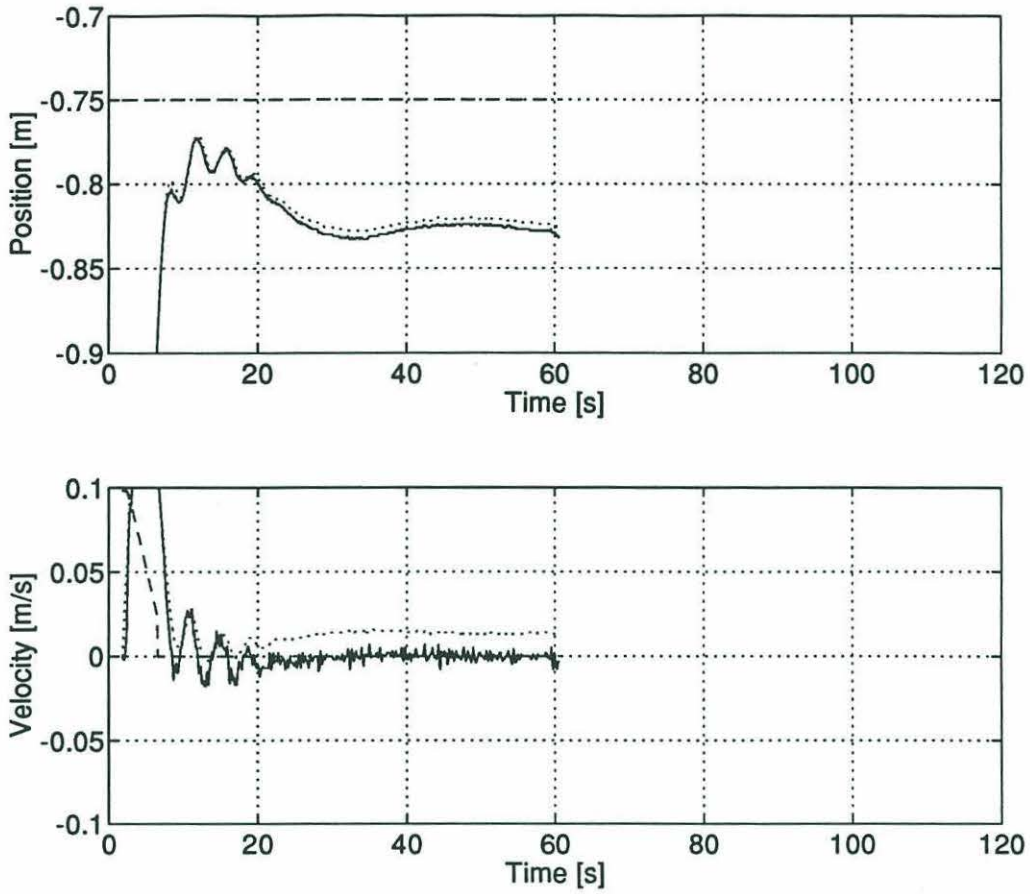

Figure 5.2: CLOSE VIEW OF VEHICLE TRAJECTORY WITH DELAY AND DEADBAND COMPENSATIONS DISABLED AND SATURATION COMPENSATION AND THE OBSERVER FORCE INPUT ENABLED - The solid lines indicate the SHARPS position and its filtered derivative. The dashed lines mark the desired trajectory of the vehicle and the dotted curves are the state estimates. The range of the vertical axes has been restricted for detailed viewing of the traces in Figure 5.1. The sudden change in position at 60 s is caused by contact with the wall of the test tank. Data logging was terminated immediately following the encounter. The noise amplification inherent in calculating velocity from even relatively smooth position measurements is apparent during the period of hover.

oscillations decay slowly and strongly resemble ringing if the delay compensation is disabled. Decay is more rapid and the excursions fairly small, as in this run, when the observer force input is enabled. The frequency of oscillation is the same in each trial, but the peak amplitudes vary in cases with decay. Examples will be given later in this section. To the extent that the calculation has meaning for the brief appearance of the limit cycle in this case, the Keulegan-Carpenter number is $KC = 0.1$ and the period is 5 s.

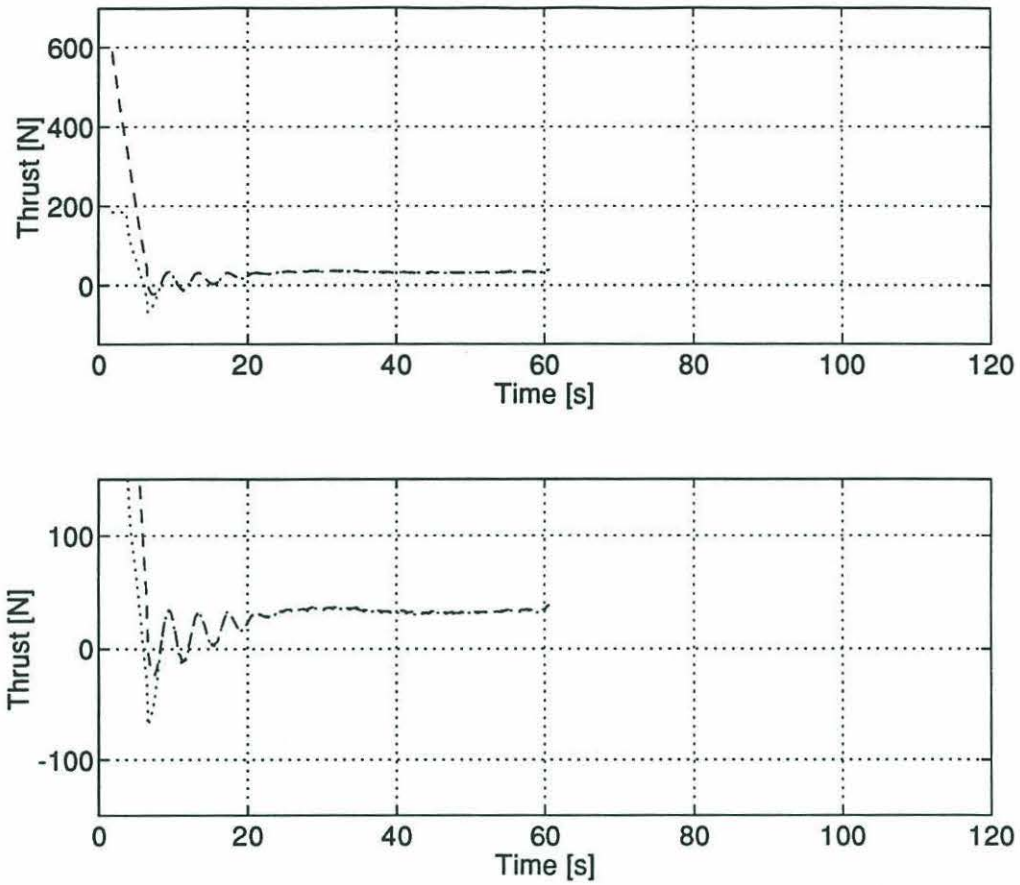

Figure 5.3: ACTUATOR COMMANDS WITH DELAY AND DEADBAND COMPENSATIONS DISABLED AND SATURATION COMPENSATION AND THE OBSERVER FORCE INPUT ENABLED - The dashed lines mark the thrust command sent to the vehicle while the dotted lines show the thrust command sent to the observer. Both plots present the same data set, however, the range of the vertical axis on the second plot is restricted to permit a more detailed inspection.

As predicted by the simulation, and confirmed here, the uncompensated system with complete observer architecture is both stable and reasonably well behaved. Now consider the effect of disabling the observer force input while maintaining the status of the three variable forms of compensation (saturation enabled, deadband and delay disabled). The results are shown in Figures 5.4–5.6. Comparison should be made to Figures 4.7 and 4.8 of the simulation. The vehicle system exhibits a slowly suppressed appearance of the limit cycle in response to the input step. Thruster saturation is approached at the extrema of the state error. Peak values of the commanded thrust exceed 130 N. A period of steady translation during the oscillations would have

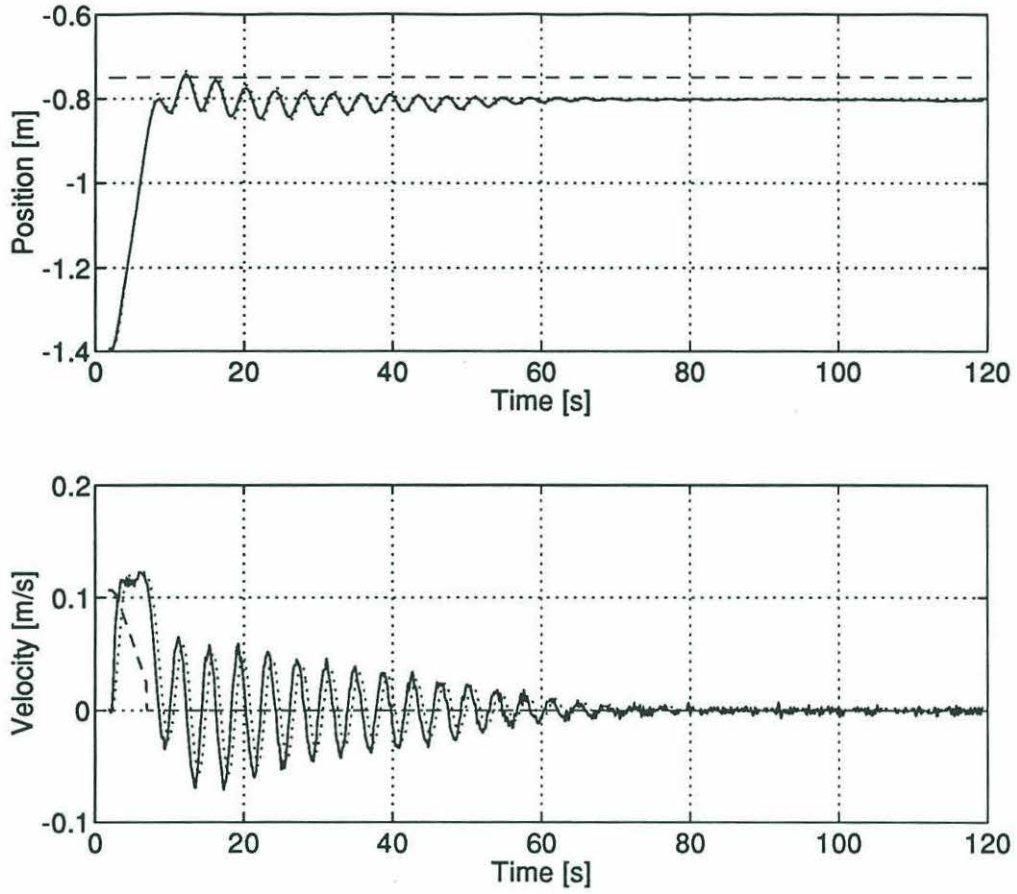

Figure 5.4: VEHICLE TRAJECTORY WITH SATURATION COMPENSATION ENABLED AND DELAY AND DEADBAND COMPENSATIONS AND THE OBSERVER FORCE INPUT DISABLED - The solid lines indicate the SHARPS position and its filtered derivative. The dashed lines mark the desired trajectory of the vehicle and the dotted curves are the state estimates.

saturated the actuators as occured in Figure 4.8, but would also have reduced the duration of the excitation.

Achieving steady state with a constant position error of 5 cm required an elapsed time of approximately 80 s. The magnitude of the error is less than in the previous case with the same compensation and the observer force input enabled. While the tracking error does not exhibit the same slow variations seen previously, there is a slow divergence in the final twenty seconds of the run. The oscillation period is 4 s with extrema about the mean of 2.5 cm and 5 cm/s. The Keulegan-Carpenter number is $KC = 0.2$. Damping to steady state with a persistent low level oscillation is achieved in approximately 50 s by the simulation, but this is during a period of

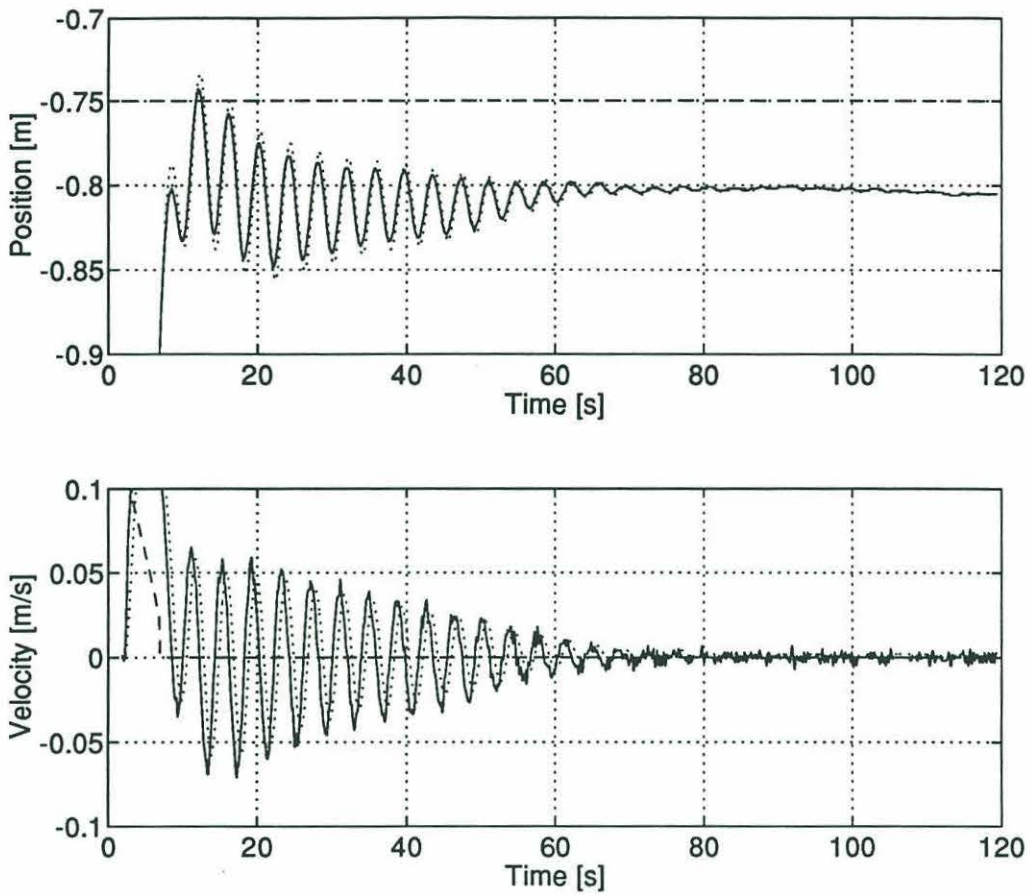

Figure 5.5: CLOSE VIEW OF VEHICLE TRAJECTORY WITH SATURATION COMPENSATION ENABLED AND DELAY AND DEADBAND COMPENSATIONS AND THE OBSERVER FORCE INPUT DISABLED - The solid lines indicate the SHARPS position and its filtered derivative. The dashed lines mark the desired trajectory of the vehicle and the dotted curves are the state estimates. The range of the vertical axes has been restricted for detailed viewing of the traces in Figure 5.4.

steady translation at relatively high thrust when the effects of the thruster dynamics and deadband are less apparent. During hover with constant small forcing from the environment, as here in the vehicle test, oscillations may be expected to persist for a longer period because of the characteristics of the actuators at low thrust.

When the velocity is nonzero, the actual position is in advance of the measurements. Therefore, during oscillations, the actual position and velocity have small phase lags compared to the SHARPS measurements in time series plots such as those used here. But the position and velocity estimates during the oscillations here both show a phase *lead* compared to the SHARPS measurements. Although the sign is

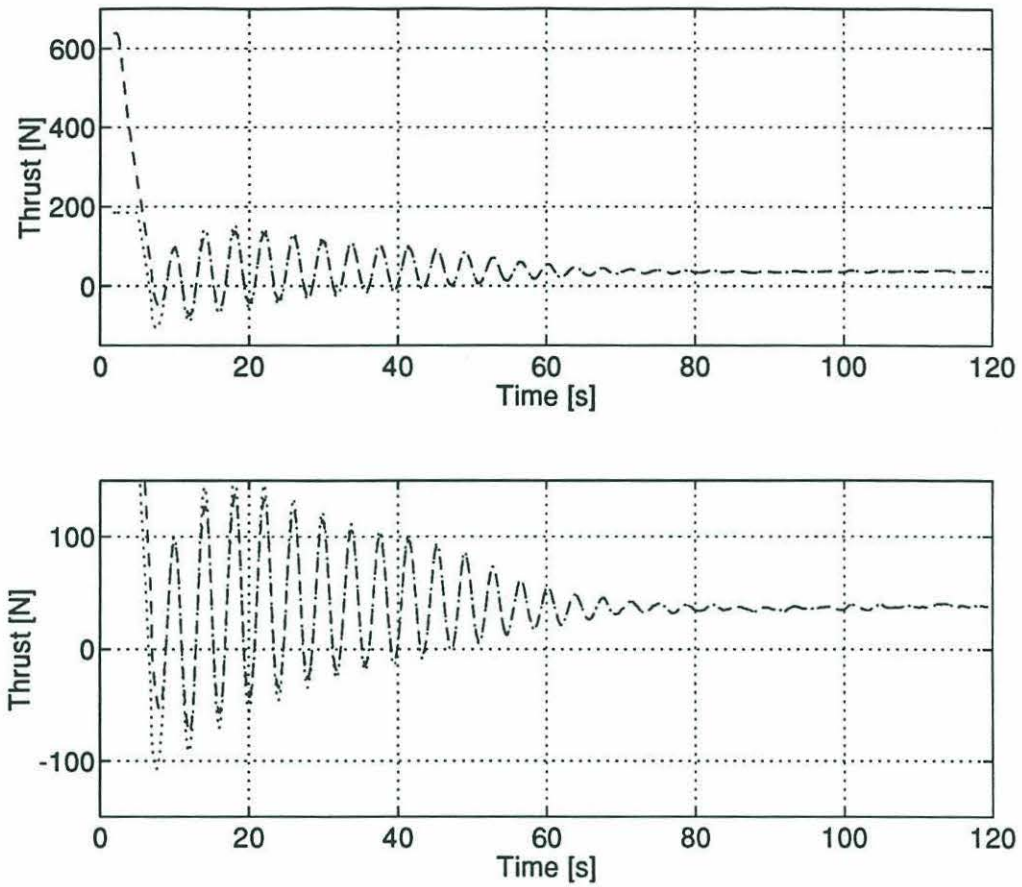

Figure 5.6: ACTUATOR COMMANDS WITH SATURATION COMPENSATION ENABLED AND DELAY AND DEADBAND COMPENSATIONS AND THE OBSERVER FORCE INPUT DISABLED - The dashed lines mark the thrust command sent to the vehicle while the dotted lines show the thrust command sent to the observer. Both plots present the same data set, however, the range of the vertical axis on the second plot is restricted to permit a more detailed inspection.

reversed, the magnitude of the position lead is approximately consistent with the magnitudes of the velocity and the measurement delay.[4] The same observation can be made of most of the remaining runs, although the magnitude of the lead is reduced in the compensated runs.

The simplest explanation implicates the logging system. All logged information, including SHARPS measurements and state estimates, is stored in a single array that is accessible to all three transputers. Logging and vehicle control processes are run on

[4]The phase lag associated with the velocity filter is unknown and may eliminate or alter the sign of the phase difference when plotting actual and "measured" velocities during oscillations. For that reason it is not used in this analysis.

separate transputers, all of which are synchronized to new SHARPS measurements. The observations are explained if the logger copies the array after the new measurements are recorded but before the observer algorithm writes the new state estimates. If the estimates are one period out of date, the expected phase lag becomes the observed phase lead. Note that this is only a logging error. The delay pertinent to the observer and controllers is still one half of the measurement period. Note also that the reduced lead in the compensated runs is consistent with the explanation. The observer balance between measurement and model based information will place the estimate between the actual and measured states. Disabling the observer force input ties the estimate more closely to the measurement adding net lead to the trace. The compensated runs, with the observer balance restored, slide the estimate towards the actual state adding net lag to the trace. ROV Hylas is not available to confirm this hypothesis, however the conclusions reached here are independent of small phase differences in logged quantities.

With the model fettered by the disabled observer force input, position estimates during hover closely follow the SHARPS measurements. Velocity estimates no longer exhibit the constant offset from the "measured" velocity nor the 5 cm/s error seen during the short translation. These observations are matched by the behavior of the simulation (Figures 4.4 and 4.7).

System performance without the observer force input is stable, but otherwise unsatisfactory when compared to the initial uncompensated case with the observer force input enabled. Oscillations in the step response exhibit significantly greater persistence and amplitude. System performance was accurately predicted by the simulation in both cases. In particular, the prediction by the simulation that limit cycle behaviors are most extreme when the observer force input is disabled is confirmed. Before considering the system configuration with all three compensations enabled and complete observer architecture, it will be instructive to view four examples of sustained or slowly damped limit cycle behavior. The observer force input is disabled for each of the four runs. Delay compensation is enabled for the first three runs (Figures 5.7–5.9) and disabled for the fourth run (Figure 5.10). The status of the deadband and satura-

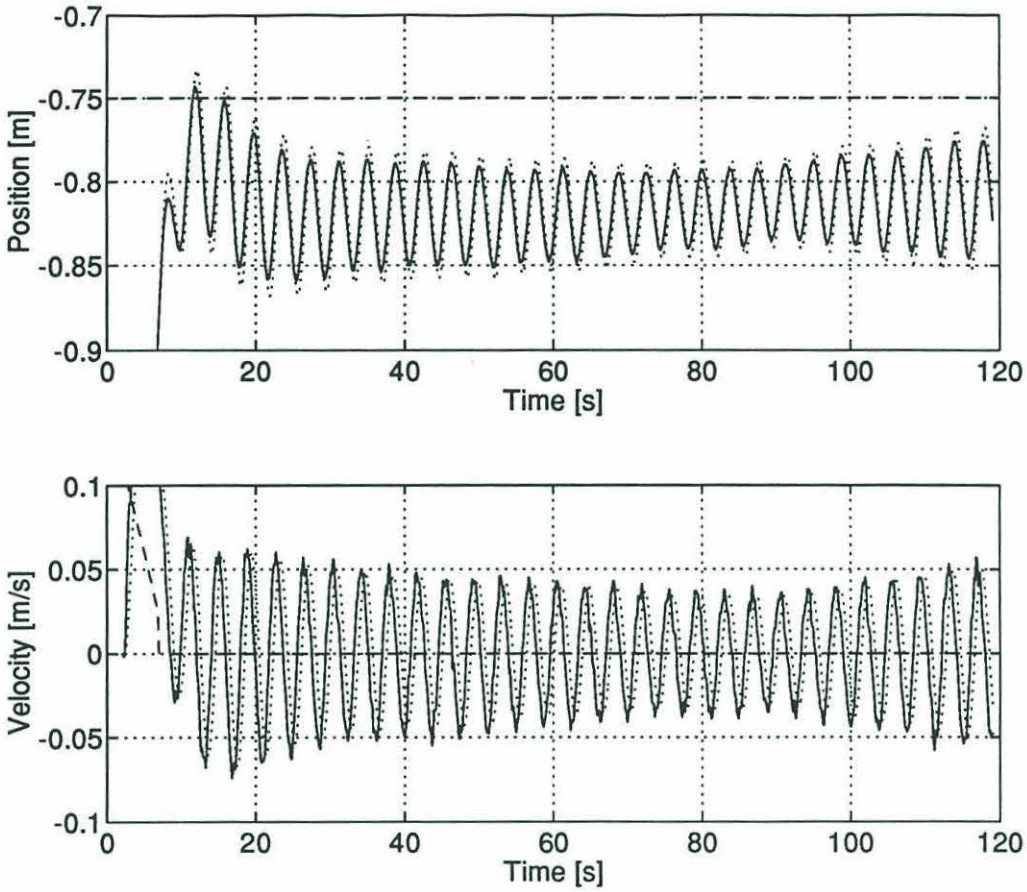

Figure 5.7: CLOSE VIEW OF VEHICLE TRAJECTORY WITH DELAY, DEADBAND, AND SATURATION COMPENSATIONS ENABLED AND THE OBSERVER FORCE INPUT DISABLED - The solid lines indicate the SHARPS position and its filtered derivative. The dashed lines mark the desired trajectory of the vehicle and the dotted curves are the state estimates. The range of the vertical axes has been restricted for detailed viewing of the traces.

tion compensations is indicated in the captions. Conditions are otherwise unchanged from the two cases already presented.

As previously mentioned, changing the structure of the observer by disabling the observer force input allows the limit cycle to persist in the presence of constant forcing from the environment. The limit cycle will persist indefinitely (Figures 5.7–5.9) if observer delay compensation is used. It will be slowly suppressed if the delay compensation is disabled (Figures 5.5 and 5.10). Note that the decay in the latter cases takes place inside a linear envelope rather than the exponential envelope around the oscillations of a lightly damped second order step response. As seen in Figure 5.2,

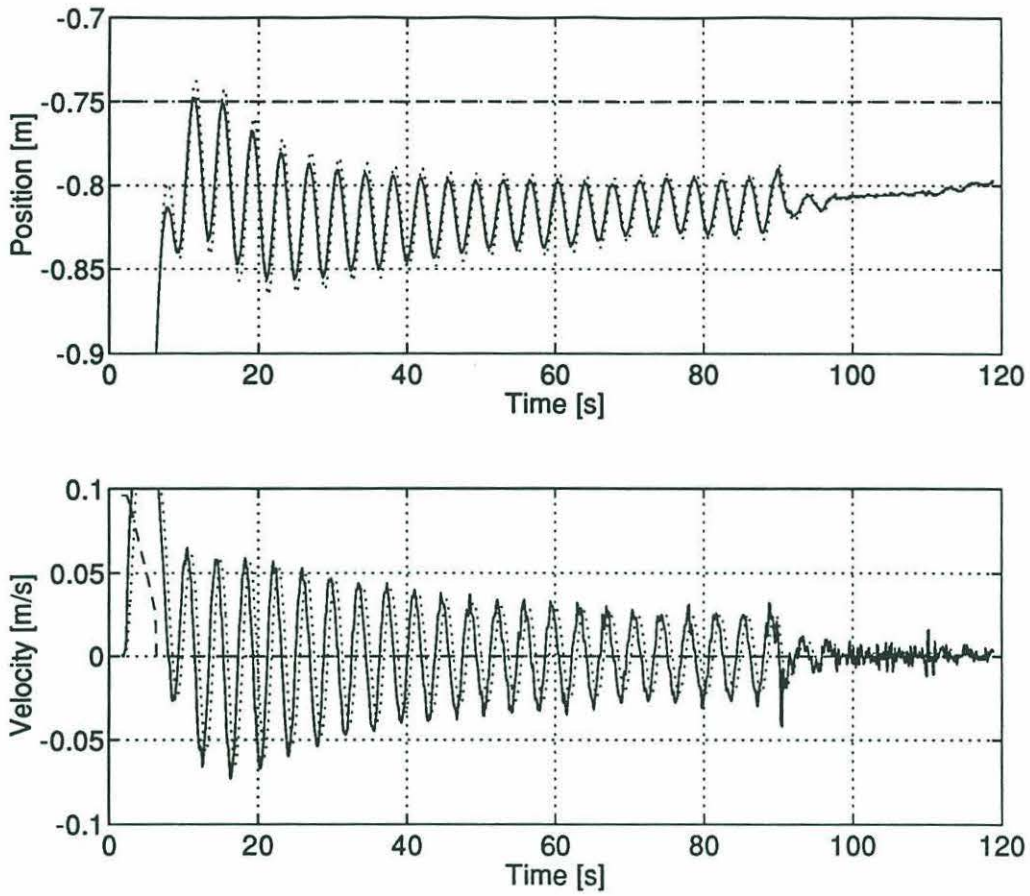

Figure 5.8: CLOSE VIEW OF VEHICLE TRAJECTORY WITH DELAY AND DEADBAND COMPENSATIONS ENABLED AND SATURATION COMPENSATION AND THE OBSERVER FORCE INPUT DISABLED - The solid lines indicate the SHARPS position and its filtered derivative. The dashed lines mark the desired trajectory of the vehicle and the dotted curves are the state estimates. The range of the vertical axes has been restricted for detailed viewing of the traces. The limit cycle was terminated by sustained contact between the vehicle and the wall of the test tank.

the suppression is very rapid when the observer force input is enabled.

The Keulegan-Carpenter number of the the three sustained limit cycles is $KC = 0.22$. Calculating from the large oscillations immediately following the step, the Keulegan-Carpenter number for the two slowly decaying cases is also $KC = 0.22$. The period is 4 s in all cases. Note that there are small variations of peak velocity and mean position during the sustained cases over the time scale of the run.

The simulation can be configured to duplicate the conditions of the vehicle trials. In Figures 5.11 and 5.12, environmental forcing has been set to -15 N and the input

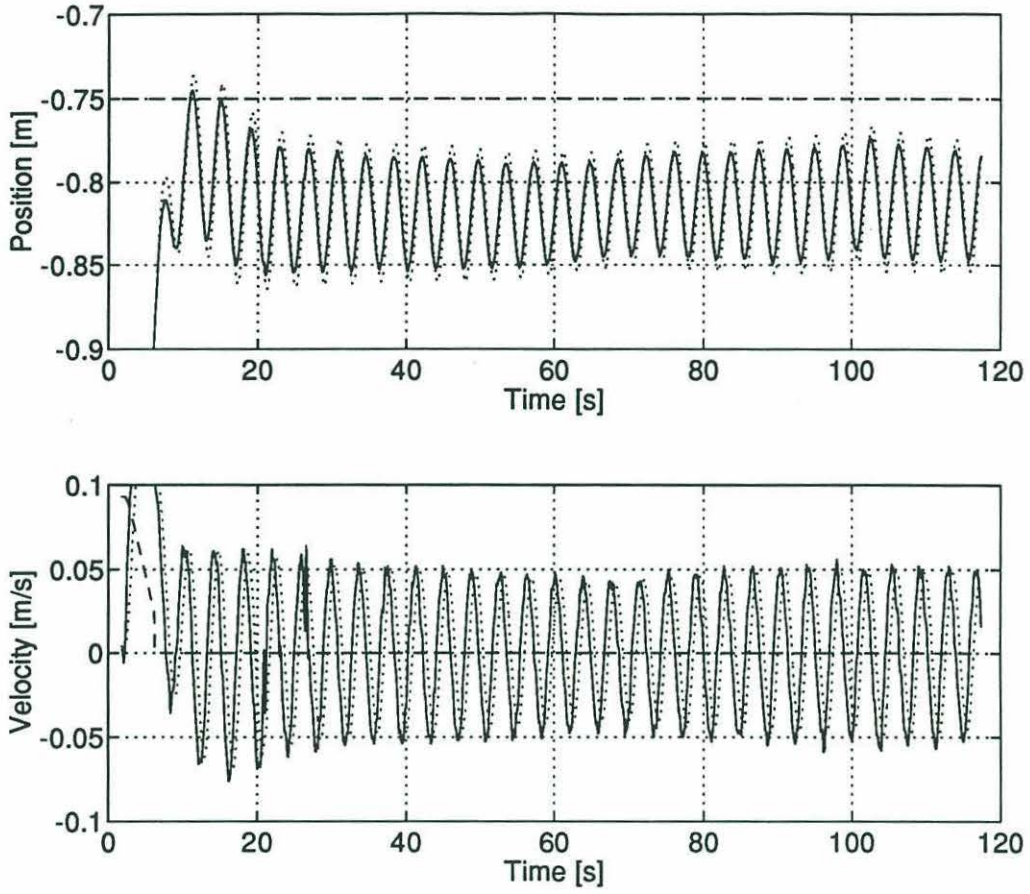

Figure 5.9: CLOSE VIEW OF VEHICLE TRAJECTORY WITH DELAY AND SATURATION COMPENSATIONS ENABLED AND DEADBAND COMPENSATION AND THE OBSERVER FORCE INPUT DISABLED - The solid lines indicate the SHARPS position and its filtered derivative. The dashed lines mark the desired trajectory of the vehicle and the dotted curves are the state estimates. The range of the vertical axes has been restricted for detailed viewing of the traces. The vehicle made contact with the wall of the test tank at 20 and 27 s, but the contact was not sustained and the limit cycle persisted.

step has a magnitude of 0.65 m. The output of the observer controller is passed through a deadband and saturation characteristic with the deadband set to 20 N, while the deadband in the simulated vehicle is set to 15 N. The measurement delay and the delay compensation are both set to half of the SHARPS period. Delay, deadband, and saturation compensations are enabled in both runs. The observer force input is disabled in Figure 5.11 and enabled in Figure 5.12. Comparison should be made to Figure 5.7 above and Figure 5.14 to be presented below. The simulation was run for 120 s to approximate the trial periods. The vertical axes span the same

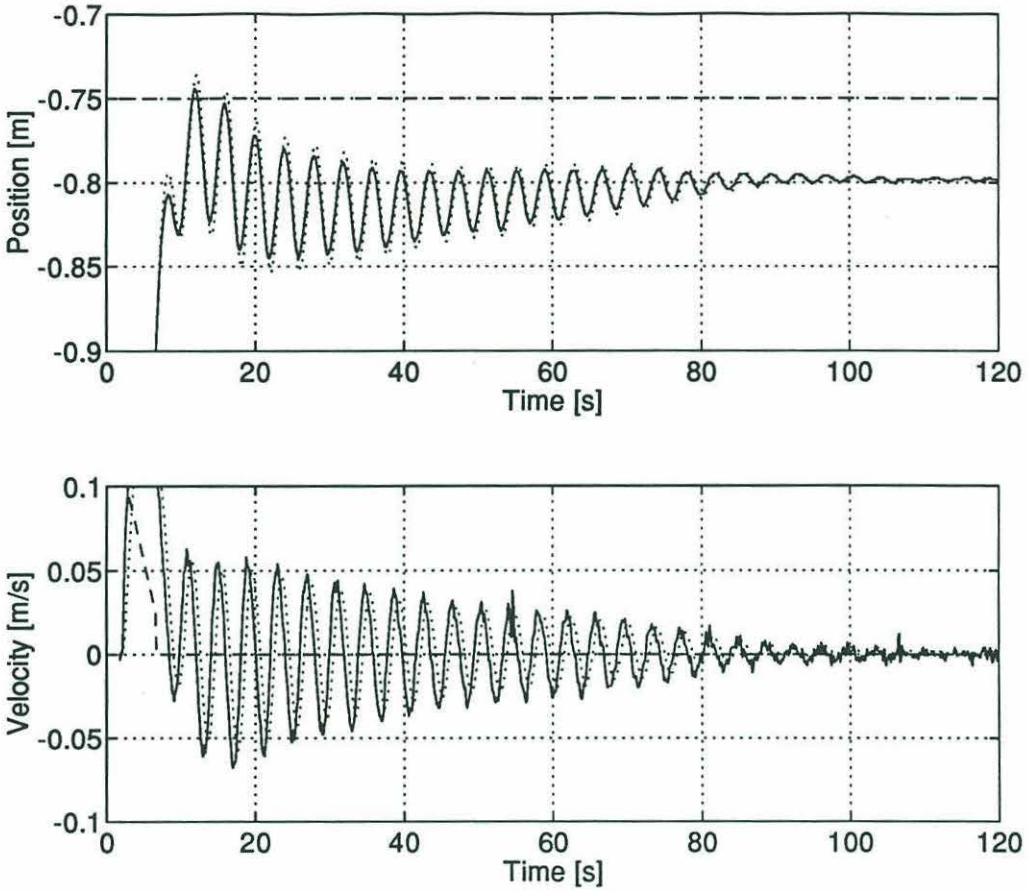

Figure 5.10: Close View of Vehicle Trajectory with Deadband Compensation Enabled and Delay and Saturation Compensations and the Observer Force Input Disabled - The solid lines indicate the SHARPS position and its filtered derivative. The dashed lines mark the desired trajectory of the vehicle and the dotted curves are the state estimates. The range of the vertical axes has been restricted for detailed viewing of the traces.

range as those of the vehicle trials discussed above.

Several observations should be made here. In the presence of constant environmental forcing, both the vehicle and the simulation exhibit a sustained limit cycle when the observer force input is disabled. The oscillations are rapidly suppressed in both cases when the observer force input is enabled. However, unlike the vehicle system, disabling the delay compensation does not cause slow suppression of the oscillations in the simulation. Some characteristics of the oscillations are also different. The period of the simulation limit cycle is 8 s with peak velocities of 2.5 cm/s. The period and peak velocity are 4 s and 5 cm/s for ROV Hylas. However, the changes

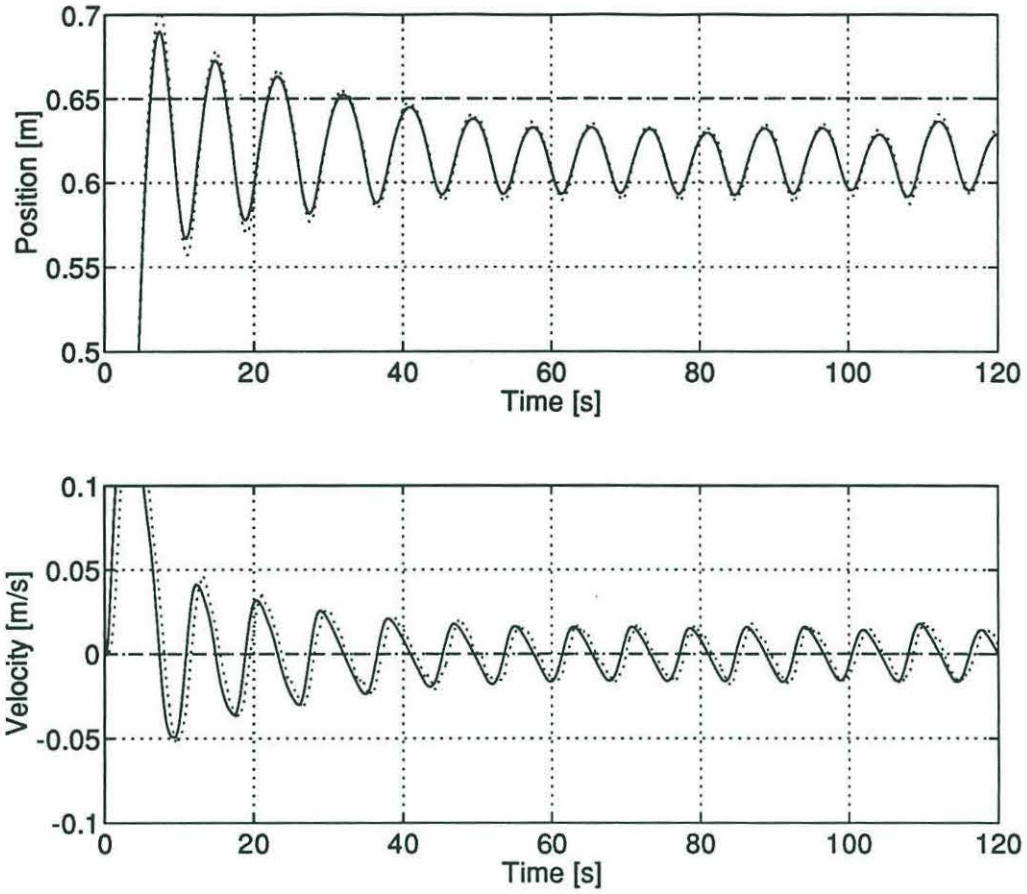

Figure 5.11: CLOSE VIEW OF SIMULATED VEHICLE TRAJECTORY WITH DELAY, DEADBAND, AND SATURATION COMPENSATIONS ENABLED AND THE OBSERVER FORCE INPUT DISABLED - The solid curves mark the trajectory of the simulated vehicle. The dashed lines mark the desired trajectory of the vehicle and the dotted curves are the state estimates. The range of the vertical axes has been restricted for detailed viewing of the traces.

are in inverse proportion to each other, so the Keulegan-Carpenter number of the simulation is identical to the Keulegan-Carpenter number of the vehicle, $KC = 0.22$.

Although they are not shown here, simulation runs with greater duration show the same slow variations in peak velocity and mean position during the limit cycle exhibited by the vehicle. The time scale of the variations is approximately twice as long, similar to the change in the period of oscillation. Raising the level of environmental forcing in the simulation shortens the period of the limit cycle while leaving the peak velocities largely unchanged. This is consistent with the simulation runs of Chapter 4. In particular, this is consistent with the short period exhibited by the

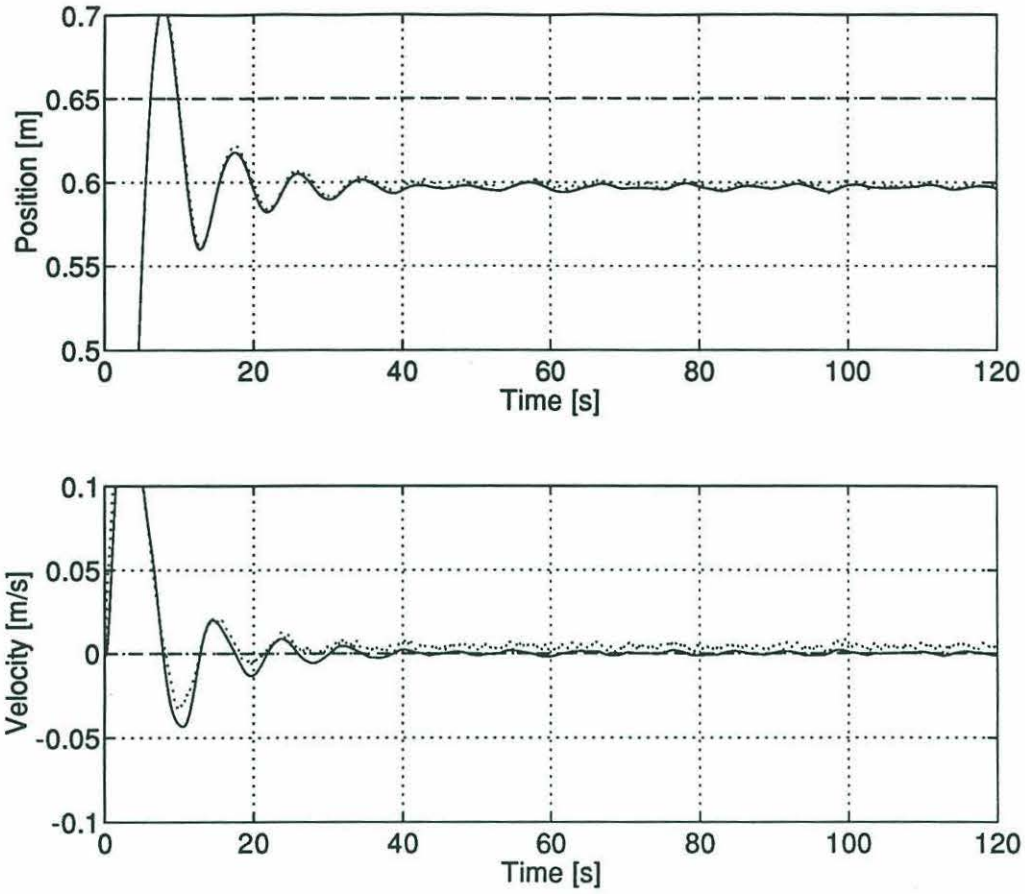

Figure 5.12: CLOSE VIEW OF SIMULATED VEHICLE TRAJECTORY WITH DELAY, DEADBAND, AND SATURATION COMPENSATIONS AND THE OBSERVER FORCE INPUT ENABLED - The solid curves mark the trajectory of the simulated vehicle. The dashed lines mark the desired trajectory of the vehicle and the dotted curves are the state estimates. The range of the vertical axes has been restricted for detailed viewing of the traces.

slowly suppressed limit cycle of Figure 4.7. In that case, mean thruster levels were high due to translation rather than environmental forcing. As the forcing is reduced to zero, the Keulegan-Carpenter number is raised to $KC = 0.3$ by the lengthening period, consistent with empirical observations of ROV Jason.

The mean position of the simulation run in Figure 5.11 and the static final position of the simulation run in Figure 5.12 match the corresponding vehicle trial values in Figures 5.7 and 5.14. Clearly, the quantitative accuracy of the simulation is highest in the steady or slowly changing situations where the hydrodynamic model is most accurate. Qualitative accuracy is still very high during more dynamic behavior. While

predictions of the period and velocity extrema of the limit cycle have a factor of two error, the magnitude of the position extrema is accurate and the Keulegan-Carpenter number is correct in all cases. The slow variations in peak velocity and mean position during the sustained limit cycle under environmental forcing are exhibited by both simulation and vehicle system. Additionally, the circumstances under which a limit cycle will be suppressed or will be sustained were predicted by the simulation, as was the linear suppression envelope. Numerous other examples of quantitative and qualitative agreement are documented in this chapter.

Based on the close agreement of the simulation with the vehicle system, it is possible to make an additional argument concerning the source of the "ringing" oscillations observed with both the simulation and ROV Hylas. The thruster dynamics, which cause the limit cycle, can be turned off within the simulation. When they are, both the short duration ringing seen when the observer force input is enabled and the long duration ringing seen when the observer force input is disabled are eliminated. The step response in both cases is a single overshoot peak in both position and velocity followed by steady hover with the expected constant position error.

When the observer force input is disabled, the observer becomes a second order filter, calculating velocity estimates by taking the derivative of the SHARPS measurements. The vehicle trials presented above demonstrate that even a simple linear observer, with no compensation, produces a significant system performance improvement compared to such a filter. Simulation runs in Chapter 4 led to the same conclusion and showed that compensation for the nonlinearities inherent in the vehicle system could further improve system performance.

The fully compensated configuration with complete observer architecture is presented in Figures 5.13–5.15. Comparison should be made to the simulation run shown in Figure 4.21 with the understanding that the deadband compensations used in the simulation and vehicle trials are essentially different. In the simulation, the output of the vehicle controller was augmented with deadband compensation to improve both the state estimates and the dynamic performance of the system. The vehicle trials were conducted with deadband compensation applied to the output of the observer

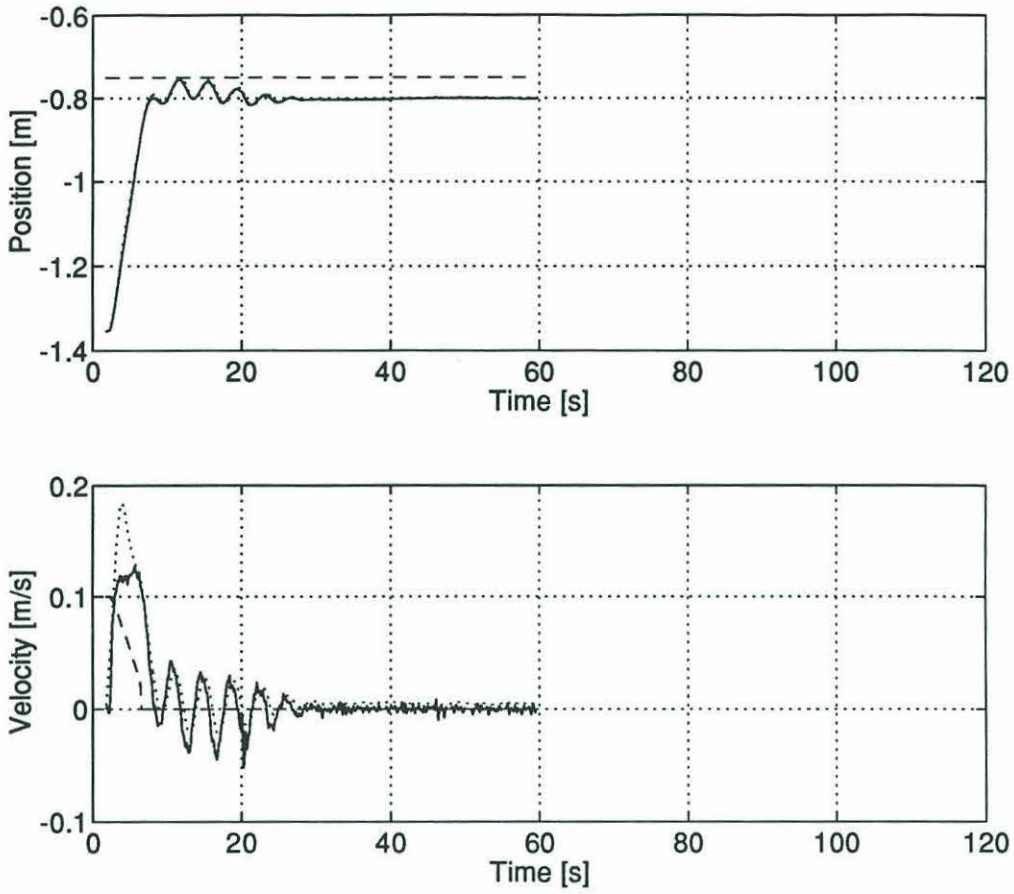

Figure 5.13: VEHICLE TRAJECTORY WITH DELAY, DEADBAND, AND SATURATION COMPENSATIONS AND THE OBSERVER FORCE INPUT ENABLED - The solid lines indicate the SHARPS position and its filtered derivative. The dashed lines mark the desired trajectory of the vehicle and the dotted curves are the state estimates.

controller so that the model was driven by a closer approximation of the actual output of the thrusters. This produces equivalent improvements in the state estimates, but not in the system performance characteristics related to the deadband.

Limit cycle excitation in the compensated, full architecture case persists for 20 s compared to 12 s in the uncompensated, full architecture case. The simulation indicates that the duration will not be reduced by shifting the deadband compensation to the vehicle controller. Peak thruster levels and the extrema of position and velocity deviations during the oscillations are elevated by approximately 30 %. The period of the oscillations is approximately 4 s with peak velocities of 3 cm/s. This yields a Keulegan-Carpenter number of $KC = 0.13$, but the limited number of oscillations

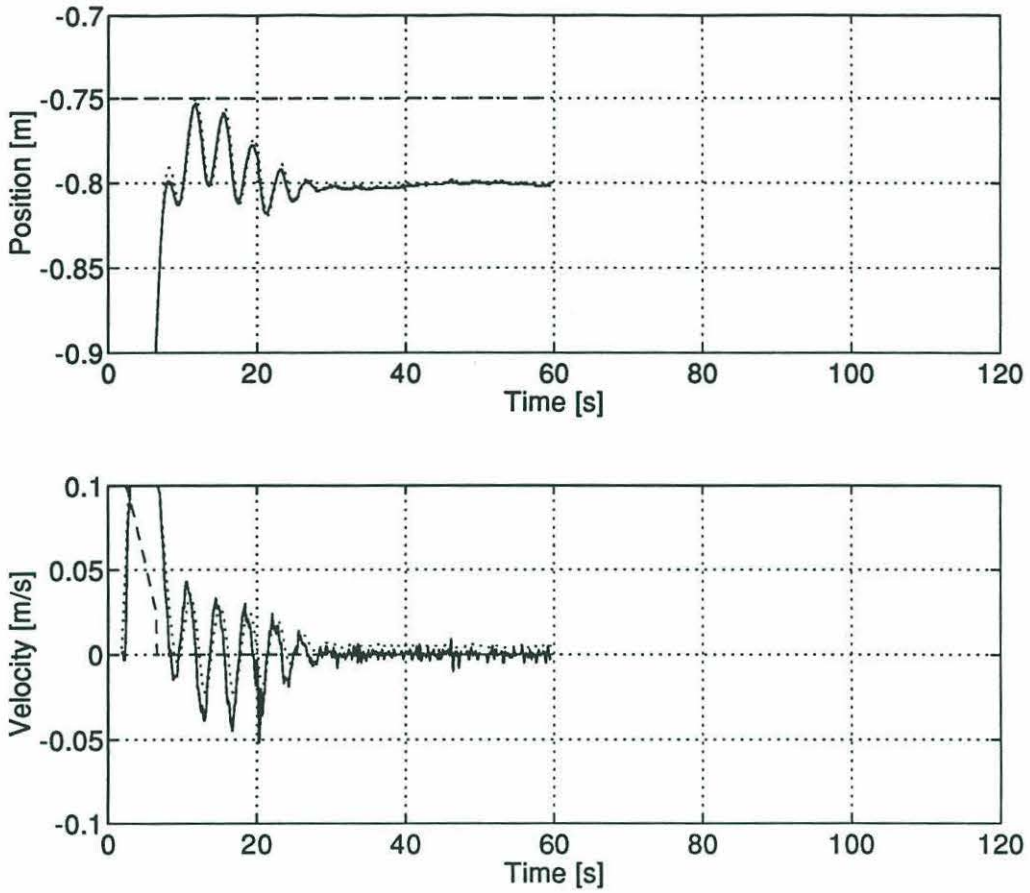

Figure 5.14: CLOSE VIEW OF VEHICLE TRAJECTORY WITH DELAY, DEADBAND, AND SATURATION COMPENSATIONS AND THE OBSERVER FORCE INPUT ENABLED - The solid lines indicate the SHARPS position and its filtered derivative. The dashed lines mark the desired trajectory of the vehicle and the dotted curves are the state estimates. The range of the vertical axes has been restricted for detailed viewing of the traces in Figure 5.13.

make this less relevant. It is interesting to note, however, that the Keulegan-Carpenter number for the sustained limit cycle of the compensated, full architecture simulation run made without environmental forcing (Figure 4.14) was $KC = 0.17$. The simulation indicates that KC increases as mean thrust is reduced; the values show reasonable agreement. Prediction by the simulation of the duration of the excitation (Figure 5.12) is accurate, although the frequency of the excitation is not.

Once steady, the vehicle exhibits a constant 5 cm position error. The error in the uncompensated, full architecture case was 50 % larger (7.5 cm) and exhibited a slow variation about the mean of approximately 1 cm amplitude (Figure 5.2). The

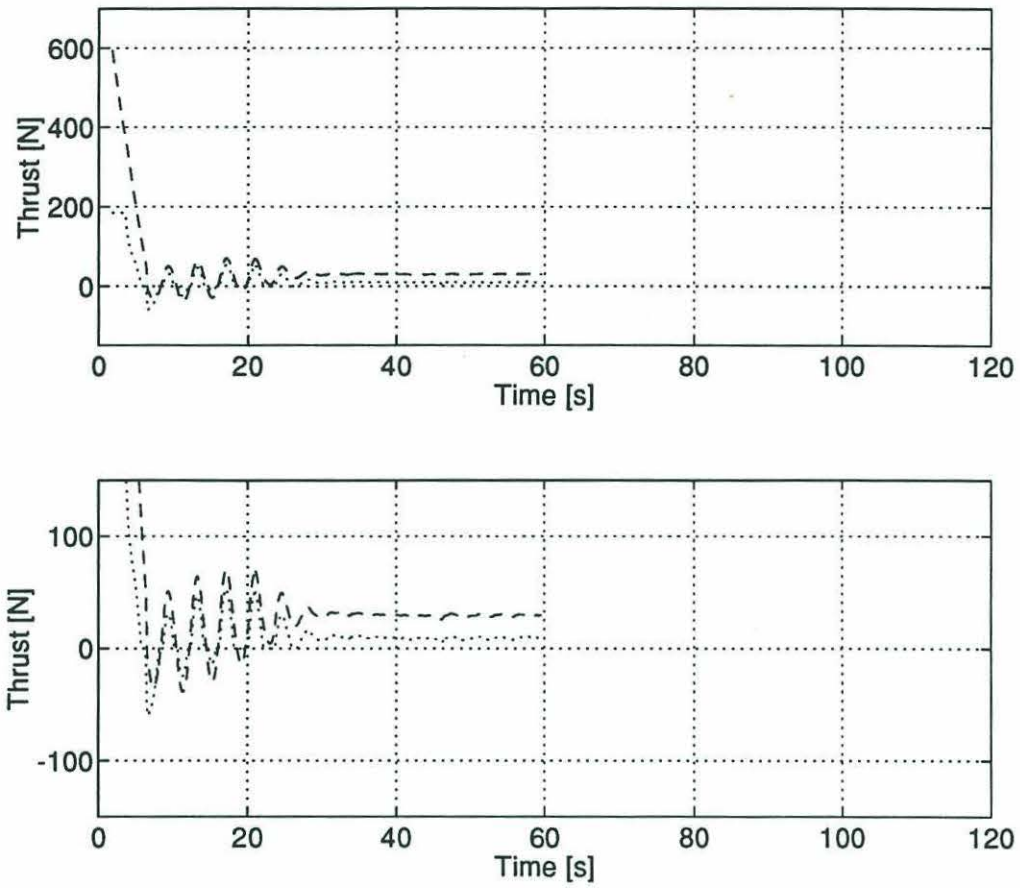

Figure 5.15: ACTUATOR COMMANDS WITH DELAY, DEADBAND, AND SATURATION COMPENSATIONS AND THE OBSERVER FORCE INPUT ENABLED - The dashed lines mark the thrust command sent to the vehicle while the dotted lines show the thrust command sent to the observer. Both plots present the same data set, however, the range of the vertical axis on the second plot is restricted to permit a more detailed inspection.

PD error of the compensated, full architecture system is free of variation. More importantly for this investigation, the state estimates have improved compared to those in the uncompensated, full architecture trial. The constant 0.5 cm error in estimated position during hover has been eliminated. And the 1.5 cm/s error in estimated velocity during hover has been reduced below 0.5 cm/s.

The step response trials have demonstrated that the observer and controller structure developed in this investigation produce a stable and relatively well behaved vehicle system. The basic linear observer provides a significant performance improvement over a simple velocity filter. State estimation and trajectory following are both further

enhanced by compensation for system nonlinearities. These trials also suggest some improvements in the test conditions for future investigation. In particular, more realistic desired trajectories should be used. Neutral buoyancy would also be desirable. This topic will be discussed at greater length in Section 5.4.

5.3.2 Perturbation and Variable Trajectory Trials

Perturbation tests using the horizontal thrusters were limited to two trials. In the first (Figures 5.16 and 5.17), the observer force input and the delay, deadband, and saturation compensations were all disabled. The second test (Figures 5.18 and 5.19) was conducted with all four switchable conditions enabled.[5] The vehicle was commanded to hover at $-0.75\ m$ under closed loop control in each trial. Logging was then initiated and the horizontal thrusters were activated manually using the joystick. The scale of the position and velocity axes is similar to corresponding axes in the "close view" plots of Section 5.3.1. The duration of the runs is one rather than two minutes.

The commanded levels of horizontal thrust are shown in the plots. Forward and reverse thrust were provided by two thrusters mounted port and starboard at the aft end of the vehicle (refer to Figures 2.2 and 2.3). Heading torque and lateral thrust (the latter was not used) were provided by two thrusters mounted forward on the starboard side and aft on the port side. Thrust lines of the lateral and vertical thrusters intersect. Interaction of the vertical thrusters with the aft thrusters is less direct. The positive output of the vertical thrusters caused by the negative buoyancy leaves the wakes continuously vulnerable to interference.

The initial seconds of each run exhibit behaviors already demonstrated by the step response tests. When both the observer force input and the delay compensation are disabled, the system is susceptible to slowly suppressed limit cycle excitation and slow changes in the tracking error during hover. When the observer force input and compensation are enabled, limit cycle excitation is quickly suppressed and the tracking error during hover is constant.

[5] In hindsight, a perturbation test without compensation, but with the structure of the observer intact would have been useful. Unfortunately, no such trial was performed.

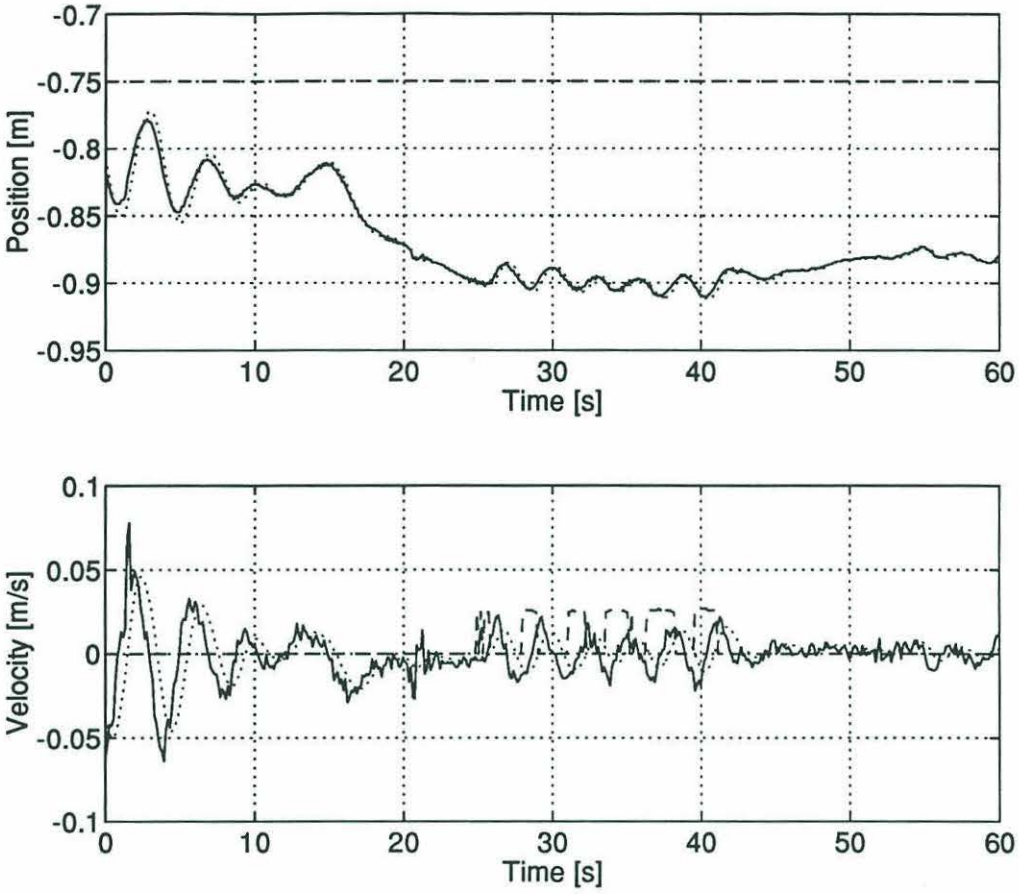

Figure 5.16: VEHICLE TRAJECTORY DURING PERTURBATION TRIAL WITH DELAY, DEADBAND, AND SATURATION COMPENSATIONS AND THE OBSERVER FORCE INPUT DISABLED - The solid lines indicate the SHARPS position and its filtered derivative. The dashed lines mark the desired trajectory of the vehicle and the dotted curves are the state estimates. The oscillations visible in the initial ten seconds of the run are an example of the limit cycle excitation discussed in Section 5.3.1. The vehicle was not able to achieve a steady hover before logging began. The nonzero values of desired velocity visible between 25 *s* and 45 *s* are caused by position excursions beyond the 15 *cm* watch circle around the desired position (Section 5.2).

The trajectory following error of the compensated, full architecture system is smaller and more consistent over the duration of the run. This is most clearly seen in the vertical thrust records (Figures 5.17 and 5.19). The uncompensated, full architecture system is slower to correct the extrema in the tracking error and oscillates several times before achieving a steady offset. The correction of the compensated, full architecture system is faster and monotonic. The difference can be quantified using the 15 *cm* watch circle as the critical boundary. The elapsed time between first

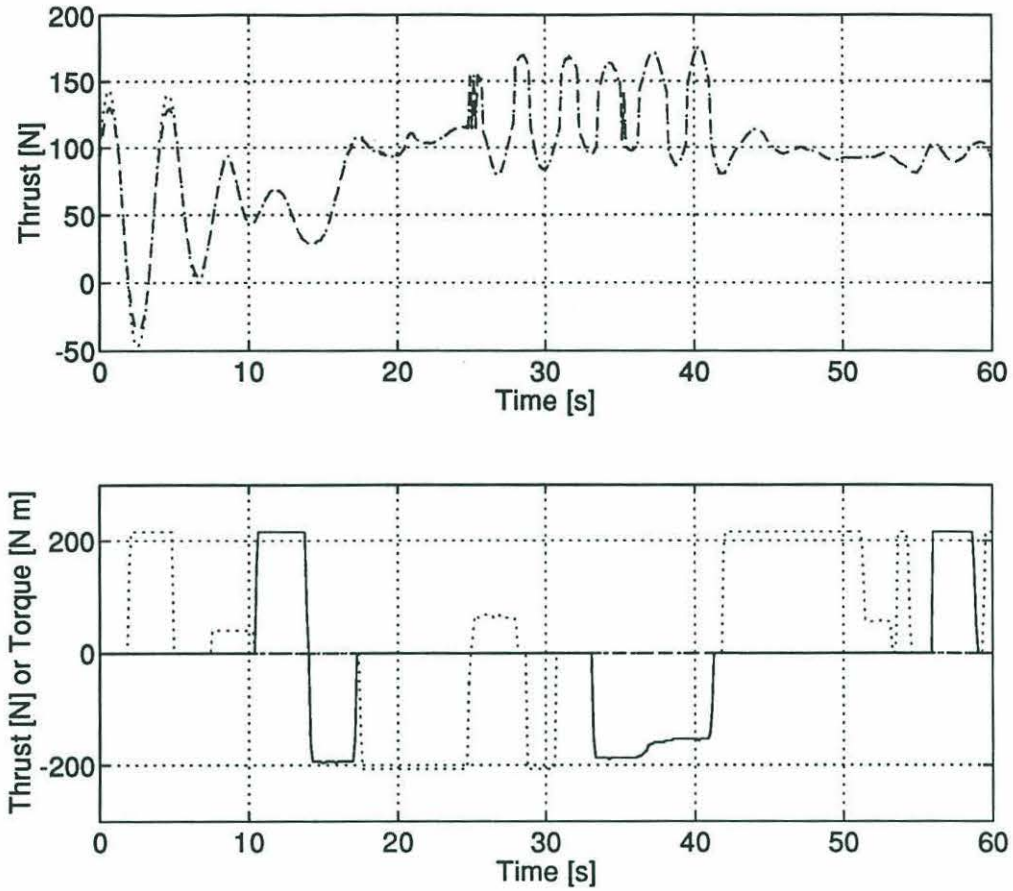

Figure 5.17: ACTUATOR COMMANDS DURING PERTURBATION TRIAL WITH DELAY, DEADBAND, AND SATURATION COMPENSATIONS AND THE OBSERVER FORCE INPUT DISABLED - In the upper plot the dashed lines mark the thrust command sent to the vehicle while the dotted lines show the thrust command sent to the observer. Commanded thrust and torque levels for the horizontal thrusters are recorded in the lower plot. The solid line indicates forward thrust while the dotted line denotes torque about the vertical axis. The dashed line is lateral thrust which was not used. The sudden jumps in commanded thrust levels between 25 s and 45 s are associated with the position excursions beyond the 15 cm watch circle around the desired position (Section 5.2).

passage outside the watch circle and final return inside is 15 s for the uncompensated, full architecture system and 5 s for the compensated, full architecture system. Arguably, a portion of the difference can be attributed to changes in the application of the perturbations. As expected, position estimates in the uncompensated, full architecture system generally follow the SHARPS measurements.

State estimates for the compensated, full architecture system show steady offsets from the SHARPS measurements of approximately 1 cm in position and 2 cm/s

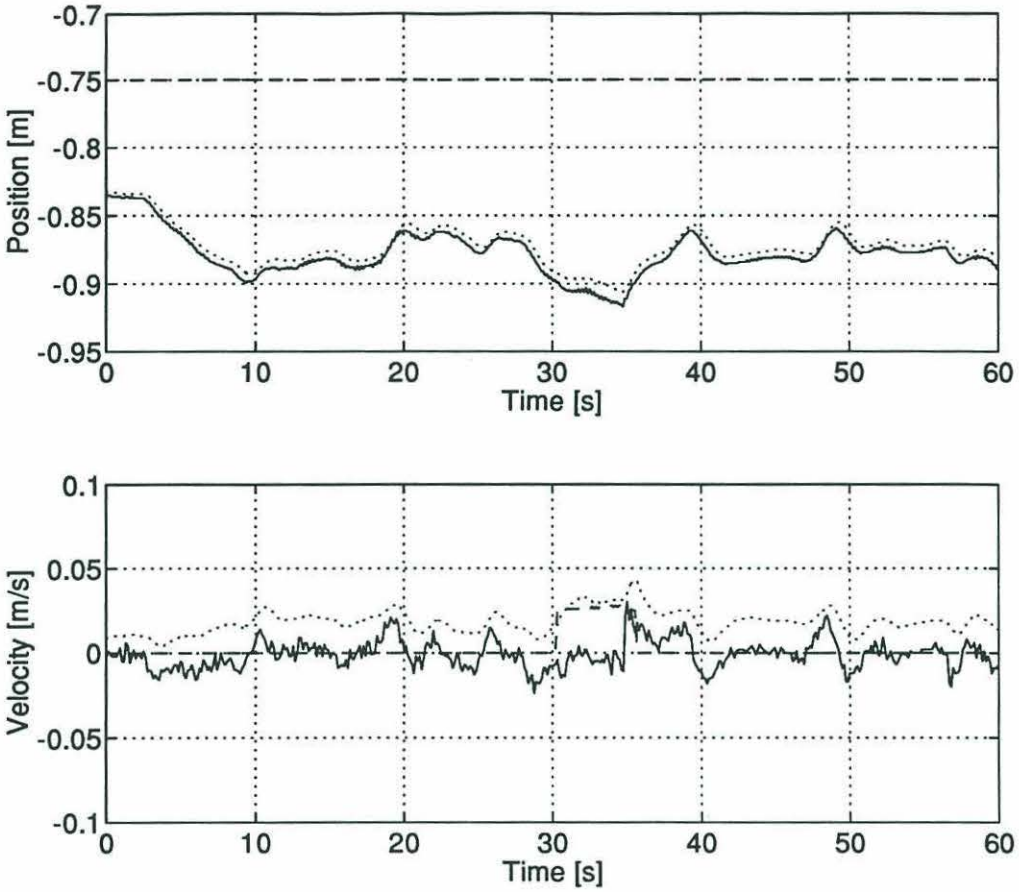

Figure 5.18: VEHICLE TRAJECTORY DURING PERTURBATION TRIAL WITH DELAY, DEADBAND, AND SATURATION COMPENSATIONS AND THE OBSERVER FORCE INPUT ENABLED - The solid lines indicate the SHARPS position and its filtered derivative. The dashed lines mark the desired trajectory of the vehicle and the dotted curves are the state estimates. The vehicle is holding a steady hover when logging begins. The jump in desired velocity from 30 s to 35 s is caused by the position excursion beyond the 15 cm watch circle around the desired position (Section 5.2).

in velocity. The small magnitude of the vehicle velocity implies that the delayed position measurements are fairly accurate. The estimation errors are caused by the character of the perturbation. Because of the wake interaction, the output of the vertical thrusters is less than expected by the system. The primary effect of this deficit is the observable increase in the PD position error. Comparison of the average position error here to the error in Figure 5.14 indicates that the thrust deficit is in the range 20 N to 30 N. The reduced thrust is physically equivalent to adding ballast; the trajectory following error must be larger to balance the environmental forcing.

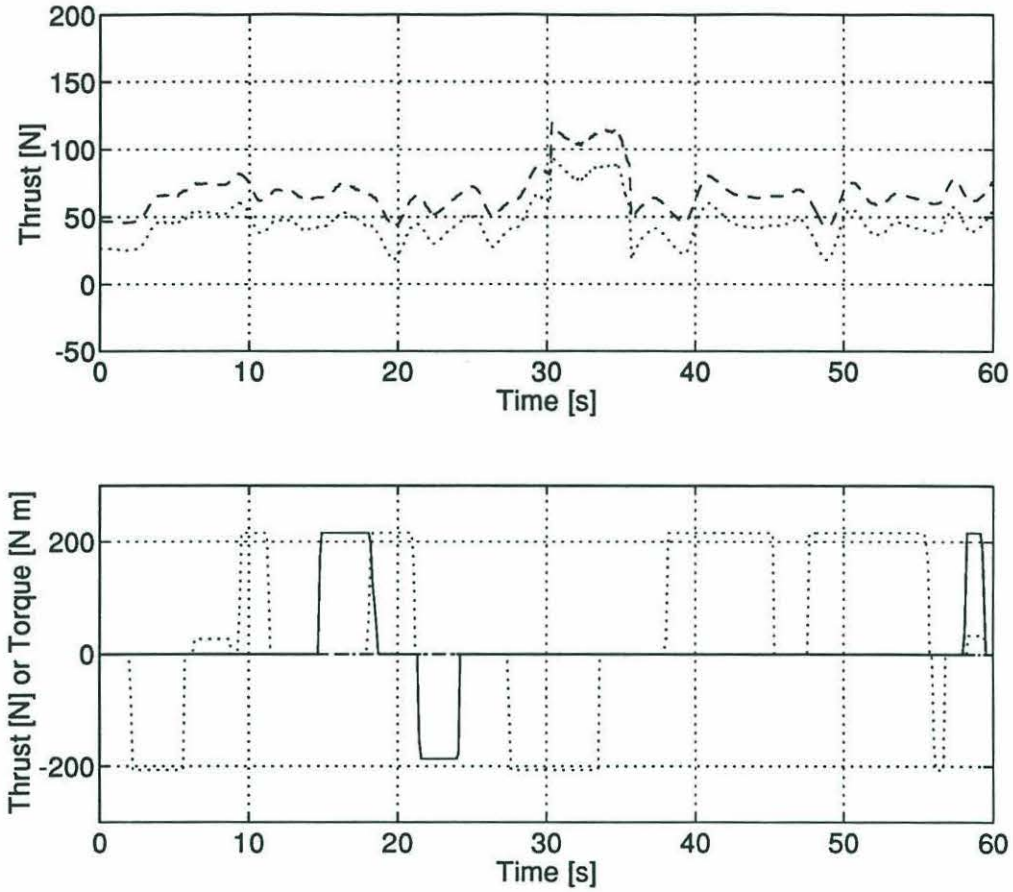

Figure 5.19: ACTUATOR COMMANDS DURING PERTURBATION TRIAL WITH DELAY, DEADBAND, AND SATURATION COMPENSATIONS AND THE OBSERVER FORCE INPUT ENABLED - In the upper plot the dashed lines mark the thrust command sent to the vehicle while the dotted lines show the thrust command sent to the observer. Commanded thrust and torque levels for the horizontal thrusters are recorded in the lower plot. The solid line indicates forward thrust while the dotted line denotes torque about the vertical axis. The dashed line is lateral thrust which was not used. The jump in commanded thrust from 30 *s* to 35 *s* is associated with the position excursion beyond the 15 *cm* watch circle around the desired position (Section 5.2).

The state estimation error is a secondary effect of the thrust deficit. Unlike the deadband, the perturbation thrust deficit is not compensated for by the observer. As a result, the estimator model experiences 20 N to 30 N of upward forcing not applied to the vehicle, driving the model to a position above the vehicle and closer to the desired position. To balance the observer and controller equations, the model acquires a positive average velocity. The estimated velocity has no physical meaning; it is an artifact of balancing the loop to maintain a steady depth. In essence, the

model is fooled by the circumstances. The state estimates simply reflect the balance between model based and measurement based information. The uncompensated, full architecture system has no model to fool, so the uncompensated estimates do not exhibit a constant error. But the compensated, full architecture system, because of the internal balance of the estimator and controller loop, exhibits a smaller trajectory following error and better system performance.

A final run for evaluation of the compensated, full architecture system is presented in Figures 5.20 and 5.21. The vehicle was manually positioned at $-1.3\ m$ and logging was initiated. Closed loop control was then enabled with an initial desired position of $-0.75\ m$. The initial points of the plot traces coincide with the first SHARPS period under closed loop control. The observer force input and the delay, deadband, and saturation compensations were enabled throughout the trial. Changes in the desired position were entered from the keyboard of the PC. The horizontal thrusters were activated with the joystick several times during the final portion of the run.

A new behavior exhibited in this trial is the long overshoot associated with the negative steps in desired position. The negative buoyancy of the vehicle adds constructively to the downward thrust of the actuators during the downward translation. Velocity is greater than expected and the vehicle overshoots. During the positive steps the negative buoyancy adds destructively to the upward thrust and there is no overshoot. As a result there is no ringing during the correction after the downward overshoot. This can be most clearly seen for the downward step near 150 s in the record.[6]

Trajectory following performance of the system is good overall. The path followed by the vehicle indicates physically consistent desired trajectories with velocity ramps and plateaus similar to those used with the simulation are within the performance

[6]The single regime hydrodynamic model used during these trials contributes to the severity of the downward overshoot. Controller output during the translation is based on the hover values of the vehicle parameters as discussed in Section 5.1. The large contribution of the feed forward quadratic drag term is particularly significant because the square law is strongly biased towards the higher velocity downward translation compared to the lower velocity upward correction. The overshoot would be considerably smaller if the two regime hydrodynamic model of the vehicle was used in the observer and controllers.

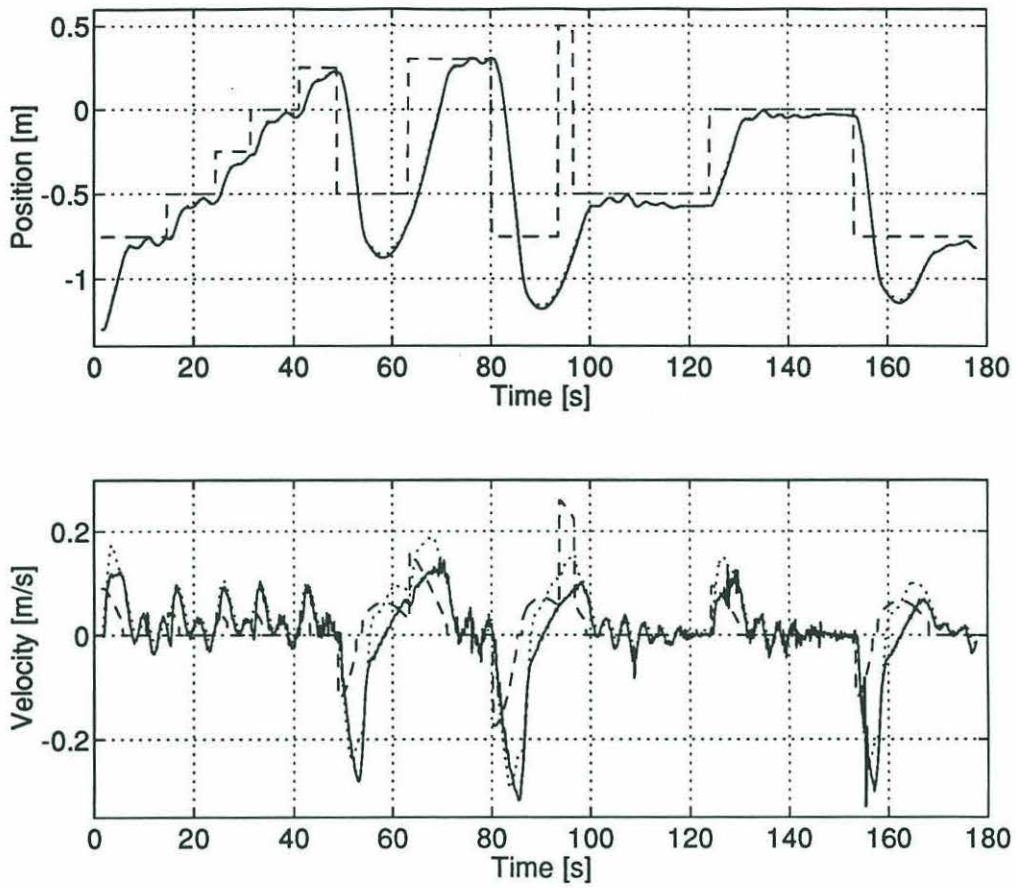

Figure 5.20: VEHICLE TRAJECTORY WITH CHANGING DESIRED TRAJECTORY AND DELAY, DEADBAND, AND SATURATION COMPENSATIONS AND THE OBSERVER FORCE INPUT ENABLED - The solid lines indicate the SHARPS position and its filtered derivative. The dashed lines mark the desired trajectory of the vehicle and the dotted curves are the state estimates.

capabilities of ROV Hylas. State estimates are very good. The magnitude and sign of the difference between the estimated and measured positions is consistent with the velocity, the measurement delay, and the hypothesized state estimate logging delay (Figure 5.22). Position estimates appear to be accurate with an error less than 1 *cm*.

5.4 Conclusions

The most important qualities demonstrated by the vehicle trials are system stability and the ability of the vehicle to follow a trajectory under closed loop control. The ability of the observer and controller algorithms developed during this investigation to

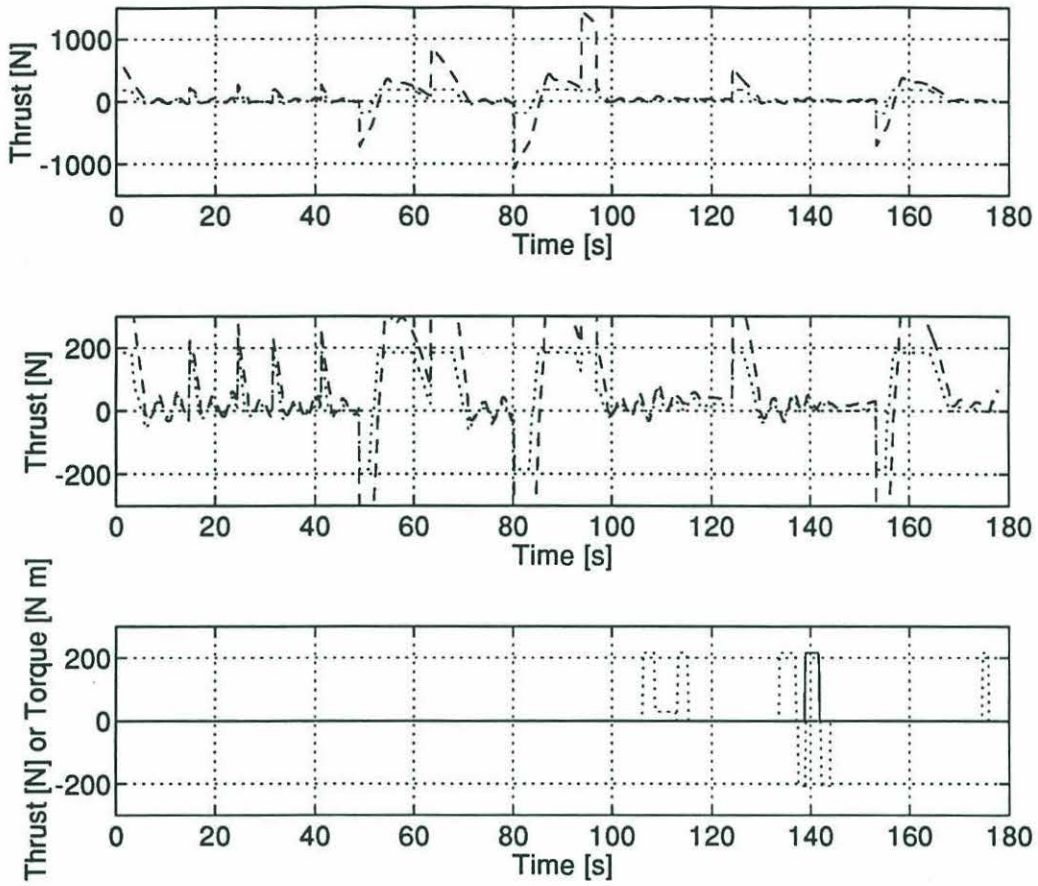

Figure 5.21: ACTUATOR COMMANDS WITH CHANGING DESIRED TRAJECTORY AND DELAY, DEADBAND, AND SATURATION COMPENSATIONS AND THE OBSERVER FORCE INPUT ENABLED - In the upper two plots the dashed lines mark the thrust command sent to the vehicle while the dotted lines show the thrust command sent to the observer. Both plots present the same data set, however, the range of the vertical axis on the second plot is restricted to permit a more detailed inspection. Commanded thrust and torque levels for the horizontal thrusters are recorded in the lower plot. The solid line indicates forward thrust while the dotted line denotes torque about the vertical axis. The dashed line is lateral thrust which was not used.

control an underwater vehicle has been demonstrated empirically. These trials have confirmed the fundamental importance of the observer force input in the underlying linear structure of the algorithms in reducing the effects of the thruster limit cycle. They have also shown that system performance is significantly improved by compensating for the nonlinearities inherent in the system. Because the state estimator is independent of the controller, fully nonlinear control algorithms, such as sliding mode control, can replace the existing PD control modules with relative ease. More

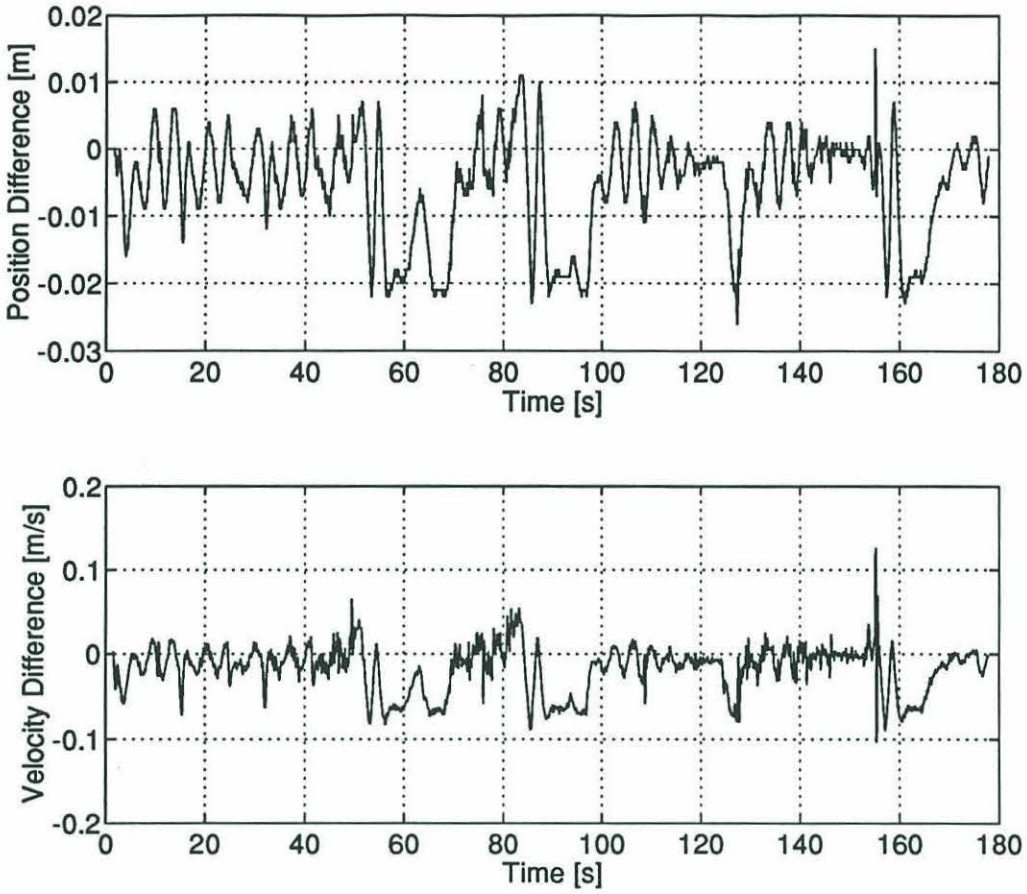

Figure 5.22: POSITION AND VELOCITY DIFFERENCES WITH CHANGING DESIRED TRAJECTORY AND DELAY, DEADBAND, AND SATURATION COMPENSATIONS AND THE OBSERVER FORCE INPUT ENABLED - The curves mark the difference between the SHARPS measurement and the state estimate, $\mathbf{x}_{measured} - \hat{\mathbf{x}}$. The traces are consistent with the velocity, the measurement delay, and the hypothesized state estimate logging delay.

advanced control protocols also require the full state of the vehicle and the trials presented here demonstrate that the described observer can provide that input with satisfactory accuracy.

The vehicle trials have also shown that the vehicle simulation described in Chapter 4 is an accurate test platform for investigations of system behavior. Extensive preliminary evaluation of observer and controller algorithms can be accomplished quickly and inexpensively on the computer. The results have a high degree of qualitative accuracy and good quantitative accuracy during static and steady motions. Greater dynamic accuracy will require a more detailed hydrodynamic model of the

vehicle. For example, detailed measurements of the time evolution of the hydrodynamic parameters during uniform acceleration and deceleration would be useful. Accurate measurements of the drag for a range of steady velocities to confirm that portion of the model would also be desirable. However, the added benefits of a significantly extended model would probably be outweighed by the effort required by the experiments. Ultimately, the vehicle is the test platform that matters.

Although system stability and closed loop control have been demonstrated, several further experiments are suggested. To confirm and improve upon the observations made here, trials should be conducted with the ballasting of ROV Hylas adjusted for neutral buoyancy. More realistic desired trajectories with physically consistent position and velocity components should be used. The trajectory used for simulation runs, suitably adjusted for the confines of the test tank, is one example. Velocity ramps, steady translation, and hover are all within the physical capabilities of ROV Hylas. Additionally, the final results of the system identification procedure should be incorporated in the observer and controllers, and the compensation suite employed in the simulation should be evaluated. In particular, the potential performance enhancement of deadband compensation in the vehicle controller should be tested. Finally, as suggested for the system identification procedure and the simulation, the state estimator should be expanded to four degrees of freedom.

Chapter 6

Conclusion

A full accounting of the conclusions drawn from this research and suggested directions for continued investigation can be found in the preceding chapters. Section 6.1 provides an overview of the work summarizing the important results. Section 6.2 similarly summarizes the main areas where work remains to be done.

6.1 Summary and Conclusions

The investigation documented in this thesis focuses on the development of an accurate and stable state estimator for an underwater vehicle. Full state information is used to close a control loop around the vehicle. The control loop can enhance vehicle performance and is essential for autonomous and semiautonomous operation.

Developing the state estimator and closing a stable, well behaved control loop around ROV Hylas required an accurate hydrodynamic model of the vehicle. The model is an integral part of the observer equation and is also used when designing the controller and during the calculation of observer and controller gains. The system identification of ROV Hylas was accomplished using the technique of numerical minimization. The development of this method is described in Chapter 2. Numerical minimization is well suited to the study of underwater vehicles. Several capabilities recommend it, most notably flexibility in evaluating different models, including those with multiple degrees of freedom and coupling.

When this approach was applied to ROV Hylas for the oscillatory flow regime of the hover limit cycle, the vehicle was shown to have an effective mass three times the size of the dry mass and a large viscous drag term that is quadratic in velocity. The form of the model is given by

$$F = (1 + C_M^*)m\dot{U} + \frac{1}{2}\rho A C_D^* U|U| \tag{2.1}$$

where m is the dry mass of the vehicle and A is the projected area along the direction of motion. U is the relative velocity between fluid and vehicle and ρ is fluid density. Forcing is denoted by F. The dimensionless coefficients of added mass and quadratic drag, as determined by numerical minimization are

$$\begin{aligned} C_M^* &= 2 \\ C_D^* &= 8. \end{aligned} \tag{2.26}$$

These results are well supported by the work of other researchers and show that vehicles with structural similarity to ROV Hylas possess strong hydrodynamic similarity to a rough cylinder.

Observer and controller algorithms are described in Chapter 3. The algorithms are based on a two regime hydrodynamic model of the vehicle. The multiple flow regime architecture of the observer and controllers and the flexible numerical minimization approach to hydrodynamic modelling are arguably the most important products of this investigation. The algorithms also compensate for other portions of the vehicle system, most notably the measurement delay and the thrusters. Compensation is incorporated into an underlying linear architecture. A dual controller structure was adopted to provide suitable force inputs to the vehicle and the observer. The vehicle controller adds a feed forward quadratic drag term and thruster deadband compensation to a PD control law that is based on a linear model of the system. The observer controller uses the same PD control law passed through a thruster saturation filter. These and other compensations are intended to improve the state estimates and enhance vehicle performance and system stability.

The vehicle system was then tested in simulation. There it is possible to freely vary the structure and parameters of the system and evaluate the resulting performance and stability (Chapter 4). The tests indicated that the proposed observer and controller architecture is stable and well behaved. The results also indicated that the full architecture of the observer is essential to the reduction of limit cycle effects and that compensation for the nonlinearities improves both the state estimates and the tracking performance of the vehicle. The fully compensated system with complete observer architecture compares favorably with a system enjoying perfect state information for feedback. Vehicle trials demonstrated the high degree of qualitative and quantitative accuracy of which the simulation is capable. The simulation can fairly be regarded as a preliminary test platform for the evaluation of alternative observer and controller algorithms.

Vehicle trials were used for final evaluation of the observer and controllers (Chapter 5). The algorithms were used to guide ROV Hylas along several desired trajectories while the structure and parameters of the system were varied. The underlying linear structure was shown to provide stable control of the vehicle. The importance of the observer force input was confirmed and compensation for the nonlinearities was shown to enhance the trajectory following and state estimator performance. The system, as designed, is well behaved and provides a high level of performance during autonomous or semiautonomous operation.

6.2 Directions for Continued Research

Initial efforts should focus on additional vehicle trials. These are required to test the results of the completed analysis of the system identification data, the two regime observer and controller architecture, and the full suite of nonlinear compensations. The tests should employ more realistic desired trajectories than those used here, with physically consistent position and velocity components. Trials may still reasonably be restricted to the test tank at this stage.

The most fruitful direction to be taken is the extension of the system identification

procedure, the simulation, and the observer and controller algorithms to four degrees of freedom. Numerical minimization should be applied to a larger selection of hydrodynamic regimes for use in the system software and in the simulation. These regimes should include steady translations and uniform accelerations and decelerations. After software verification in the test tank, vehicle trials should be transferred to the less restrictive and more challenging dockside environment. Desired trajectories for these trials should combine motions in all four degrees of freedom.

When four degree of freedom vehicle trials are successfully completed, the algorithms and procedures documented in this thesis may be applied to operational vehicles for use in the ocean.

Appendix A

System Identification Results

This appendix contains figures and tables summarizing the results of the nine ROV Hylas system identification runs. The figures and table presented for each run are equivalent to Figures 2.8, 2.9, 2.10, 2.11, 2.12, and Table 2.1 in Chapter 2 of the text.

The ranges of the time, position, and velocity axes of the trajectory plots have been tailored for each individual run to minimize the loss of graphic resolution that would result if a common set of axes were used for all data sets. However, the four models associated with each run share a common set of axes to facilitate comparison between models. The case made in Chapter 2 for both the analysis and its conclusions was illustrated using the trajectory of run 2bp3. All of the important features of the model trials for that run can be found to varying degrees in the trials of the other runs presented here. In the shorter runs, some features may be less dramatic. However, given a model, the shorter runs demonstrate that only a few oscillations are needed for an accurate determination of the hydrodynamic parameters. As discussed in Chapter 2, this makes the technique robust to a more heavily damped system and a simpler experimental apparatus than other methods.

The runs are marked with codes such as 2bp1, 1b2, or 2bs3. The first digit indicates the number of springs used. The "b" character indicates the spring model and is the same in all cases. A "p" or "s", if present, indicates that the springs were arranged in "parallel" or "series". The final digit is the trial number with that spring arrangement.

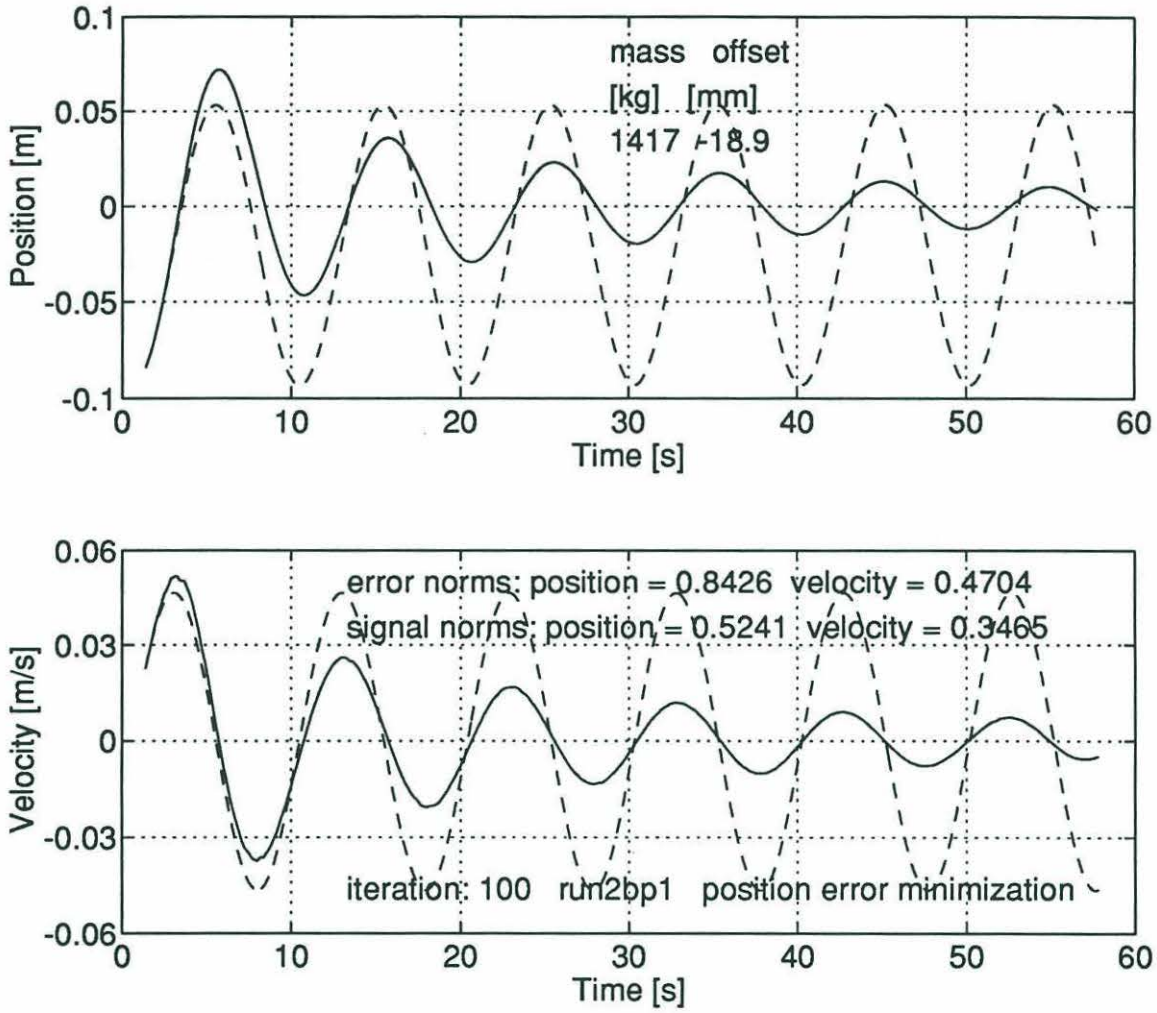

Figure A.1: NUMERICAL MINIMIZATION - INERTIA MODEL - RUN 2BP1 - The vehicle trajectory is marked by the solid line. The dashed trace is the path followed by the model.

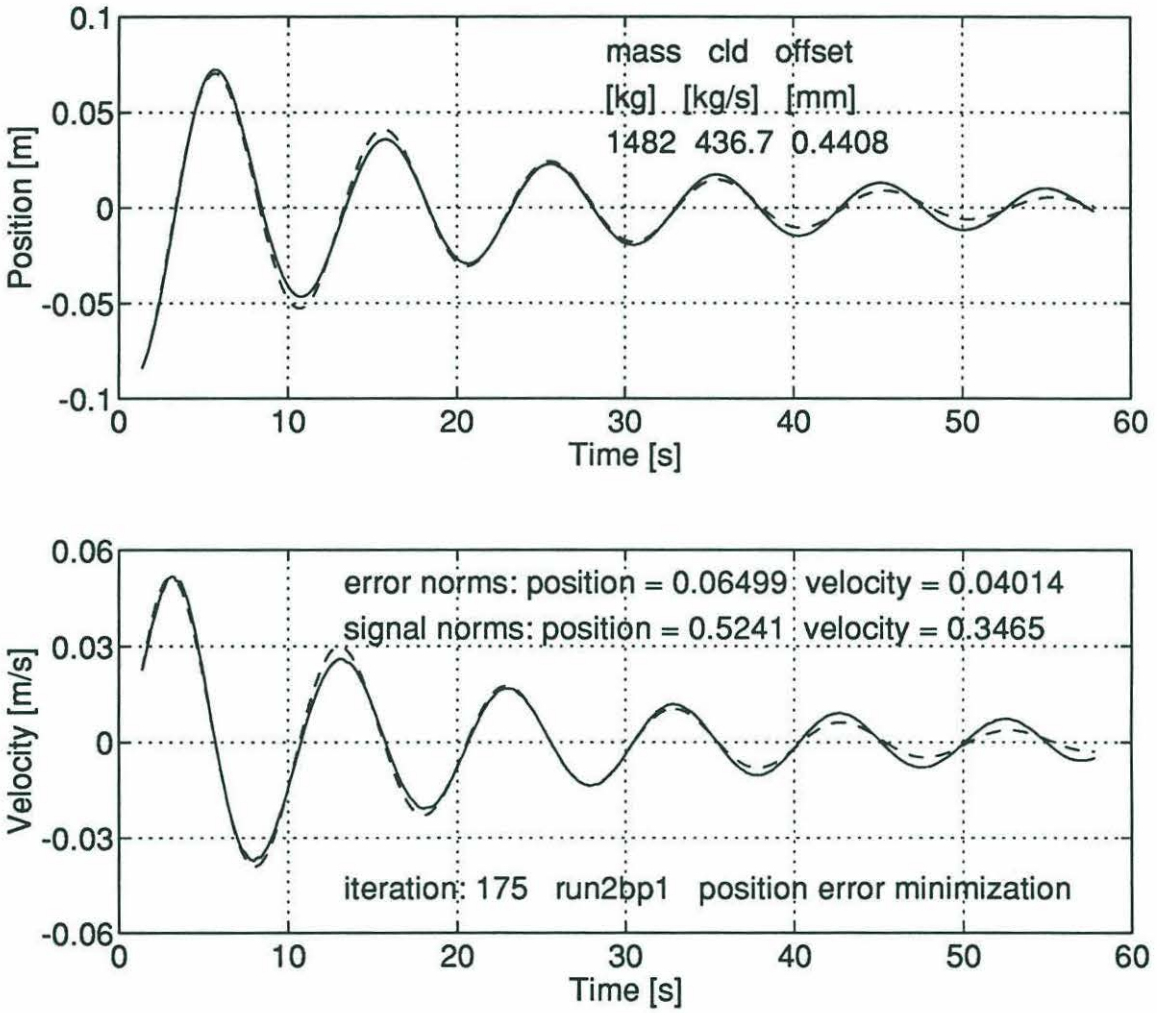

Figure A.2: NUMERICAL MINIMIZATION - INERTIA WITH LINEAR DRAG MODEL - RUN 2BP1 - The vehicle trajectory is marked by the solid line. The dashed trace is the path followed by the model.

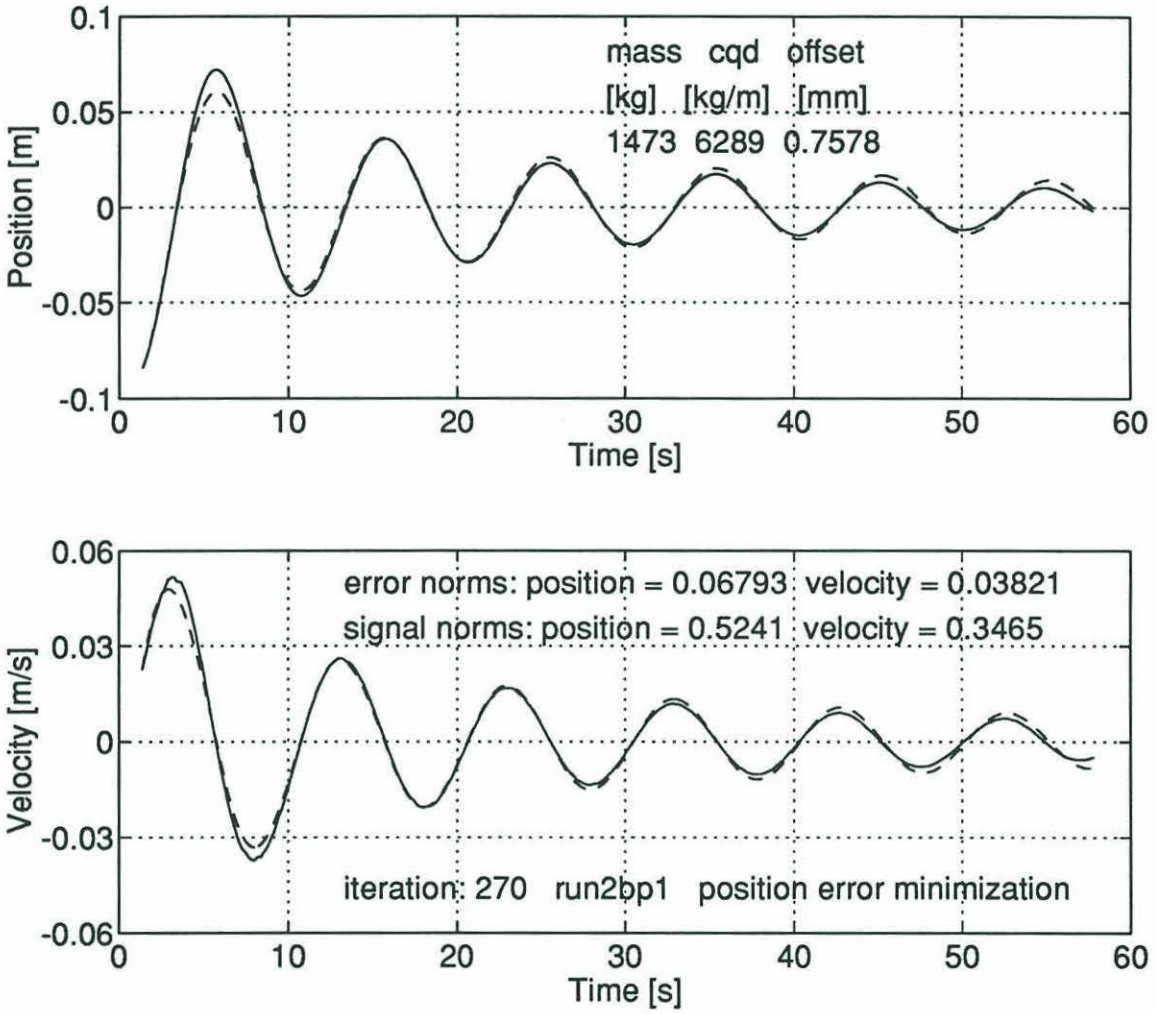

Figure A.3: NUMERICAL MINIMIZATION - INERTIA WITH QUADRATIC DRAG MODEL - RUN 2BP1 - The vehicle trajectory is marked by the solid line. The dashed trace is the path followed by the model.

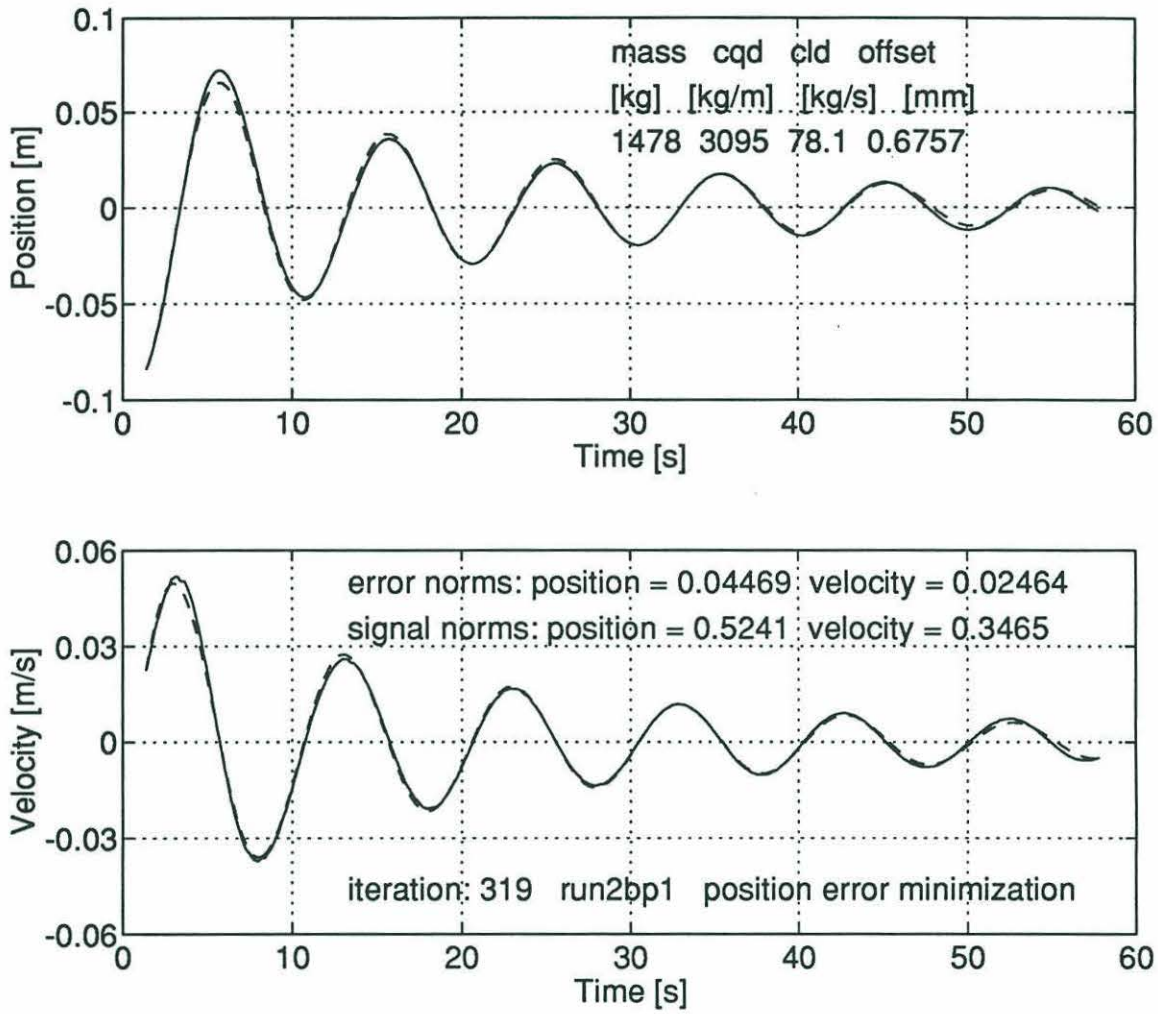

Figure A.4: NUMERICAL MINIMIZATION - INERTIA WITH QUADRATIC AND LINEAR DRAG MODEL - RUN 2BP1 - The vehicle trajectory is marked by the solid line. The dashed trace is the path followed by the model.

Model	m_{eff} $[kg]$	c_{qd} $[kg/m]$	c_{ld} $[kg/s]$	F_{spring}	$F_{inertia}$	F_{q-drag}	F_{l-drag}
				$[N]$			
inertia	1417			14.77	13.74		
inertia with linear drag	1482		437	14.77	14.38		7.12
inertia with quadratic drag	1473	6289		14.77	14.29	1.67	
inertia with quadratic and linear drag	1478	3095	78	14.77	14.34	.82	1.27

Table A.1: RUN 2BP1 - Two springs in parallel, effective spring constant: 597.9 N/m.

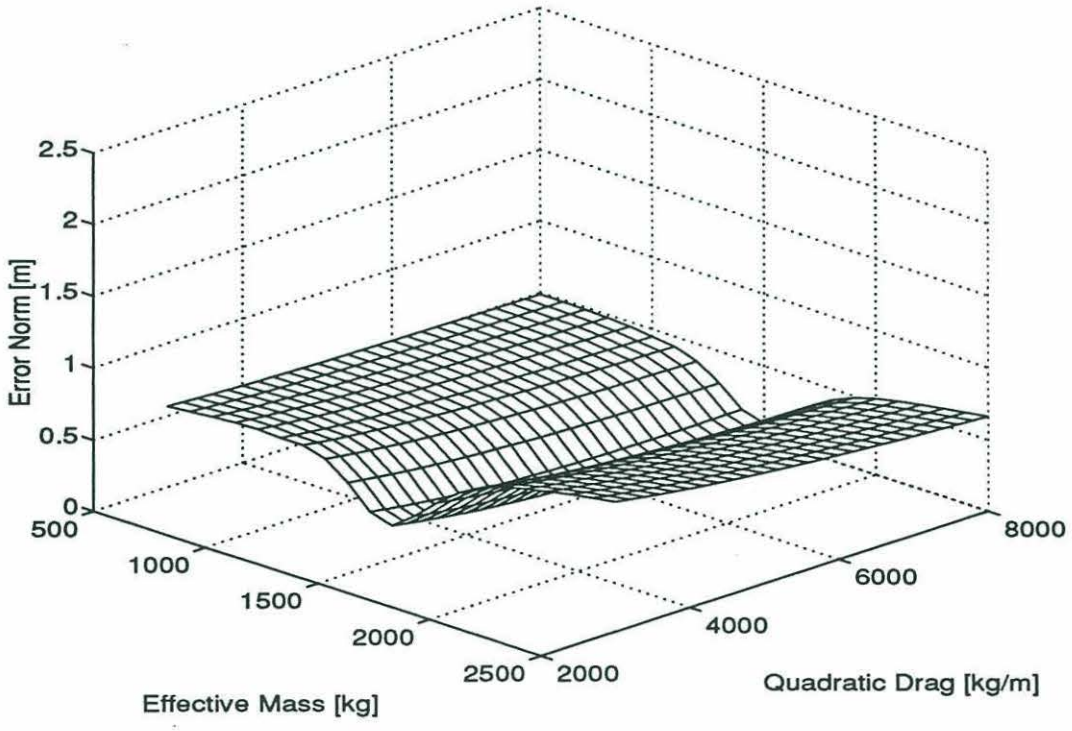

Figure A.5: ERROR NORM SURFACE FOR THE INERTIA WITH QUADRATIC DRAG MODEL AND VEHICLE TRAJECTORY 2BP1

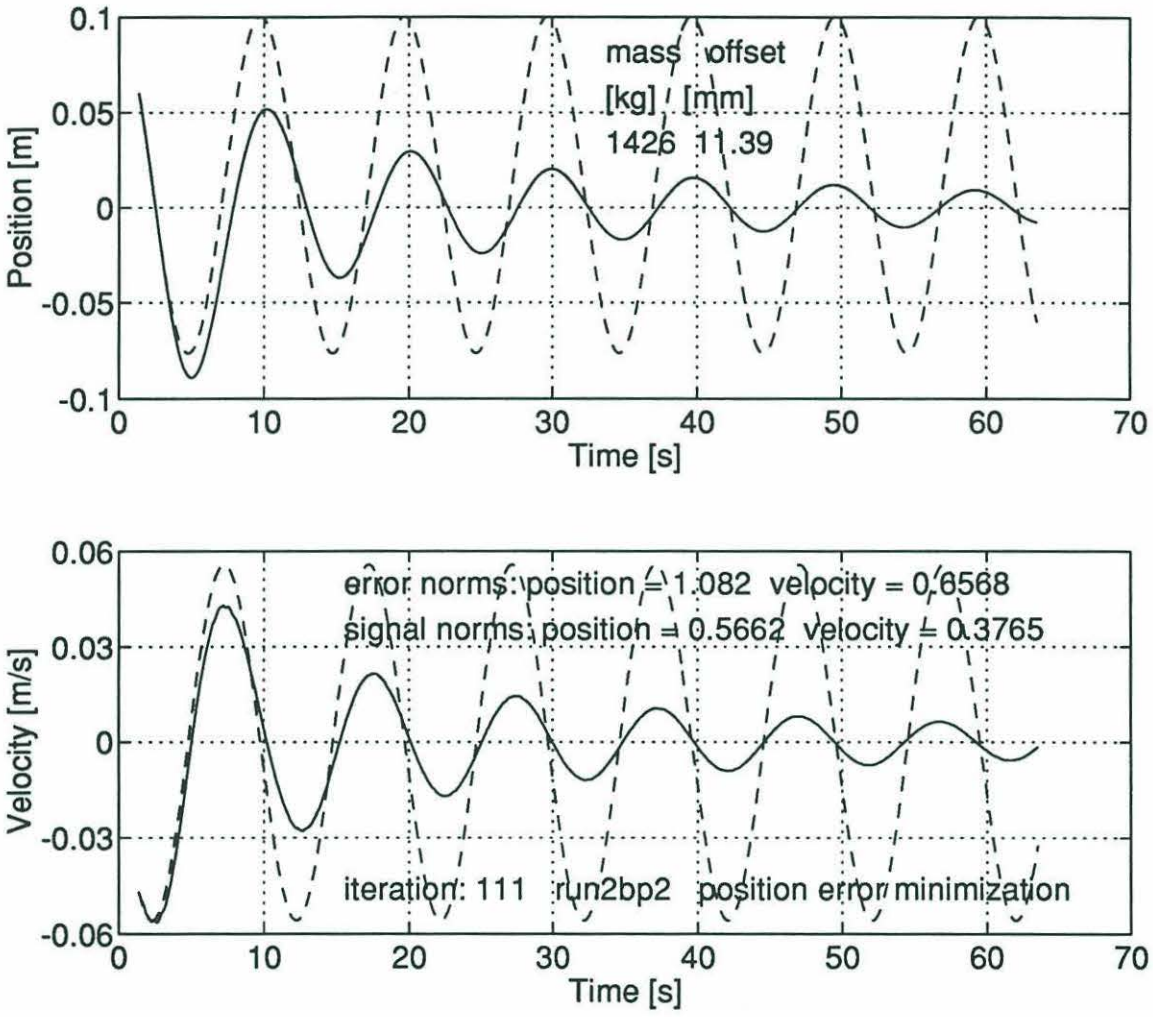

Figure A.6: NUMERICAL MINIMIZATION - INERTIA MODEL - RUN 2BP2 - The vehicle trajectory is marked by the solid line. The dashed trace is the path followed by the model.

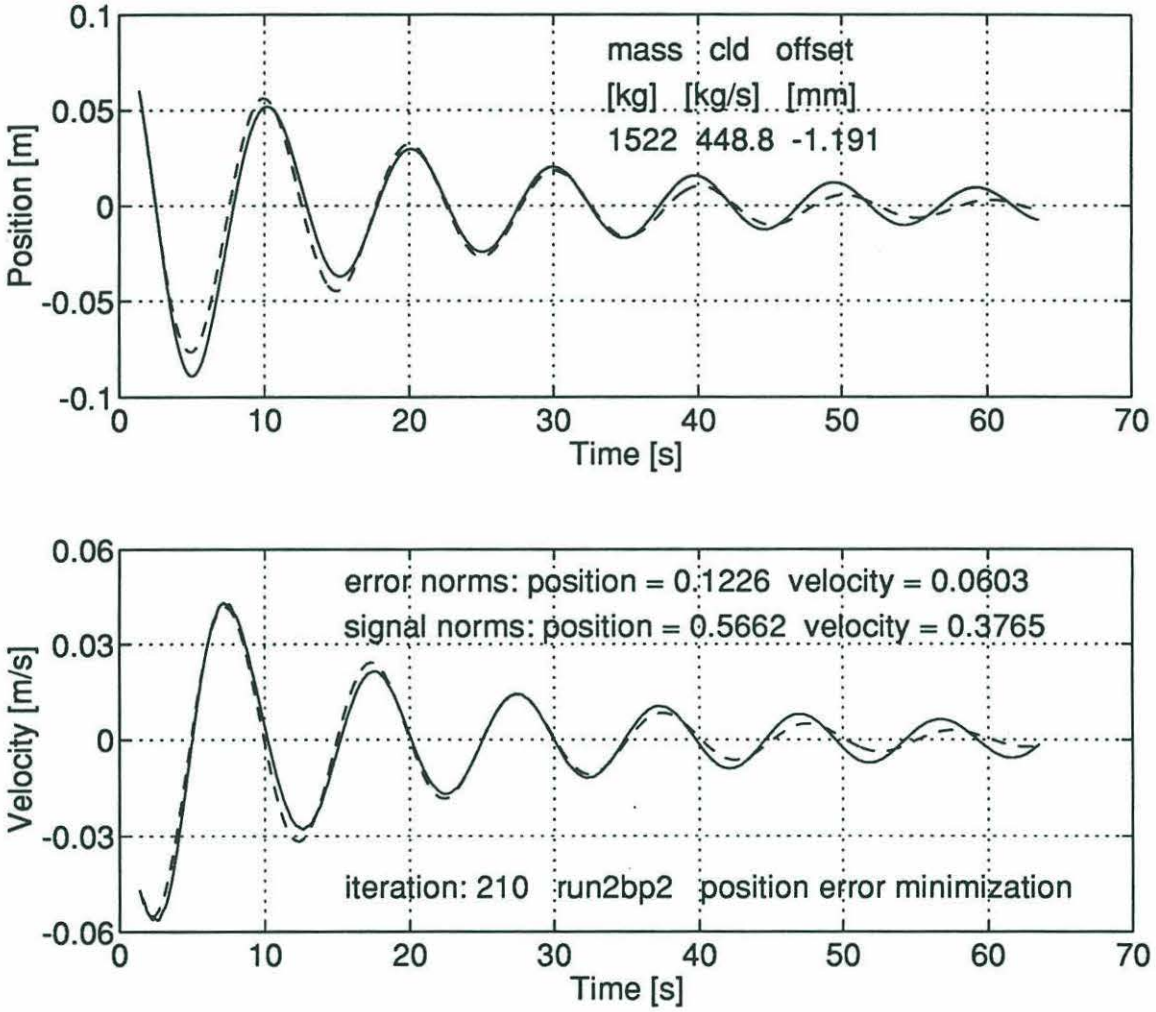

Figure A.7: NUMERICAL MINIMIZATION - INERTIA WITH LINEAR DRAG MODEL - RUN 2BP2 - The vehicle trajectory is marked by the solid line. The dashed trace is the path followed by the model.

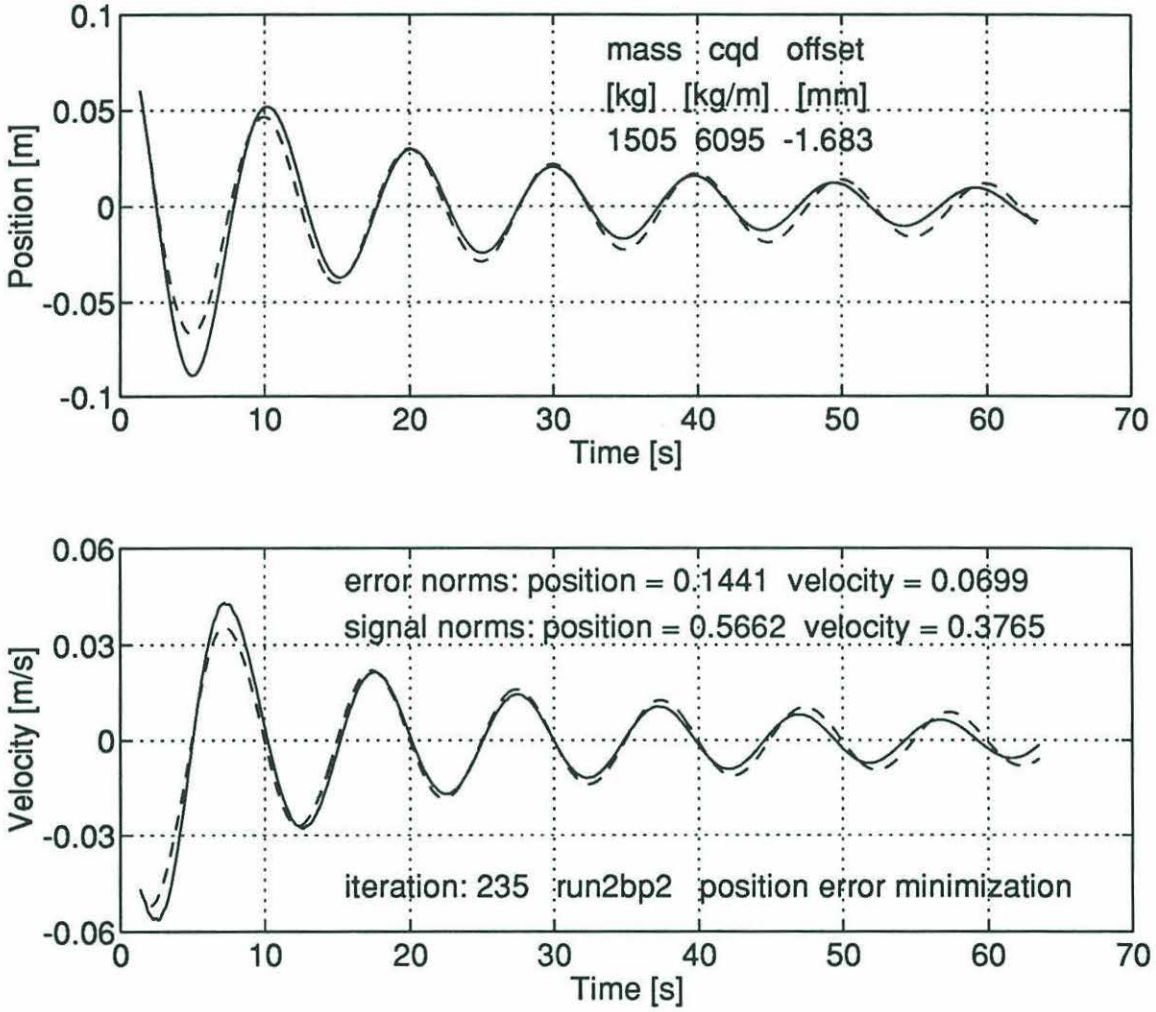

Figure A.8: NUMERICAL MINIMIZATION - INERTIA WITH QUADRATIC DRAG MODEL - RUN 2BP2 - The vehicle trajectory is marked by the solid line. The dashed trace is the path followed by the model.

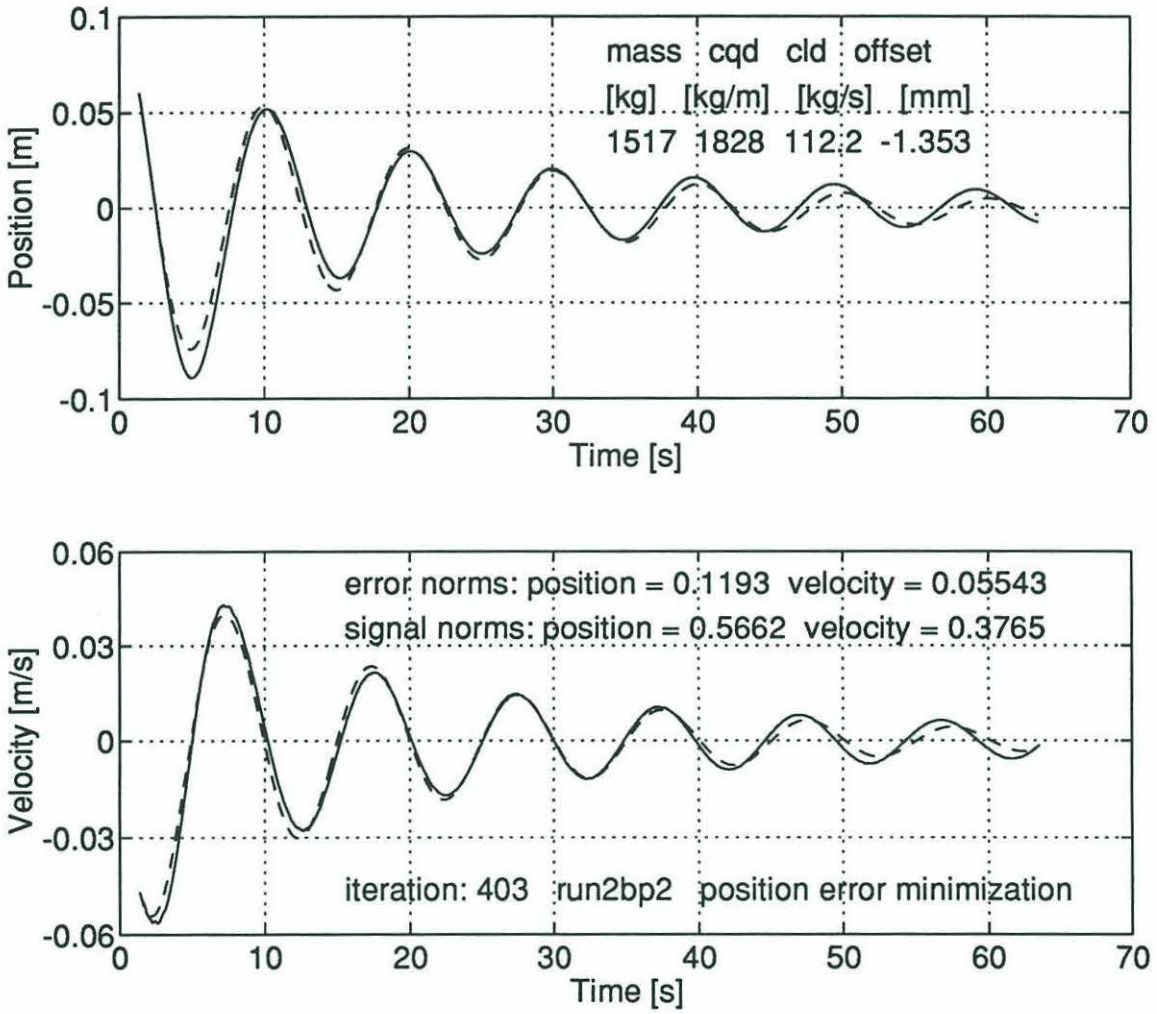

Figure A.9: NUMERICAL MINIMIZATION - INERTIA WITH QUADRATIC AND LINEAR DRAG MODEL - RUN 2BP2 - The vehicle trajectory is marked by the solid line. The dashed trace is the path followed by the model.

Model	m_{eff} $[kg]$	c_{qd} $[kg/m]$	c_{ld} $[kg/s]$	F_{spring}	$F_{inertia}$	F_{q-drag}	F_{l-drag}
				$[N]$			
inertia	1426			15.07	13.69		
inertia with linear drag	1522		449	15.07	14.61		7.54
inertia with quadratic drag	1505	6095		15.07	14.45	1.72	
inertia with quadratic and linear drag	1517	1828	112	15.07	14.56	.52	1.89

Table A.2: RUN 2BP2 - Two springs in parallel, effective spring constant: 597.9 N/m.

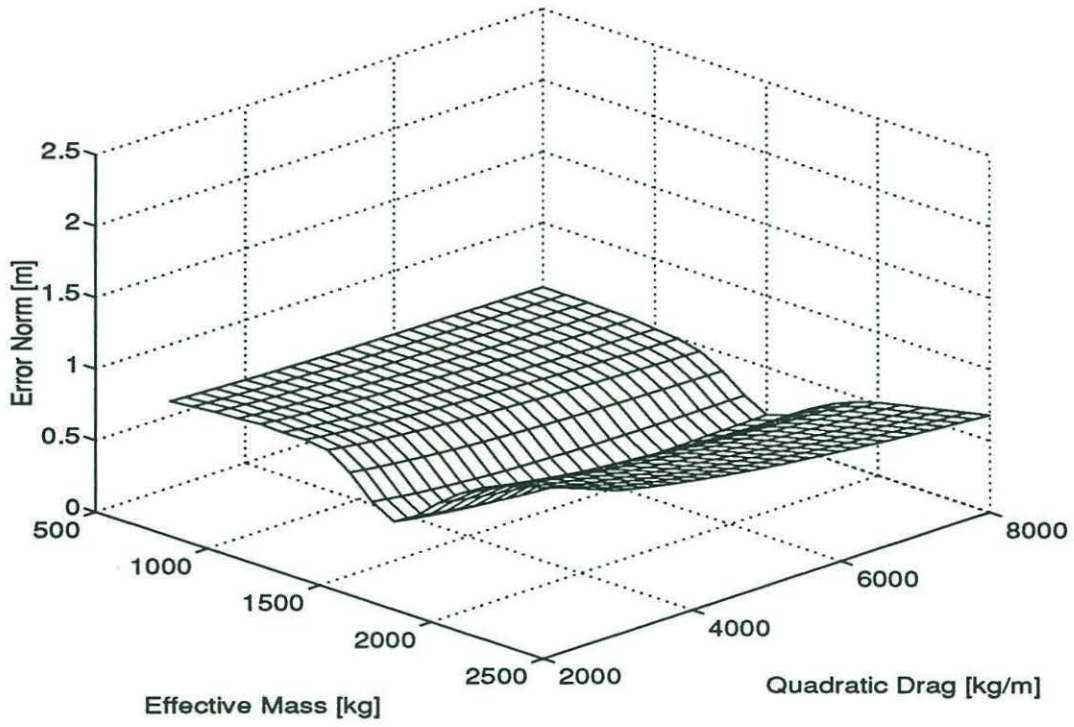

Figure A.10: ERROR NORM SURFACE FOR THE INERTIA WITH QUADRATIC DRAG MODEL AND VEHICLE TRAJECTORY 2BP2

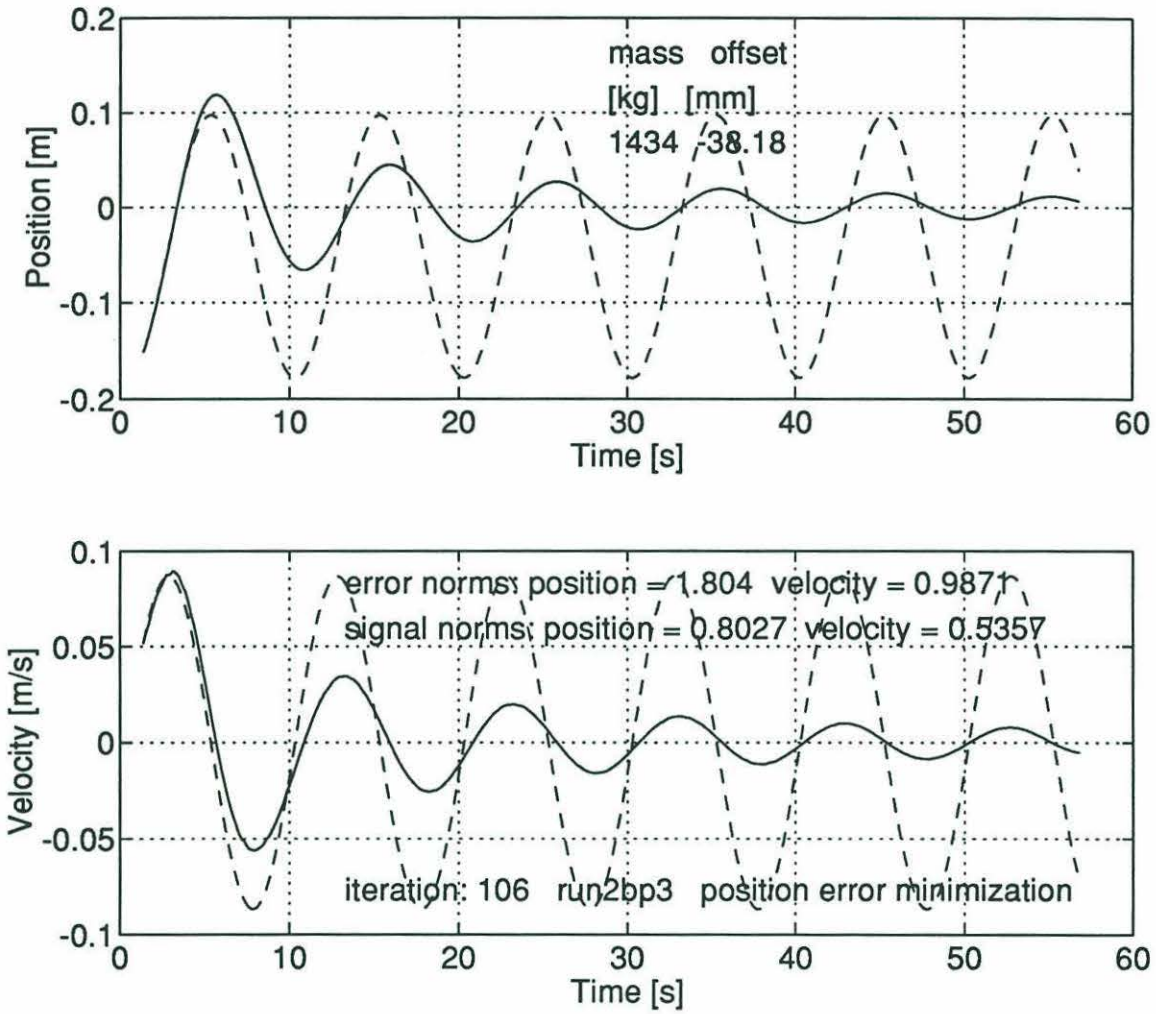

Figure A.11: NUMERICAL MINIMIZATION - INERTIA MODEL - RUN 2BP3 - The vehicle trajectory is marked by the solid line. The dashed trace is the path followed by the model.

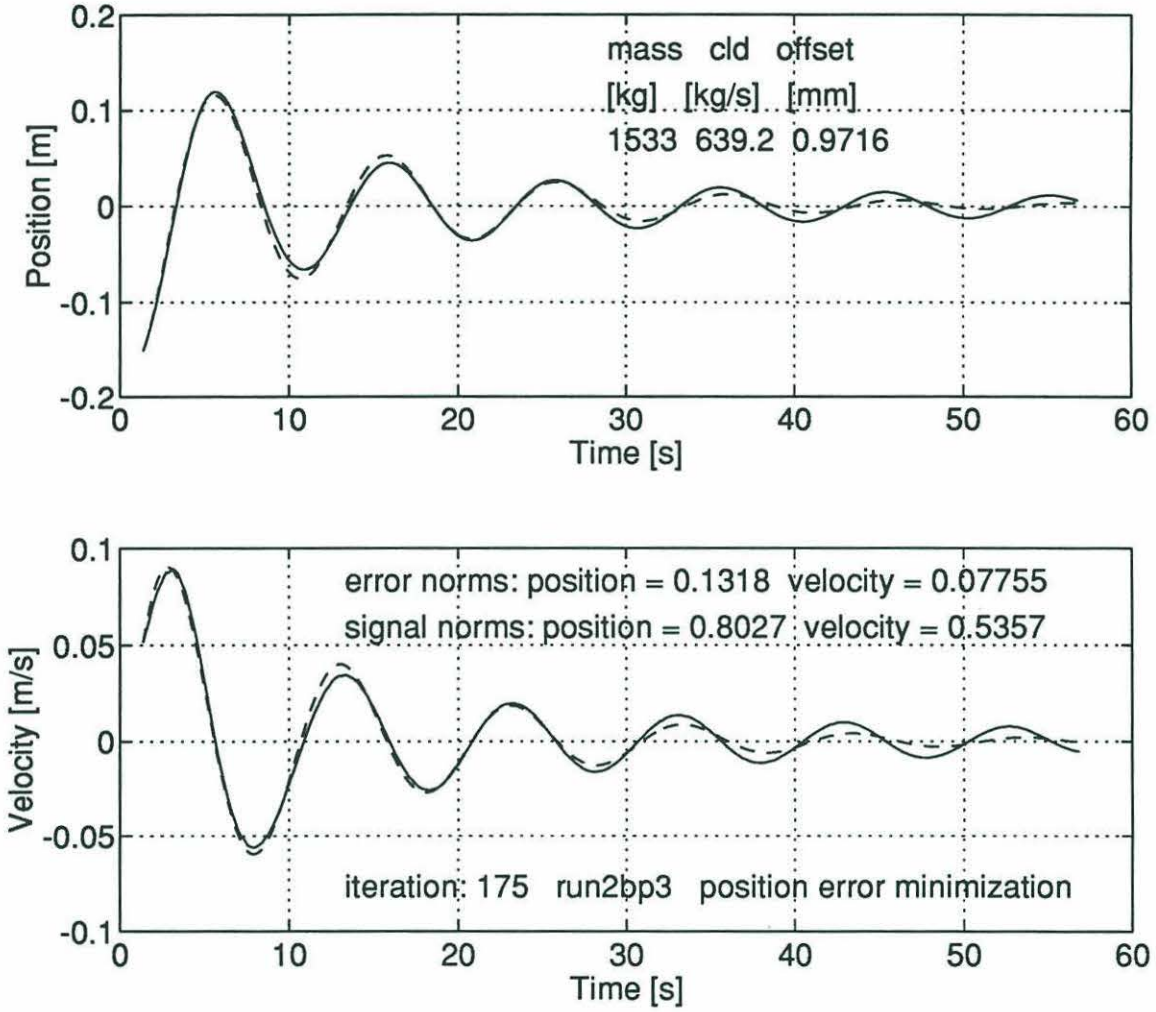

Figure A.12: NUMERICAL MINIMIZATION - INERTIA WITH LINEAR DRAG MODEL - RUN 2BP3 - The vehicle trajectory is marked by the solid line. The dashed trace is the path followed by the model.

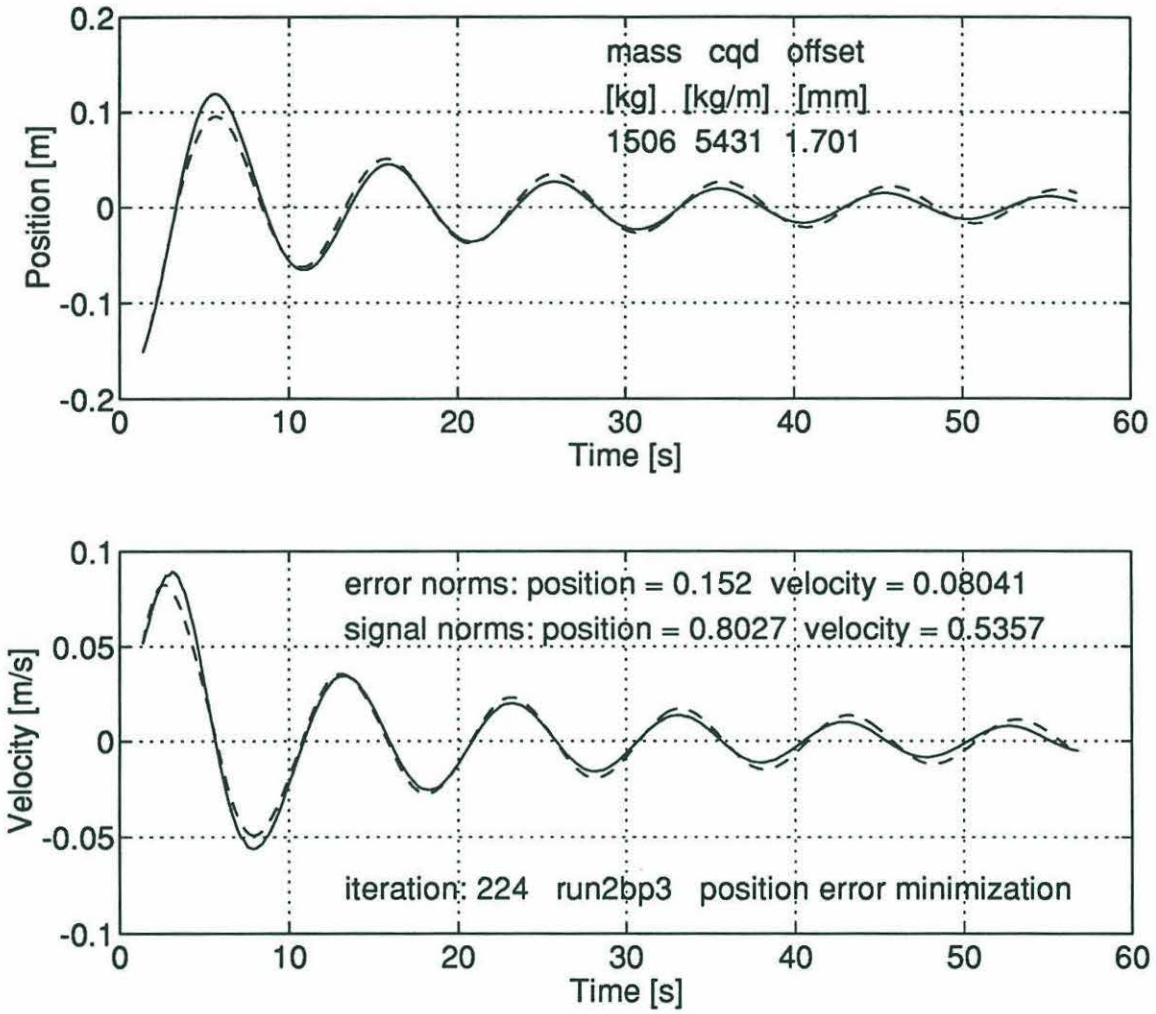

Figure A.13: NUMERICAL MINIMIZATION - INERTIA WITH QUADRATIC DRAG MODEL - RUN 2BP3 - The vehicle trajectory is marked by the solid line. The dashed trace is the path followed by the model.

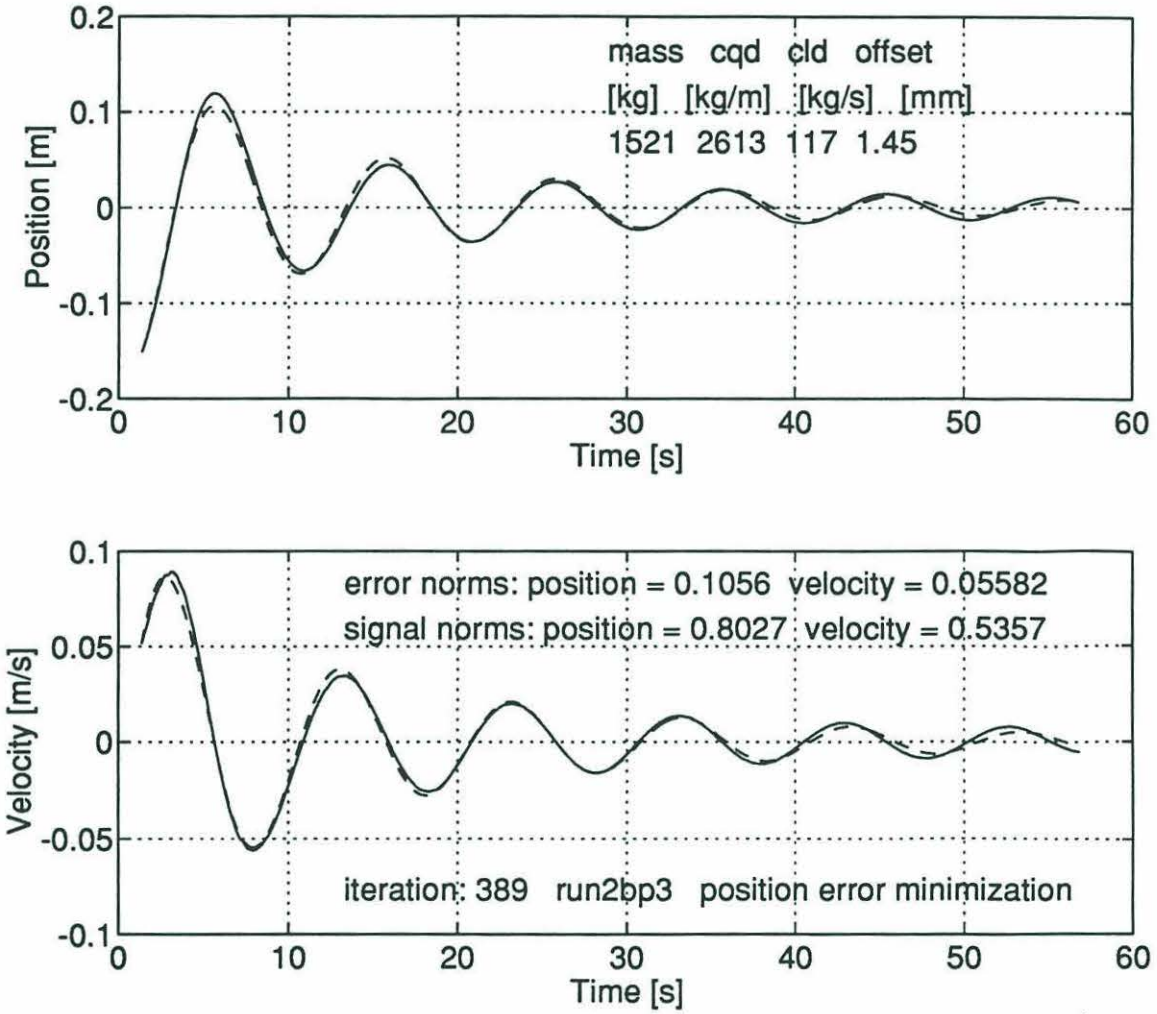

Figure A.14: NUMERICAL MINIMIZATION - INERTIA WITH QUADRATIC AND LINEAR DRAG MODEL - RUN 2BP3 - The vehicle trajectory is marked by the solid line. The dashed trace is the path followed by the model.

Model	m_{eff} $[kg]$	c_{qd} $[kg/m]$	c_{ld} $[kg/s]$	F_{spring}	$F_{inertia}$	F_{q-drag}	F_{l-drag}
				$[N]$			
inertia	1434			22.6604	20.08		
inertia with linear drag	1533		639	22.66	21.46		16.11
inertia with quadratic drag	1506	5431		22.66	21.08	3.45	
inertia with quadratic and linear drag	1521	2613	117	22.66	21.29	1.66	2.95

Table A.3: RUN 2BP3 - Two springs in parallel, effective spring constant: 597.9 N/m.

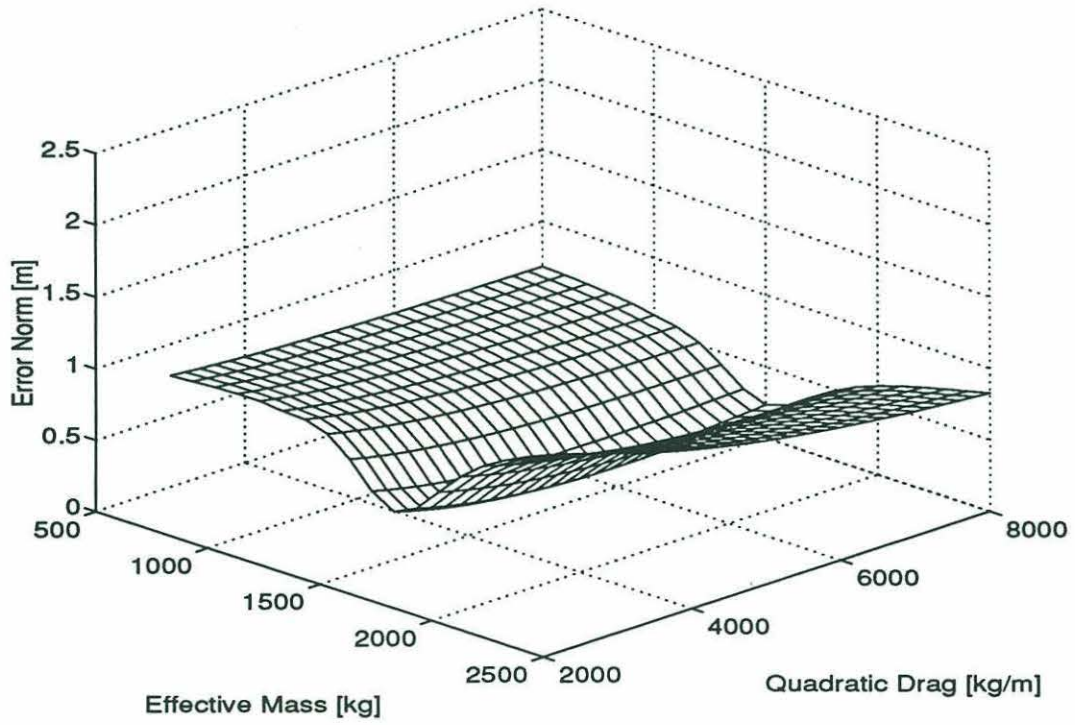

Figure A.15: ERROR NORM SURFACE FOR THE INERTIA WITH QUADRATIC DRAG MODEL AND VEHICLE TRAJECTORY 2BP3

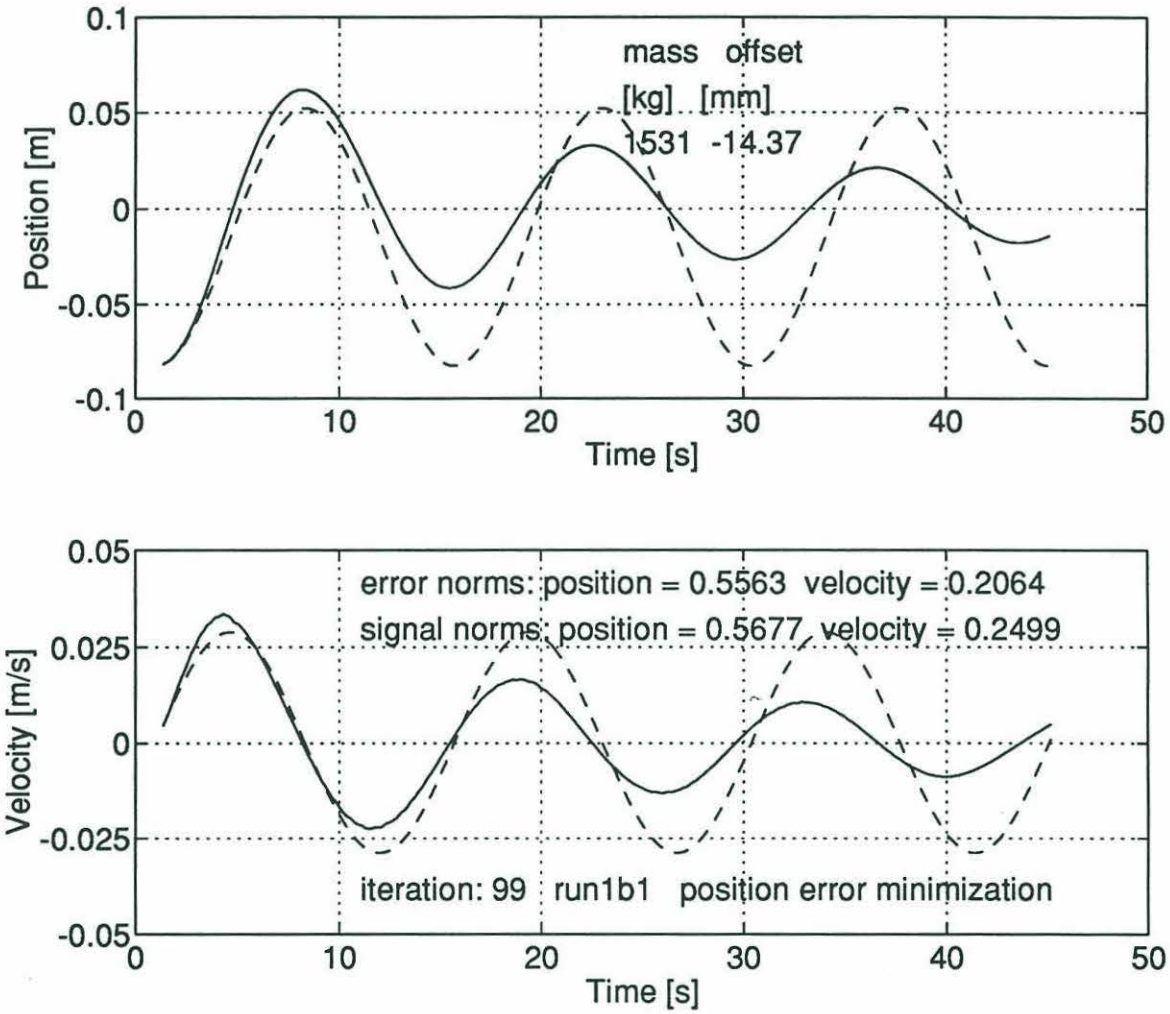

Figure A.16: NUMERICAL MINIMIZATION - INERTIA MODEL - RUN 1B1 - The vehicle trajectory is marked by the solid line. The dashed trace is the path followed by the model.

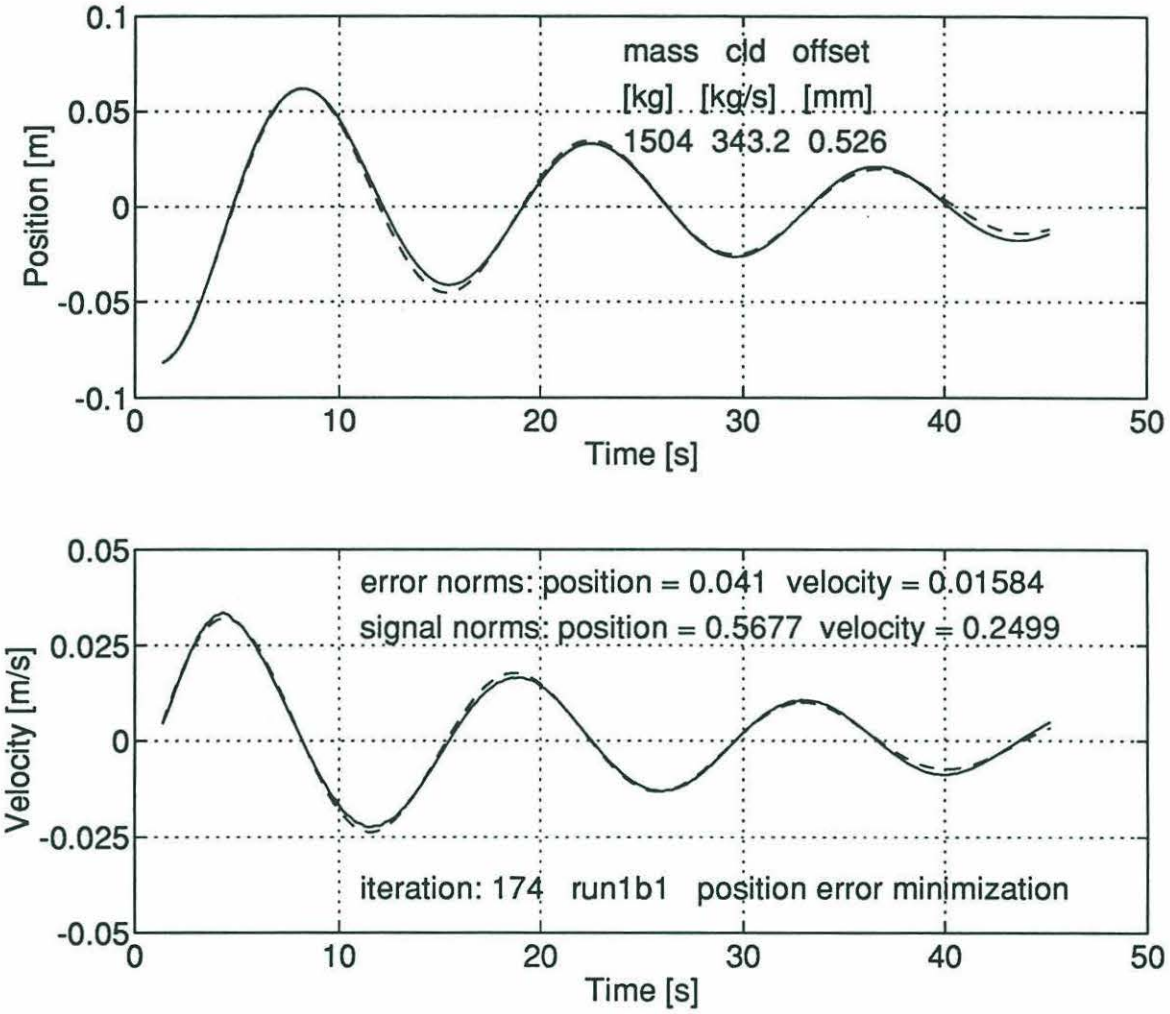

Figure A.17: NUMERICAL MINIMIZATION - INERTIA WITH LINEAR DRAG MODEL - RUN 1B1 - The vehicle trajectory is marked by the solid line. The dashed trace is the path followed by the model.

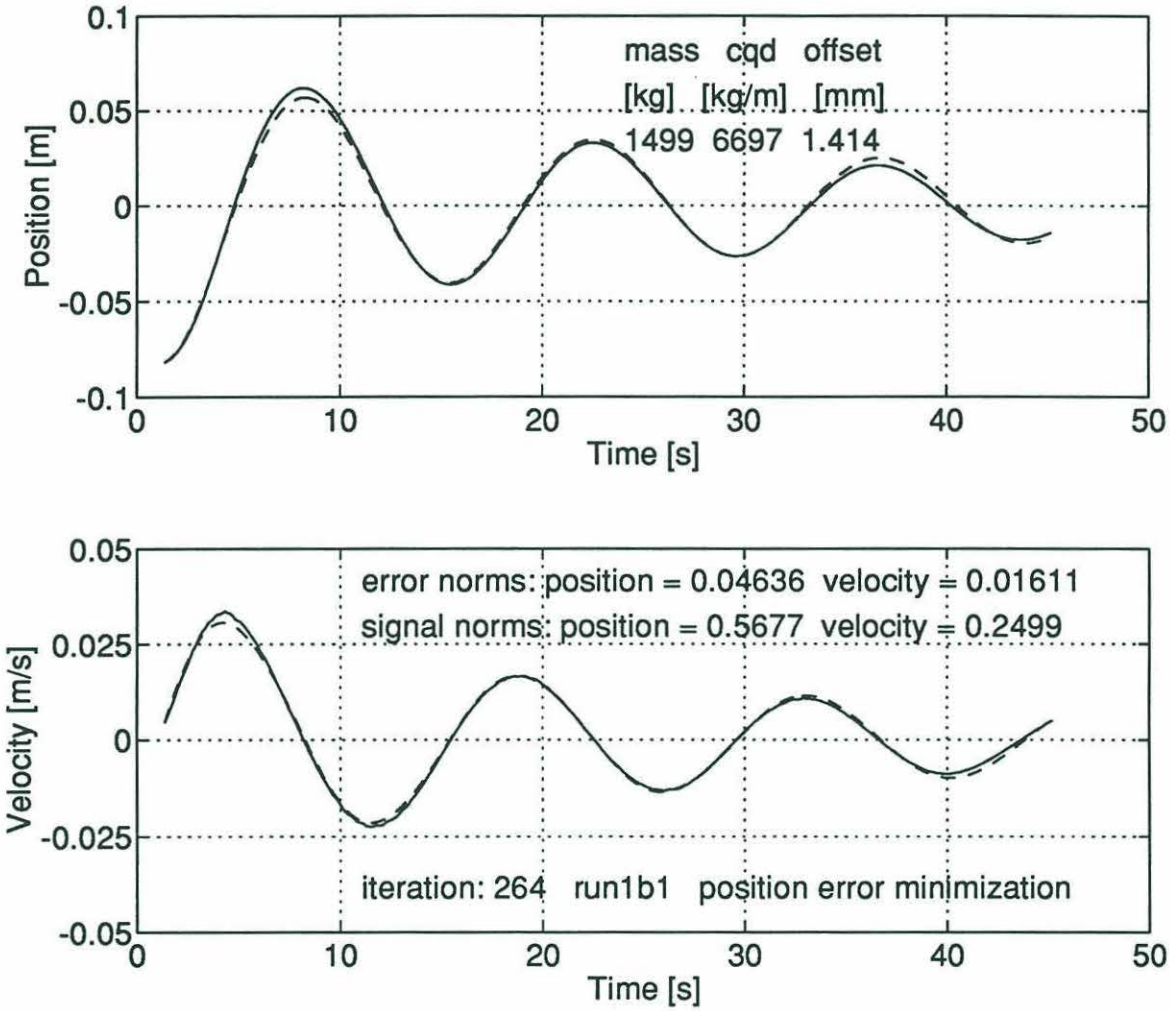

Figure A.18: NUMERICAL MINIMIZATION - INERTIA WITH QUADRATIC DRAG MODEL - RUN 1B1 - The vehicle trajectory is marked by the solid line. The dashed trace is the path followed by the model.

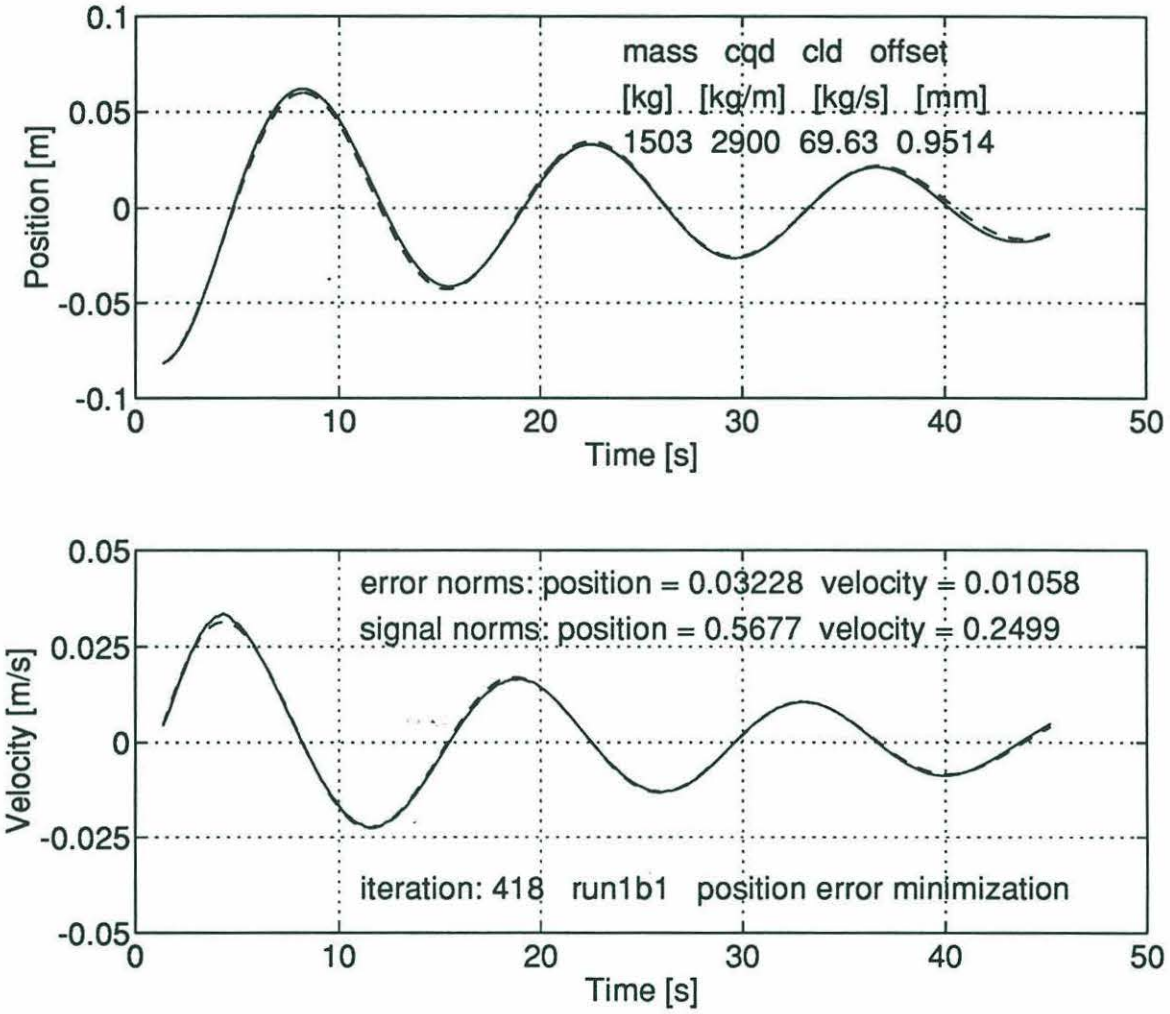

Figure A.19: NUMERICAL MINIMIZATION - INERTIA WITH QUADRATIC AND LINEAR DRAG MODEL - RUN 1B1 - The vehicle trajectory is marked by the solid line. The dashed trace is the path followed by the model.

Model	m_{eff} $[kg]$	c_{qd} $[kg/m]$	c_{ld} $[kg/s]$	F_{spring}	$F_{inertia}$	F_{q-drag}	F_{l-drag}
				$[N]$			
inertia	1531			8.90	8.88		
inertia with linear drag	1504		343	8.90	8.72		4.53
inertia with quadratic drag	1499	6697		8.90	8.69	1.17	
inertia with quadratic and linear drag	1503	2900	70	8.90	8.72	.51	.92

Table A.4: RUN 1B1 - Single spring, effective spring constant: 294.6 N/m.

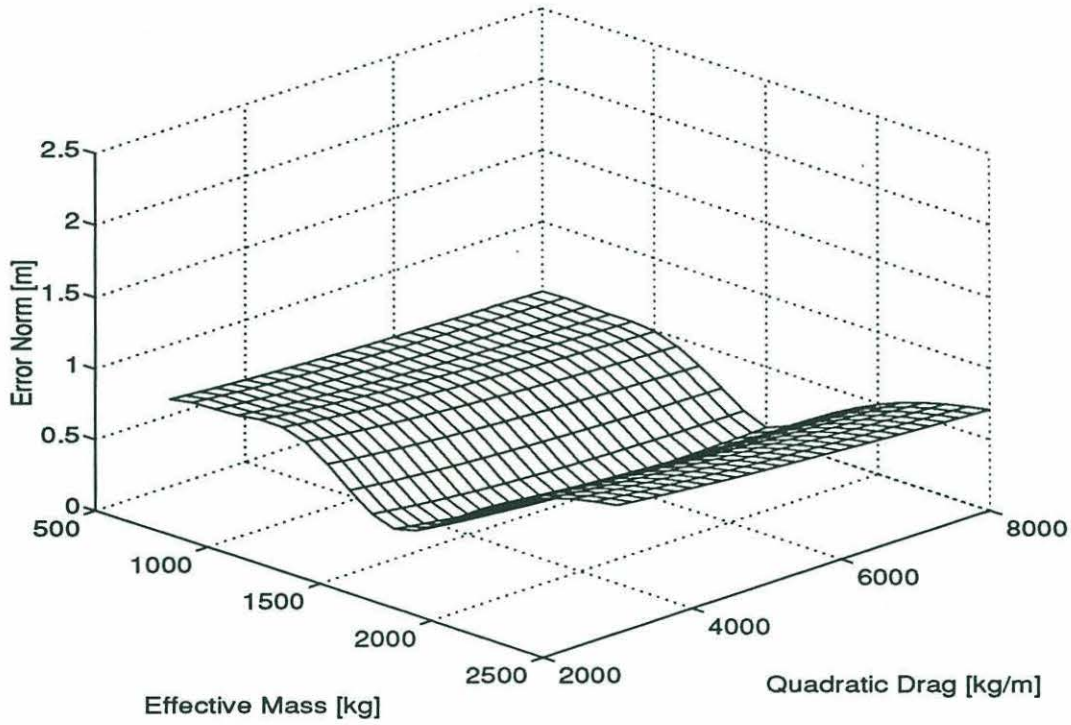

Figure A.20: ERROR NORM SURFACE FOR THE INERTIA WITH QUADRATIC DRAG MODEL AND VEHICLE TRAJECTORY 1B1

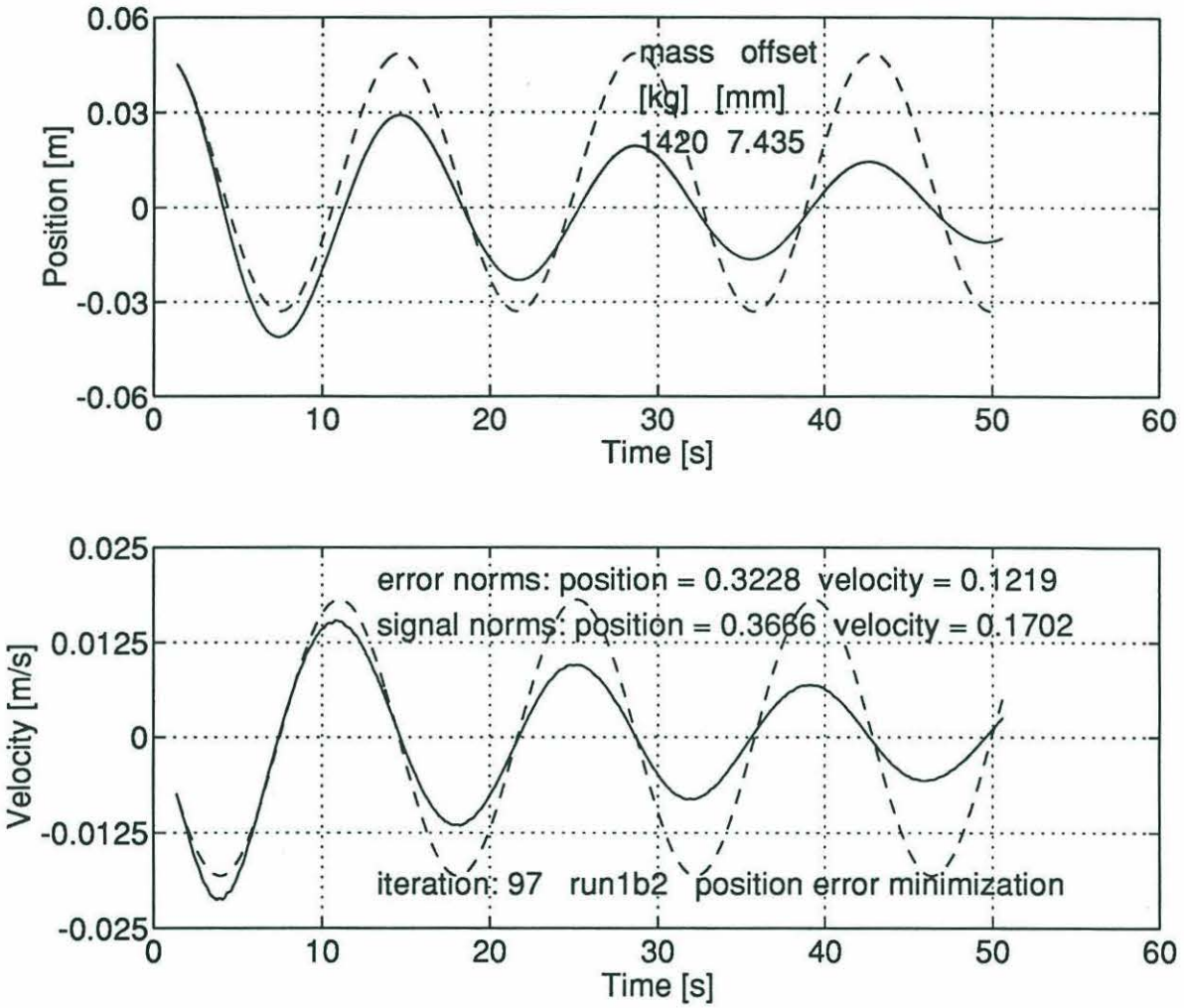

Figure A.21: NUMERICAL MINIMIZATION - INERTIA MODEL - RUN 1B2 - The vehicle trajectory is marked by the solid line. The dashed trace is the path followed by the model.

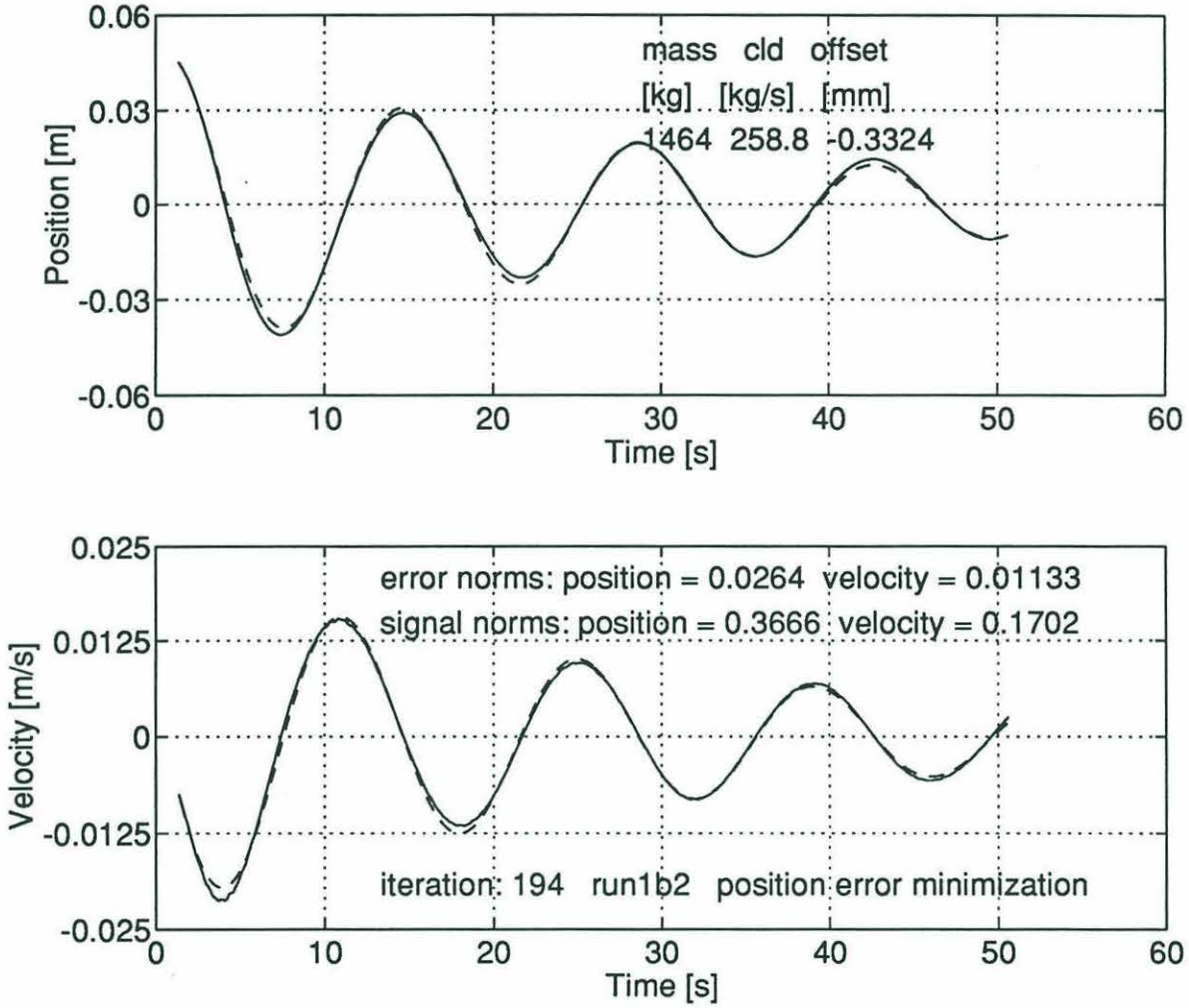

Figure A.22: NUMERICAL MINIMIZATION - INERTIA WITH LINEAR DRAG MODEL - RUN 1B2 - The vehicle trajectory is marked by the solid line. The dashed trace is the path followed by the model.

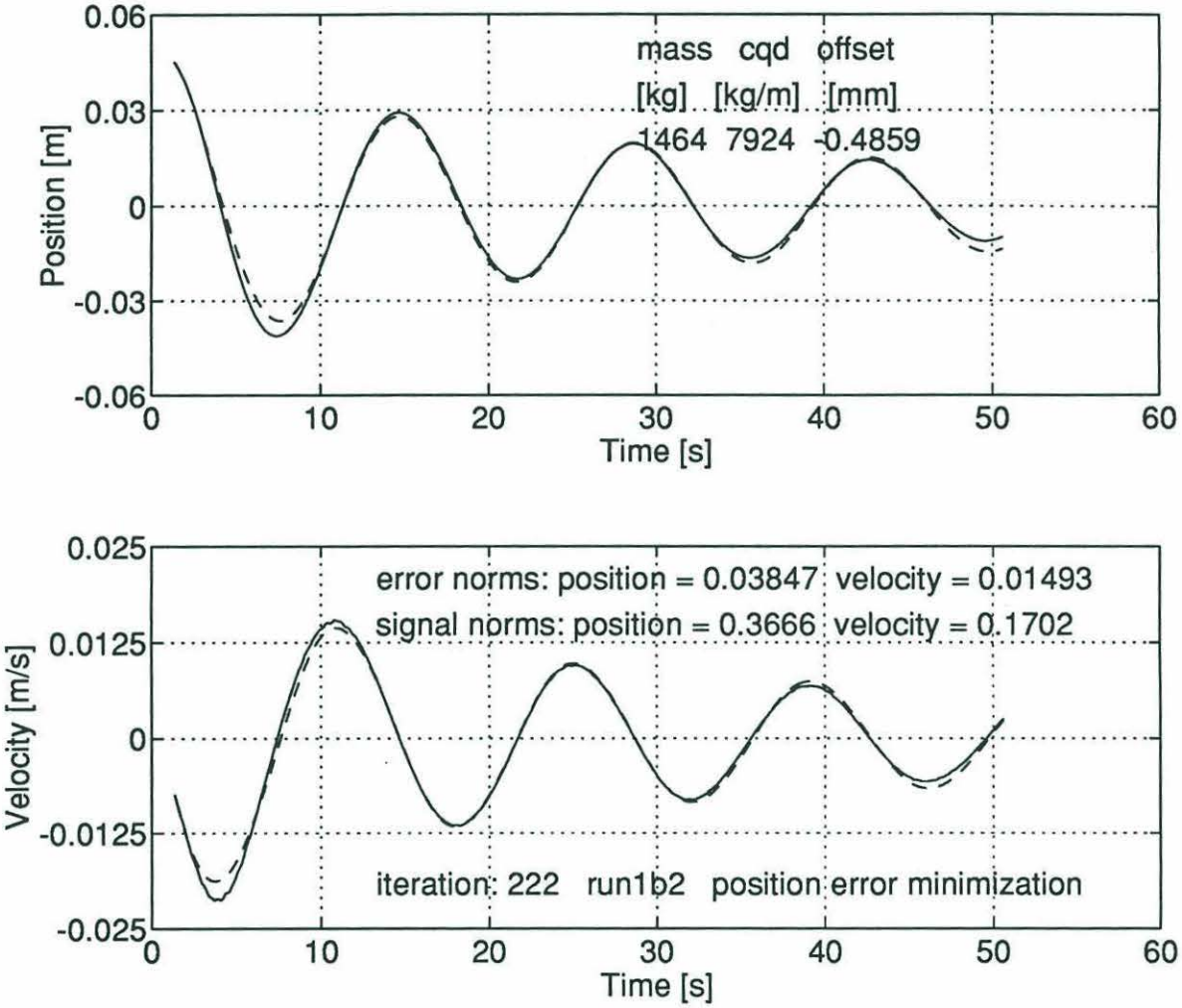

Figure A.23: NUMERICAL MINIMIZATION - INERTIA WITH QUADRATIC DRAG MODEL - RUN 1B2 - The vehicle trajectory is marked by the solid line. The dashed trace is the path followed by the model.

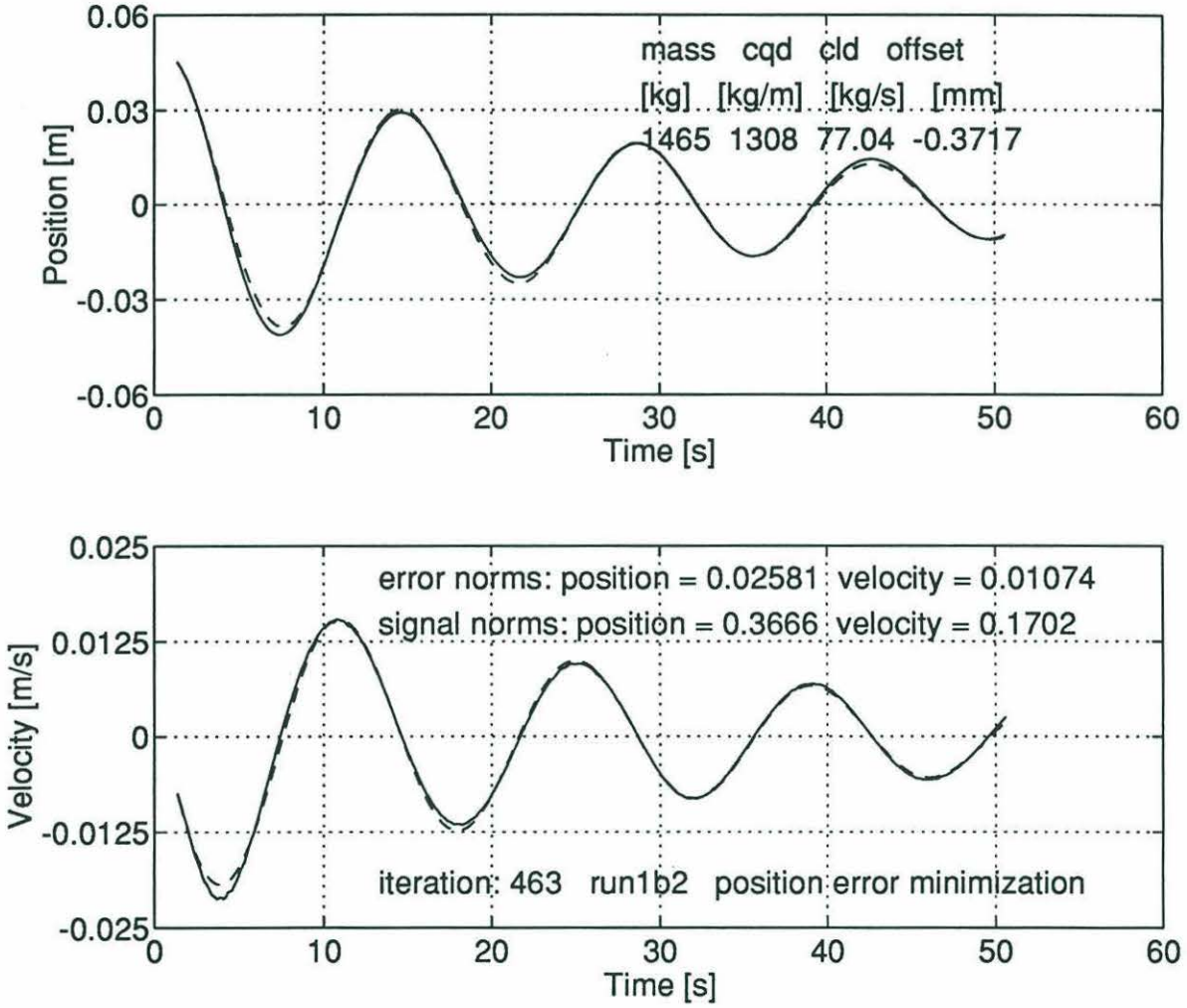

Figure A.24: NUMERICAL MINIMIZATION - INERTIA WITH QUADRATIC AND LINEAR DRAG MODEL - RUN 1B2 - The vehicle trajectory is marked by the solid line. The dashed trace is the path followed by the model.

Model	m_{eff} $[kg]$	c_{qd} $[kg/m]$	c_{ld} $[kg/s]$	F_{spring}	$F_{inertia}$	F_{q-drag}	F_{l-drag}
				$[N]$			
inertia	1420			5.42	5.25		
inertia with linear drag	1464		259	5.42	5.42		2.20
inertia with quadratic drag	1464	7924		5.42	5.42	.57	
inertia with quadratic and linear drag	1465	1308	77	5.42	5.42	.09	.65

Table A.5: RUN 1B2 - Single spring, effective spring constant: 294.6 N/m.

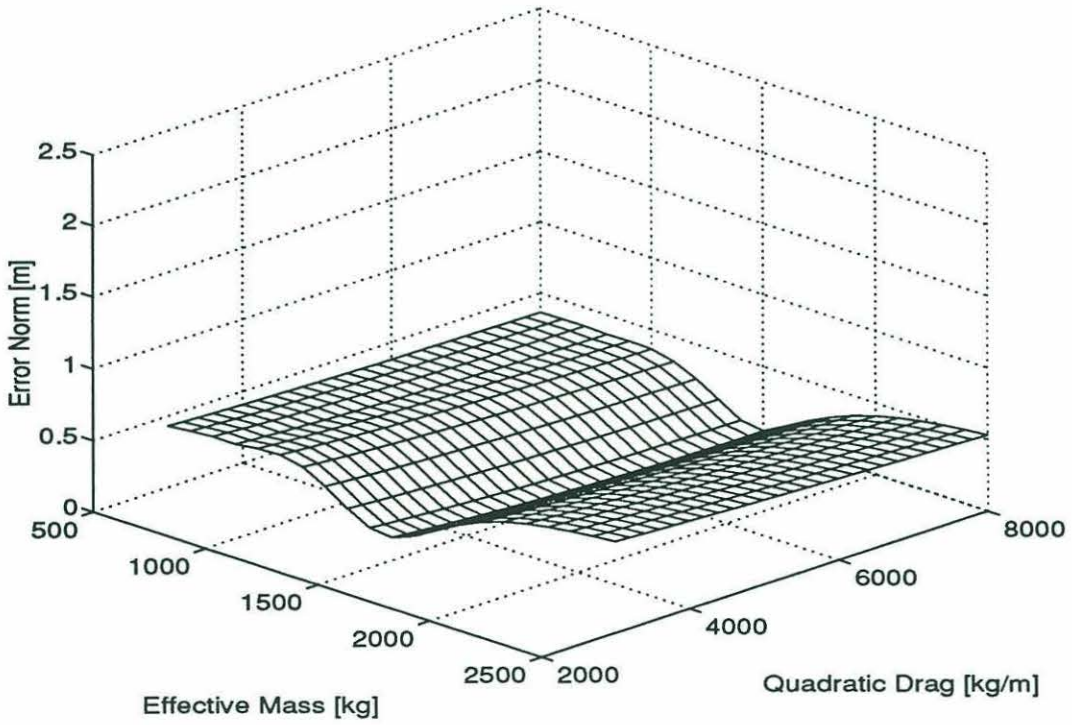

Figure A.25: ERROR NORM SURFACE FOR THE INERTIA WITH QUADRATIC DRAG MODEL AND VEHICLE TRAJECTORY 1B2

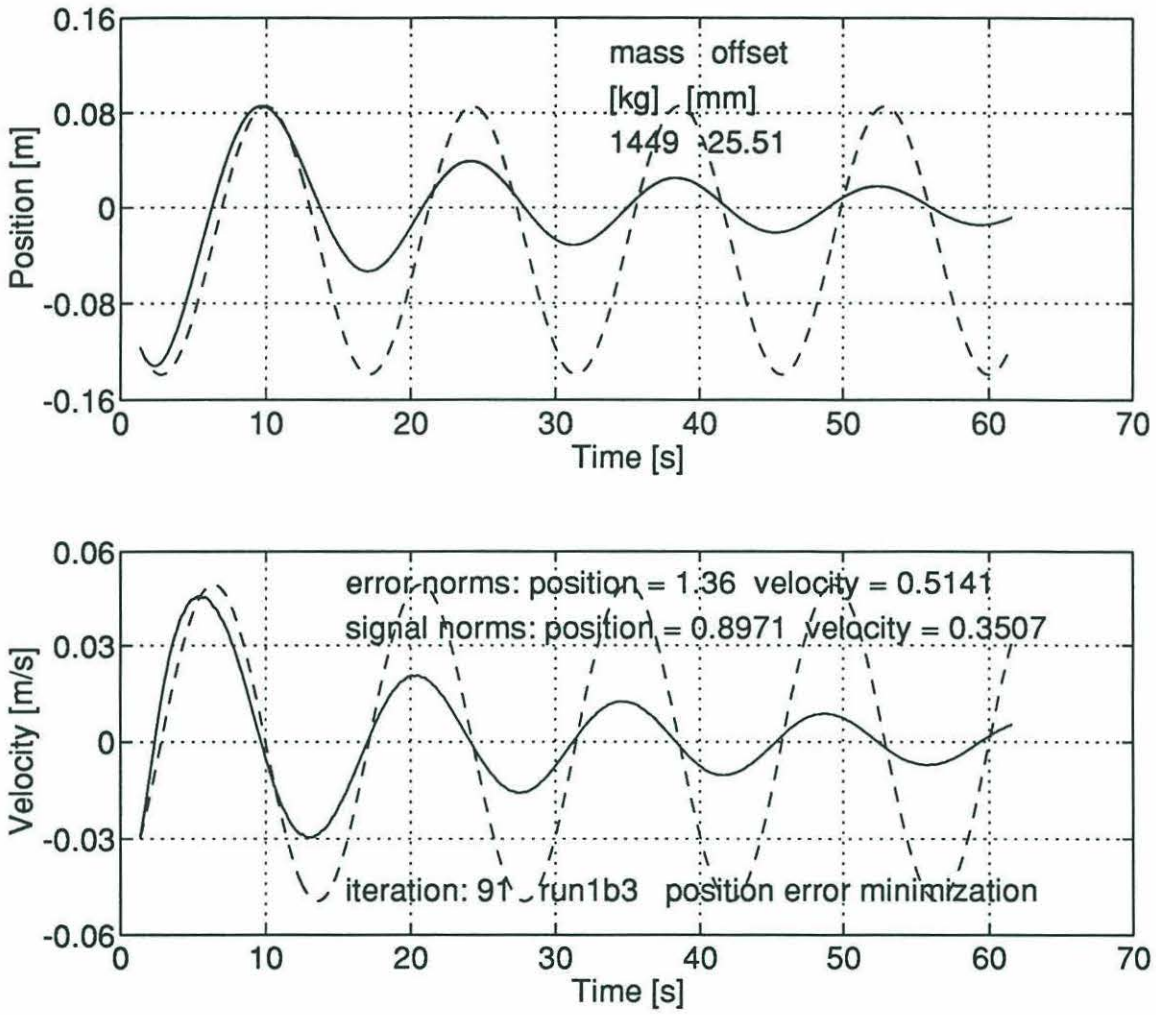

Figure A.26: NUMERICAL MINIMIZATION - INERTIA MODEL - RUN 1B3 - The vehicle trajectory is marked by the solid line. The dashed trace is the path followed by the model.

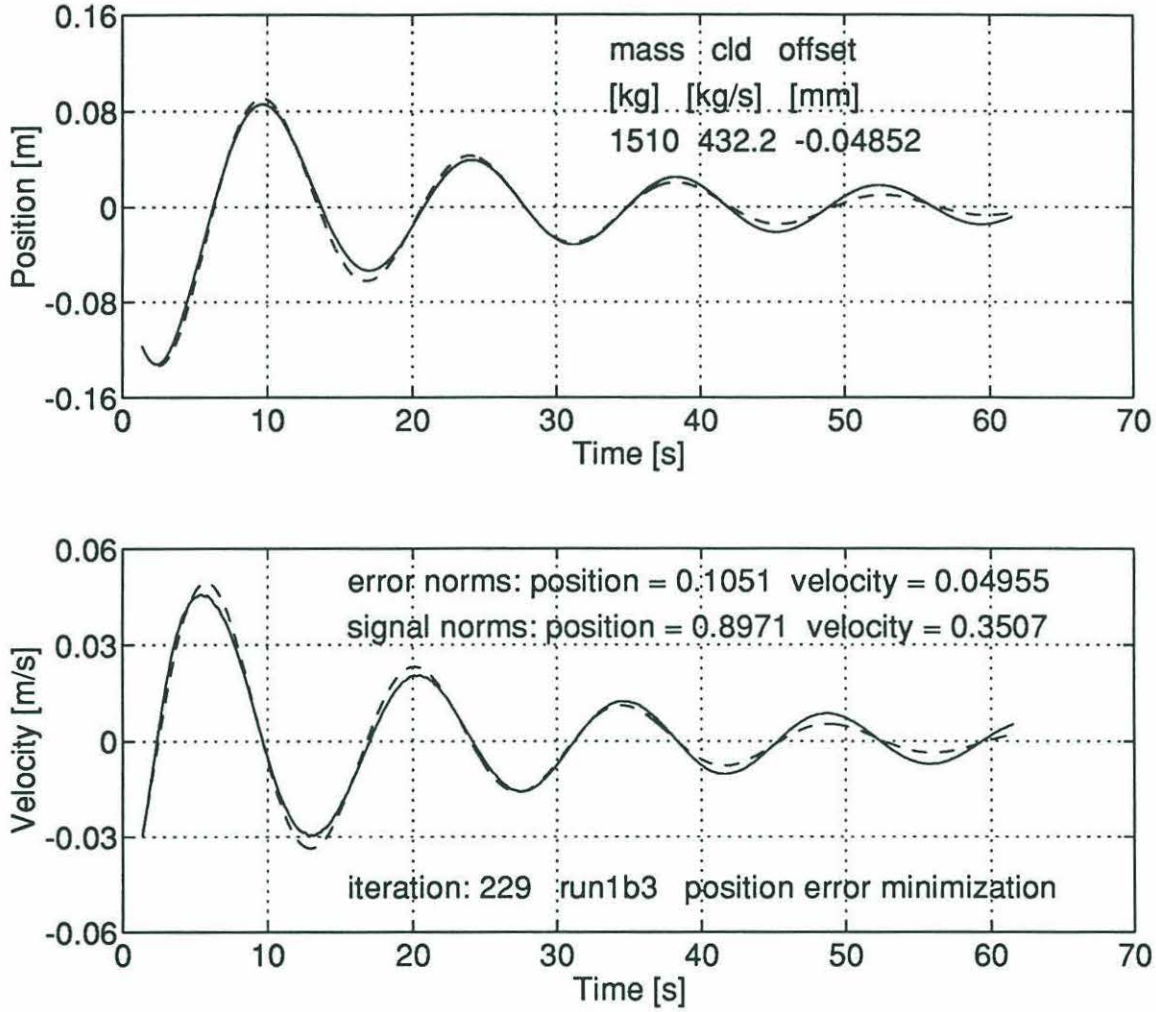

Figure A.27: NUMERICAL MINIMIZATION - INERTIA WITH LINEAR DRAG MODEL - RUN 1B3 - The vehicle trajectory is marked by the solid line. The dashed trace is the path followed by the model.

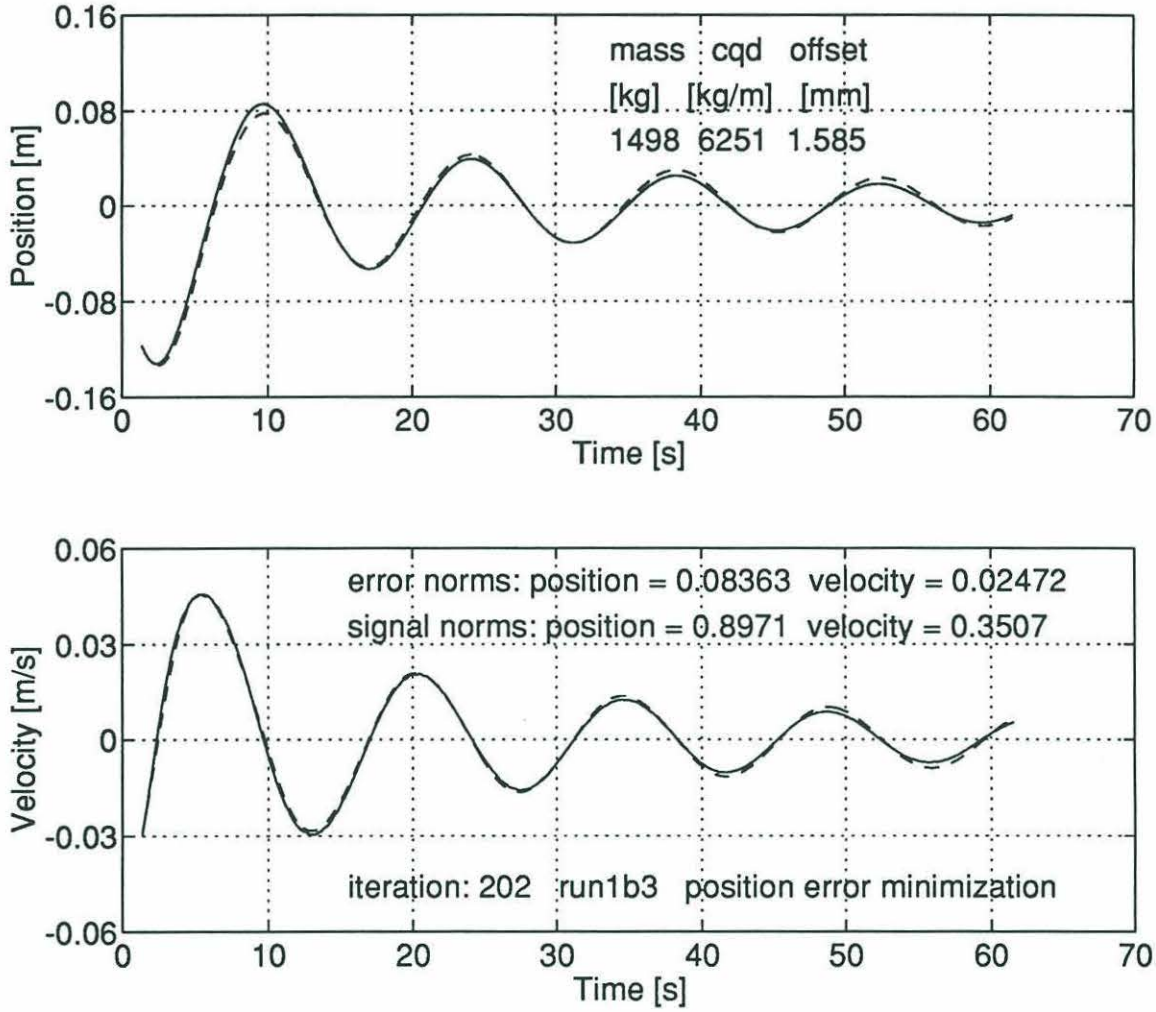

Figure A.28: NUMERICAL MINIMIZATION - INERTIA WITH QUADRATIC DRAG MODEL - RUN 1B3 - The vehicle trajectory is marked by the solid line. The dashed trace is the path followed by the model.

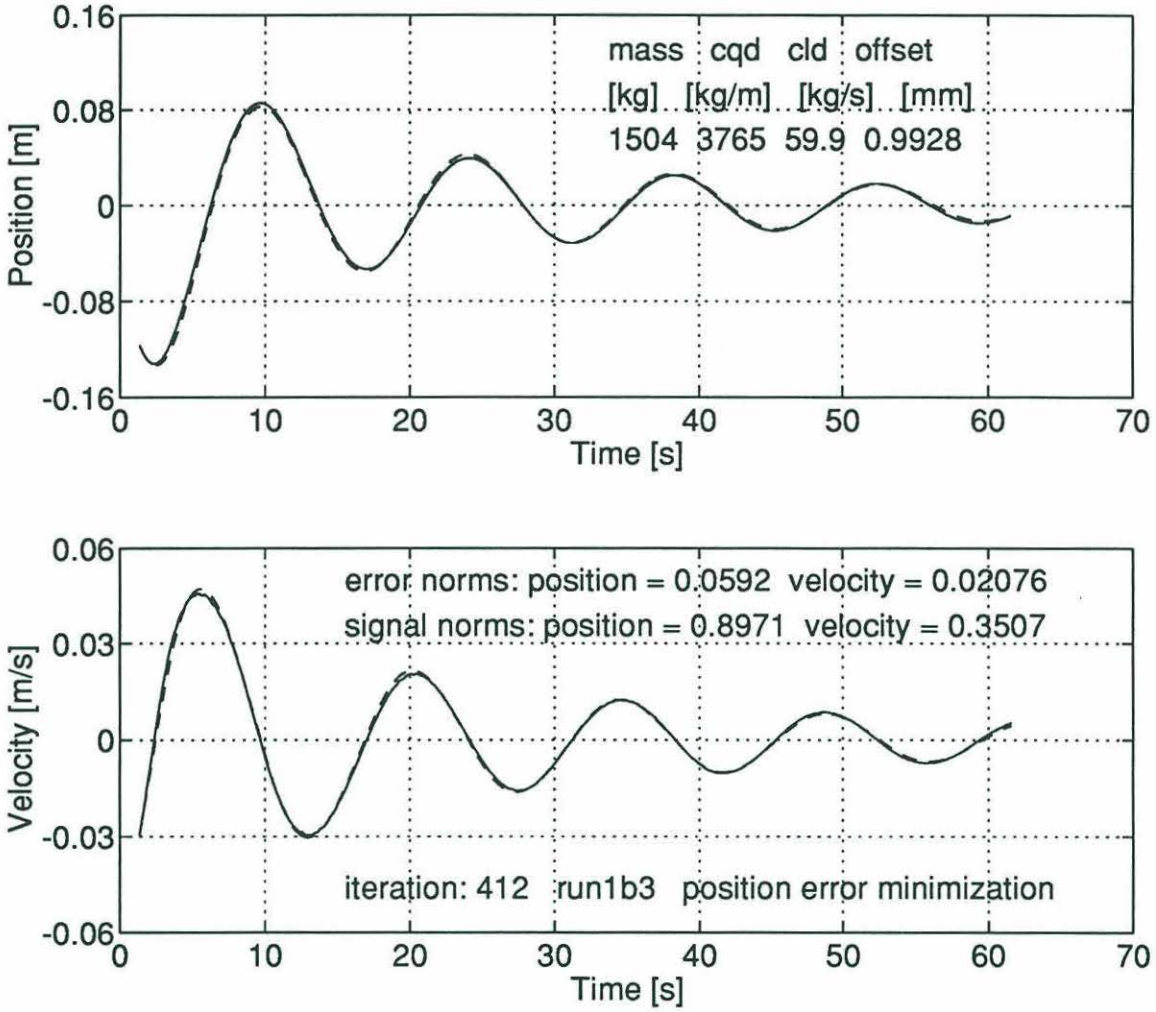

Figure A.29: NUMERICAL MINIMIZATION - INERTIA WITH QUADRATIC AND LINEAR DRAG MODEL - RUN 1B3 - The vehicle trajectory is marked by the solid line. The dashed trace is the path followed by the model.

Model	m_{eff} $[kg]$	c_{qd} $[kg/m]$	c_{ld} $[kg/s]$	F_{spring}	$F_{inertia}$	F_{q-drag}	F_{l-drag}
				$[N]$			
inertia	1449			11.96	11.59		
inertia with linear drag	1510		432	11.96	12.08		6.83
inertia with quadratic drag	1498	6251		11.96	12.98	1.56	
inertia with quadratic and linear drag	1504	3765	59	11.96	12.03	.94	.95

Table A.6: RUN 1B3 - Single spring, effective spring constant: 294.6 N/m.

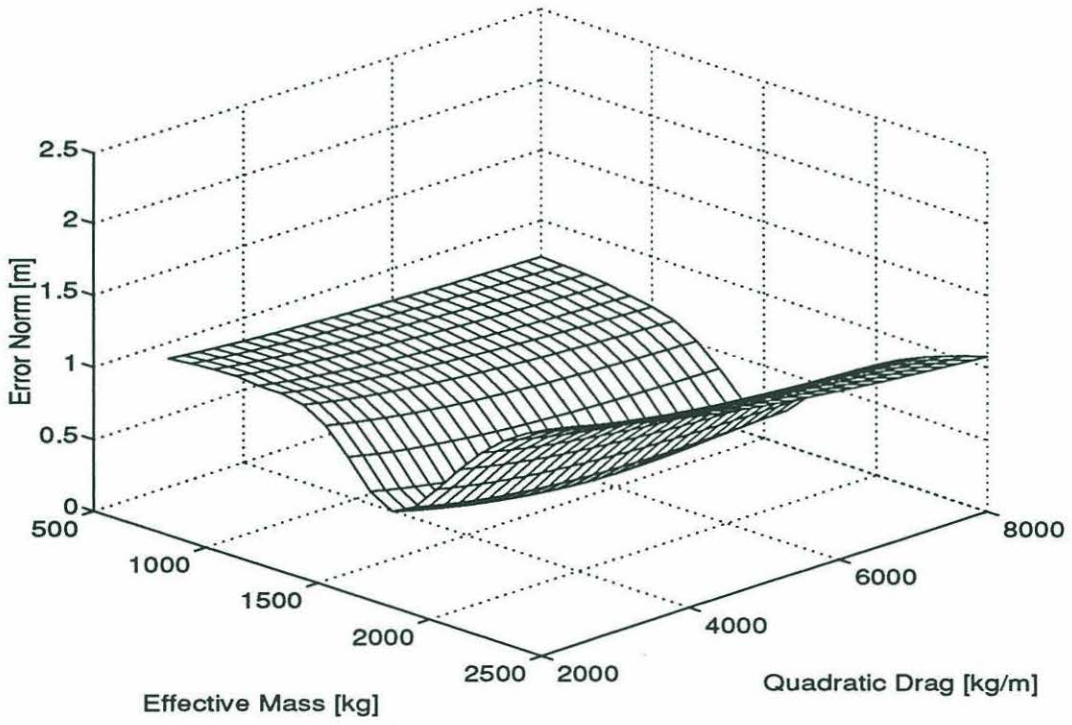

Figure A.30: ERROR NORM SURFACE FOR THE INERTIA WITH QUADRATIC DRAG MODEL AND VEHICLE TRAJECTORY 1B3

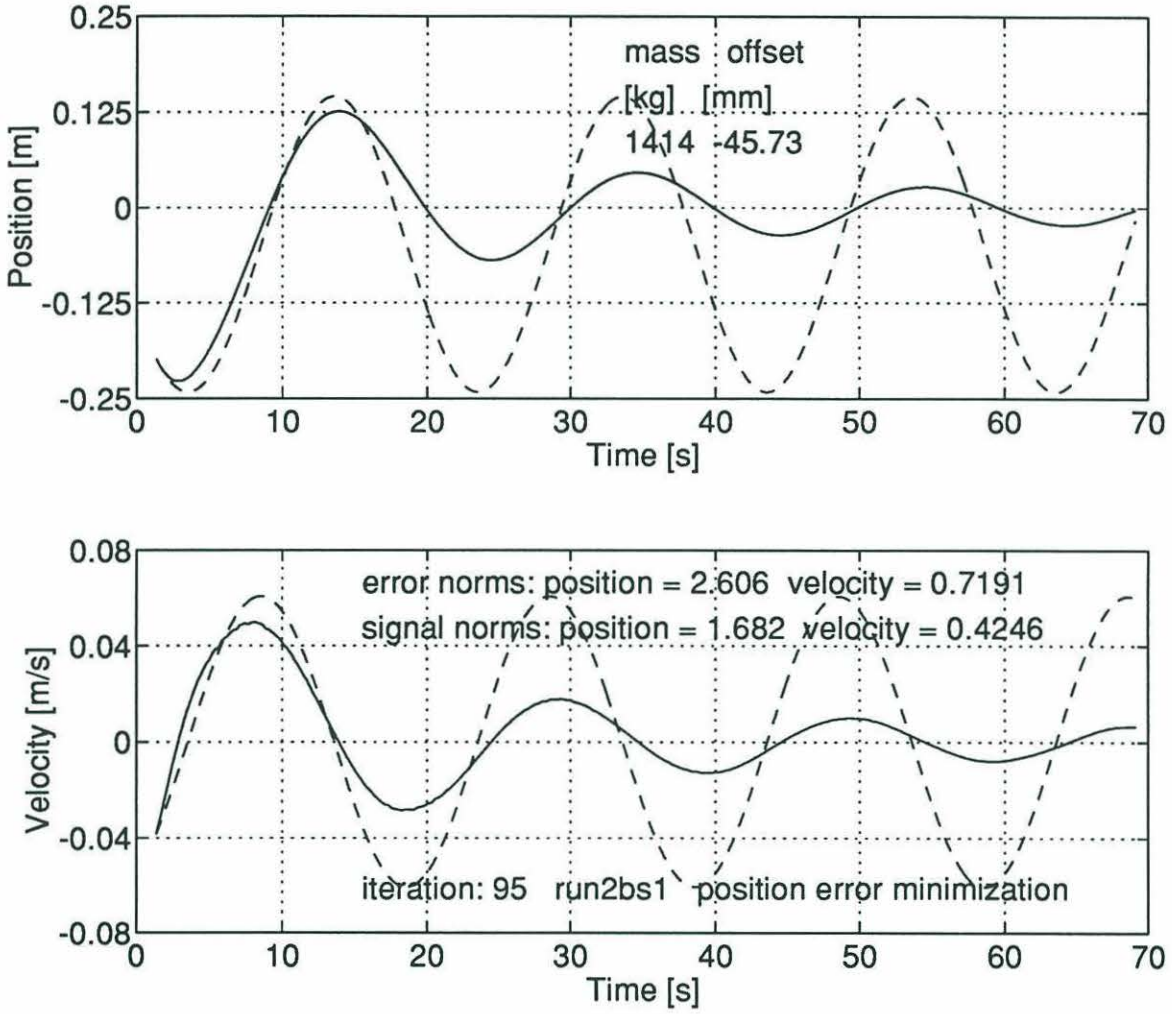

Figure A.31: NUMERICAL MINIMIZATION - INERTIA MODEL - RUN 2BS1 - The vehicle trajectory is marked by the solid line. The dashed trace is the path followed by the model.

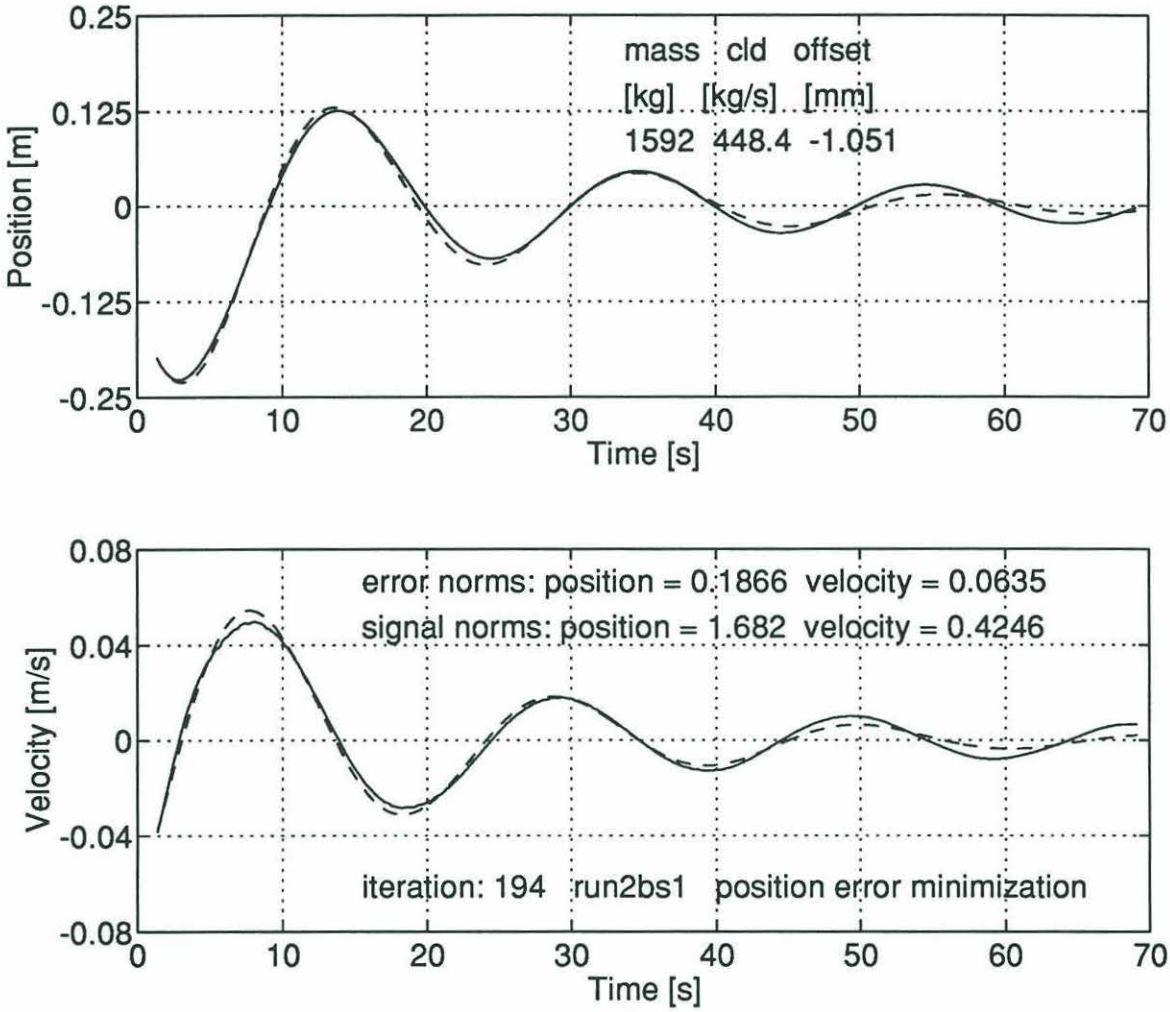

Figure A.32: NUMERICAL MINIMIZATION - INERTIA WITH LINEAR DRAG MODEL - RUN 2BS1 - The vehicle trajectory is marked by the solid line. The dashed trace is the path followed by the model.

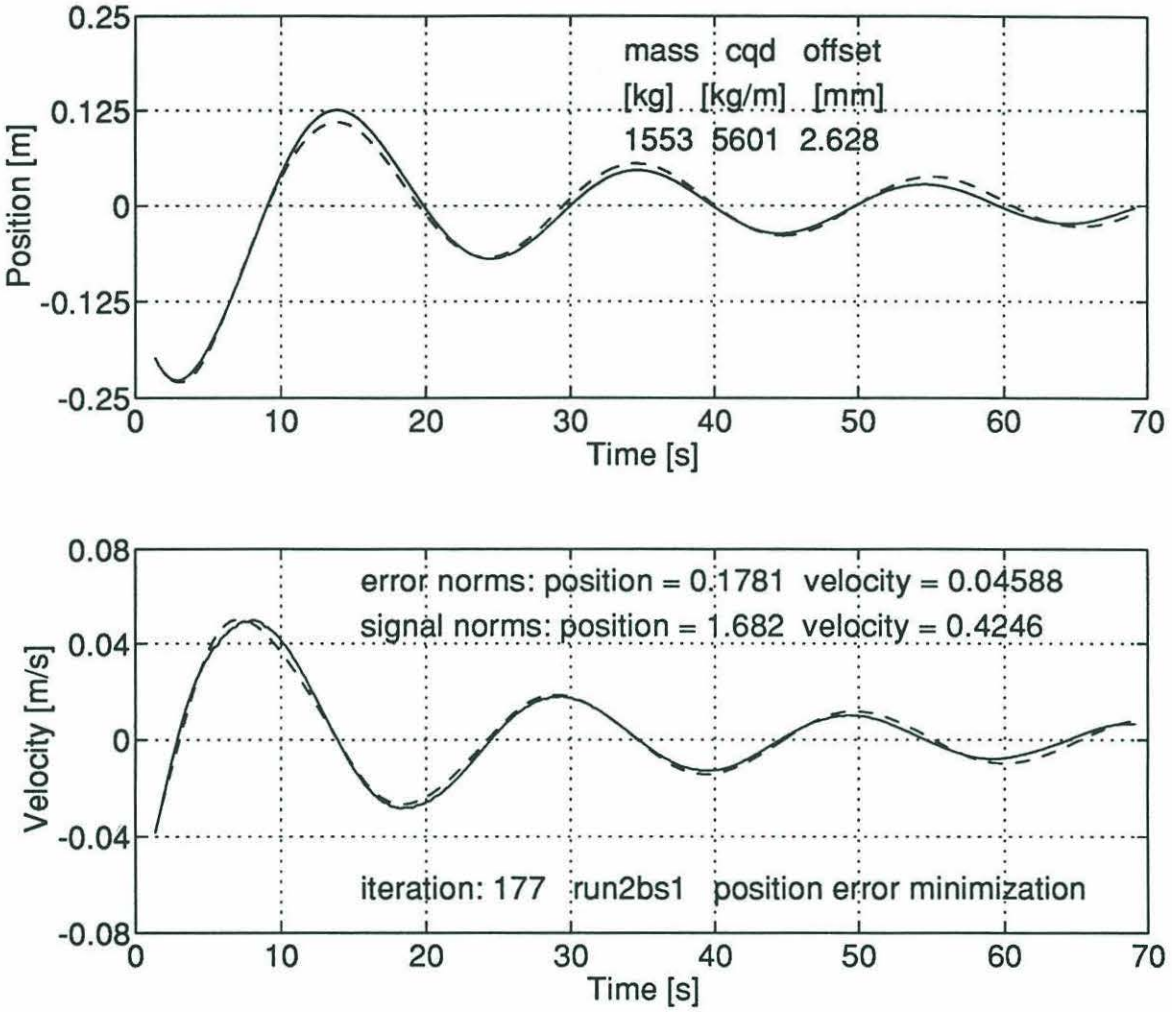

Figure A.33: NUMERICAL MINIMIZATION - INERTIA WITH QUADRATIC DRAG MODEL - RUN 2BS1 - The vehicle trajectory is marked by the solid line. The dashed trace is the path followed by the model.

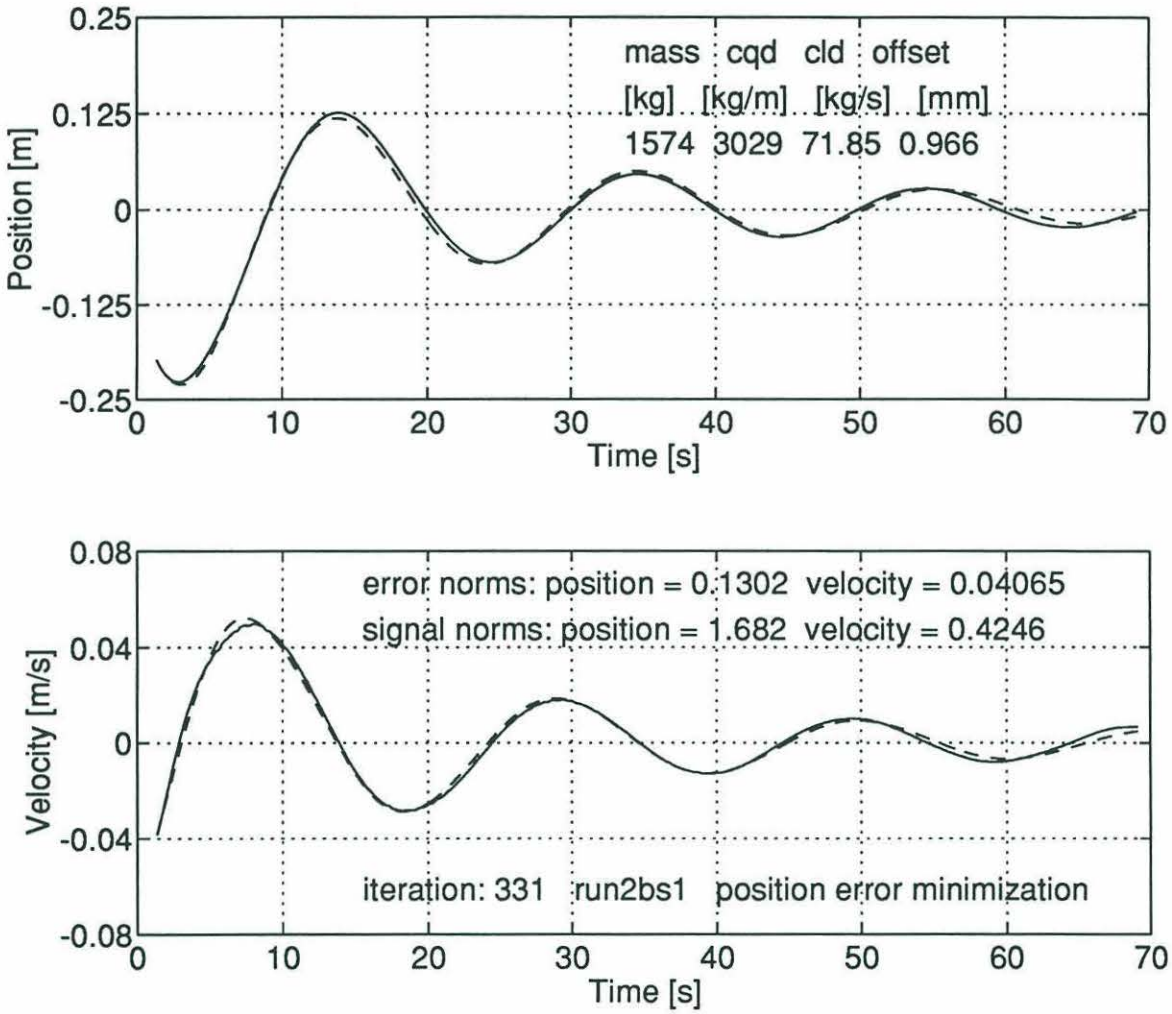

Figure A.34: NUMERICAL MINIMIZATION - INERTIA WITH QUADRATIC AND LINEAR DRAG MODEL - RUN 2BS1 - The vehicle trajectory is marked by the solid line. The dashed trace is the path followed by the model.

Model	m_{eff} $[kg]$	c_{qd} $[kg/m]$	c_{ld} $[kg/s]$	F_{spring}	$F_{inertia}$	F_{q-drag}	F_{l-drag}
				$[N]$			
inertia	1414			10.45	9.33		
inertia with linear drag	1592		448	10.45	10.51		8.03
inertia with quadratic drag	1553	5601		10.45	10.25	1.79	
inertia with quadratic and linear drag	1574	3029	72	10.45	10.39	.97	1.29

Table A.7: RUN 2BS1 - Two springs in series, effective spring constant: 146.7 N/m.

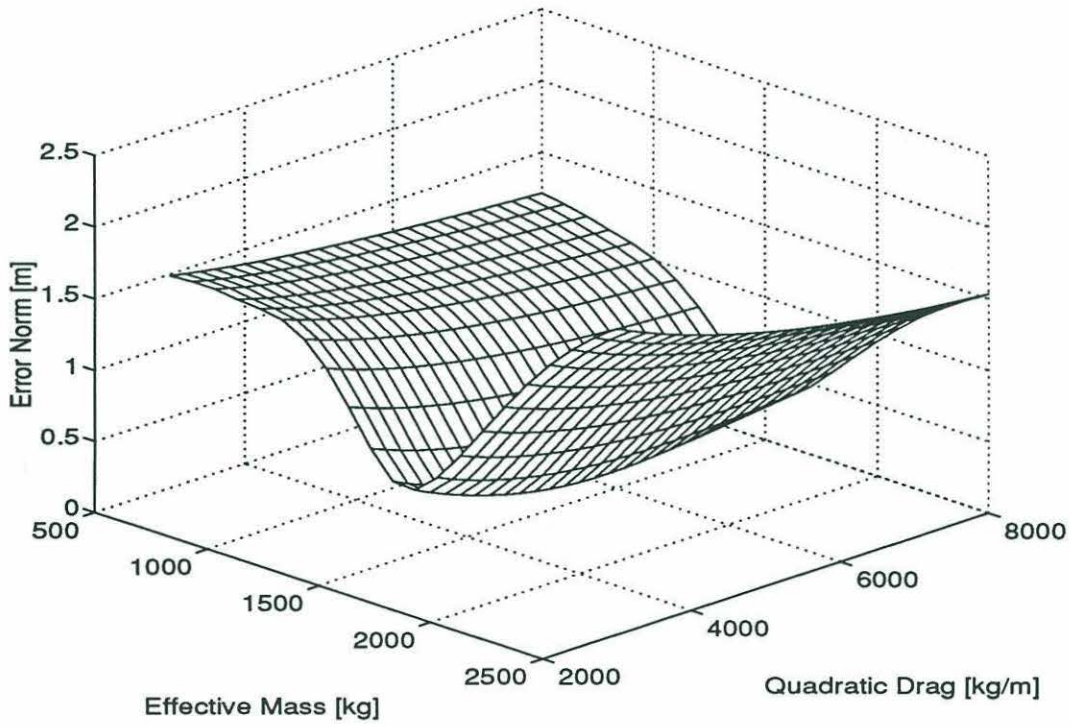

Figure A.35: ERROR NORM SURFACE FOR THE INERTIA WITH QUADRATIC DRAG MODEL AND VEHICLE TRAJECTORY 2BS1

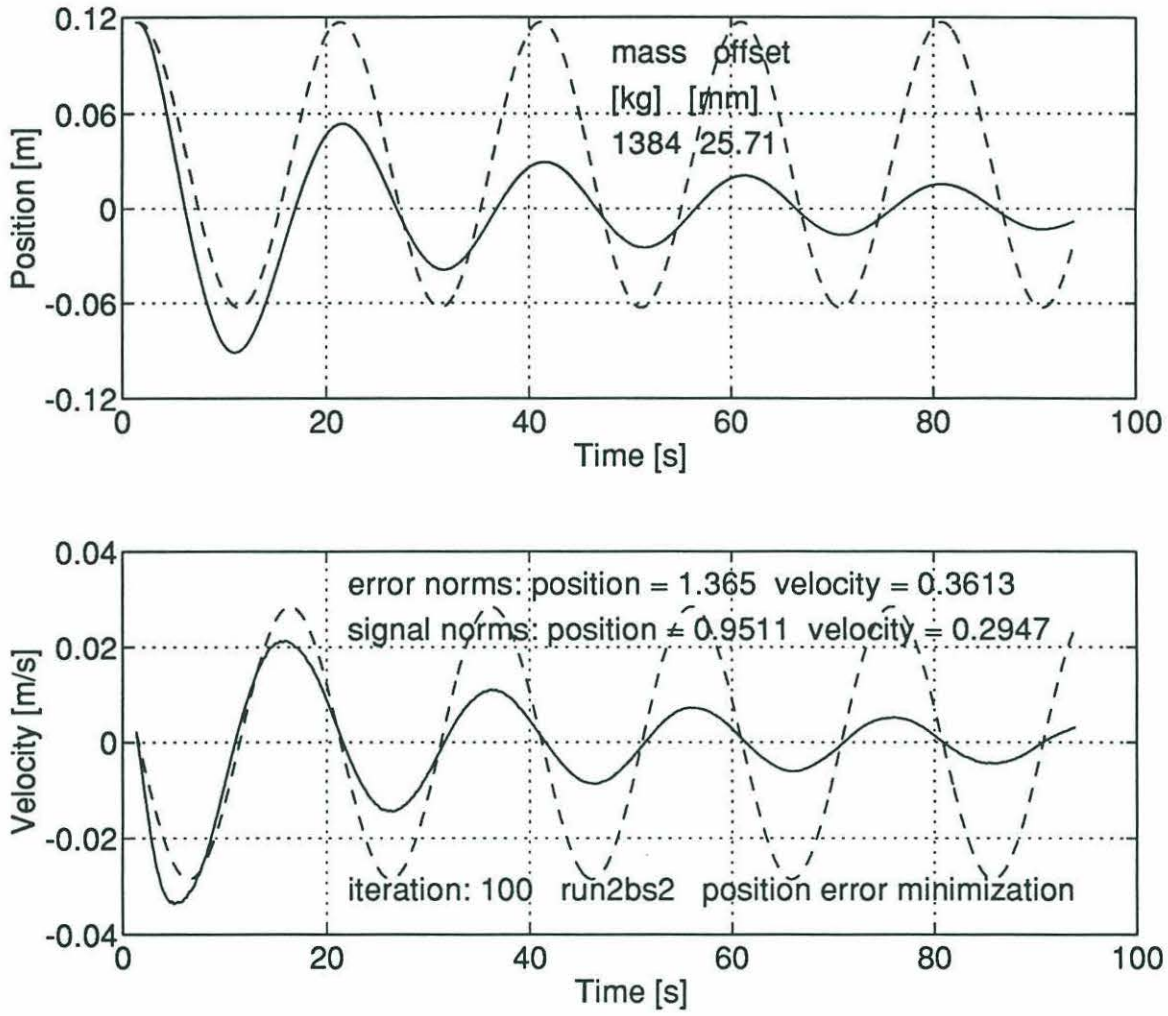

Figure A.36: NUMERICAL MINIMIZATION - INERTIA MODEL - RUN 2BS2 - The vehicle trajectory is marked by the solid line. The dashed trace is the path followed by the model.

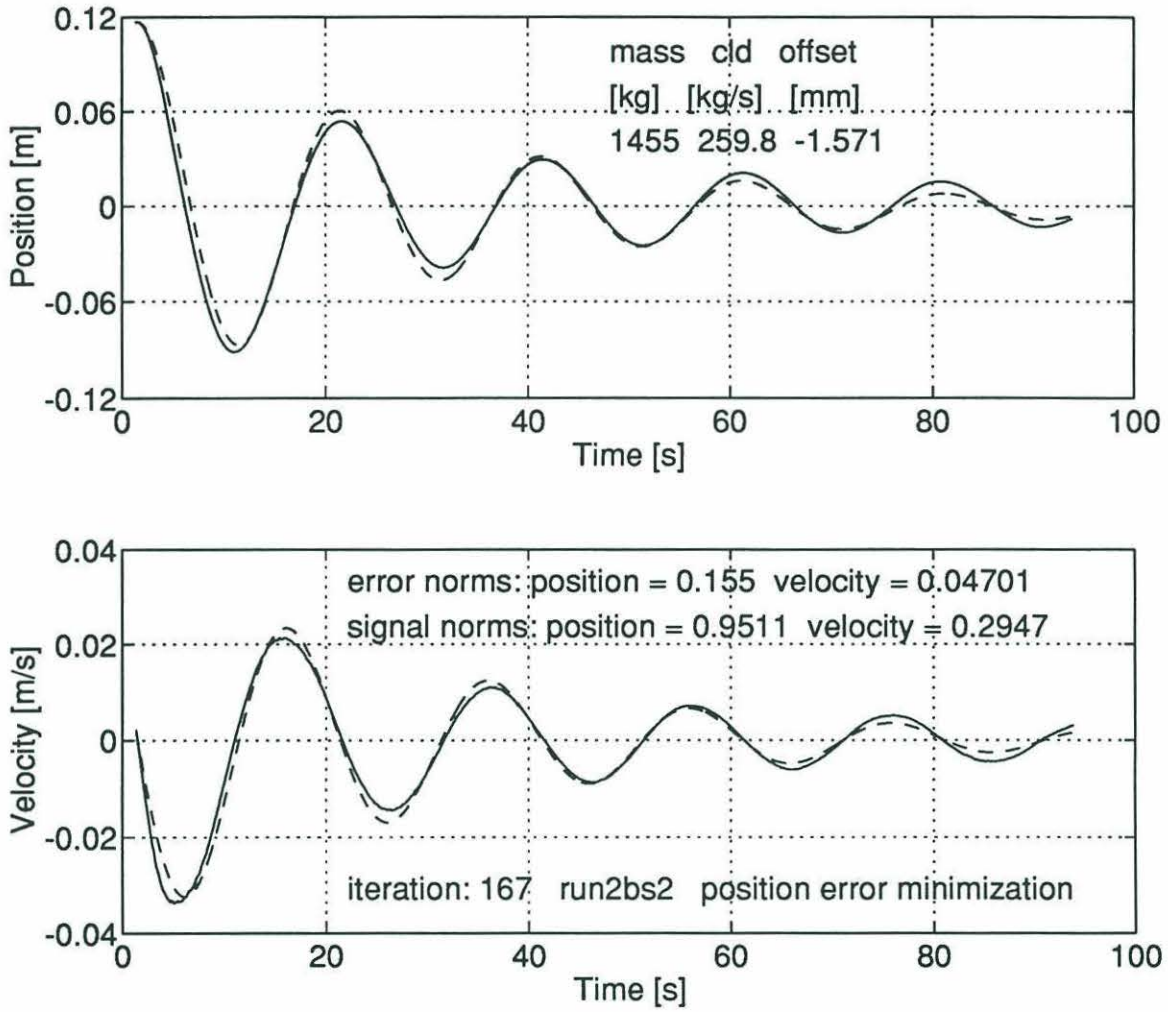

Figure A.37: NUMERICAL MINIMIZATION - INERTIA WITH LINEAR DRAG MODEL - RUN 2BS2 - The vehicle trajectory is marked by the solid line. The dashed trace is the path followed by the model.

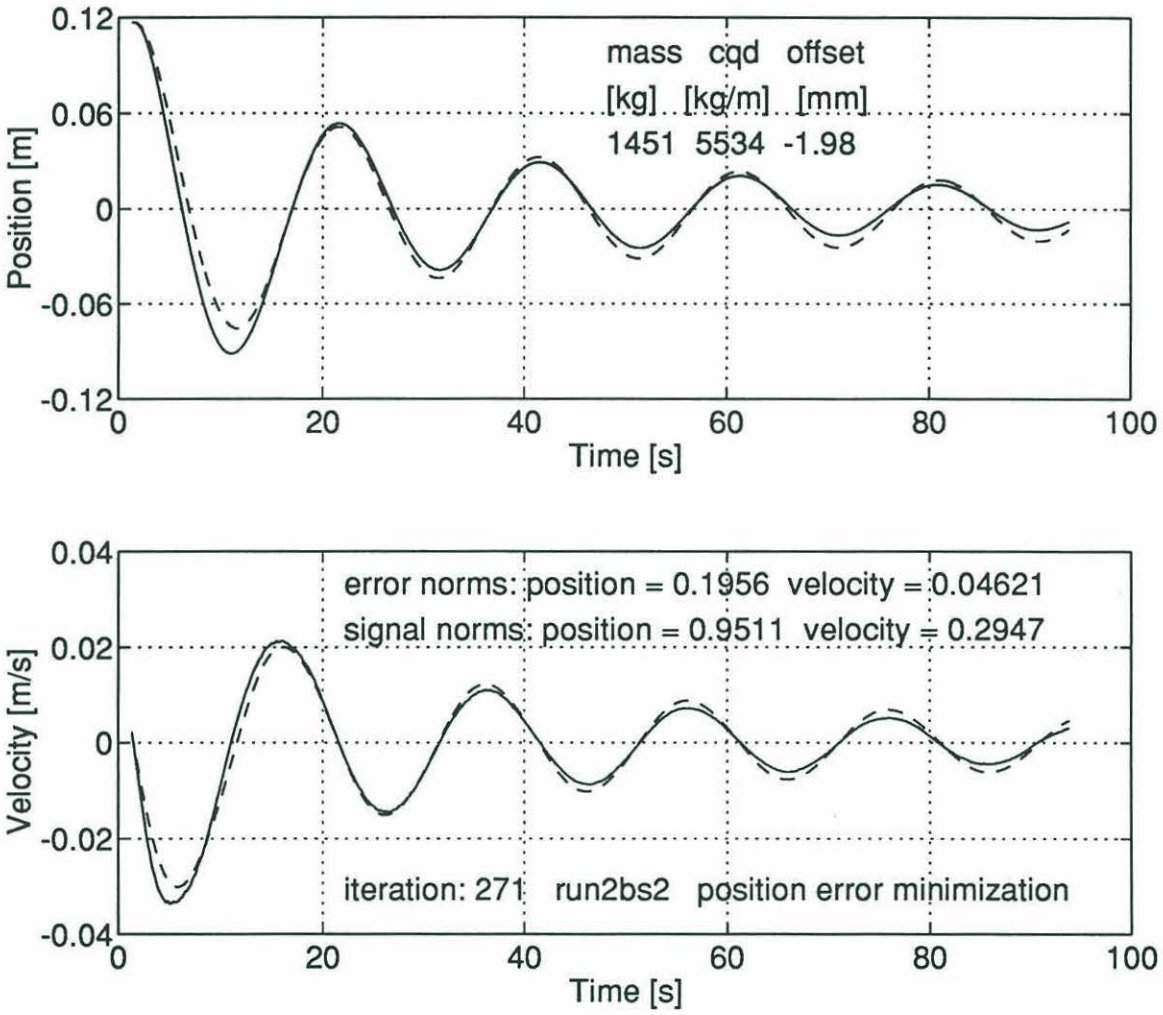

Figure A.38: NUMERICAL MINIMIZATION - INERTIA WITH QUADRATIC DRAG MODEL - RUN 2BS2 - The vehicle trajectory is marked by the solid line. The dashed trace is the path followed by the model.

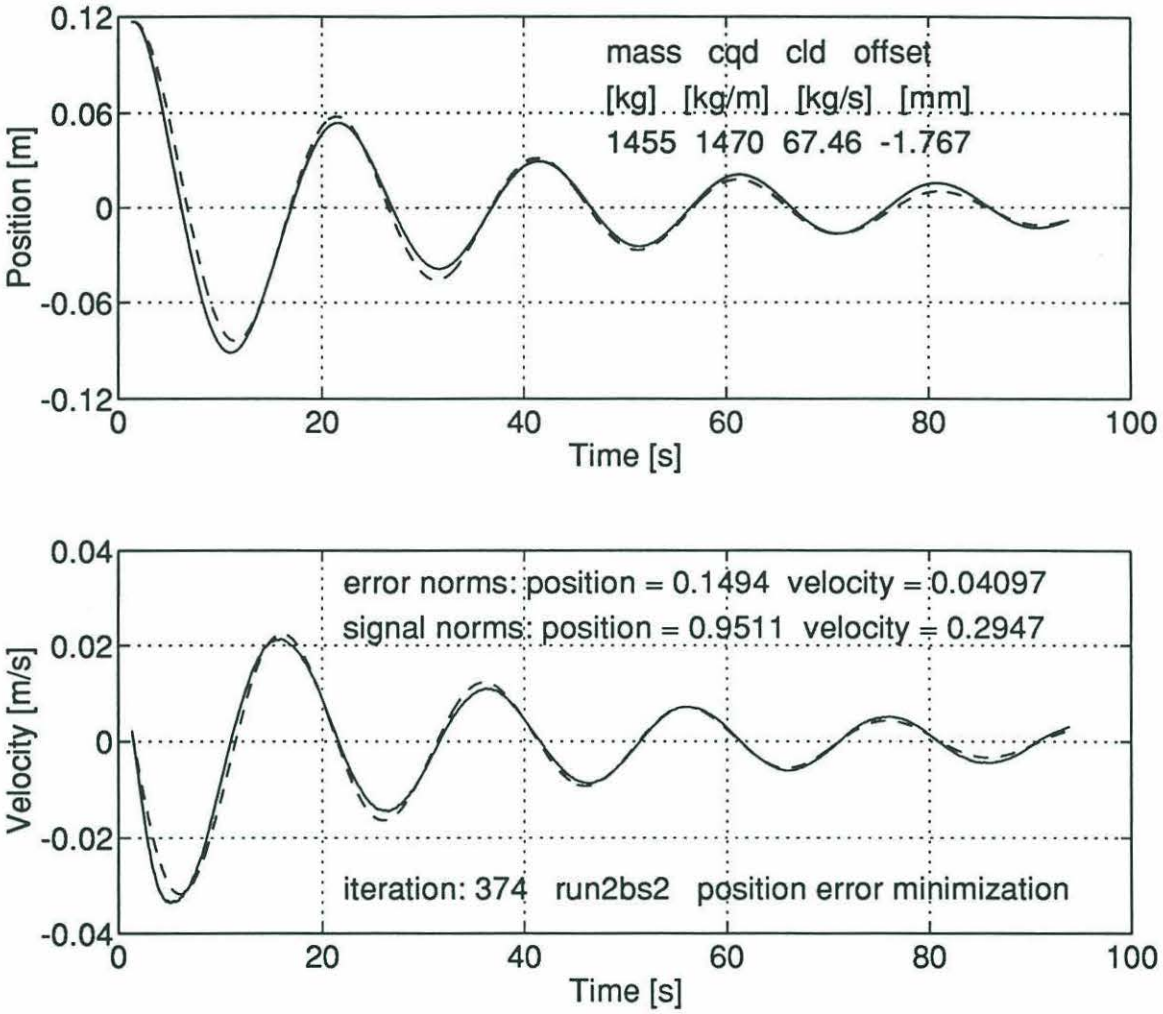

Figure A.39: NUMERICAL MINIMIZATION - INERTIA WITH QUADRATIC AND LINEAR DRAG MODEL - RUN 2BS2 - The vehicle trajectory is marked by the solid line. The dashed trace is the path followed by the model.

Model	m_{eff} $[kg]$	c_{qd} $[kg/m]$	c_{ld} $[kg/s]$	F_{spring}	$F_{inertia}$	F_{q-drag}	F_{l-drag}
				$[N]$			
inertia	1384			5.09	4.98		
inertia with linear drag	1455		260	5.09	5.24		2.78
inertia with quadratic drag	1451	5534		5.09	5.22	.63	
inertia with quadratic and linear drag	1455	1470	67	5.09	5.24	.17	.72

Table A.8: RUN 2BS2 - Two springs in series, effective spring constant: 146.7 N/m.

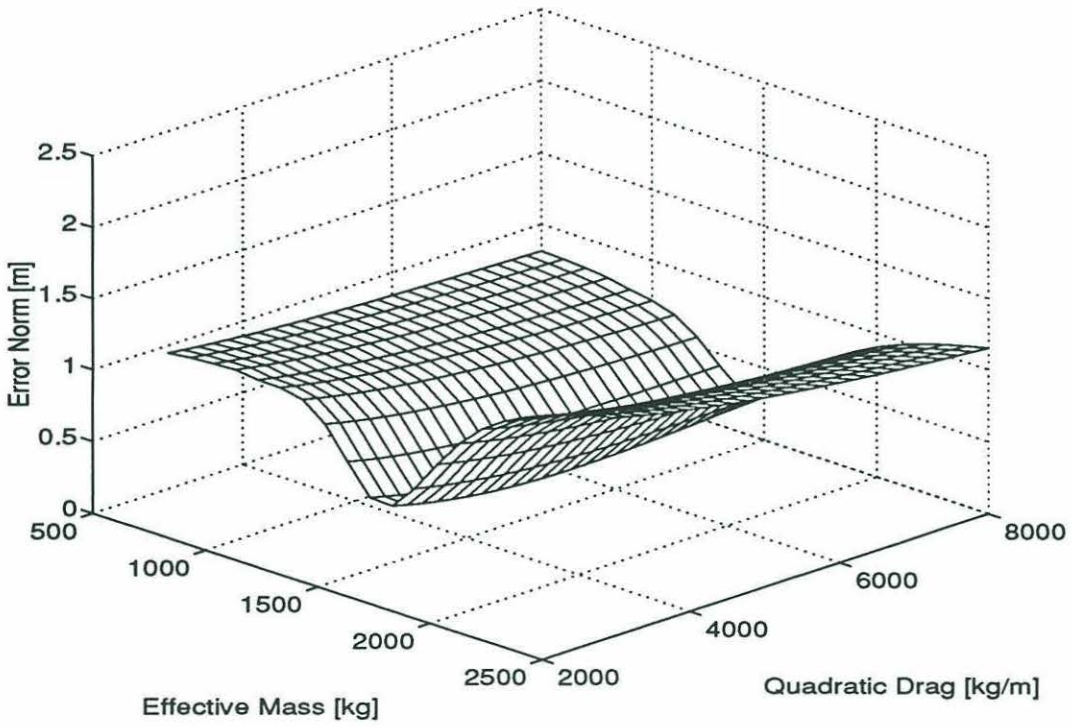

Figure A.40: ERROR NORM SURFACE FOR THE INERTIA WITH QUADRATIC DRAG MODEL AND VEHICLE TRAJECTORY 2BS2

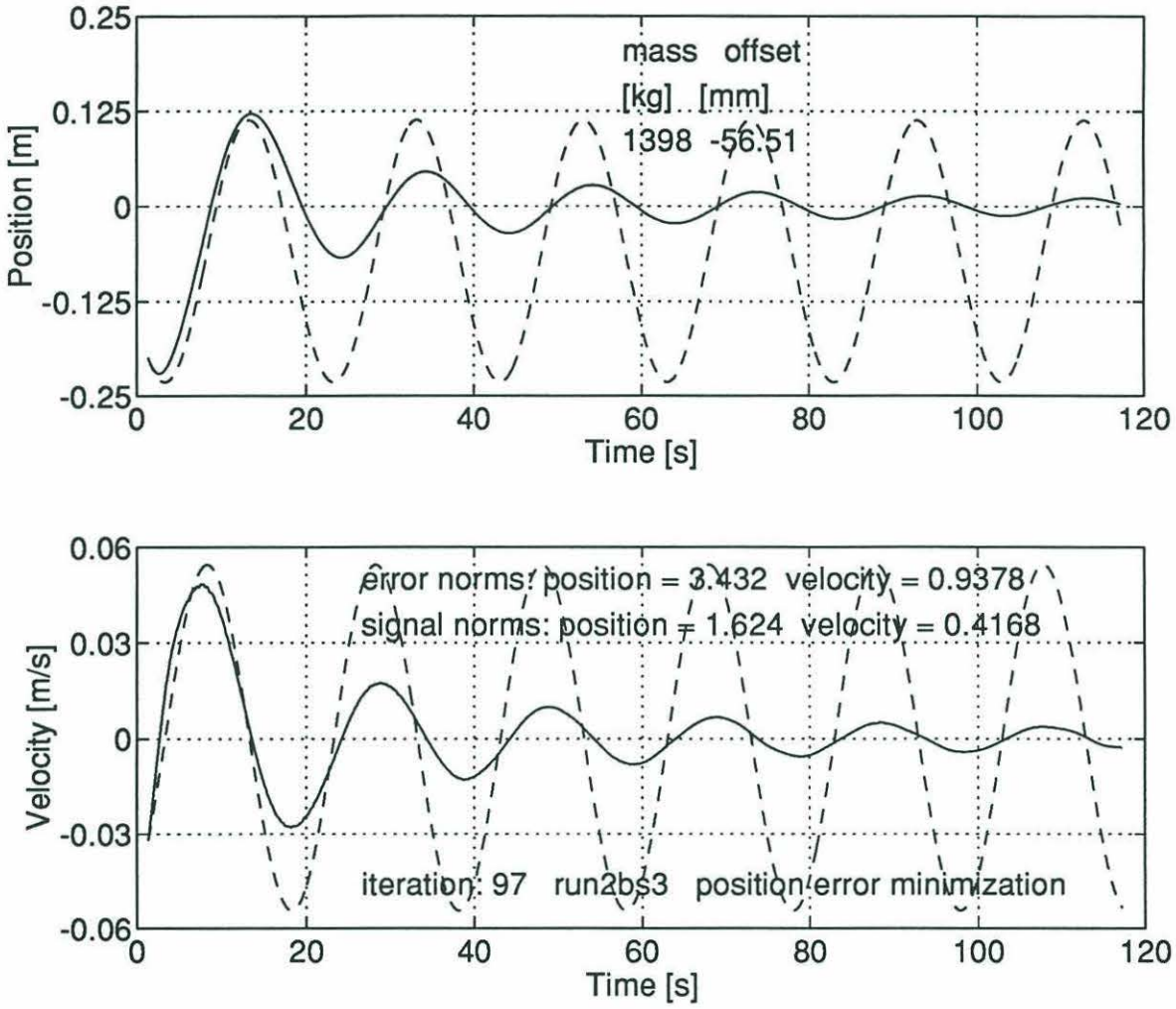

Figure A.41: NUMERICAL MINIMIZATION - INERTIA MODEL - RUN 2BS3 - The vehicle trajectory is marked by the solid line. The dashed trace is the path followed by the model.

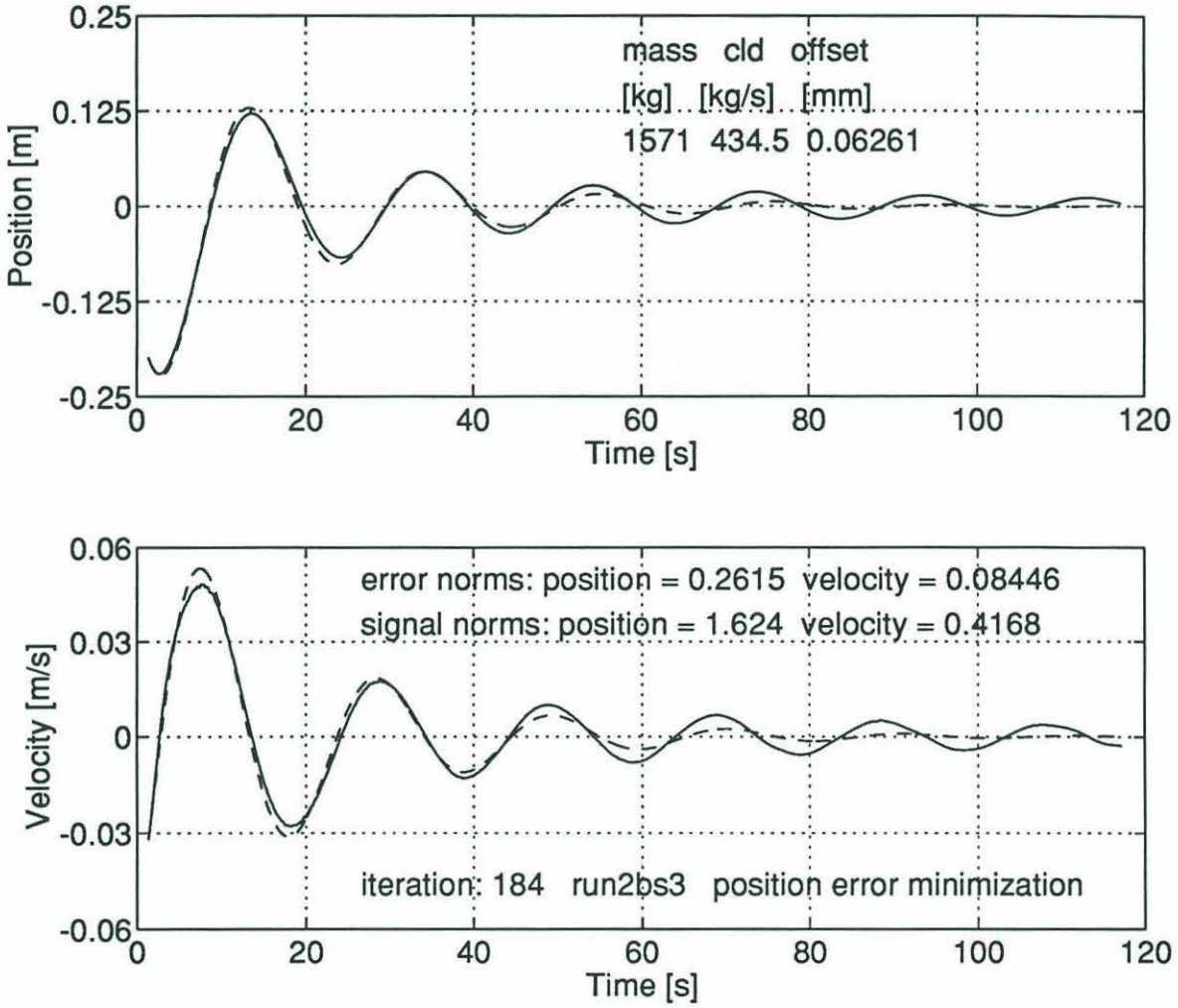

Figure A.42: NUMERICAL MINIMIZATION - INERTIA WITH LINEAR DRAG MODEL - RUN 2BS3 - The vehicle trajectory is marked by the solid line. The dashed trace is the path followed by the model.

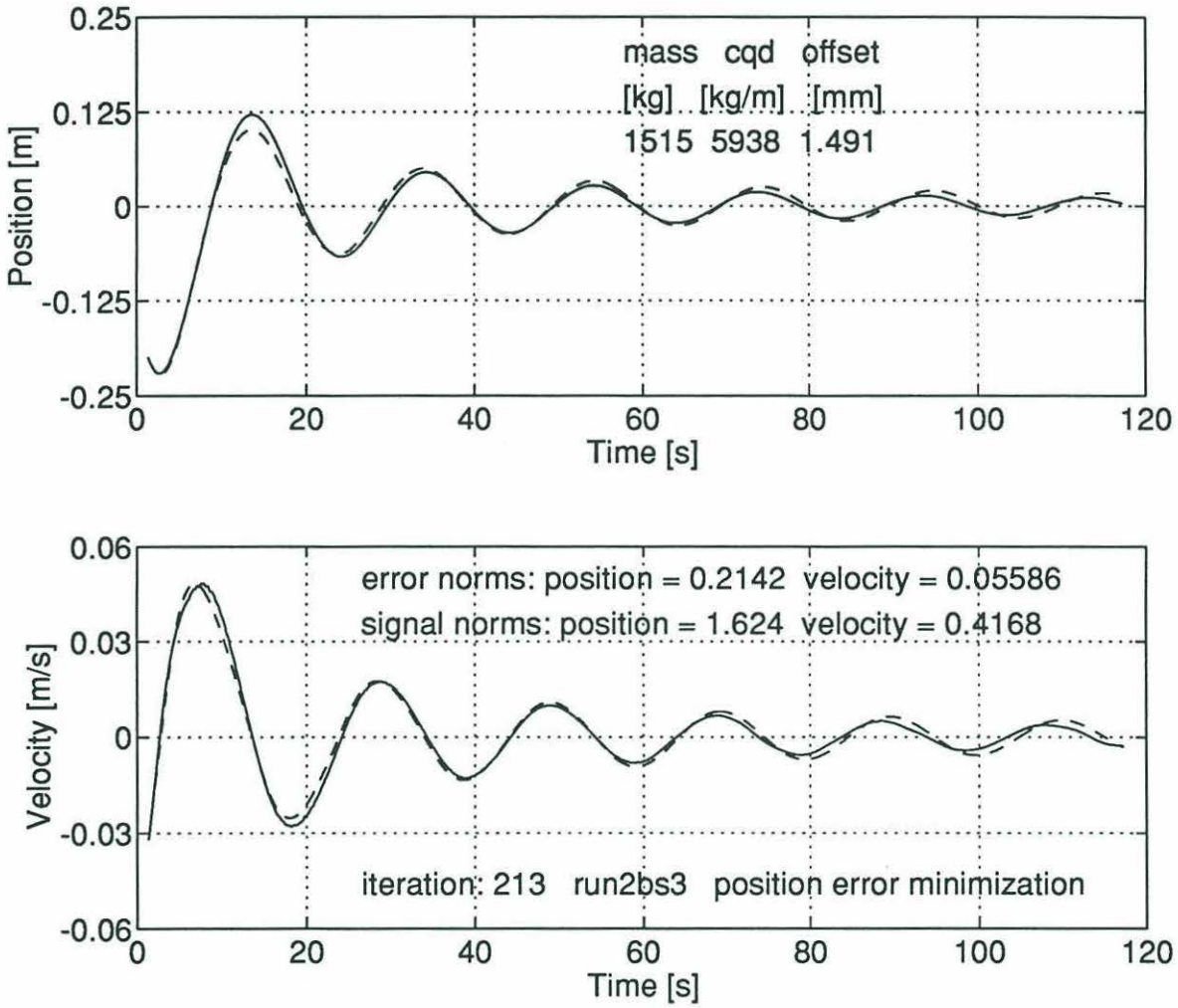

Figure A.43: NUMERICAL MINIMIZATION - INERTIA WITH QUADRATIC DRAG MODEL - RUN 2BS3 - The vehicle trajectory is marked by the solid line. The dashed trace is the path followed by the model.

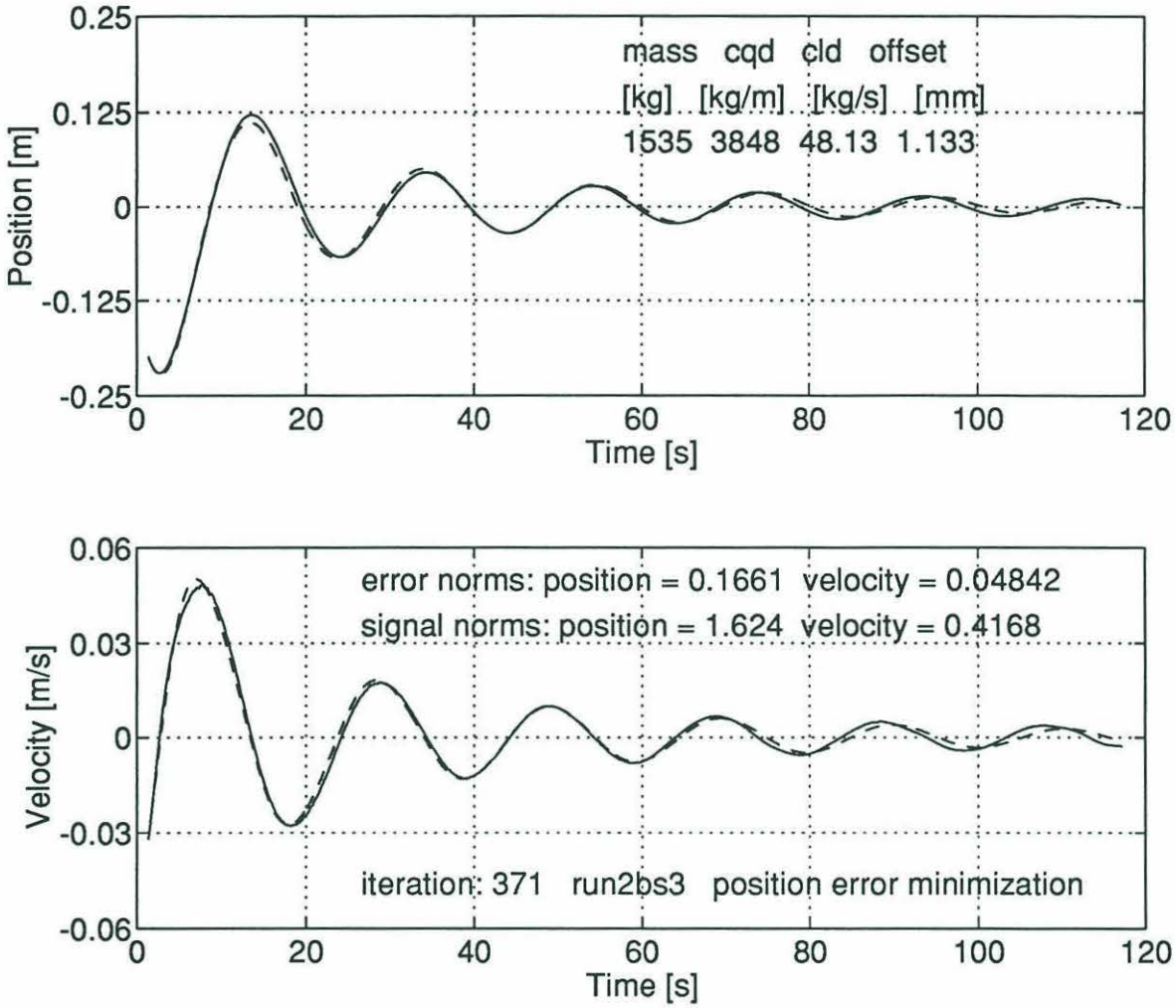

Figure A.44: NUMERICAL MINIMIZATION - INERTIA WITH QUADRATIC AND LINEAR DRAG MODEL - RUN 2BS3 - The vehicle trajectory is marked by the solid line. The dashed trace is the path followed by the model.

Model	m_{eff} $[kg]$	c_{qd} $[kg/m]$	c_{ld} $[kg/s]$	F_{spring}	$F_{inertia}$	F_{q-drag}	F_{l-drag}
				$[N]$			
inertia	1398			7.73	6.85		
inertia with linear drag	1571		435	7.73	7.70		5.87
inertia with quadratic drag	1515	5938		7.73	7.42	1.08	
inertia with quadratic and linear drag	1535	3848	48	7.73	7.52	.70	.65

Table A.9: RUN 2BS3 - Two springs in series, effective spring constant: 146.7 N/m.

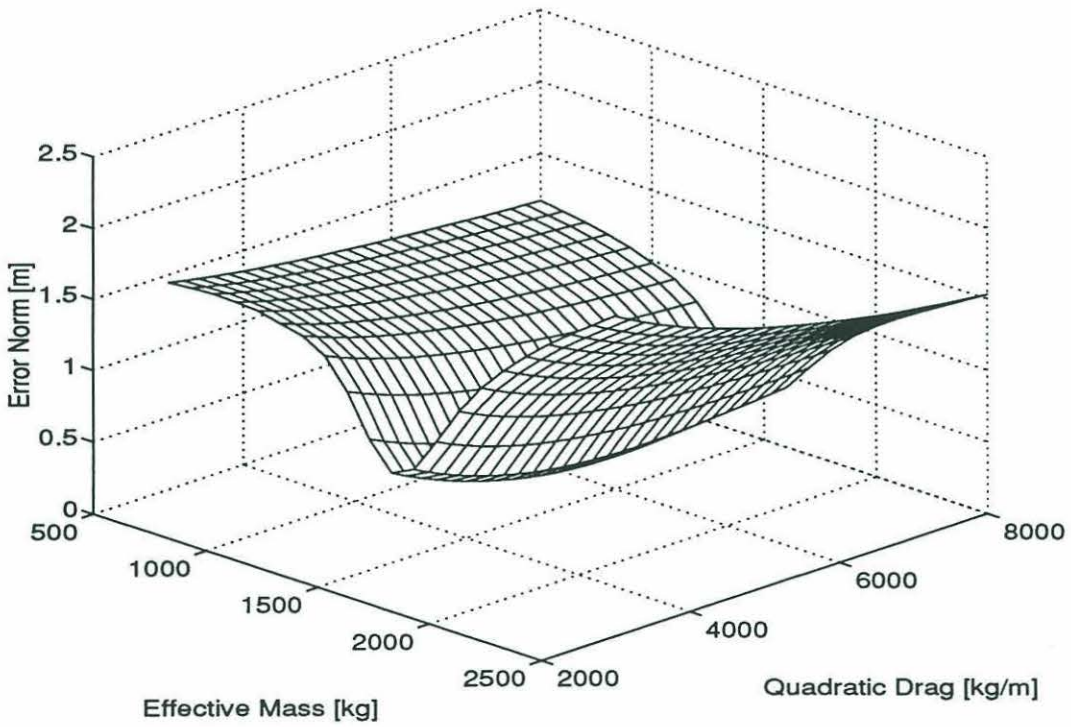

Figure A.45: ERROR NORM SURFACE FOR THE INERTIA WITH QUADRATIC DRAG MODEL AND VEHICLE TRAJECTORY 2BS3

Bibliography

[1] Bearman, P. W., Downie, M. J., Graham, J. M. R., Obasaju, E. D., "Forces On Cylinders in Viscous Oscillatory Flow at Low Keulegan-Carpenter Numbers", *Journal of Fluid Mechanics* (1985), Vol. 154, pp. 337-356.

[2] Beyer, W. H., CRC Standard Mathematical Tables (28th ed.), CRC Press, Boca Raton, FL, 1987.

[3] Bozic, S. M., Digital and Kalman Filtering, Edward Arnold, London, 1979.

[4] Cooke, J. G., "Incorporating Thruster Dynamics in the Control of an Underwater Vehicle", Engineer's/Master's Thesis, MIT/WHOI Joint Program in Oceanographic Engineering, 1989.

[5] Cooke, J. G., Yoerger, D. R., Slotine, J.-J. E., "The Influence of Thruster Dynamics on Underwater Vehicle Behavior and Their Incorporation Into Control System Design", *IEEE Journal of Oceanic Engineering*, Vol. 15, No. 3, July 1990.

[6] Faltinsen, O. M., Sea Loads On Ships and Offshore Structures, Cambridge University Press, Cambridge, 1990.

[7] Franklin, G. F., Powell, J. D., Workman, M. L., Digital Control of Dynamic Systems (2nd ed.), Addison-Wesley, New York, 1990.

[8] Friedland, B., Control System Design, McGraw-Hill, New York, 1986.

[9] Gelb, A. (ed.), Applied Optimal Estimation, MIT Press, Cambridge, 1974.

[10] Graham, D., McRuer, D., Analysis of Nonlinear Control Systems, John Wiley and Sons, New York, 1961.

[11] Graham, J. M. R., "The Forces on Sharp-edged Cylinders in Oscillatory Flow at Low Keulegan-Carpenter Numbers", *Journal of Fluid Mechanics* (1980), Vol. 97, pp. 331-346.

[12] Kalman, R. E., "A New Approach to Linear Filtering and Prediction Problems", *Transactions of the ASME, Journal of Basic Engineering*, Vol. 82D, March 1960, pp. 35-45.

[13] Kalman, R. E., Bucy, R. S., "New Results in Linear Filtering and Prediction Theory", *Transactions of the ASME, Journal of Basic Engineering*, Vol. 83D, December 1961, pp. 95-108.

[14] Luenberger, D. G., Introduction to Dynamic Systems, John Wiley and Sons, New York, 1979.

[15] Morison, J. R., O'Brien, M. P., Johnson, J. W., Schaaf, S. A., "The Force Exerted By Surface Waves On Piles", *Petroleum Transactions* (1950), Vol. 189, pp. 149-157.

[16] Morrison, A. T., III, Yoerger, D. R., "Determination of the Hydrodynamic Parameters of an Underwater Vehicle During Small Scale, Nonuniform, 1-Dimensional Translation", *Proceedings OCEANS '93*, IEEE/OES, October 1993, Vol. II, pp. 277-282.

[17] Ogata, K., Modern Control Engineering, Prentice-Hall, Englewood Cliffs, NJ, 1970.

[18] Press, W. H., Flannery, B. P., Teukolsky, S. A., Vetterling, W. T., Numerical Recipes in C, Cambridge University Press, Cambridge, 1988.

[19] Sagatun, S. I., Fossen, T. I., "The Norwegian Experimental Remotely Operated Vehicle Hydrodynamic Properties", Division of Engineering Cybernetics, Norwegian Institute of Technology, Trondheim, Norway.

[20] Sagatun, S. I., "Modelling and Control of Underwater Vehicles: A Lagrangian Approach", Doctoral Thesis, March 1992, Division of Engineering Cybernetics, Norwegian Institute of Technology, Trondheim, Norway.

[21] Sage, A. P., Melsa, S. A., System Identification, Academic Press, New York, 1971.

[22] Sarpkaya, T., Garrison, C. J., "Vortex Formation and Resistance in Unsteady Flow", *Journal of Applied Mechanics*, Vol. 30, No. 1, *Transaction of the ASME*, Vol. 85, Series E, March 1963, pp. 16-24.

[23] Sarpkaya, T., Isaacson, M., Mechanics of Wave Forces On Offshore Structures, Van Nostrand Reinhold Company, New York, NY, 1981.

[24] Sarpkaya, T., "Force On a Circular Cylinder in Viscous Oscillatory Flow at Low Keulegan-Carpenter Numbers", *Journal of Fluid Mechanics* (1986), Vol. 165, pp. 61-71.

[25] Sarpkaya, T., "In-line and Transverse Forces On Smooth and Rough Cylinders In Oscillatory Flow at High Reynolds Numbers", Naval Postgraduate School Interim Report, Prepared for the National Science Foundation, July, 1986.

[26] Sarpkaya, T., "Nonimpulsively Started Steady Flow About a Circular Cylinder", *AIAA Journal*, Vol. 29, No. 8, August 1991, pp. 1283-1289.

[27] Sarpkaya, T., personal communication, July 12, 1993.

[28] Slotine, J.-J. E., Li, W., Applied Nonlinear Control, Prentice-Hall, Englewood Cliffs, NJ, 1991.

[29] Sorenson, H. W., "Kalman Filtering Techniques", Advances in Control Systems, Vol. 3, Leondes, C. T., ed., Academic Press, New York, 1966, pp. 219-292.

[30] Sorenson, H. W., "Least-squares Estimation: from Gauss to Kalman", *IEEE Spectrum*, July, 1970, pp. 63-68.

[31] Wang, C.-Y., "On High-frequency Oscillatory Viscous Flows", *Journal of Fluid Mechanics* (1968), Vol. 32, pp. 55-68.

[32] Yoerger, D. R., personal communications, 1989-91.